JYU DISSERTATIONS 326

Elli Selenius

Optical Properties of Metal Clusters and Cluster Arrangements

UNIVERSITY OF JYVÄSKYLÄ
FACULTY OF MATHEMATICS
AND SCIENCE

JYU DISSERTATIONS 326

Elli Selenius

Optical Properties of Metal Clusters and Cluster Arrangements

Esitetään Jyväskylän yliopiston matemaattis-luonnontieteellisen tiedekunnan
suostumuksella julkisesti tarkastettavaksi
joulukuun 11. päivänä 2020 kello 12.

Academic dissertation to be publicly discussed, by permission of
the Faculty of Mathematics and Science of the University of Jyväskylä,
on December 11, 2020 at 12 o'clock noon.

JYVÄSKYLÄN YLIOPISTO
UNIVERSITY OF JYVÄSKYLÄ

JYVÄSKYLÄ 2020

Editors
Timo Sajavaara
Department of Physics, University of Jyväskylä
Päivi Vuorio
Open Science Centre, University of Jyväskylä

Permanent link to this publication: http://urn.fi/URN:ISBN:978-951-39-8433-5

ISBN 978-951-39-8433-5 (PDF)
URN:ISBN:978-951-39-8433-5
ISSN 2489-9003 Jyväskylä University Printing House, Jyväskylä 2020

ABSTRACT

Selenius, Elli
Optical Properties of Metal Clusters and Cluster Arrangements
University of Jyväskylä, 2020, 70 p.(+included articles)
(JYU Dissertations
ISSN 2489-9003; **326**)
ISBN 978-951-39-8433-5 (PDF)

Metal clusters are nanoparticles that have from two to thousands of metal atoms. The properties of metal clusters are extremely size-dependent, and adding or removing even one atom can make a difference. The optical response of clusters is influenced by their composition, shape, size, charge, and environment. This tunability makes metal clusters and cluster arrangements ideal candidates for several applications ranging from cancer imaging and treatment to photovoltaic devices. Especially clusters with plasmons, strong collective excitations of the valence electrons, are of interest. In this thesis, the plasmon resonance in metal clusters and cluster arrangements is investigated computationally. The density functional theory and the simple jellium model are employed to study the principles of the plasmon resonance from the electronic perspective. The evolution of the localized surface plasmon resonance is followed in clusters with 8–138 valence electrons. The coupling of plasmons of the individual clusters is observed for dimers and larger cluster assemblies. The emergence of charge transfer plasmons at low energies is observed for systems with conductive linking or sufficiently small inter-cluster separation. Several tools, such as transitions contribution maps and visualization of the induced density are used to analyze the features which make an absorption peak plasmonic, and to distinguish different types of plasmons. A new quantitative index is developed to study the charge transfer nature of excitations, helping in the identification of the charge transfer plasmons. The detailed analysis of the optical excitations in these model systems can help to interpret the absorption spectra of more complex, real cluster systems.

Keywords: metal clusters, jellium, plasmons, density functional theory, optical absorption, electronic structure

Author

Elli Selenius
Department of Physics
Nanoscience Center
University of Jyväskylä
Finland

Supervisor

Academy Professor Hannu Häkkinen
Department of Physics
Department of Chemistry
Nanoscience Center
University of Jyväskylä
Finland

Co-Supervisor

University Researcher Sami Malola
Department of Physics
Nanoscience Center
University of Jyväskylä
Finland

Reviewers

Professor Puru Jena
Department of Physics
Virginia Commonwealth University
USA

Professor (emeritus) Martti Puska
Aalto University
Finland

Opponent

Professor Tapio Rantala
Department of Physics
Tampere University
Finland

YHTEENVETO (FINNISH SUMMARY)

Metalliklusterit ovat nanopartikkeleita, jotka koostuvat kahdesta tai usemmasta, enintään tuhansista metalliatomeista. Metalliklusterien ominaisuudet riippuvat voimakkaasti klusterin koosta, ja jopa yhden atomin lisäämisellä tai poistamisella voi olla suuri vaikutus. Klusterien optiseen vasteeseen vaikuttavat klusterin koostumus, muoto, koko, varaus ja ympäristö. Muuntelemalla näitä ominaisuuksia voidaan valmistaa haluttuun käyttötarkoitukseen sopivia klusterisysteemejä. Metalliklustereilla onkin runsaasti sovelluskohteita syöpäterapiasta aurinkokennoihin. Erityisen kiinnostuksen kohteena ovat klusterit, joiden valenssielektronit värähtelevät kollektiivisesti tietyllä resonanssitaajuudella. Näitä kollektiivisia elektronien virityksiä kutsutaan plasmoneiksi. Tässä väitöskirjassa metalliklusterien ja klusterisysteemien plasmoniresonansseja tutkitaan laskennallisesti. Tiheysfunktionaaliteorian ja jellium-mallin avulla plasmoneja tarkastellaan elektronien näkökulmasta. Lokalisoituneen pintaplasmoniresonanssin kehitystä seurataan klustereissa, joissa on 8 – 138 valenssielektronia, ja plasmonien kytkeytymistä tarkastellaan kahden ja useamman klusterin järjestelmissä. Klusterirakennelmissa, jotka koostuvat toisiinsa yhdistetyistä tai hyvin lähekkäisistä klustereista, havaitaan myös varauksensiirtoplasmoneja. Erilaisten plasmonipiikkien tunnistamiseen absorptiospektristä käytetään muuan muassa yksittäisten elektronisiirtymien analysointia sekä indusoidun tiheyden visualisoimista. Väitöskirjatyössä esitellään myös uusi tapa määritellä, kuinka paljon varausta klusterien välillä siirtyy hetkellisesti kollektiivisen värähtelyn aikana. Tämän varauksensiirtoindeksin avulla varauksensiirtoplasmonit voidaan tunnistaa spektristä. Väitöskirjassa esitelty perusteellinen tutkimus metalliklusterien optisista ominaisuuksista yksinkertaistetuissa mallisysteemeissä voi auttaa tulkitsemaan oikeiden, monimutkaisten klusterisysteemien optisia vasteita.

PREFACE

The work included in this thesis was carried out in the Nanoscience Center of the University of Jyväskylä between 2016 and 2020, under the supervision of academy professor Hannu Häkkinen and university researcher Sami Malola. I would like to thank both my supervisors for their guidance and support during these years, and for giving me the best possible start on my academic career. I am grateful for the interesting and challenging projects I have been able to participate in, and for all the help and encouragement I have received.

I thank Dr. Mikael Kuisma for comments and feedback, and for always coming up with a detailed suggestion or solution to any problem presented to him. Thanks also to Dr. Lauri Lehtovaara for swift advice, honest feedback, and interesting discussions. I wish to thank professor Puru Jena and professor emeritus Martti Puska for thoroughly reviewing my thesis and giving valuable comments and feedback, and professor Tapio Rantala for agreeing to act as my opponent.

I am grateful for the Emil Aaltonen Foundation and the Finnish Cultural Foundation for helping to enable this research by funding periods of my thesis work. I also want to acknowledge CSC - The Finnish IT Center for Science for the generous computational resources, especially the grand challenge project COUPLES, that have made my work possible.

I would like to thank everyone in the Nanoscience Center for making it a great environment to do interdisciplinary research. I have had many stimulating discussions and received advice from several of my colleagues. I especially want to thank all my previous and current group members - for suggestions on research, for sharing experiences about the academic life, and for generally being really nice people to work with. Thanks to Sami K. for all the programming help and DFT discussions during the years, and to Emmi for giving advice on all conference-related questions, from poster templates to dress code. Special thanks to Omar - for making my life easier by teaching me about bash aliases, for helping me rediscover my passion for science when it seemed to be lost, and for being a great friend.

Finally, I would like to thank my family. My parents kindled my interest in science by teaching me to be curious and to appreciate the wonders of the world. Whenever I need encouragement, advice, or diversion from work, my parents and my brother and sister are there for me. Thank you for all the love and support.

In Jyväskylä, November 19, 2020
Elli Selenius

LIST OF ABBREVIATIONS

NP	Nanoparticle
LSPR	Localized surface plasmon resonance
BDP	Bonding dipole plasmon
CTP	Charge transfer plasmon
TCM	Transition contribution map
DTCM	Dipole transition contribution map
CTR	Charge transfer ratio
DFT	Density functional theory
K-S	Kohn-Sham
LDA	Local density approximation
TDDFT	Time-dependent density functional theory
lr-TDDFT	Linear-response time-dependent density functional theory
PAW	Projector augmented-wave method
e-h	electron-hole
VPR	Volume density response proportion
GPI	Generalized plasmonicity index
TIPR	Transition inverse participation ratio
TD-DFTP	Time-dependent density functional perturbation theory
PDOS	Projected density of states
HOMO	Highest occupied molecular orbital
LUMO	Lowest unoccupied molecular orbital

CONTENTS

ABSTRACT
YHTEENVETO (FINNISH SUMMARY)
PREFACE
LIST OF ABBREVIATIONS
CONTENTS
LIST OF INCLUDED ARTICLES

1 INTRODUCTION 1

2 THEORY AND METHODS 5
2.1 Density functional theory 5
2.1.1 Local density approximation 8
2.1.2 Linear response time-dependent density functional theory 9
2.2 Jellium model 11
2.3 GPAW 12
2.4 Analysis of the optical excitations 13
2.4.1 Measures for the plasmonicity 13
2.4.1.1 Transition contribution maps 14
2.4.1.2 Induced density 15
2.4.1.3 Charge transfer ratios 16

3 RESULTS AND DISCUSSION 19
3.1 Single clusters 20
3.2 Dimers 29
3.2.1 Homodimers 30
3.2.2 Heterodimer 35
3.3 Two-dimensional cluster arrangements 38
3.4 Three-dimensional cluster arrangements 43

4 CONCLUSIONS AND OUTLOOK 49

REFERENCES 52

INCLUDED ARTICLES

LIST OF INCLUDED ARTICLES

PI **Elli Selenius**, Sami Malola, Hannu Häkkinen. Analysis of Localized Surface Plasmon Resonance in Spherical Jellium Clusters and Their Assemblies. *The Journal of Physical Chemistry C*, **121** (48), 27036–27052, (2017).

PII **Elli Selenius**, Sami Malola, Mikael Kuisma, Hannu Häkkinen. Charge Transfer Plasmons in Dimeric Electron Clusters. *The Journal of Physical Chemistry C*, **124** (23), 12645–12654, (2020).

PIII **Elli Selenius**, Sami Malola, Hannu Häkkinen. Analysis of the Plasmonic Excitations in Assemblies of Three-Dimensional Electron Clusters. *Physical Review B*, accepted, (2020).

In articles [PI]–[PIII], the author carried out all the calculations, participated in the analysis of the data, and wrote the first draft.

The author has also contributed to the following publications:

LIST OF OTHER ARTICLES

API Peng Yuan, Ruihua Zhang, **Elli Selenius**, Pengpeng Ruan, Yangrong Yao, Yang Zhou, Sami Malola, Hannu Häkkinen, Boon K. Teo, Yang Cao, and Nanfeng Zheng. Thiol-stabilized atomically precise, superatomic silver nanoparticles for catalysing cycloisomerization of alkynyl amines. *National Science Review*, **5** (5), 694–702 (2018).

APII P. Yuan, R. Zhang, **Elli Selenius**, P. Ruan, Y. Yao, Y. Zhou, Sami Malola, Hannu Häkkinen, B. K. Teo, Y. Cao, N. Zheng. Solvent-mediated assembly of atom-precise gold-silver nanoclusters to semiconducting one-dimensional materials *Nature Communications*, **11**, 2229 (2020)

APIII H. Shen, **Elli Selenius**, P. Ruan, X. Li, P. Yuan, Omar Lopez-Estrada, Sami Malola, S. Lin, B. K. Teo, Hannu Häkkinen and N. Zheng. Solubility-Driven Isolation of a Metastable Nonagold Cluster with Body-Centered Cubic Structure. *Chemistry - A European Journal*, **26** (38), 8465–8470 (2020).

1 INTRODUCTION

Going from the macroscopic world to nanoscale, the properties of materials can be very different from their bulk counterparts. One example is the optical absorption of metal nanoparticles (NPs). Long before any explanation was given for the phenomenon, colloidal metal particles have been utilized in making stained glass, used for example in church windows. One of the earliest documented uses of gold and silver NPs in stained glass is the Lycurgus cup, a Roman glass goblet from the 4th century, which appears green when observed in reflected light and red in transmitted light [1].

Faraday was the first to systematically study the colors of colloidal gold particles [2]. In the 19th century, he prepared many colloidal fluids with diffused gold particles of various sizes, and observed the different colors. However, it was Mie in 1908 who first developed an equation for the scattering of light by spherical metal particles [3]. In the Mie theory, the strength of the scattering at a certain wavelength is related to the radius of the particle and the material.

The phenomenon behind the different colors is the localized surface plasmon resonance (LSPR). At the resonance frequency, the valence electrons of the metal atoms in the NP oscillate collectively with respect to the positive ion cores, causing a peak in the absorption spectrum. The color corresponding to this frequency is thus absent from the light transmitted through the material containing the NPs, such as a glass window or a colloidal solution. The collective electron density oscillations are concentrated near the surface of the particle.

The LSPR frequency and other optical properties of metal NPs depend, besides on the composition, on the size, shape, and dielectric environment of the particles [4]. If two or more NPs are placed in an arrangement with sufficiently short interparticle separations, the plasmons of the individual clusters will interact, which also affects the optical response [5]. Because of this tunability, plasmonic NPs and their assemblies are used in several applications, such as photothermal cancer therapy and cancer cell imaging [6, 7], photovoltaic devices [8], and in measuring

distances in the nanoscale [9].

Small metal NPs, which have from two to thousands of atoms, are called metal clusters. The properties of the clusters are defined by the atomic composition, geometric structure, electronic charge, and chemical environment [10]. In this size range, the attributes of the particles are also extremely size-dependent. Among other properties, such as the stability and magnetization, the optical absorption of a cluster can change drastically if even one atom is added or removed [11, 12, 13]. This makes metal clusters particularly interesting subjects to study.

Although metal clusters were studied before, the interest in clusters grew significantly in the early 1980's, when the electronic shells structure of simple metal clusters was found. This phenomenon was simultaneously predicted theoretically by Ekardt [14] and Beck [15] using the self-consistent jellium model, and observed experimentally in the pioneering studies of Knight et al. [16] and Kappes et al. [17]. Since the valence electrons of the metal atoms are delocalized and move in the potential of the positive ion cores, they fill electron states similarly as electrons in atoms. This shell structure manifests for example as peaks in the abundance spectrum of metal clusters, showing that certain cluster sizes are considerably more stable than those having less or more atoms. The number of atoms in these clusters are called magic numbers, and the number of valence electrons correspond to electronic shell closings. For sodium and other alkali metals with one s-type valence electron, for example, the first magic numbers are 8, 20, 34, 40, and 58.

Since clusters possess similar properties to atoms with the same shell structure, a parallel with the periodic table of elements can be made for clusters. Following this idea, Khanna and Jena introduced the term superatom to describe stable clusters with shell-closures [18]. They also proposed that clusters have potential to be used as building blocks for new materials with tailor-made properties [19, 18].

In the early studies in the 1980s, bare metal clusters produced and detected in a beam were usually investigated [11]. Deposited on a surface, bare clusters often aggregate to form bigger metal particles [20, 21, 22]. Starting from the 1990s, a new branch of the cluster science was developed: the synthesis and study of ligand-protected metal clusters [10]. The ligand layer has the effect of stabilizing the clusters and preventing aggregation, facilitating the construction of cluster crystals. Häkkinen and co-workers expanded the superatom model for these ligand-protected clusters, developing electron-counting rules to account for the role of ligands in the electronic shell structure [23]. Recently, several crystals of ligand-protected gold and silver clusters have been synthesized [10, 24, 25, 13], as well as polymers of clusters connected by metal atoms [26, 27, 28] and self-assembled superstructures of clusters [29].

For small clusters and cluster arrangements with very narrow gaps, the Mie theory is not anymore sufficient. For clusters of a few nanometers of size and cluster arrangements with separations of less than one nanometer, the classical treatment does not accurately reproduce the optical properties, and quantum me-

chanical techniques have to be used [30, 31]. The time-dependent density functional theory is nowadays widely employed in optical calculations for clusters [32, 33, 34, 35, 36, 37].

For the smallest cluster sizes, the absorption spectra might be molecule-like, not supporting a plasmon peak but rather having several discrete excitations [38]. The cluster size where the transition to surface plasmonic behaviour happens depends on the cluster type, with LSPR-like excitations observed in sodium clusters of only 8 atoms [39], while the cross-over region in thiolate-protected gold clusters is observed to be somewhere between 100 and 300 gold atoms [40, 41].

For plasmonic clusters, the absorption spectra may contain features caused by surface plasmon resonance, core plasmon resonances, non-coupled single-particle excitations, and combinations of these [12]. In arrangements of two or more clusters, the individual plasmons can additionally hybridize, forming a bonding dipole plasmon (BDP) in the case of a dimer [5, 42]. With linked clusters or sufficiently close separations a new type of collective excitation, the charge transfer plasmon (CTP), can emerge [30], which involves electron density oscillations between the clusters. Therefore, it is not always trivial to classify the absorption peaks in the spectrum. To facilate this analysis, various approaches have been proposed to identify plasmonic excitations, especially LSPR peaks [43, 33, 44, 45, 32, 46, 47, 48].

This thesis aims to add to the knowledge of plasmons in small metal clusters and cluster assemblies. The optical properties of these systems were studied using the density functional theory code GPAW [49, 50] and the jellium model. The simple jellium model treats only the valence electrons explicitely and represents the rest of the atoms by a uniform, positive background density. Thus, with the combination of density functional theory and jellium, the effect of the atomic cores is neglected and the system is simplified, but the valence electrons are modeled accurately. This enables the detailed study of the plasmonic phenomena from the electronic perspective. The jellium density was chosen to be that of sodium, which is the metal best represented by the this model.

In the included articles [PI]–[PIII], we studied the birth of the LSPR in separate clusters, and coupling of the plasmons and emergence of the CTP in dimers and planar and three-dimensional assemblies. We used the (dipole) transition contribution scheme (D)TCM [40, 51] and analysis of the induced transition densities to asses the collectivity of the excitations, the additivity of the transitions to the dipole moment, and the distribution of the electron density oscillations. We also develop a new index, the charge transfer ratio (CTR), to quantify the charge transfer nature of excitations in the absorption spectra.

The spectra of the separate clusters agreed qualitatively with experimental results for sodium clusters [39]. However, the other systems do not have a one-to-one match in real cluster systems. Rather, they are simplified models, and we hope that the understanding gained from these systems will help in the analysis of the more complex, realistic systems in the future.

This thesis is organized as follows: In chapter 2, I present the main computational tools and methods used and the theory behind them. In chapter 3, I recount the results of articles [PI]–[PIII]. In chapter 4, I summarize the main findings of this thesis and introduce possible avenues for future studies.

2 THEORY AND METHODS

In this chapter I will present the main tools and methods used in articles [PI]–[PIII] and the theory behind them. I will start with the theory enabling the quantum mechanical calculations of these cluster systems, the density functional theory. After that, I will introduce the jellium model used to represent the clusters and the GPAW code employed in the calculations. Finally, I will present various analysis tools for analyzing the plasmoninicity of absorption peaks, starting with a short review of the literature and finishing with the methods used in this thesis.

2.1 Density functional theory

Finding out the ground-state energy E of a quantum mechanical system of N identical particles requires solving the Schödinger equation:

$$\hat{H}\Psi(\mathbf{r_1}, \mathbf{r_2}, ..., \mathbf{r_N}) = E\Psi(\mathbf{r_1}, \mathbf{r_2}, ..., \mathbf{r_N}), \tag{1}$$

where $\hat{H}$ is the Hamiltonian operator and $\Psi(\mathbf{r_1}, \mathbf{r_2}, ..., \mathbf{r_N})$ the ground-state wavefunction. Here $\mathbf{r_i} = (x_i, y_i, z_i)$ are the spatial coordinates of the particles. Typically in condensed matter physics, the particles are electrons moving in the potential of the nuclei V. Since the nuclei are moving many orders of magnitude slower than the electrons, they can be considered to be fixed when solving the Schödinger equation for the electrons. Making this Born-Oppenheimer approximation, the Hamiltonian can be separated to the nuclear and electronic part. In this case, using atomic units, the Hamiltonian for the electronic part can be written as

$$\hat{H} = \hat{T} + \hat{W} + \hat{V}, \tag{2}$$

with the kinetic energy operator

$$\hat{T} = \sum_{i=1}^{N} -\frac{1}{2}\nabla_i^2, \tag{3}$$

the interaction term

$$\hat{W} = \frac{1}{2}\sum_{i\neq j}^{N} w(\mathbf{r_i}, \mathbf{r_j}), \tag{4}$$

and the contribution from interactions of the electrons with the external potential

$$\hat{V} = \sum_{i=1}^{N} v(\mathbf{r_i}). \tag{5}$$

Here $w(\mathbf{r_i}, \mathbf{r_j})$ is the two-particle interaction and $v(\mathbf{r_i})$ the interaction of electron i with the external potential. The electron density of the ground state can be calculated from the wavefunction:

$$n(\mathbf{r}) = N \int d\mathbf{r_2} \int d\mathbf{r_3} ... \int d\mathbf{r_N}\, \Psi^*(\mathbf{r}, \mathbf{r_2}, ..., \mathbf{r_N})\Psi(\mathbf{r}, \mathbf{r_2}, ..., \mathbf{r_N}). \tag{6}$$

Solving the ground-state energy requires dealing with 3N spatial variables, which makes the problem very complex. In 1964, Hohenberg and Kohn showed that there is a one-to-one correspondence between the external potential V and the electron density n [52]. As a consequence of this, the ground-state wavefunction is a unique functional of the density. Furthermore, the energy, and in fact any ground-state observable, is a functional of the electron density and it can be written as $E[n]$. Thus, the problem of finding the ground-state energy is greatly simplified, because now there are only three spatial coordinates (x, y, z) in the calculation.

Since the energy is the expectation value of the Hamiltonian operator, it can be now written as $E[n] = \langle\Psi[n]|\hat{H}|\Psi[n]\rangle$. Hohenberg and Kohn further showed that for a system with a constant number of particles N and a non-degenerate ground state, and for the set of all densities n, the correct ground state density n_0 corresponding to the ground state energy E_0 for Hamiltonian H_0 gives the minimum energy, so that

$$E[n] = \langle\Psi[n]|\hat{H_0}|\Psi[n]\rangle > \langle\Psi[n_0]|\hat{H_0}|\Psi[n_0]\rangle = E_0, \tag{7}$$

if $n \neq n_0$. This variational principle indicates that E_0 can be found by minimizing $E[n]$ with respect to n. This approach is called the density functional theory (DFT). Since $\hat{T}$ and $\hat{W}$ are the same for all electronic systems, the energy from the external potential $\langle\Psi[n]|\hat{V}|\Psi[n]\rangle$ is the term changing between different systems.

The following year from the publication of the Hohenberg-Kohn theorem, Kohn together with Sham developed an iterative scheme to solve the ground-state energy and density using DFT [53]. Their idea was to construct a system of N non-interacting electrons with the same ground-state density as the real interacting N-electron system with an external potential of v_0. These non-interacting electrons move in the effective potential v_{eff} that includes all the interaction terms. This system is called the Kohn-Sham (K-S) system, the wavefunctions of the non-interacting particles $\psi_i(\mathbf{r})$ K-S orbitals, and the energies of the orbitals ϵ_i K-S energies. This construction results in a group of single-particle K-S equations:

$$\left[-\frac{1}{2}\nabla^2 + v_{eff}(\mathbf{r})\right]\phi_i(\mathbf{r}) = \epsilon_i\phi_i(\mathbf{r}) \tag{8}$$

$$n(\mathbf{r}) = \sum_i^N \phi_i^*(\mathbf{r})\phi_i(\mathbf{r}) = \sum_i^N |\phi_i(\mathbf{r})|^2 \tag{9}$$

$$v_{eff}[n](\mathbf{r}) = v_0(\mathbf{r}) + v_H[n](\mathbf{r}) + v_{xc}[n](\mathbf{r}) \tag{10}$$

$$v_{xc}[n](\mathbf{r}) = \frac{\delta E_{xc}[n]}{\delta n(\mathbf{r})}. \tag{11}$$

Equation 8 is the Schrödinger equation for the non-interacting electrons, and equation 10 defines the effective potential. There $v_0(\mathbf{r})$ is the potential of the nuclei that depends on the system and $v_H(\mathbf{r}) = \int d\mathbf{r}' \frac{n(\mathbf{r}')}{|\mathbf{r}-\mathbf{r}'|}$ the so called Hartree potential, which contains the classical Coulomb repulsion. The exchange-correlation potential $v_{ex}[n](\mathbf{r})$ is calculated by taking the functional derivative with respect to the density of the corresponding exchange-correlation energy $E_{xc}[n]$, as stated in equation 11.

This exchange-correlation energy is defined as

$$E_{xc}[n] = T[n] + W[n] - E_H[n] - T_s[n], \tag{12}$$

where $T[n]$ and $W[n]$ are the full kinetic and interaction energy, respectively, $T_s[n] = \sum_i^N \int d\mathbf{r} |\nabla \phi_i(\mathbf{r})|^2$ is the kinetic energy of the non-interacting particles, and $E_H = \frac{1}{2} \int d\mathbf{r} \int d\mathbf{r}' \frac{n(\mathbf{r})n(\mathbf{r}')}{|\mathbf{r}-\mathbf{r}'|}$ the Hartree energy due to the Hartree potential.

The exchange-correlation energy thus contains the contributions to the kinetic energy that are due to the interacting nature of the electrons, as well as the quantum mechanical contributions to the interaction energy. The exchange part arises from the Pauli principle, which leads to the antisymmetric nature of the many-electron wavefunction with respect to the exchange of two electrons. The rest of the non-classical correlations between the movements of the electrons are contained in the correlation part.

Now the full ground-state energy of the interacting system can be formulated as

$$E[n] = V_0[n] + E_H[n] + T_s[n] + E_{xc}[n], \tag{13}$$

where $V_0[n] = \int d\mathbf{r}\, v_0(\mathbf{r}) n(\mathbf{r})$ is the energy contribution from the external potential. Then, to solve for the energy all that is left is to have an approximation for the exchange-correlation energy. One such approximation will be described in chapter 2.1.1.

With the aid of equations 8–11, we can now iteratively solve for $n(\mathbf{r})$ and $\phi_i(\mathbf{r})$. The process is outlined in figure 1. First we need to make an Ansatz for the wavefunctions ϕ_i, and then the iterations are continued until the density is converged, i.e. it changes less than some predetermined criteria during subsequent iterations. After the convergence, the ground-state energy can be calculated.

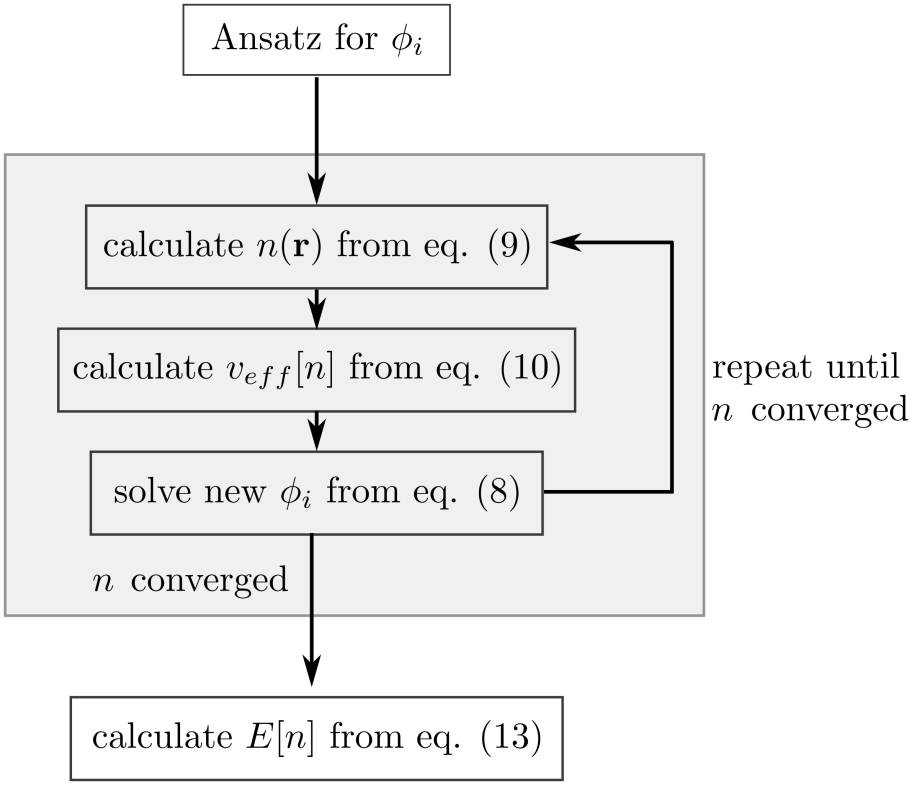

FIGURE 1 The iterative process to solve the Kohn-Sham equations.

2.1.1 Local density approximation

The simplest approximation for the exchange-correlation energy is to treat the system locally as homogeneous electron gas, where the external potential and thus also the electron density is the same everywhere. Then E_{xc} can be written as [53]

$$E_{xc}[n] = \int d\mathbf{r} n(\mathbf{r}) \epsilon_{xc}[n](\mathbf{r}), \tag{14}$$

where $\epsilon_{xc}[n]$ is the exchange-correlation energy for one electron in homogeneous electron gas. This is called the local density approximation (LDA), and it is appropriate for systems with slowly-changing electron density, i.e. systems that are close to homogeneous.

This energy can further be divided into the exchange and correlation parts separately:

$$\epsilon_{xc}[n](\mathbf{r}) = \epsilon_x[n](\mathbf{r}) + \epsilon_c[n](\mathbf{r}). \tag{15}$$

The analytic expression for the exchange energy of the homogeneous electron gas is known exactly [54]:

$$\epsilon_x[n] = -\frac{3}{4}\left(\frac{3}{\pi}\right)^{1/3} n^{1/3}. \tag{16}$$

However, an approximation is needed for the correlation part. Perdew and Wang developed an accurate expression for ϵ_c [55], that is now widely used in DFT calculations utilizing LDA. In all the articles [PI]–[PIII] included in this thesis, the

exchange-correlation energy is calculated using this form of the LDA approximation.

Although the LDA is the simplest exchange-correlation approximation and more accurate ones have since been developed, it is still frequently used in combination with the jellium model [30, 56, 43, 57]. In the jellium model the ionic potentials are smoothed out and the electron density does not generally have large variations inside the clusters. LDA can also reproduce CTPs, as was shown in the Supporting Information of article [PII].

2.1.2 Linear response time-dependent density functional theory

To be able to study non-stationary phenomena such as optical excitations, an extension of DFT for time-dependent systems is needed. In that case, the starting point is the time-dependent Schrödinger equation

$$i\frac{\partial\Psi(\mathbf{r_1},\mathbf{r_2},...,\mathbf{r_N},t)}{\partial t} = \hat{H}\Psi(\mathbf{r_1},\mathbf{r_2},...,\mathbf{r_N},t) \tag{17}$$

where the wavefunction $\Psi(\mathbf{r_1},\mathbf{r_2},...,\mathbf{r_N},t)$ now depends also on time. The Hohenberg-Kohn theorem of stationary systems does not directly translate to non-stationary cases, since there is no variational principle for time-dependent states. However, in 1984 Runge and Gross proved that also in time-dependent cases there is a one-to-one-correspondence between the external potential and the density (up to a constant), and that the time-dependent wavefunction is uniquely defined by the density up to a phase-factor [58]. They further introduced methods for obtaining the time-dependent density, providing the basis for a general time-dependent DFT (TDDFT).

In the case of small perturbations, the study of the changes in the system can be limited to the linear response, so that only the first-order term of the series expansion of the density is needed. This approximation is called linear-response TDDFT (lr-TDDFT). Instead of densities, the density matrix $\mathbf{P}$ and its linear response $\delta\mathbf{P}$ can also be used in the calculations. This matrix formulation developed by Casida [59, 60] was used in the calculation of the optical spectra in the articles included in this thesis.

In the Casida approach, the calculations are performed in the frequency space, making a Fourier transformation from the time variable t to the frequency variable ω. Because of this, the equations for the non-stationary system no longer explicitly depend on time, and the time evolution of the system is not followed. Rather, the frequencies that are related to the excitation energies are solved.

The calculations can be performed in the K-S basis, starting from time-dependent K-S equations. In the following, the main steps of this approach in calculating the optical spectra will be summarized. Using the notation of [59], the indexing for the K-S orbitals is $\phi_{i\sigma}$, where i refers to the spatial part of the wavefunction and σ

to the spin. In the following, the indices i, j, k, and l are used for the spatial part and σ and τ for the spin.

The frequencies ω_I and oscillator strengths f_I of the electronic excitations in the optical spectra can be obtained as the poles and residues, respectively, of the dynamical polarizability $\boldsymbol{\alpha}(\omega) = \delta\boldsymbol{\mu}(\omega)/\boldsymbol{\mathcal{E}}(\omega)$. Here $\delta\boldsymbol{\mu}(\omega)$ is the induced dipole moment of the system and $\boldsymbol{\mathcal{E}}(\omega)$ the electric field. Casida showed in [59] that the ω_I and f_I can be calculated from the pseudo-eigenvalue equation

$$\boldsymbol{\Omega}(\omega)\mathbf{F}_I = \omega^2\mathbf{F}_I. \tag{18}$$

The elements of the $\boldsymbol{\Omega}$ matrix are defined by

$$\begin{aligned}\Omega_{ij\sigma,kl\tau} = {} & \delta_{\sigma,\tau}\delta_{i,k}\delta_{j,l}(\epsilon_{l\tau} - \epsilon_{k\tau})^2 \\ & + 2\sqrt{(f_{i\sigma} - f_{j\sigma})(\epsilon_{j\sigma} - \epsilon_{i\sigma})}K_{ij\sigma,kl\tau}(\omega)\sqrt{(f_{k\tau} - f_{l\tau})(\epsilon_{l\tau} - \epsilon_{k\tau})}.\end{aligned} \tag{19}$$

Here $\epsilon_{i\sigma}$ and $f_{i\sigma}$ are the K-S energies and occupation numbers of the K-S state $\phi_{i\sigma}$. $K_{ij\sigma,kl\tau}(\omega)$ are the elements of the coupling matrix $\mathbf{K}$, which couples the response of the density matrix to the response of the electronic part of the effective potential. It can be calculated as [60]

$$K_{ij\sigma,kl\tau} = \int d\mathbf{r}\, d\mathbf{r}'\, \phi^*_{i\sigma}(\mathbf{r})\phi_{j\sigma}(\mathbf{r}) \left[\frac{1}{|\mathbf{r} - \mathbf{r}'|} + \frac{\delta^2 E_{xc}[n_\uparrow, n_\downarrow]}{\delta n_\uparrow(\mathbf{r})\delta n_\downarrow(\mathbf{r})}\right] \phi_{k\tau}(\mathbf{r}')\phi^*_{l\tau}(\mathbf{r}'), \tag{20}$$

where the up-and down-spin densities have been written separately and the exchange-correlation energy is given explicitly as a functional of both these spin-densities.

The optical excitation energies $\hbar\omega_I$ are obtained from the eigenvalues of equation 18, ω_I^2. The components for the oscillator strengths for light oscillating in $a = x, y, z$ directions, $f_{I,a}$, can in turn be calculated from the eigenvectors $\mathbf{F}_I$ [59, 61]:

$$f_{I,a} = \frac{2m_e}{\hbar e^2}\left|\sum_{i,j,\sigma}(\boldsymbol{\mu}_{ij\sigma})_a\sqrt{(f_{i\sigma} - f_{j\sigma})(\epsilon_{i\sigma} - \epsilon_{j\sigma})}F_{I,ij\sigma}\right|^2, \tag{21}$$

where the states have been ordered so that $f_{i\sigma} > f_{j\sigma}$. $\boldsymbol{\mu}_{ij\sigma}$ is the transition dipole moment between K-S states i and j, and it can be calculated as

$$\boldsymbol{\mu}_{ij\sigma} = -e\langle\phi_{i\sigma}|\mathbf{r}|\phi_{j\sigma}\rangle. \tag{22}$$

Equations 18–22 show that in lr-TDDFT the electric field is not explicitly used in the calculation of the excitation energies and oscillator strengths, which are computed using only the K-S orbitals, occupation numbers and energies obtained from the ground-state calculation. The same exchange-correlation functionals that are used for the stationary case can mostly be used also in lr-TDDFT.

2.2 Jellium model

Treating clusters of tens or hundreds of atoms with DFT can become computationally very heavy. One way to simplify the calculations is to treat only the valence electrons explicitely and combine the core electrons and nuclei into a homogeneous, positive background. This so-called self-consistent jellium model was developed for metal slabs in the 1970s by Lang and Kohn [62, 63], and formulated for finite spherical clusters in the 1980s by Ekardt [14, 64, 65] and Beck [15, 66].

In the jellium model, the external potential in equation 13 becomes [12]

$$V_0[n] = \int d\mathbf{r} v_0(\mathbf{r}) n(\mathbf{r}) = -e^2 \int d\mathbf{r} d\mathbf{r}' \frac{n_J(\mathbf{r}') n(\mathbf{r})}{|\mathbf{r} - \mathbf{r}'|}, \tag{23}$$

where $n_J(\mathbf{r})$ is the jellium background density. Since the positive background is modeled as homogeneous, $n_J(\mathbf{r}) = 0$ outside of the cluster and $n_J(\mathbf{r}) = n_{J0}$ inside, where n_{J0} is a constant. This constant density can in turn be calculated from a parameter called the Wigner-Seitz radius, r_s, as

$$n_{J0} = \left(\frac{4\pi r_s^3}{3} \right)^{-1}. \tag{24}$$

Thus, the jellium model is characterized by a single parameter, the Wigner-Seitz radius, which is defined by the material and which describes the valence-electron density. The bulk value is used, and it can be obtained either experimentally or computationally.

Because only the valence electrons are explicitely treated and they are considered to move freely in the potential of the whole cluster, some metals are better described by the jellium model than others. Group I metals with s type valence electrons, like sodium, are best suited for this approach. For metals where the d electrons have an important role the simple jellium model has to be modified, such as adding a polarizable background to the inner part of the jellium cluster [67].

The spherical jellium model can accurately depict only the cluster sizes having close to spherical shapes, which correspond to certain magic numbers of atoms with an electron shell closing. After its initial publication, the jellium cluster model was soon extended to ellipsoidal [68] and later triaxial [69] shapes. Models where the sharp jellium edge is replaced with a diffuse surface potential also exist [70]. Koskinen, Lipas, and Manninen developed the ultimate jellium model, where the positive jellium density is totally deformable both in shape and in charge density [71]. This parameterless model can predict the shapes of neutral clusters from the perspective of valence electrons.

For all the above-mentioned models, the contribution from the external potential to the ground-state energy (equation 13) can be written analytically. However,

the jellium model itself is not restricted to any specific shapes or symmetries, and any geometries can be built for example in codes utilizing real-space grids as discussed in chapter 2.3.

For sodium clusters, even the simple homogeneous jellium model has shown to reproduce experimental trends in for example ionization potentials and static polarizabilities [11]. The calculated results for the optical spectra [72, 73, 74] also agree qualitatively with the experimental ones [39].

Nowadays, new efficient DFT codes and the increased computational power of supercomputers make it possible to perform atomistic calculations of clusters of even hundreds of metal atoms. However, the efficiency and simplicity of the jellium model keep it still as an attractive alternative, and it is frequently used for example in the study of plasmons [75, 56, 76, 43, 77, 57, 78]. The lack of the atomic structure in the jellium model has been shown to cause a significant effect on some plasmon-related properties, such as the electric field enhancement between two plasmonic clusters, but the trends for BDPs and CTPs are still reproduced [79, 80, 81]. Thus, the jellium model is suitably for the study of the plasmon phenomenon from the electronic perspective.

2.3 GPAW

Density-functional calculations are often performed using certain basis sets, such as linear combinations of atomic orbitals or plane waves, to represent the K-S wavefunctions. In that case the accuracy of the calculation depends on how good the representation is, which is usually related to the size of the basis set.

However, the Kohn-Sham equations can also be solved using a real-space grid. Then the wavefunctions are represented by a value in each grid point, and finite-difference versions of the operators are used. In this method the accuracy of the calculations is controlled by one simple variable, the grid-spacing. One advantage of grid-based methods is easy parallelization, since a simple domain decomposition over grid points can be used [82].

GPAW [49, 50] is a DFT code utilizing real-space grids and the projector augmented-wave (PAW) method developed by Blöchl [83]. All the DFT calculations presented in this thesis were performed with GPAW.

In the PAW method, the all-electron K-S wavefunctions $|\phi_n\rangle$ are smoothed in the region close to the atomic nuclei by a linear transformation $\mathcal{T}$ to get pseudo wavefunctions $|\widetilde{\phi}_n\rangle = \mathcal{T}|\phi_n\rangle$. Only the valence electrons are treated in the K-S scheme, and the core electrons are frozen. This smoothening out of the K-S orbitals is helpful, since it gets rid of the strong oscillations of the wavefunctions near the strong potential of the nuclei.

However, using the already smooth background density of the jellium model, these transformations are not needed. GPAW then becomes simply a finite-difference solver for the Kohn-Sham equations. In the GPAW version 1.1.0 used in all the calculations included in this thesis, the external jellium potential is given in the Hartree term of equation 10. Thus, in a technical sense, there is no external potential.

The uniform jellium background is defined by the total positive charge and the grid points among which the charge is equally divided. In the case of neutral clusters as in this thesis, this charge is $+n_e\, e$, where n_e is the number of electrons in the calculation and e the elementary charge. Since any set of points in the real-space grid can be chosen for the jellium background, it is easy to construct different cluster geometries, such as large assemblies of clusters or dimers connected by jellium channels, regardless of the symmetry.

2.4 Analysis of the optical excitations

For metal clusters, there has been much debate about what is a plasmon, and how one can distinguish LSPR peaks from single-particle excitations or other kind of collective excitations. In systems of several clusters, CTPs provide a new class of excitations to complicate the picture. To recognize the plasmonic excitations, some aspects to analyze are the collectivity of the excitation, the distribution of the induced density, and the additivity of the electron-hole (e-h) contributions to the transition dipole moment. Several plasmonicity indices or measures have been developed, based on one or several of these attributes. In the beginning of section 2.4.1, I will shortly review some of these methods. In sections 2.4.1.1-2.4.1.3, I will introduce the analysis tools used in the articles included in this thesis. We did not use one index, but rather combined several quantitative and qualitative tools to get a picture of the plasmonic nature of the absorption peaks.

2.4.1 Measures for the plasmonicity

In LSPR, the electron density oscillations happen mostly at the surface of the cluster. Thus, the distribution of the induced density can been used to assess the LSPR nature of excitations [64, 33, 76].

To separate cases when several non-coupled e-h transitions near the same energy contribute to the spectral feature and when the excitation is really collective, the electron-electron interaction can be tuned in the calculation. Puska et al. calculated the optical response of small metal clusters both for interacting and non-interacting electrons using the random phase approximation, to see which features are present only in the interacting case [84]. More recently, Bernadotte

et al. monitored the effect of the coupling by introducing a scaling parameter in the TDDFT calculations depicting the electron-electron interaction, and varying it from zero (no interaction) to one (full interaction) [44]. Following this approach, Piccini et al. simplified the analysis by only calculating the interacting, standard TDDFT spectrum and the K-S spectrum for non-interacting electrons [45].

The contributing e-h transitions can also be analyzed based on how they affect the total transition dipole moment. Large additivity of the individual transitions to the total dipole moment has been associated with plasmonic excitations, and this can be used to identify the LSPR peaks, as demonstrated by Aikens and co-workers for silver clusters [32, 38].

In a pursuit to represent the LSPR character or at least some aspect of it as a single number, various plasmonicity indices have been developed. Li et al. introduced the volume density response proportion (VPR), which quantifies how much of the electron density response is located inside the cluster, in an effort to separate the bulk plasmons and single-particle excitations from the LSPR peaks [33]. Bursi et al. developed the so-called plasmonicity index, which attempts to measure the plasmonic character through the induced potential of the excitation [46]. This measure was later further developed to the generalized plasmonicity index (GPI), which also uses the induced potential, but is normalized to directly compare different systems [43]. Casanova et al. developed the transition inverse participation ratio (TIPR) based on the transition occupation numbers to quantify the collectivity of an excitation [47]. This index has the value of one if only one e-h transition is contributing to the excitation, and achieves its maximum value in the case of all the electrons participating equally.

Gieseking et al. combined three criteria to classify plasmonic excitations in bare and ligand-protected noble metal clusters: collectivity, additivity to the dipole moment, and superatomic character [48]. The superatomic character refers to contributions of transitions from superatomic (delocalized) orbitals. The collectivity is quantified by using the TIPR index.

2.4.1.1 Transition contribution maps

To gain insight into the nature of the features of the absorption spectrum, we employed the time-dependent density functional perturbation theory (TD-DFTP) [85] as implemented in GPAW. A cosinoidal laser field polarized in the direction of interest and with the energy of the studied feature is simulated to excitate the system. Using the K-S basis to linearize the equations for the excited system, we can solve the absorption coefficients C_{ip}^{ω} for all the transitions from initial electron states i to final hole states p contributing to the analyzed excitation at frequency ω.

In the TCM scheme [40], the squared magnitudes of these coefficients are used to build a two-dimensional map, which shows the strengths of the individual e-h

contributions to the excitation as a contour map. The x axis shows the energy of the occupied K-S states (ε_{occ}) and the y axis the energy of the unoccupied K-S states ($\varepsilon_{\text{unocc}}$). A Gaussian broadening is applied for the transitions with respect to both axis. Each dot in this contour plot indicates one single-particle transition, and the density of the contour lines shows the relative strength of the contribution. Thus, the equation of the map can be written as (see the supporting information of reference [40])

$$TCM(\varepsilon_{\text{occ}}, \varepsilon_{\text{unocc}}) = \sum_{i}^{\text{occ}} \sum_{p}^{\text{unocc}} |C_{ip}^{\omega}|^2 \exp\left[-\left(\frac{\varepsilon_{\text{occ}} - \varepsilon_i}{\Delta\varepsilon} \right)^2 - \left(\frac{\varepsilon_{\text{unocc}} - \varepsilon_p}{\Delta\varepsilon} \right)^2 \right]. \tag{25}$$

We also used the related DTCM method [51] for some of the systems. In DTCM, we visualize the contributions to the transition dipole moment:

$$DTCM(\varepsilon_{\text{occ}}, \varepsilon_{\text{unocc}}) = \sum_{i}^{\text{occ}} \sum_{p}^{\text{unocc}} 2C_{ip}^{\omega}\, \omega\, \mu_{ip} \exp\left[-\left(\frac{\varepsilon_{\text{occ}} - \varepsilon_i}{\Delta\varepsilon} \right)^2 - \left(\frac{\varepsilon_{\text{unocc}} - \varepsilon_p}{\Delta\varepsilon} \right)^2 \right], \tag{26}$$

where ω is the frequency of the analyzed excitation and μ_{ip} the dipole moment of the transition $i \rightarrow p$ in the direction of the laser field. The DTCM contributions can be positive or negative, having an additive or weakening effect on the total transition dipole moment. In the DTCM figures, these contributions are shown as red (positive) and blue (negative).

Both TCM and DTCM give information about the collectivity of the excitation and the participating e-h transitions, thus aiding in the analysis of the possible plasmonic nature of the studied spectral feature. The DTCM scheme also gives information about the additivity to the dipole moment. Recently, the DTCM scheme has been used for example to study plasmons in atomic arrays of two different metals [86, 87] and the coupling of plasmons of metal clusters with the optical excitations of organic molecules [88].

We combine the (D)TCM analysis with the Y_{lm} analysis of the superatomic orbitals [23], where the orbitals of each cluster are projected into spherical harmonics to resolve their symmetry. According to the analysis, the different type of orbitals (S, P, D, ...), are then visualized with different colors as projected density of states (PDOS) plots sharing the energy axes of the (D)TCM contour plot. This combination allows us immediately see the symmetries of the initial and final orbitals of the e-h transitions.

2.4.1.2 Induced density

The TD-DFPT calculation also allows us to compute the induced transition density corresponding to each studied spectral feature. In article [PI], we plotted radially the induced density around the single clusters, dividing the calculation cell into narrow, concentric shells, and summing the induced density inside each

cell. This allows the visual inspection of the spherical distribution of the induced density.

The radial distribution is useful only for single, spherical clusters. For the planar cluster arrangements of the spherical 8-electron clusters studied in the same article, we instead visualized the cross-sections of the induced density with a certain isosurface value. This does not give information about the changes in the magnitude, but reveals the charge oscillations inside of the clusters and makes it easier to recognize for example bonding combinations of the individual localized surface plasmons.

In article [PII], we visualized the induced density using both 3D isosurfaces, and a contour plot of the induced density in the dimer plane. Compared to the cross-section of the induced density, the contour plot gives information about the strength of induced density along the dimer plane and thus tells more about the distribution of the charge oscillations.

2.4.1.3 Charge transfer ratios

To identify the CTPs from the absorption spectra more reliably than with only visual inspection of the induced density, we need a way to somehow quantify the charge transfer nature of the excitations. To this end, we developed an index, the Charge Transfer Ratio for dimer systems ($\mathrm{CTR_d}$) in article [PII]:

$$\mathrm{CTR_d} = \left| \frac{D \int_A \rho_{\mathrm{ind}}(\mathbf{r})\, d\mathbf{r}}{\int_{A+B} x\, \rho_{\mathrm{ind}}(\mathbf{r})\, d\mathbf{r}} \right|. \tag{27}$$

Here D is the distance between the centers of the two clusters, ρ_{ind} the induced density, $\mathbf{r}$ the position in the real-space grid, and x the coordinate along the dimer axis. The induced density is computed for a cosinoidal laser field with the dipole moment in x direction. For the integration, the calculation cell is divided into parts A and B, making the cut halfway between the surfaces of the two clusters. For homodimers, the parts are simply the left and right half of the calculation box. Thus, the integral in the numerator is performed over the left side of the calculation box, and the one in the denominator over the whole calculation cell. For symmetry reasons, $\int_A \rho_{\mathrm{ind}}(\mathbf{r})\, d\mathbf{r} = -\int_B \rho_{\mathrm{ind}}(\mathbf{r})\, d\mathbf{r}$, so the choice of side A or side B for the numerator does not matter.

Equation 27 amounts to comparing the dipole moment of the charge transfer excitations (numerator) to the transition dipole moment of the system (denominator). The former is a measure of how much excess induced density is on one side of the systems, i.e. how much charge is transferred from one cluster to the other, while the latter serves as a normalization.

If the charge oscillations happen only inside or around each cluster separately, without electrons transferred between the clusters, the integral of the induced density on side A (and B) is zero. Thus the whole $\mathrm{CTR_d}$ index is zero when there

is no charge transfer between the clusters. The larger the $\mathrm{CTR_d}$ value is, the more the charge density is oscillating between the two clusters during the excitation. Depending on the distribution of the charges on sides A and B along the dimer axis, the index can also be above 1. Without taking the absolute value $\mathrm{CTR_d}$ could also reach negative values, but since the strength is the measure of the charge transfer, we keep the index positive. A derivation for the index can be found in the supporting information of article [PII].

Since this formulation of the CTR only works for systems of two clusters, for article [PIII] we developed another form of the index for arbitrary arrangements of spherical cluster. Here, the computation cell is divided between each cluster in a Wigner-Seitz cell type definition, assigning each grid-point to the cluster the center of which it is closest to. For systems with reflection symmetry in the studied direction, it can be written as:

$$\mathrm{CTR_{ws}} = \frac{|\sum_{i \text{ in left}} \int_{\text{cluster } i} \rho_{\text{ind}}(\mathbf{r})\, d\mathbf{r}|}{\int_{\text{all}} |\rho_{\text{ind}}(\mathbf{r})|/2\, d\mathbf{r}}. \tag{28}$$

The system is divided to left and right sides similarly as for $\mathrm{CTR_d}$, since the arrangements are assumed to be symmetrically positioned in the calculation cell. The index i refers to the individual clusters, which are numbered for the purpose of this calculation. A cluster in the arrangement can be either on the left side, in the middle, or on the right side. The volume of "cluster i" over which the integration is performed in the numerator is defined using the Wigner-Seitz cell method. This division works well for the spherical, identical clusters used in the study.

Because of the symmetry, during the excitations all the clusters on the middle have a zero net charge, and all the clusters on the left are either positively or negatively charged, and the clusters on the right equally negatively or positively charged. Therefore, to study the net charge transfer between clusters, we only need to study the induced densities of the clusters on the left side (or equally on the right side). This is achieved in the numerator by summing over the clusters on the left.

For systems without the reflection symmetry, the definition of left and right sides is not anymore trivial. However, without the summation in the numerator, the $\mathrm{CTR_{ws}}$ can be calculated for each cluster separately. The positive values can then be summed together to get a measure of the total charge transfer for an arrangement of any symmetry.

The $\mathrm{CTR_{ws}}$ index is normalized by the integral of the total positive induced density, which is formulated in the demoninator as the integral of the absolute value of the induced density over the whole calculation cell, divided by two. With this normalization and taking the absolute value in the nominator, the $\mathrm{CTR_{ws}}$ is always between 0 and 1. A value of 0 signifies that there is no charge transfer between the clusters, while 1 corresponds to an excitation where all the electron density oscillations are charge transfer oscillations between the left and right sides of the system.

Since we only need the cube file of the induced transition density as the input for both CTR indices, they can be computed post-processing after the TD-DFPT calculations needed for the DTCM analysis. Now we can obtain a numerical value corresponding to the charge transfer at each studied excitation energy, allowing us to follow how the nature of the excitations in the absorption spectrum is changing with respect to energy.

3 RESULTS AND DISCUSSION

In articles [PI]–[PIII], we analyzed the optical properties of jellium clusters and cluster arrangements using the DFT code GPAW. The jellium density was chosen to be the density of sodium, using a Wigner-Seitz radius of 2.08 Å. Thus, an 8-electron jellium cluster, for example, models an 8-atom sodium cluster.

The positive jellium background of all the studied clusters was kept spherical. Therefore, we chose the cluster sizes so that the numbers of electrons correspond to magic numbers for a spherical potential. The clusters with these magic numbers of electrons are closed-shell and have significant HOMO-LUMO gaps. The first nine of the magic numbers and the corresponding electron configurations are listed in table 1.

TABLE 1 The first nine magic numbers of electrons for a spherical potential and the corresponding electron configurations. [N] refers to the electron configuration for N electrons.

# el.	configuration
8	$1S^2 1P^6$
18	[8] $1D^{10}$
20	[18] $2S^2$
34	[20] $1F^{14}$
40	[34] $2P^6$
58	[40] $1G^{18}$
92	[58] $2D^{10} 1H^{22} 3S^2$
138	[92] $2F^{14} 1I^{26} 3P^6$
186	[138] $2G^{18} 1J^{30}$

In article [PI], we studied the birth of the LSPR in separate jellium clusters ranging from 8 to 186 electrons. We also analyzed some planar arrangements of 2–6 clusters. In article [PII], the studied systems are dimers and we concentrated on

the study of CTPs. Three-dimensional geometric cluster arrangements were the focus of article [PIII]. In all these articles, one main objective was to find ways to recognize and classify different types of plasmonic excitations in the spectra.

In the following, I will first discuss the LSPR and its size-evolution in the separate clusters, then BDPs and CTPs in dimers, the optical response of the planar arrangements, and finally plasmons in the three-dimensional arrangements.

3.1 Single clusters

For the separate clusters, we studied clusters with 8, 20, 34, 40, 58, 92, 138, and 186 electrons. The smallest cluster has a radius of approximately 4.2 Å and the largest a radius of 11.9 Å. The positive jellium density was defined to be uniform for all the clusters, but the electron density that is solved by the DFT calculations experiences a spill-out from this cluster sphere. This spill-out is relatively larger for the smaller clusters. The electron density has a shell-like structure defined by the filled electron orbitals, having one or several radial minima and maxima inside the clusters.

The optical spectrum for each cluster size was calculated using lr-TDDFT. The oscillator strengths (right panels) and the broadened optical absorption spectra (left panels) can be seen in figures 2 and 3. The energies of the largest peaks are indicated and excitations that are further analysed are labelled in the panels on the right. The numbers refer to the main excitations with LSPR character and the letters to other types of excitations analyzed.

As can be seen in figures 2 and 3, each of the spectra supports one or two peaks with a large absorption strength and some smaller excitations. According to the classical Drude formula, the bulk LSPR frequency for a spherical cluster with this density is

$$E_{LSPR} = \sqrt{\frac{\hbar^2 e^2 n}{3\varepsilon_0 m_e}} \approx 3.49\,\mathrm{eV}, \tag{29}$$

where $\hbar$ is the reduced Planck constant, ε_0 is the permittivity of free space, e is the elementary charge, m_e is the mass of an electron, and n is the electron density, for which the jellium density is used. For the studied clusters, the energies of the largest peaks are between 2.54 eV and 3.00 eV. The cause for the red-shift of these energies compared to the classical one is the spill-out of the electrons, which makes the electron density lower than in the Drude formula [12].

To assess the plasmonic nature of these absorption peaks, we used TD-DFPT to perform the TCM analysis and to calculate the induced density for each of them. In addition to the clearly two-peaked spectra of the 20- and 40-electron clusters, two energies were analyzed for sizes 92 and 138 which show two strong excitations in the non-broadened oscillation spectrum, and 186 for which the second

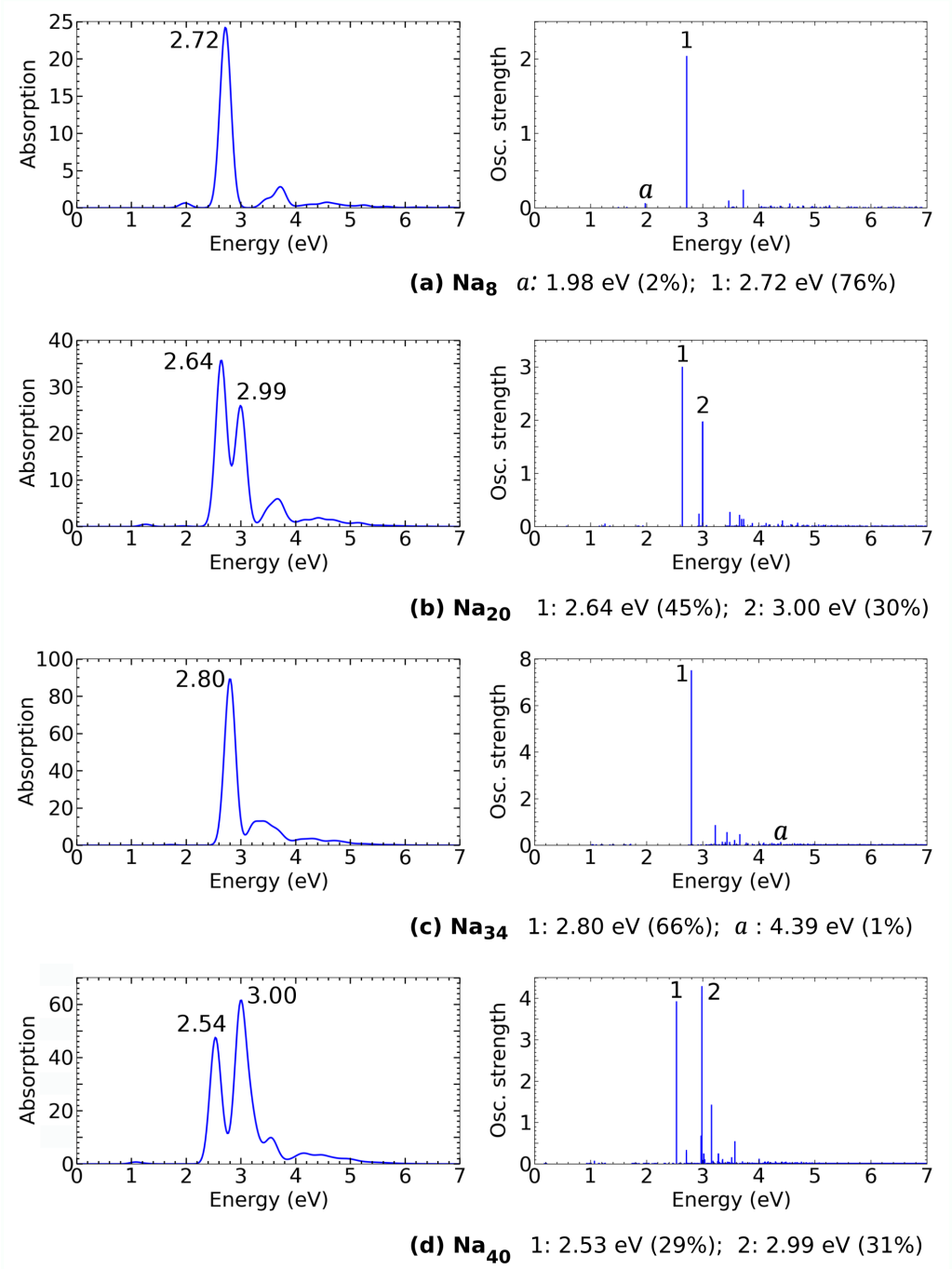

FIGURE 2 The optical absorption spectra and the oscillator strengths for the clusters with 8, 20, 34, and 40 electrons. A Gaussian broadening of 0.1 eV was used for the spectra. The energy and percentage of the total oscillator strength of the labeled excitations are indicated under the figures on the left. The energies of the largest peaks in the broadened spectra, which might differ from the exact energies of the strongest oscillations, are indicated in the figures on the right. Note that the y axis scales are different in the different panels. Reprinted with permission from Elli Selenius, Sami Malola, Hannu Häkkinen. Analysis of Localized Surface Plasmon Resonance in Spherical Jellium Clusters and Their Assemblies. *The Journal of Physical Chemistry C*, 121 (48), pp. 27036–27052, **2017**. Copyright 2017 American Chemical Society.

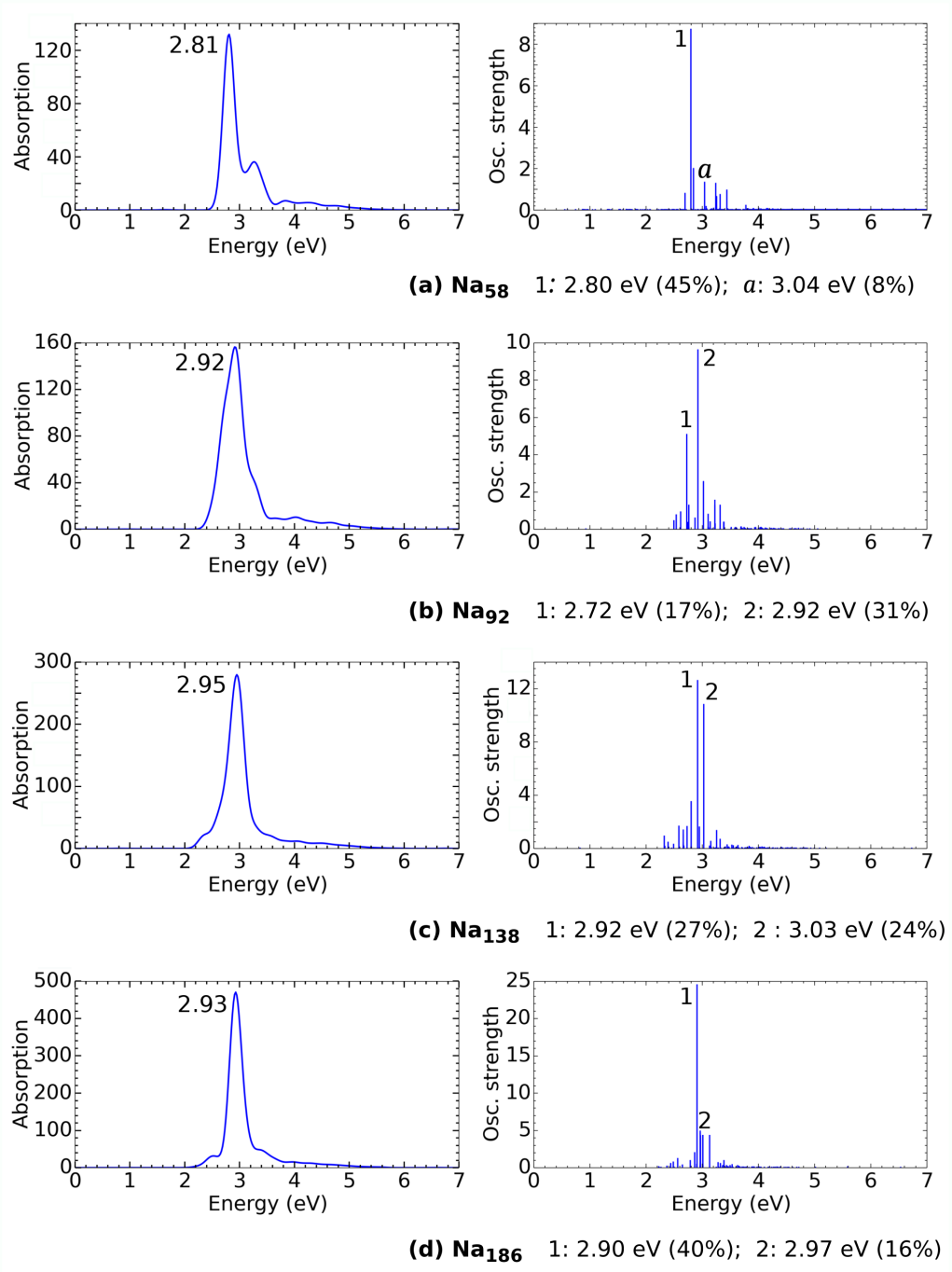

FIGURE 3 The optical absorption spectra and the oscillator strengths for the clusters with 58, 92, 138, and 186 electrons. The details are the same as for figure 2. Reprinted with permission from Elli Selenius, Sami Malola, Hannu Häkkinen. Analysis of Localized Surface Plasmon Resonance in Spherical Jellium Clusters and Their Assemblies. *The Journal of Physical Chemistry C*, 121 (48), pp. 27036–27052, **2017**. Copyright 2017 American Chemical Society.

analyzed energy includes many smaller excitations. To contrast the features with other types of excitations, we also analyzed one smaller peak for the 8-electron, 34-electron, and 58-electron system each.

The TCMs for these peaks can be seen in figures 4–6, and the corresponding induced densities plotted radially in figures 7–9. Here, the naming of the superatomic orbitals after I symmetry differs from the way introduced in table 1 and otherwise used in this thesis. In the notation used for the PDOSs of figures 4–6 letter J is skipped, so the letters K and L in these figures correspond to letters J and K in table 1, respectively.

The TCM figures show that for all the strongest excitations, labeled with 1 and 2 in the spectra, there are contributions from several e-h transitions. Furthermore, there are transitions at several different transition energies $\Delta\varepsilon_{eh} = \varepsilon_h - \varepsilon_e$, where ε_h is the energy of the final state (hole) and ε_e the energy of the initial state (electron). This indicates coupling between the individual single-particle transitions, and shows that the excitations are collective.

The induced densities for the same peaks show that even though there are some density oscillations also inside the clusters, most of the induced density is concentrated at or near the surface of the clusters. This, together with the collectivity and the large oscillator strengths, indicates that these numbered peaks are indeed LSPR peaks.

Going from smaller cluster to larger, the density of the states gets bigger and there are more occupied states, resulting in a higher number of possible transitions. As a result, the number of contributions in the TCMs grows as the cluster size gets bigger. Since the clusters are fully spherical, the transitions obey the selection rules for spherical symmetry, so that the angular momentum quantum number l of the initial and final orbital changes always by one. Thus in figure 4 b), for example, we see transitions 1S→2P, 1P→1D, and 1P→2S, but not for instance 1S→1D.

The fragmentation of the main peak for the clusters with 20 and 40 electrons is also visible in the experimental spectra for the Na_{20} and Na_{40} clusters [39]. For the 40-electron cluster, the first of these peaks is mainly caused by the e-h transition from 1P to 3D which has a $\Delta\varepsilon_{eh}$ of almost 2.75 eV. That is close to the excitation energy of 2.54 eV, as can be seen in figure 5 a). For the next peak, shown in figure 5 b), the excitation is more collective. Similarly, for the 20-, 92-, and 138-electron clusters one of the fragments is more collective while the other has strong contributions from one or a few excitations with $\Delta\varepsilon_{eh}$ close to the excitation energy. This fragmentation of the collective absorption peak due to the coupling of the plasmon with a single e-h excitation has been computationally observed and explained before for jellium clusters [73]. In the induced densities, the more collective peaks in these systems have the radially summed induced density maximum more peaked on the surface of the clusters compared to the other fragment.

Since the broadening in the TD-DFPT calculations is 0.05 eV, the TCM analysis for

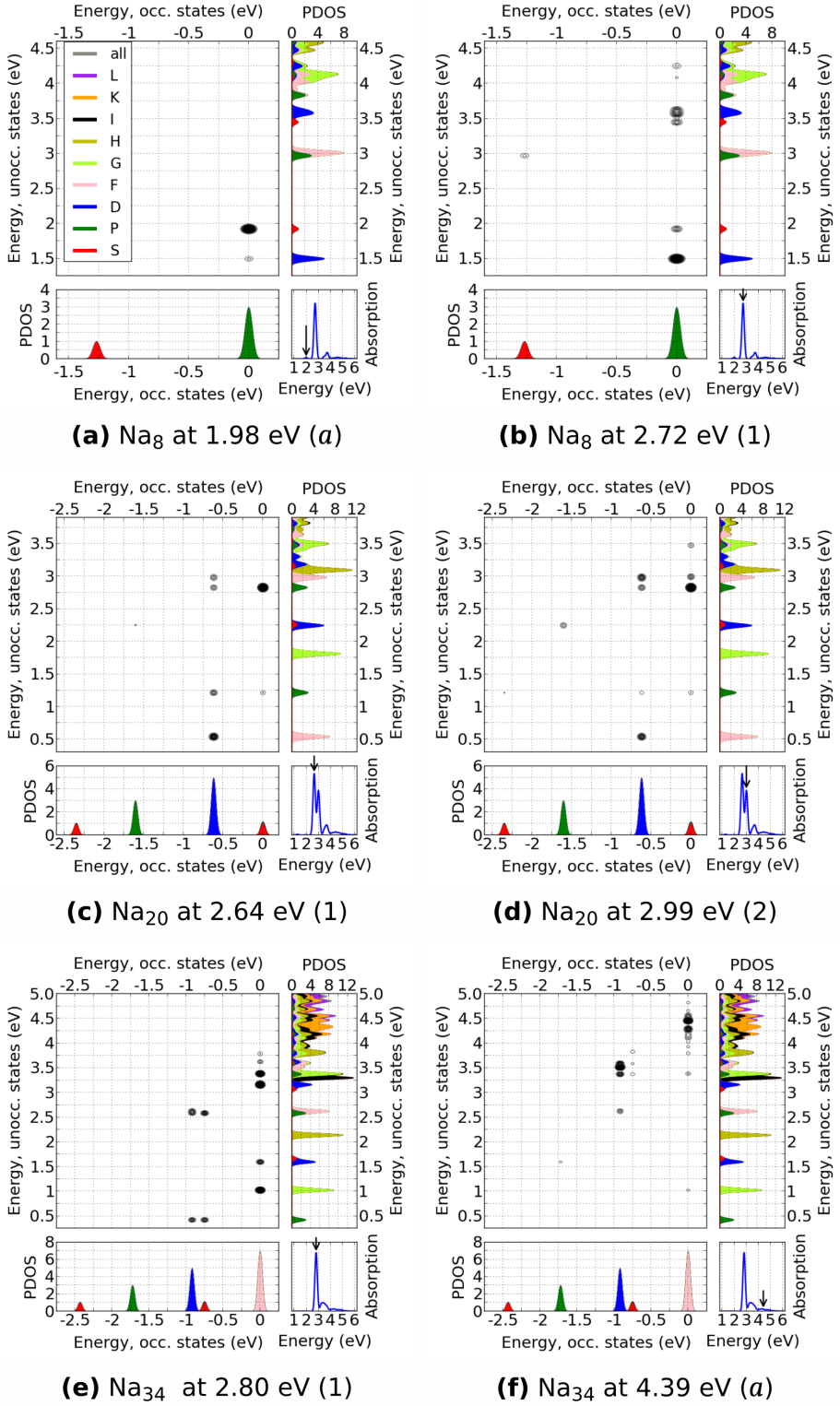

FIGURE 4 The TCMs for selected excitations for the clusters with 8, 20, and 34 electrons. The contour plot shows the relative strengths of the contributing e-h transitions. PDOS for the occupied states is shown in the bottom, and for the unoccupied on the right. The HOMO energy has been set to zero. The studied spectral feature is indicated with an arrow on the bottom right. Reprinted with permission from Elli Selenius, Sami Malola, Hannu Häkkinen. Analysis of Localized Surface Plasmon Resonance in Spherical Jellium Clusters and Their Assemblies. *The Journal of Physical Chemistry C*, 121 (48), pp. 27036–27052, **2017**. Copyright 2017 American Chemical Society.

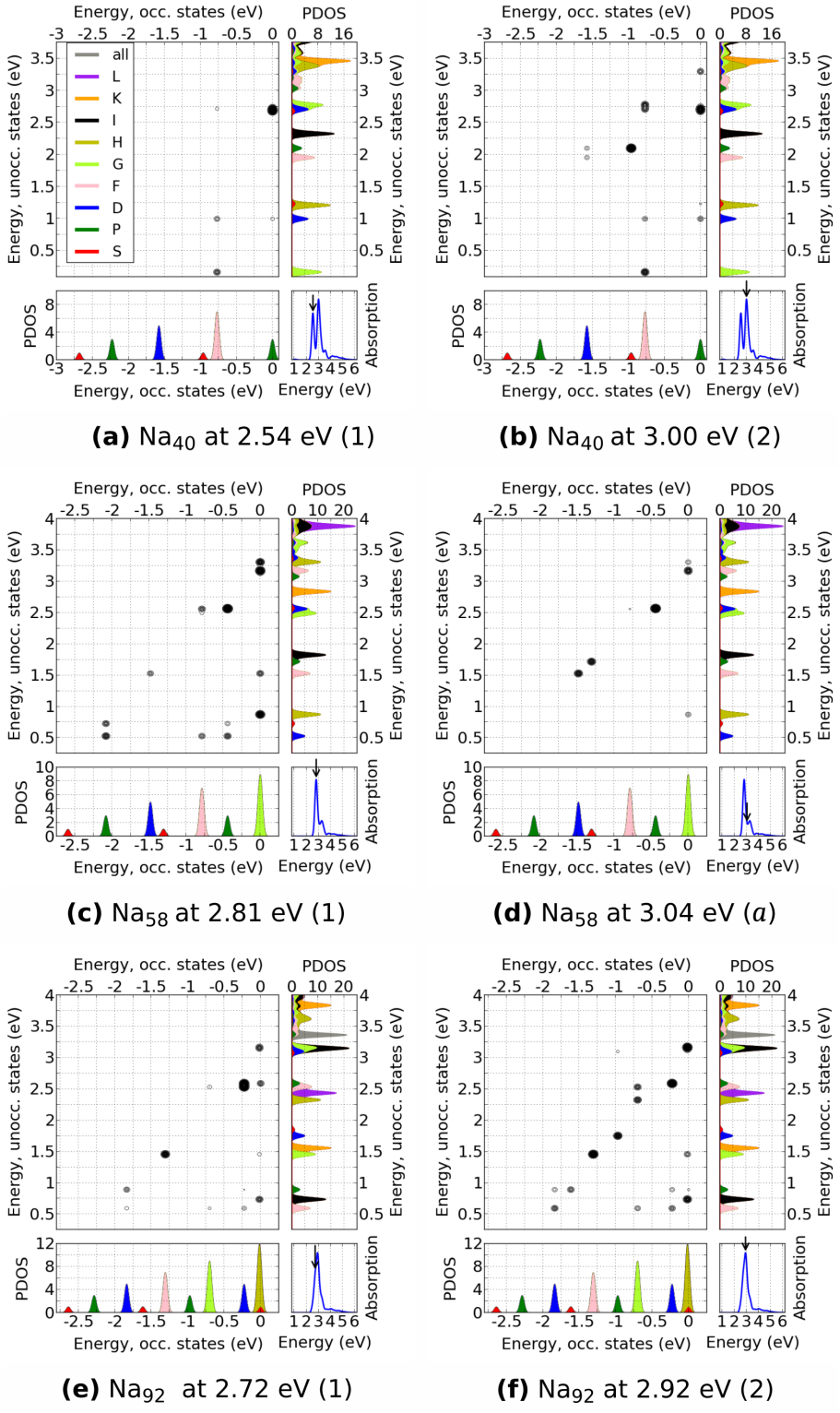

(a) Na_{40} at 2.54 eV (1)

(b) Na_{40} at 3.00 eV (2)

(c) Na_{58} at 2.81 eV (1)

(d) Na_{58} at 3.04 eV (*a*)

(e) Na_{92} at 2.72 eV (1)

(f) Na_{92} at 2.92 eV (2)

FIGURE 5 The TCMs for selected excitations for the clusters with 40, 58, and 92 electrons. The details are as for figure 4. Reprinted with permission from Elli Selenius, Sami Malola, Hannu Häkkinen. Analysis of Localized Surface Plasmon Resonance in Spherical Jellium Clusters and Their Assemblies. *The Journal of Physical Chemistry C*, 121 (48), pp. 27036–27052, **2017**. Copyright 2017 American Chemical Society.

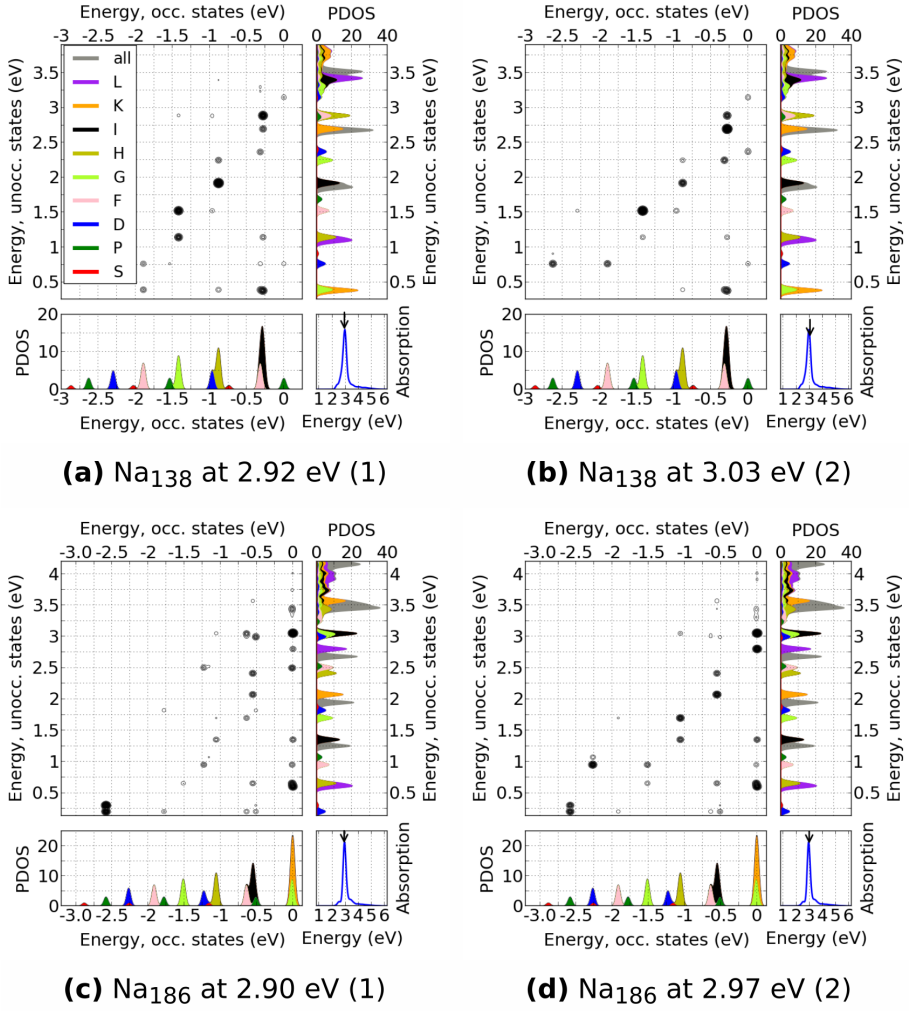

(a) Na_{138} at 2.92 eV (1)

(b) Na_{138} at 3.03 eV (2)

(c) Na_{186} at 2.90 eV (1)

(d) Na_{186} at 2.97 eV (2)

FIGURE 6 The TCMs for selected excitations for the clusters with 138, and 186 electrons. The details are as for figure 4. Reprinted with permission from Elli Selenius, Sami Malola, Hannu Häkkinen. Analysis of Localized Surface Plasmon Resonance in Spherical Jellium Clusters and Their Assemblies. *The Journal of Physical Chemistry C*, 121 (48), pp. 27036–27052, **2017**. Copyright 2017 American Chemical Society.

peak 2 for the 186-electron cluster includes several excitations of similar strength, as can be seen from figure 3 d). Comparing figures 6 c) and 6 d), the contributions with $\Delta\varepsilon_{eh}$ close to the excitation energy have more of the total weight for peak 2 than for peak 1, suggesting that the excitations analyzed for peak 2 are less collective than excitation 1. However, based on the nevertheless collective nature and the profile of the induced density seen in figure 9 d), these excitations are smaller fragments of the LSPR peak.

The peaks marked with *a* show different characteristics than the numbered peaks. For the *a*-peak of the 58-electron cluster, the induced density oscillations are smaller than for the LSPR peak 1 and the oscillations are happening inside the cluster almost as much as at the surface, as is evident from figure 8 d). The TCM in figure 5 d) shows a few strong contributions, some of them the same as for the LSPR peak and all with $\Delta\varepsilon_{eh}$ close to the excitation energy. Thus, this excitation

does not show very strong LSPR-like characteristics and it might be a smaller fragment of the LSPR peak or a combination of single e-h transitions.

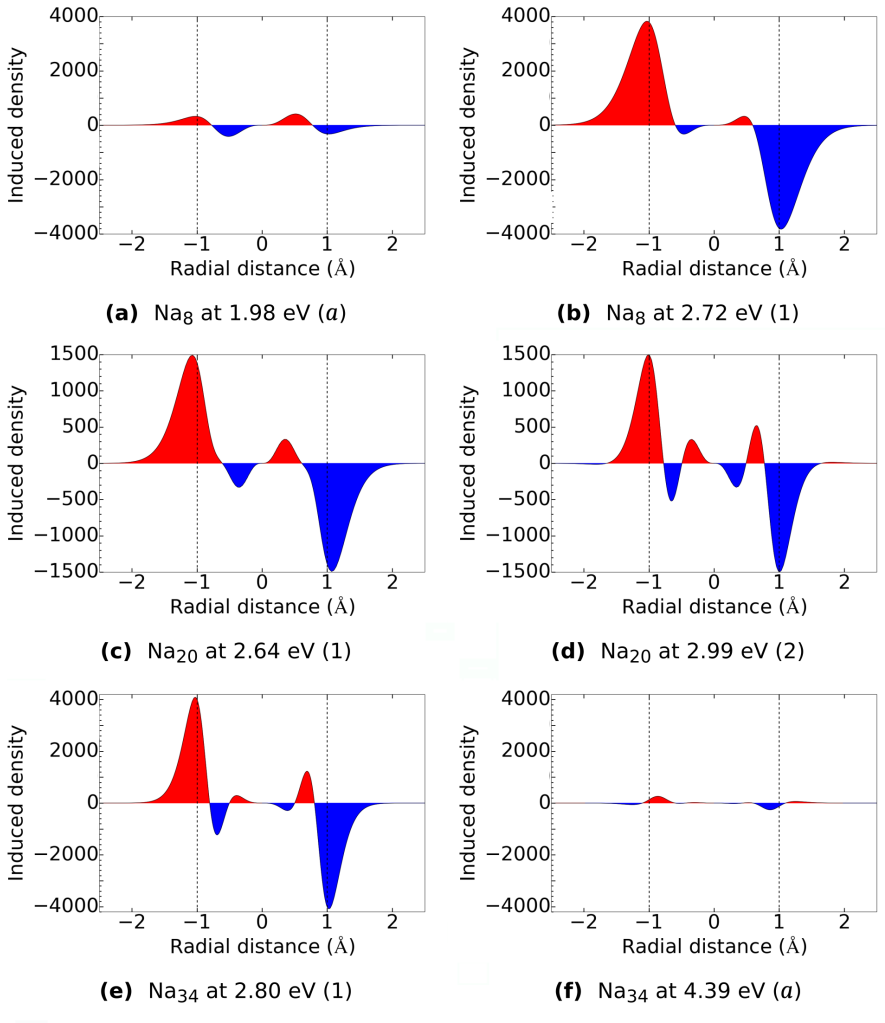

FIGURE 7 The induced densities of the clusters with 8, 20, and 34 electrons plotted radially. The density value at each radial distance is the sum of all the induced density in a spherical shell at that distance from the center. The positive and negative densities are plotted separately. Reprinted with permission from Elli Selenius, Sami Malola, Hannu Häkkinen. Analysis of Localized Surface Plasmon Resonance in Spherical Jellium Clusters and Their Assemblies. *The Journal of Physical Chemistry C*, 121 (48), pp. 27036–27052, **2017**. Copyright 2017 American Chemical Society.

The *a*-peak for the 8-electron cluster, as seen in figure 4 a), is mostly a single-particle excitation and the oscillator strength is much lower than of the collective main peak. The induced density has similar characteristics as the *a* peak of the 58-electron cluster.

The *a* peak for the 34-electron cluster at 4.39 eV is collective, but with the strongest contributions mainly with the same $\Delta\varepsilon_{eh}$, as seen in 4 f). It is located in the high-energy tail of the spectrum that all the cluster sizes support. Some of the e-h transitions are from HOMO to the continuum of unbound states above 4 eV. The

density oscillations are very weak compared to the LSPR, as seen in figure 7 f), and not peaked at the surface. Therefore this peak is also not a LSPR peak.

To summarize, our analysis showed that already the smallest studied cluster size with 8 electrons supports a feature in the optical spectrum that can be called a LSPR peak. The absorption strength of this peak gets larger with growing cluster size, as does the amount of e-h transitions participating in the excitation. The induced density, located mainly near the edge of the clusters, supports the assignment of the peaks as LSPR peaks. Other excitations in the spectra have less collective nature and the induced density is not peaked at the cluster surface.

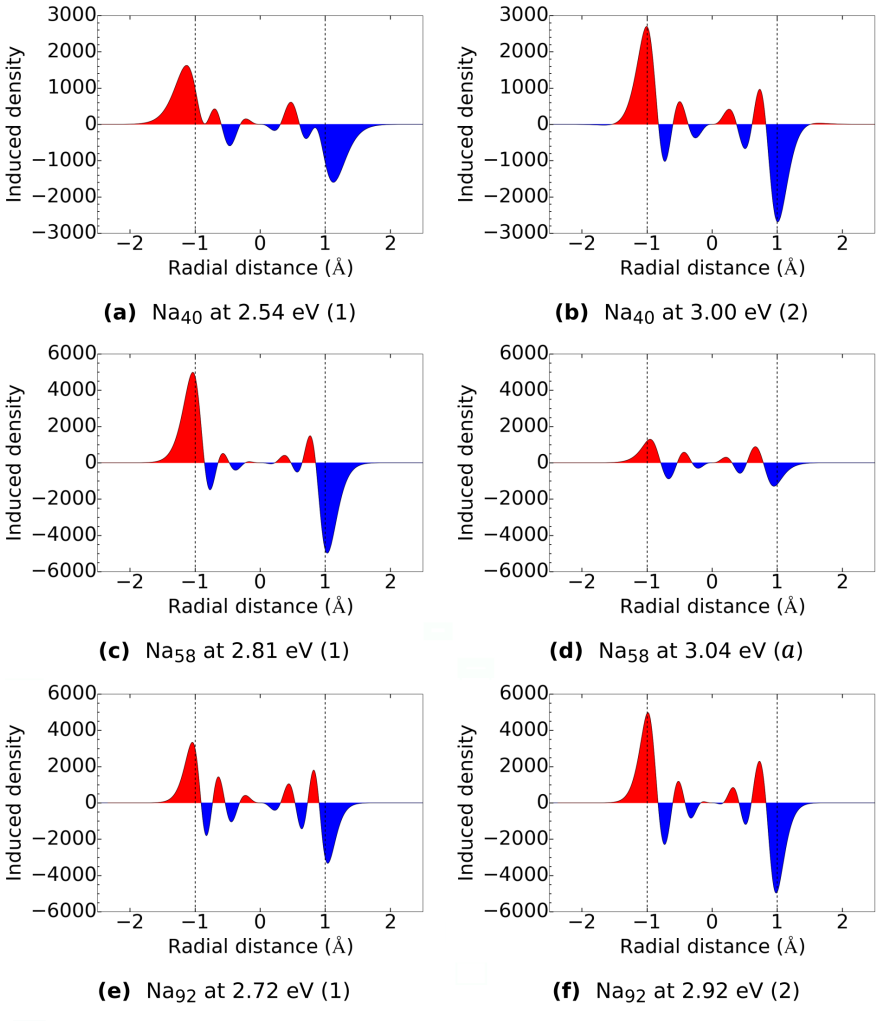

FIGURE 8 The induced densities of the clusters with 40, 58, and 92 electrons plotted radially. The details are the same as for figure 7. Reprinted with permission from Elli Selenius, Sami Malola, Hannu Häkkinen. Analysis of Localized Surface Plasmon Resonance in Spherical Jellium Clusters and Their Assemblies. *The Journal of Physical Chemistry C*, 121 (48), pp. 27036–27052, **2017**. Copyright 2017 American Chemical Society.

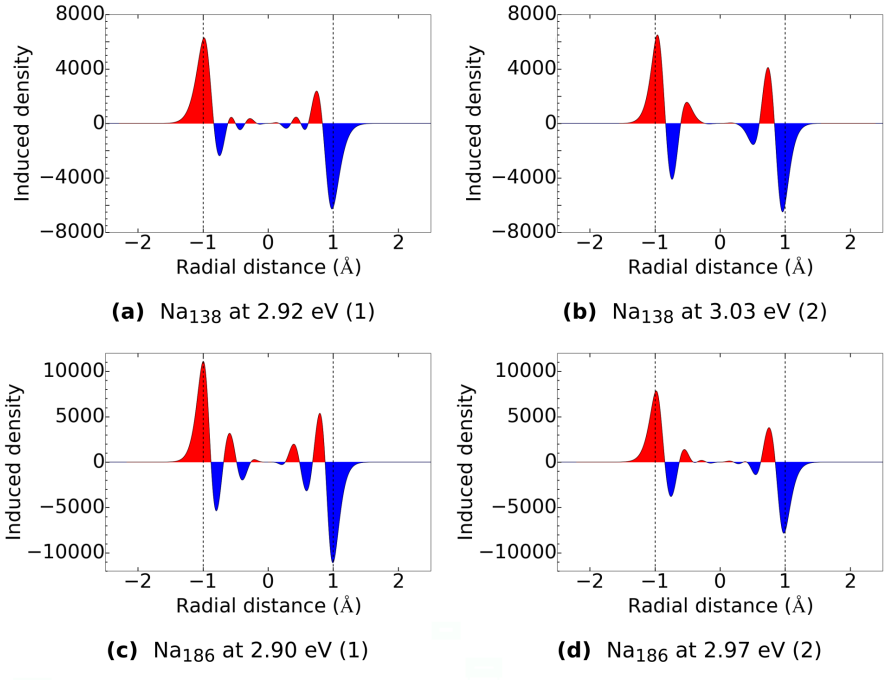

FIGURE 9 The induced densities of the clusters with 138, and 186 electrons plotted radially. The details are the same as for figure 7. Reprinted with permission from Elli Selenius, Sami Malola, Hannu Häkkinen. Analysis of Localized Surface Plasmon Resonance in Spherical Jellium Clusters and Their Assemblies. *The Journal of Physical Chemistry C*, 121 (48), pp. 27036–27052, **2017**. Copyright 2017 American Chemical Society.

3.2 Dimers

Dimeric cluster or NP systems have several applications, such as surface enhanced Raman scattering (SERS) substrates [89]. The strengthening of the Raman signals of molecules using plasmonic NPs is based on the creation of electromagnetic hot-spots with large electric field enhancements in gaps between adjacent NPs. Another application is the nanoscale ruler, which is based on the separation-dependent plasmon energy of a NP dimer [9].

Knowing the plasmonic properties of separate clusters, in article [PII] we put two jellium clusters next to each other to observe plasmon coupling and plasmons across the whole dimer. The focus was on the study of CTPs. The studied dimers consisted of the 8- and 138-electron clusters. In the broadened absorption spectra seen in figures 2 a) and 3 c), both of these clusters have a single, relatively narrow peak, so possible fragmentation or shift due to coupling is easy to observe.

Except for one heterodimer, the studied systems are homodimers consisting of two clusters of the same size. The radii of these clusters are $r = 4.1$ Å and $R = 10.8$ Å. Three different separations were used for both homodimer systems. Additionally, some of the dimers were connected with a cylindrical tunnel having the same positive background density as the spherical clusters. Since the size of

the spheres was kept the same in all the systems, the background density of these linked clusters deviates slightly (maximum 5.6 %) from the separate dimers. We used two different radii for the linker, 1.0 Å and 2.1 Å, the bigger value being the Wigner-Seitz radius used for the jellium background.

TABLE 2 Parameters for the studied dimer systems. S is the separation of the clusters, expressed in terms of the radius of the 8-electron cluster ($r \approx 4.1$ Å) or of the 138-electron cluster ($R \approx 10.7$ Å). a is the radius of the linking channel.

system	number of el.	S	a (Å)
1	8+8	$2r$	-
2	8+8	$0.5r$	-
3	8+8	0	-
4	8+8	$2r$	1.0
5	8+8	$0.5r$	1.0
6	8+8	$0.5r$	2.1
7	138+138	$0.5R$	-
8	138+138	$0.25R$	-
9	138+138	$0.1R$	-
10	138+138	$0.5R$	1.0
11	138+138+2	$0.5R$	2.1
12	8+138	$0.5R$	-

The number of electrons, separation between the jellium edges S, and the radius of the possible linking channel, a, are listed in table 2. For system **11** with 138-electron clusters, two extra electrons were added to the calculation. This was done to keep the system closed-shell - the addition of the linking channel introduced one extra occupied K-S orbital compared to the other dimers of same size, and without the additional two electrons the system would have had two filled and one empty 3P orbitals. To keep the system neutral, the same amount of positive charge was added to the jellium background, causing the jellium density to be closer to that of the single clusters.

3.2.1 Homodimers

We computed the optical spectrum for each system and performed the CTR analysis for dimers according to equation 27 at certain energies of interest. The spectra and CTR values for the dimers of 8-electron clusters can be seen in figure 10 and for the dimers of 138-electron clusters in figure 11. Since we were interested in the charge transfer and plasmon coupling, the spectra are for electric field polarized in the direction of the dimer axis. In both figures, the separate dimers are on the left and the coupled on the right, and the separation between the clusters diminishes from a) to c) to e). In figure 11 f) the spectrum of a separate 138-electron cluster is shown for comparison.

Looking at the spectrum of system **1** in figure 10 a), we can see that at this separation of $2r \approx 8.3$ Å the spectrum is still almost identical to that of the single

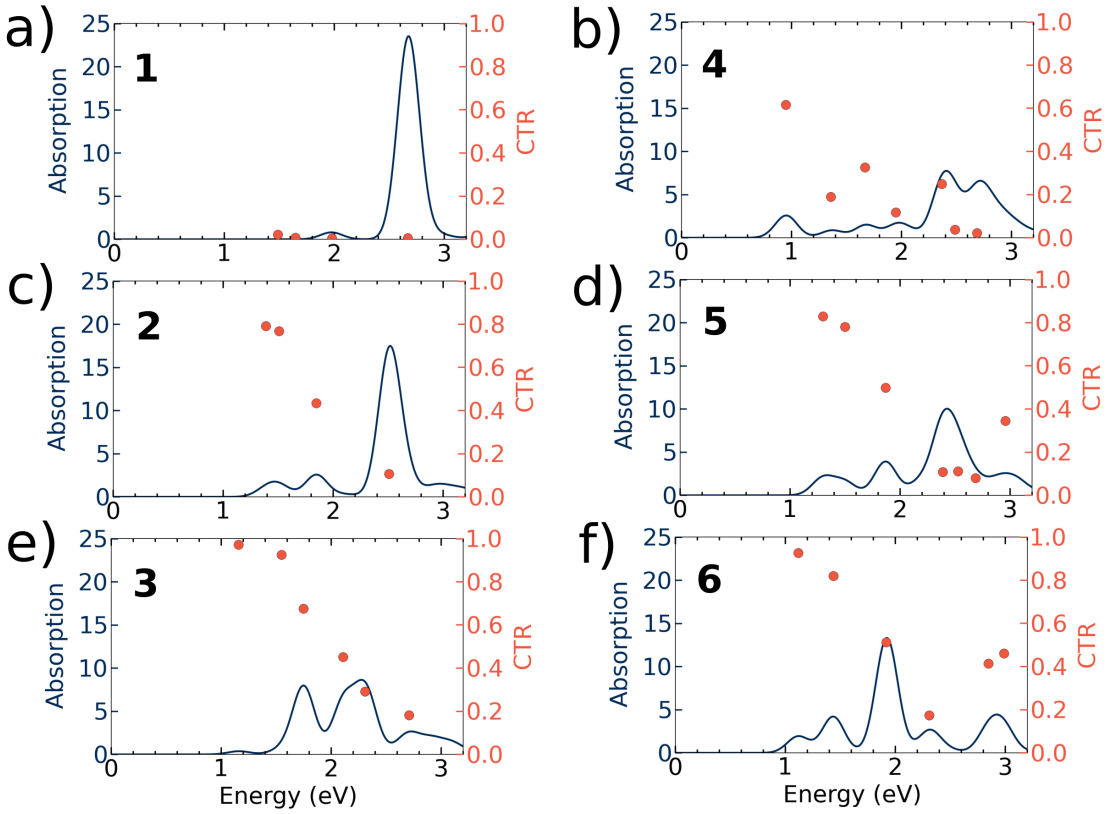

FIGURE 10 Absorption spectra and CTR values for the dimers of 8-electron clusters **1-6**. Adapted with permission from Elli Selenius, Sami Malola, Mikael Kuisma, Hannu Häkkinen. Charge Transfer Plasmons in Dimeric Electron Clusters. *The Journal of Physical Chemistry C*, 124 (23), pp. 12645–12654, **2020**. Copyright 2020 American Chemical Society.

8-electron cluster, as seen in figure 2 a). In addition, the CTR analysis shows that there are no excitations with charge transfer character. In fact, there is no electron density overlap between the two clusters, preventing any inter-cluster electron tunneling. The electron densities plotted along the dimer axis for systems **1-12** can be seen in the Supporting Information of article [PII]. The two localized plasmon peaks couple capacitively forming a BDP that is slightly red-shifted (by 0.05 eV) from the LSPR of the single cluster.

For the larger clusters, the spectrum of system **7** with a separation of $0.5r \approx 5.4$ Å already differs from the spectrum of the single 138-cluster: the peak of the dimer is red-shifted and much wider. However, there are still no low-energy excitations and thus no CTPs, as the CTR values show. The electron density overlap is negligible for this system.

For both cluster sizes, decreasing the separation and thus increasing the electron density overlap causes a drastic change in the spectra. Part of the oscillator strength is transferred to low energies where there are no excitations in the case of the separate clusters. The high CTR values at low energies show that these emerging excitations are in fact CTP peaks. Charge transfer is now possible since the electrons can tunnel or flow between the two clusters. The BDP peak is also

further fragmented. Positions of the BDP peaks are marked by the CTR values reaching their minimum.

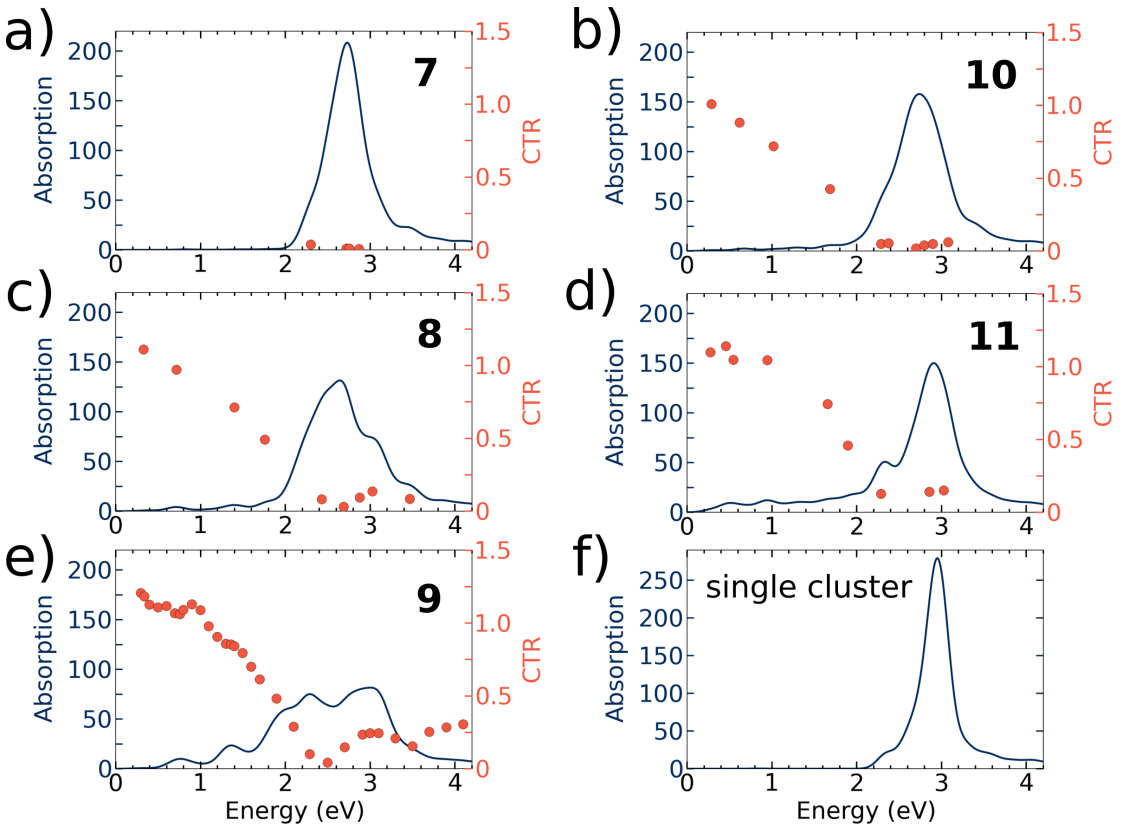

FIGURE 11 Absorption spectra and CTR values for the dimers of 138-electron clusters **7**-**11**. The spectrum of the single 138-electron cluster is included for comparison. Adapted with permission from Elli Selenius, Sami Malola, Mikael Kuisma, Hannu Häkkinen. Charge Transfer Plasmons in Dimeric Electron Clusters. *The Journal of Physical Chemistry C*, 124 (23), pp. 12645–12654, **2020**. Copyright 2020 American Chemical Society.

Linking the jellium spheres provides a channel for the electrons to flow between the clusters, and we can see CTPs for all the linked dimers. The trend with linking is similar to bringing the clusters closer together. The effect of linking is stronger for the smaller clusters since the linker is relatively larger for them, the wider linker being half and the narrower one fourth of the cluster radius. Thus, for systems **4**–**6** there is not anymore a clear main peak in the spectra and the high-CTR value excitations share a considerable percentage of the total oscillator strength.

Keeping the linker radius constant but decreasing the separation from $S = 2r$ to $S = 0.5r$ causes excitations with a large CTR value to appear at higher energies, as can be seen by comparing figures 10 b) and d). However, the spectrum for dimer **5** is less spread and has fewer peaks at low energies than the spectrum for dimer **4**. Keeping the distance at $S = 0.5r$ but making the linker wider further increases the CTR values and strengthens the CTP peaks, as seen from figure 10 f). However, the energies of the peaks are similar for dimers **5** and **6**.

For the larger dimers, both systems **10** and **11** have a separation of $S = 0.5R$,

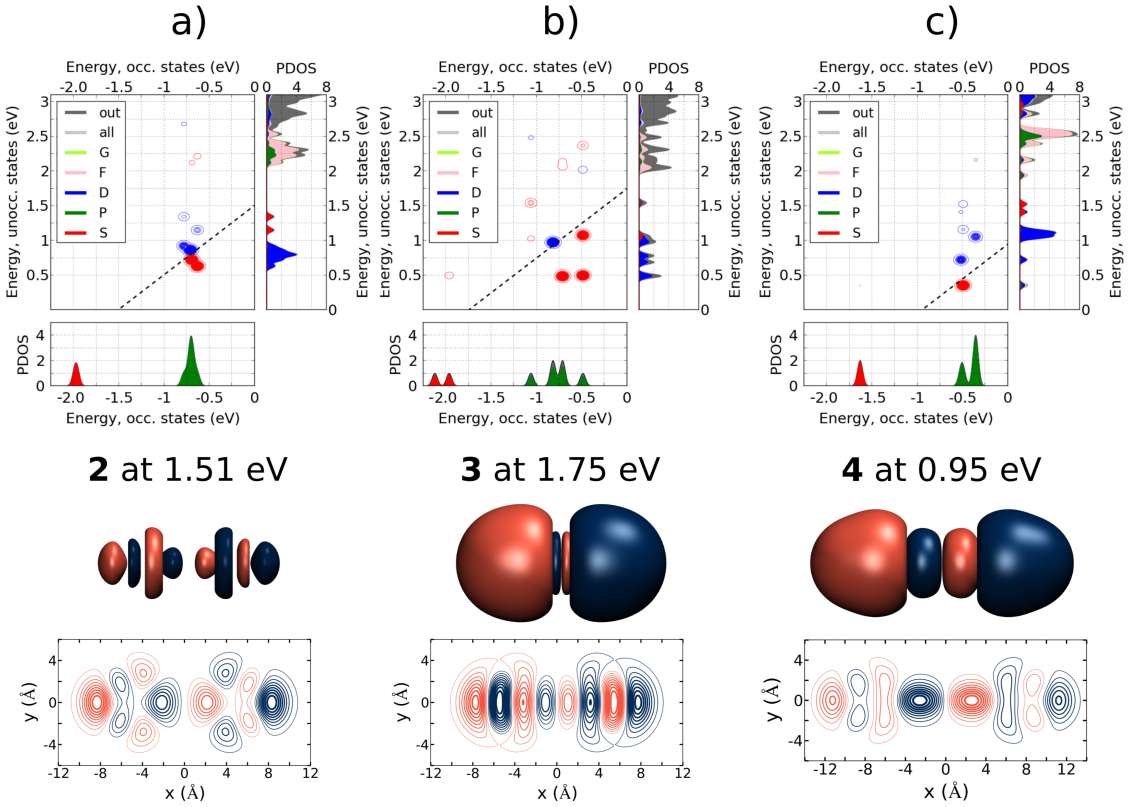

FIGURE 12 The DTCMs and the induced densities for one CTP peak for dimers **2**, **3**, and **4**. The red and blue colors of the contour map specify positive and negative contributions to the dipole moment, respectively. The dashed line indicates the e-h transitions with $\Delta\varepsilon_{eh} = E$, where E is the energy of the analyzed excitation. Here the symmetry analysis is performed separately for both clusters and the PDOSs are summed together. The Fermi energy has been set to zero. The induced densities are visualized using isosurfaces, and contour maps along the dimer plane. The isosurface values are the same for all the systems. Reprinted with permission from Elli Selenius, Sami Malola, Mikael Kuisma, Hannu Häkkinen. Charge Transfer Plasmons in Dimeric Electron Clusters. *The Journal of Physical Chemistry C*, 124 (23), pp. 12645–12654, **2020**. Copyright 2020 American Chemical Society.

but the former has the narrower linker and the latter the wider linker and two extra electrons. Here the effect of the wider linker is to bring significantly more oscillator strength to energies between 0 and 2 eV and give the BDP peak a shoulder. Since there are significantly more possible e-h transitions, the spectra for the larger clusters are more continuous than for the smaller clusters which have more distinct peaks at the lower energies.

To further study the excitations with a large CTR character, we visualized the induced densities and the contributing e-h transitions. The polarization of the laser field was in the direction of the dimer axis in the TD-DFPT calculations. In contrast to the single clusters, we now used the DTCM scheme to see whether the contributing e-h transitions have a positive or negative effect on the transition dipole moment. The strength of the DTCM contributions cannot be directly

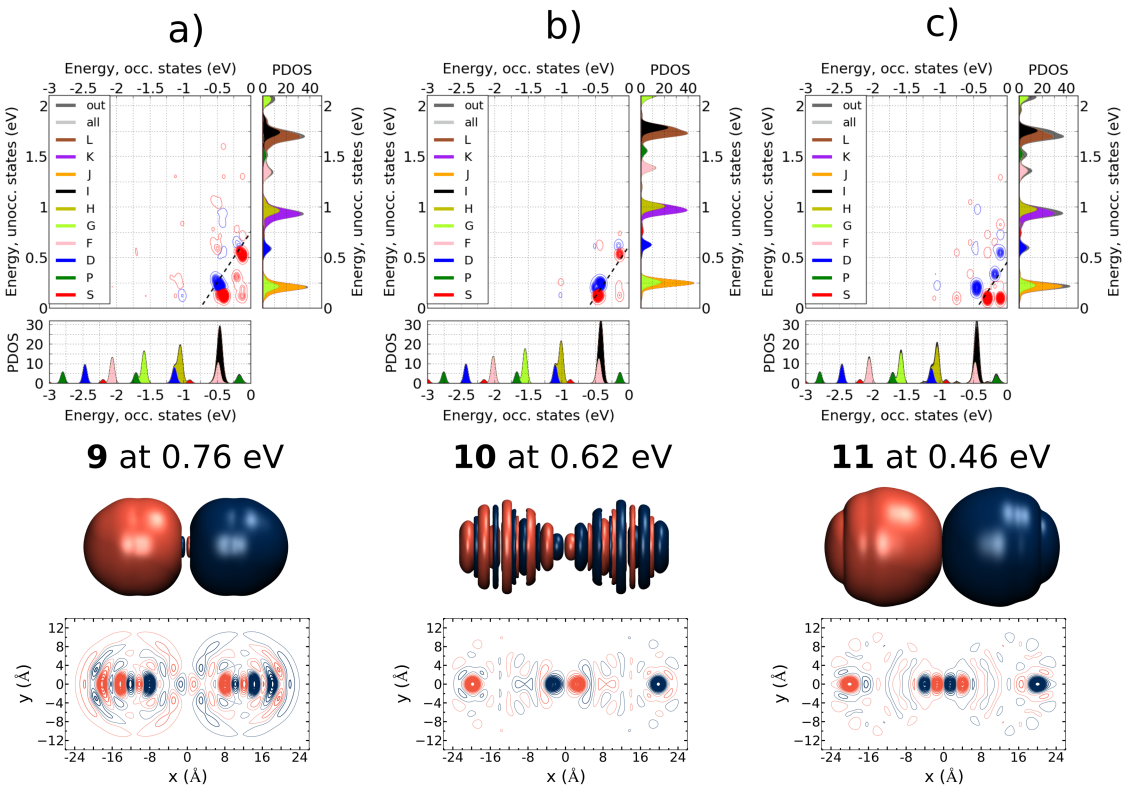

FIGURE 13 The DTCMs and isosurfaces of induced densities for dimers **9**, **10** and **11**. The details are as in figure 12. Reprinted with permission from Elli Selenius, Sami Malola, Mikael Kuisma, Hannu Häkkinen. Charge Transfer Plasmons in Dimeric Electron Clusters. *The Journal of Physical Chemistry C*, 124 (23), pp. 12645–12654, **2020**. Copyright 2020 American Chemical Society.

compared to the TCM contributions, since the former are the contributions to the transition dipole moment and the latter contributions to the absorption strength.

The DTCMs and induced densities for one CTP peak for systems **2**, **3**, and **4** are shown in figure 12, and for systems **9**, **10**, and **11** in figure 13. Now the induced densities are visualized both using isosurfaces and along the dimer plane using contour maps. In the DTCM figures, the projection for the density of states is performed separately for each cluster and the final PDOS is plotted for the sum of these values.

Let us first examine the dimers of 8-electron clusters. Since now the whole system has a cylindrical rather than spherical symmetry, the orbitals are split compared to the single 8-electron cluster, as can be seen from the PDOSs in figure 12. For example for systems **2** and **3** the lowest-energy P-symmetry orbital is the bonding state of the individual P orbitals aligned along the dimer axis, and the HOMO is the antibonding combination. For the linked dimer, system **4**, both the combinations of orbitals aligned with the dimer axis are lower in energy than the other P combinations.

The induced density has a similar shape for all the CTPs seen in figure 12. For system **2** with the separation of $S = 0.5r$, the plasmon is weaker and thus the

distribution of the induced density appears different with the chosen isosurface value. We can see that although one of the clusters is positively and the other negatively charged for all the systems, there are also oscillations in the opposite direction. Especially in the linked system **4** there is a a strong screening oscillation located in the linker.

The DTCMs also indicate the presence of these opposite electron density oscillations, showing strong negative (blue) contributions to the dipole moment in addition to the positive (red) ones. The relevant contributions are all from transitions from P-type orbitals to D-type orbitals.

For the 138-electron clusters, the isosurfaces of the induced densities resemble those of the smaller cluster. Looking at the contour maps, we can see more details of the electron density oscillations. The strongest induced dipoles for the separate dimer, system **9**, are located near the center of both the clusters separately and the direction is the same as the overall induced dipole moment. Furthermore, the induced density inside the clusters is still close to that of a separate 138-electron cluster for the LSPR peak. The linked dimers systems **10** and **11**, however, have a different structure in the induced density. The strongest density variations are located near the ends of both clusters, causing temporary dipoles in the direction of the total transition dipole. System **11** with the wider linker has additionally one extra induced dipole inside the linker, which opposes the overall transition dipole moment.

The DTCMs again show both strong positive and strong negative contributions. The main e-h transitions still mostly respect the selection rules for spherical systems, except the HOMO-LUMO transition in system **11** from a P symmetry orbital to a J symmetry orbital. In this case, both orbitals are aligned along the dimer axis and they have significant electron density inside the linker.

Our results for the larger dimers agree qualitatively with those of Rossi et al. who used real-time TDDFT to study the plasmonic response of sodium dimers of similar size, with 261 atoms in total [34]. There, first a linked and then a separate dimer was formed by stretching an initially rod-shaped cluster. For the dimers with the narrow linker, they observed two CTP peaks at energies below 1 eV and one BDP peak between 2 and 2.5 eV.

3.2.2 Heterodimer

The spectrum and CTR values for the dimer of one 8- and one 138-electron cluster are shown in figure 14 a), and a zoom of the low-energy part of the spectrum in 14 b). The sum of the spectra of the two separate clusters is also plotted for comparison.

We can see that there is coupling between the optical excitations of the two systems, since the spectrum of the dimer differs significantly from the sum spectra of the separate clusters. The largest peak at 3.08 eV is blueshifted in comparison

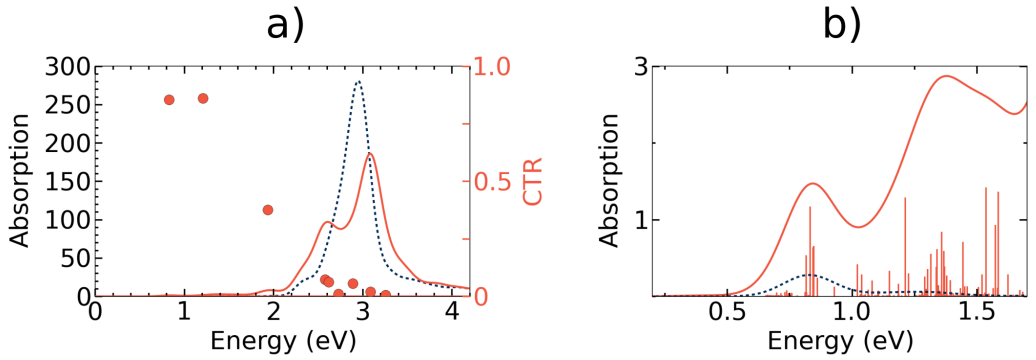

FIGURE 14 a) The absorption spectra (solid line) and CTR values for system **12**. the dashed line shows the sum of the spectra of a separate 8-electron and 138-electron cluster. b) Zoom-out of the absorption spectra between 0.2 and 1.8 eV. The oscillator strengths for the dimer are also shown. Reprinted with permission from Elli Selenius, Sami Malola, Mikael Kuisma, Hannu Häkkinen. Charge Transfer Plasmons in Dimeric Electron Clusters. *The Journal of Physical Chemistry C*, 124 (23), pp. 12645–12654, **2020**. Copyright 2020 American Chemical Society.

to the LSPR peak of the larger cluster at 2.95 eV. The peak at approximately 2.6 eV is close to the LSPR energy of the smaller cluster at 2.72 eV, but appreciably larger than it. Additionally, there are excitations between 1 and 2 eV in the dimer spectrum that are absent from the spectra of the separate clusters. These low-energy excitations have a large charge transfer character, unlike the larger peaks between 2.5 and 3.2 eV.

To find out the origins of the spectral features, we analyzed further three of these. The DTCMs and induced densities can be seen in figure 15. The first analyzed excitation at 1.21 eV with a large CTR value is seen to have both strong positive and strong negative contributions, as was seen to be characteristic for CTPs. There is a strong contribution from the 1P of the smaller cluster to the 3D of the larger cluster. The induced density, very asymmetric inside each cluster, further supports the notion of the charge density oscillating between the clusters. The bigger changes in electron density are located inside the smaller cluster.

The induced density inside the smaller cluster for the second analyzed excitation at 2.62 eV is very similar to that of a LSPR of a separate 8-electron cluster. There are weaker charge density oscillations also inside the larger cluster. The 1P→1D transition that is present for 8-electron dimers and single clusters is prominent. Additionally, many transitions between orbitals of the larger cluster contribute. Thus, it seems that this is mainly the LSPR peak of the smaller cluster, strengthened by the larger cluster.

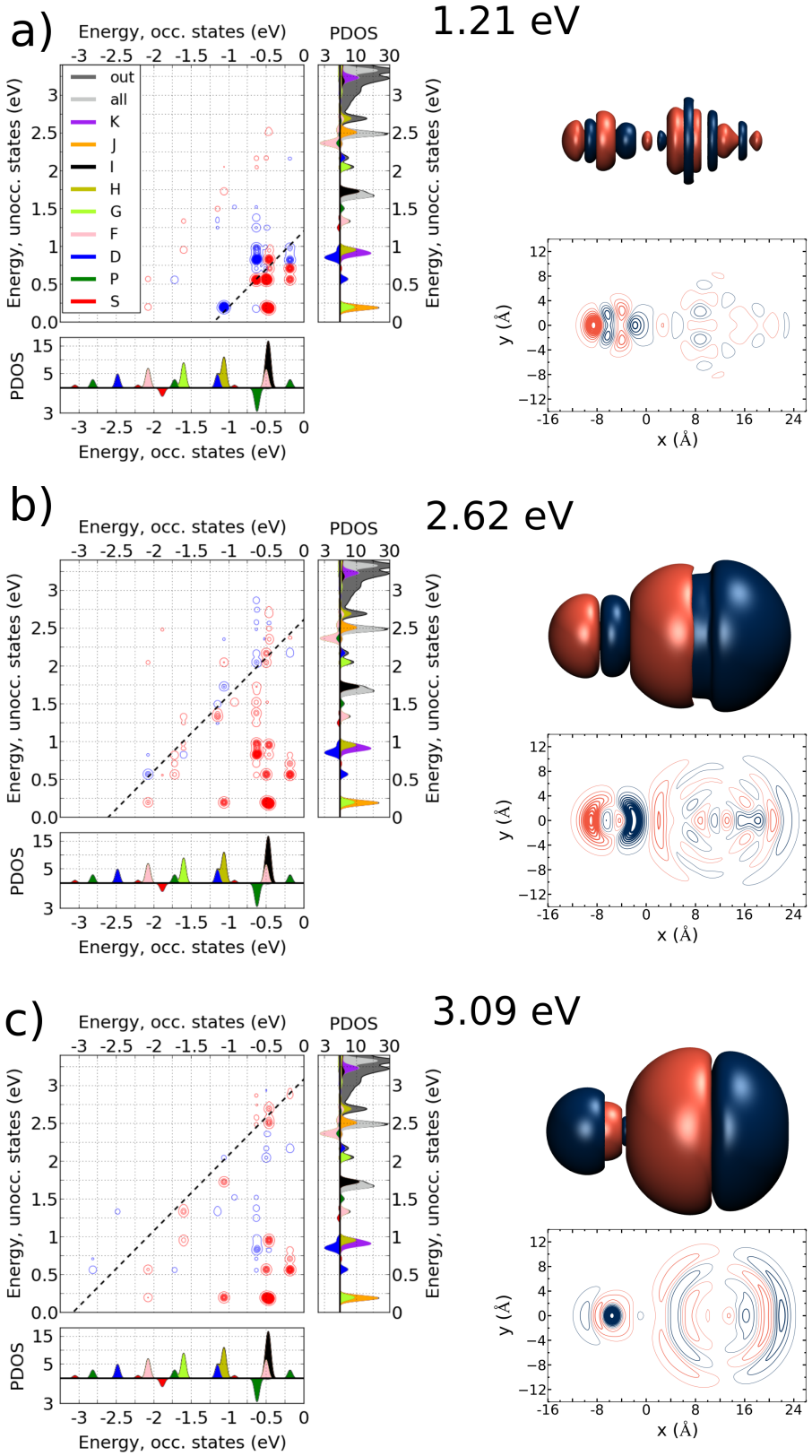

FIGURE 15 DTCMs and induced densities for three excitation energies of system **12**. The PDOS for the larger cluster is plotted up and for the smaller cluster down. The Fermi energy has been set to zero. Adapted with permission from Elli Selenius, Sami Malola, Mikael Kuisma, Hannu Häkkinen. Charge Transfer Plasmons in Dimeric Electron Clusters. *The Journal of Physical Chemistry C*, 124 (23), pp. 12645–12654, **2020**. Copyright 2020 American Chemical Society.

The excitation at 3.09 eV has, in turn, similar induced density inside the larger cluster as the single 138-electron cluster has at the LSPR energy. The smaller cluster is also participating to the transition dipole moment, but the induced density inside this cluster is quite asymmetric. Most of the transitions seen in the DTCM are positive and they are mainly between orbitals of the larger cluster. Therefore, this peak appears to be formed from the LSPR peak of the larger cluster.

Additionally, initial analysis was performed for the peak with a large CTR value visible at 0.83 eV in figure 14. This feature is present already in the spectrum of a separate 138-electron cluster, but it is more pronounced in the dimer spectrum. The DTCM and visualization of the induced density show that, even though there is charge transfer between the clusters, the contributing e-h transitions are mostly between orbitals of the larger cluster and the electron density oscillations are concentrated in the inner region of the that cluster.

Thus, in the spectrum of the heterodimer, the smaller cluster seems to be 'borrowing' oscillator strength from the larger. Due to the clear change in the spectrum and this amplification of the plasmon peak of the smaller cluster, the larger cluster can be thought of working as a sensor that detects the presence of the other cluster.

3.3 Two-dimensional cluster arrangements

Often in applications and experiments plasmonic clusters are deposited on a surface forming planar assemblies or arrays [90, 91, 92, 93]. In article [PI], we also built some planar cluster arrangements in addition to the dimer: a linear trimer, a tetramer in the shape of a square, and a hexamer in the shape of a regular hexagon. The 8-electron clusters were used and the cluster separation was kept at $S = 0.5r$ for all the systems. The same analyses were performed as for the single 8-electron cluster to compare the systems. The plane of the assemblies was designated as the xy plane. All the systems can be seen in figure 16.

To observe the plasmon couplings in different directions, we visualized the optical spectra separately for light polarized in x, y, and z directions in figure 17. The average of these directions is also shown. We can see that in the averaged spectra the main plasmon peak is split for all the arrangements of multiple clusters. Looking at the separate directions, these peaks can be seen to be the parallel and perpendicular plasmon peak. For the dimer and trimer y and z dimensions are identical and cause the perpendicular peak, and the parallel peak manifests in x direction. The tetramer is fully and the hexamer almost identical in the x and y directions which are the directions of the parallel peaks, whereas the perpendicular peak is formed in the z direction.

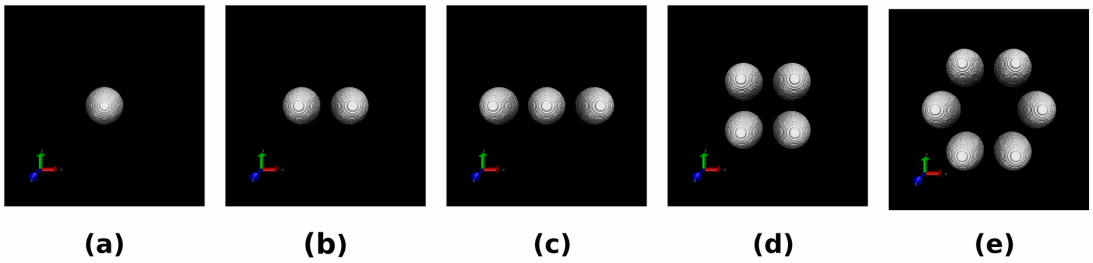

FIGURE 16 The jellium backgrounds for the planar assemblies with 1, 2, 3, 4, and 6 eight-electron cluster. The separation between the clusters is $S = 0.5r = 2.1$ Å. The x axis is shown in red, y in green, and z in blue. Reprinted with permission from Elli Selenius, Sami Malola, Hannu Häkkinen. Analysis of Localized Surface Plasmon Resonance in Spherical Jellium Clusters and Their Assemblies. *The Journal of Physical Chemistry C*, 121 (48), pp. 27036–27052, **2017**. Copyright 2017 American Chemical Society.

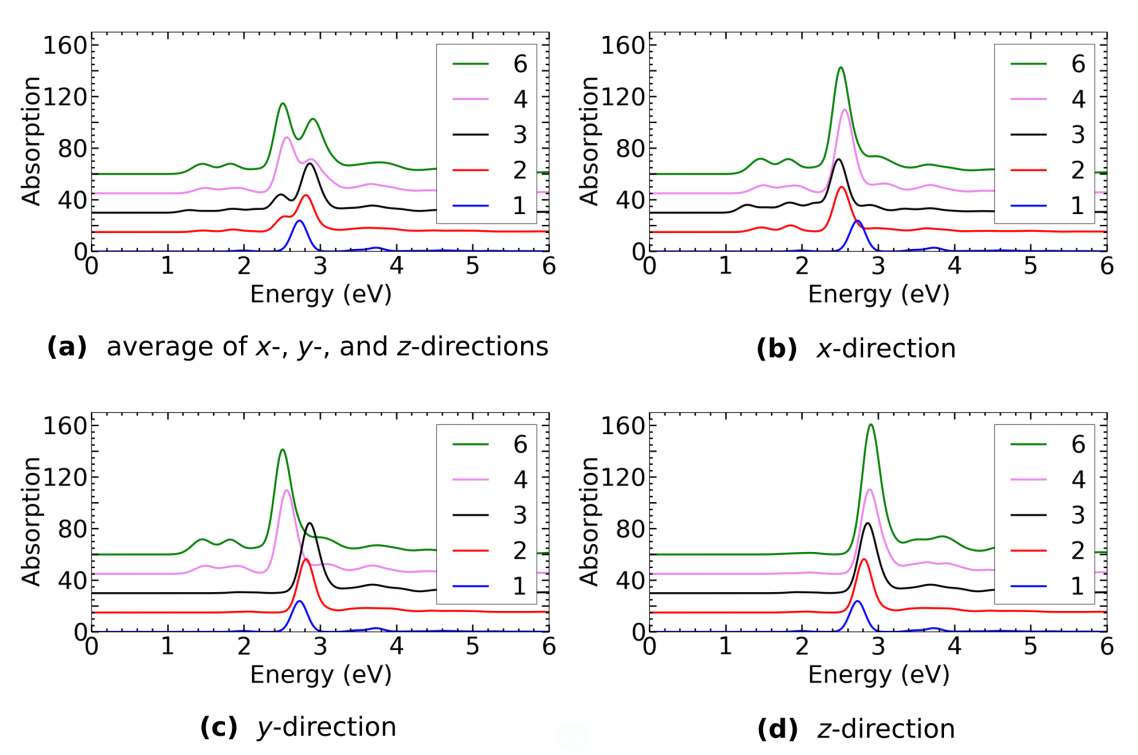

FIGURE 17 The absorption spectra for the planar systems in x, y, and z directions. The average is also shown. The zero level of the spectra has been raised by 60 units for each arrangements in comparison to the previous. Reprinted with permission from Elli Selenius, Sami Malola, Hannu Häkkinen. Analysis of Localized Surface Plasmon Resonance in Spherical Jellium Clusters and Their Assemblies. *The Journal of Physical Chemistry C*, 121 (48), pp. 27036–27052, **2017**. Copyright 2017 American Chemical Society.

The parallel peaks are redshifted from the LSPR of the single cluster, while the perpendicular peaks are blueshifted. We can see the reason by looking at the induced densities of the largest peaks in figures 18 and 19 for the parallel and

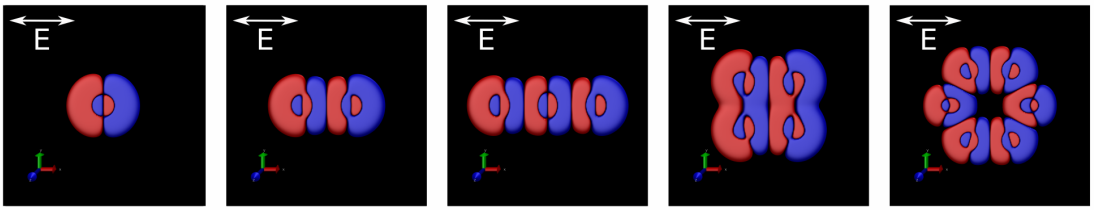

(a) single cluster at 2.72 eV (x) **(b)** dimer at 2.51 eV (x) **(c)** trimer at 2.48 eV (x) **(d)** tetramer at 2.56 eV (x) **(e)** hexamer at 2.51 eV (x)

FIGURE 18 Cross-sections of the induced densities for the parallel plasmon peaks (light polarized in the x direction) for the planar cluster arrangements along the plane of the arrangements. Reprinted with permission from Elli Selenius, Sami Malola, Hannu Häkkinen. Analysis of Localized Surface Plasmon Resonance in Spherical Jellium Clusters and Their Assemblies. *The Journal of Physical Chemistry C*, 121 (48), pp. 27036–27052, **2017**. Copyright 2017 American Chemical Society.

perpendicular polarization, respectively. For the parallel peaks, the neighboring clusters that are aligned in the direction of the polarization have their plasmons forming a bonding combination. This lowers the plasmon energy by attractive Coulombic interaction. In contrast, the plasmons of the perpendicular peaks have a repulsive interaction causing the blueshift.

TABLE 3 The energies of the parallel and perpendicular plasmon peaks for the planar arrangements in units of eV.

	single	dimer	trimer	tetramer	hexamer
parallel	2.72	2.52	2.48	2.56	2.51
perpendicular	2.72	2.81	2.86	2.88	2.90

The energies of the parallel and perpendicular plasmon peaks for each system are recorded in table 3. For the single cluster, the energy listed for both directions is the LSPR energy. The energy of the parallel plasmon peak diminishes from the dimer to the trimer, but grows again for the tetramer. The hexamer has the parallel peak located between the peaks of the dimer and tetramer, but closer to the energy of the dimer. This is explained by the geometry of the systems and the interactions of the plasmons of the individual clusters as shown in figure 18. The trimer is linear, having the induced transition density of the central cluster interacting with the induced density of the two other clusters. In the tetramer and hexamer, there are always only two clusters in a single line in the x direction. For the tetramer, there is additionally a repulsive interaction between the plasmons of the clusters in a line in the y direction. This repulsion opposes the redshifting effect, causing the higher plasmon energy of the tetramer compared to the hexamer. These results agree with experiments of chains of plasmonic nanoparticles [94, 95] and nanoparticle dimers [96].

For the perpendicular direction, the blueshift is the bigger the more clusters the arrangement has. In this case, all the interactions between neighbouring clusters are repulsive as can be seen in figure 19. As the number of clusters grows so

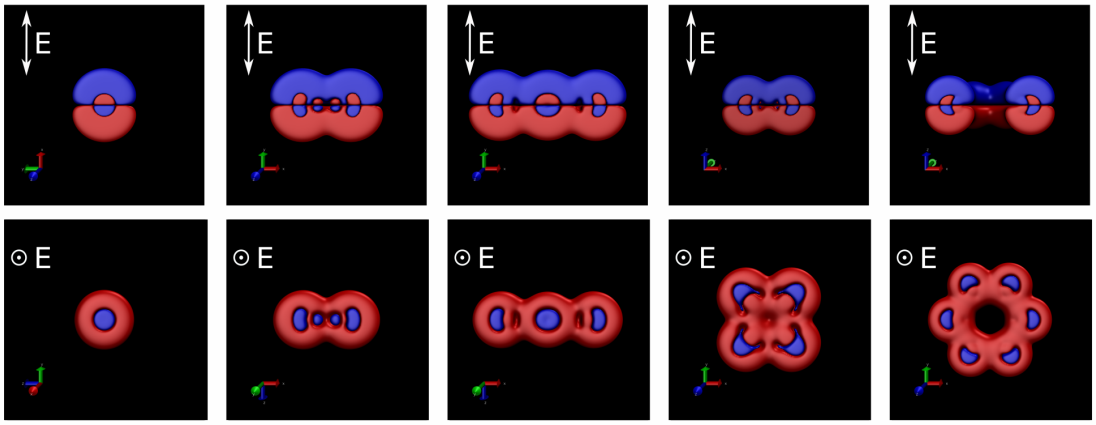

(a) single cluster at 2.72 eV (*x*) **(b)** dimer at 2.81 eV (*y*) **(c)** trimer at 2.86 eV (*y*) **(d)** tetramer at 2.88 eV (*z*) **(e)** hexamer at 2.90 eV (*z*)

FIGURE 19 Cross-sections of the induced density for the perpendicular plasmon peaks for the planar cluster arrangements along the plane of the arrangement (bottom row) and parallel to this plane, cutting across the arrangement (top row). For the tetramer in d), this plane cuts in the middle two of the clusters, for the other systems it is at the middle. Reprinted with permission from Elli Selenius, Sami Malola, Hannu Häkkinen. Analysis of Localized Surface Plasmon Resonance in Spherical Jellium Clusters and Their Assemblies. *The Journal of Physical Chemistry C*, 121 (48), pp. 27036–27052, **2017**. Copyright 2017 American Chemical Society.

does the number of interactions between neighbouring clusters, increasing the blueshift.

All the systems with 2-6 clusters have additionally two smaller absorption peaks at lower energies in the parallel spectra, approximately between 1 and 2 eV. The first one, around 1.3 - 1.5 eV, shows only 1P→1D transitions in the TCM analysis. The second at 1.8 - 1.9 eV has the strongest contribution from the 1P→2S transitions with some 1P→1D contributions. Neither the DTCM nor the CTR analysis has been performed for the larger assemblies. However, the CTR analysis for the dimer, as detailed in section 3.2.1, shows that for this system the first peak is a CTP peak and the second peak also has a relatively high CTR value. Based on the similar TCM profiles and positions in the spectra it seem likely that the peaks for the trimer, tetramer and hexamer have similar characters.

The TCMs for the plasmon peaks for light polarized in the perpendicular direction can be seen in figure 20 and for the parallel in figure 21. For the perpendicular peaks, some of the main contributions are the same as for the LSPR of the single dimer: strong contributions from 1P→1D transitions and weaker contributions from 1P→2S transitions. For the arrangements the orbitals are split, so the spread of the energies $\Delta\varepsilon_{eh}$ from these transitions is bigger. For the single cluster there were also some weaker contributions from 1P to 2S, 2D, and other higher-energy orbitals, and from 1S to 2P. For the planar systems that do not have a spherical symmetry as a whole, there are also some considerable contributions from 1P to orbitals having P and F symmetry above the 2S orbitals. These contri-

butions have more weight for the tetramer and hexamer than for the dimer and trimer. The tetramer and hexamer also experience more splitting of the orbitals.

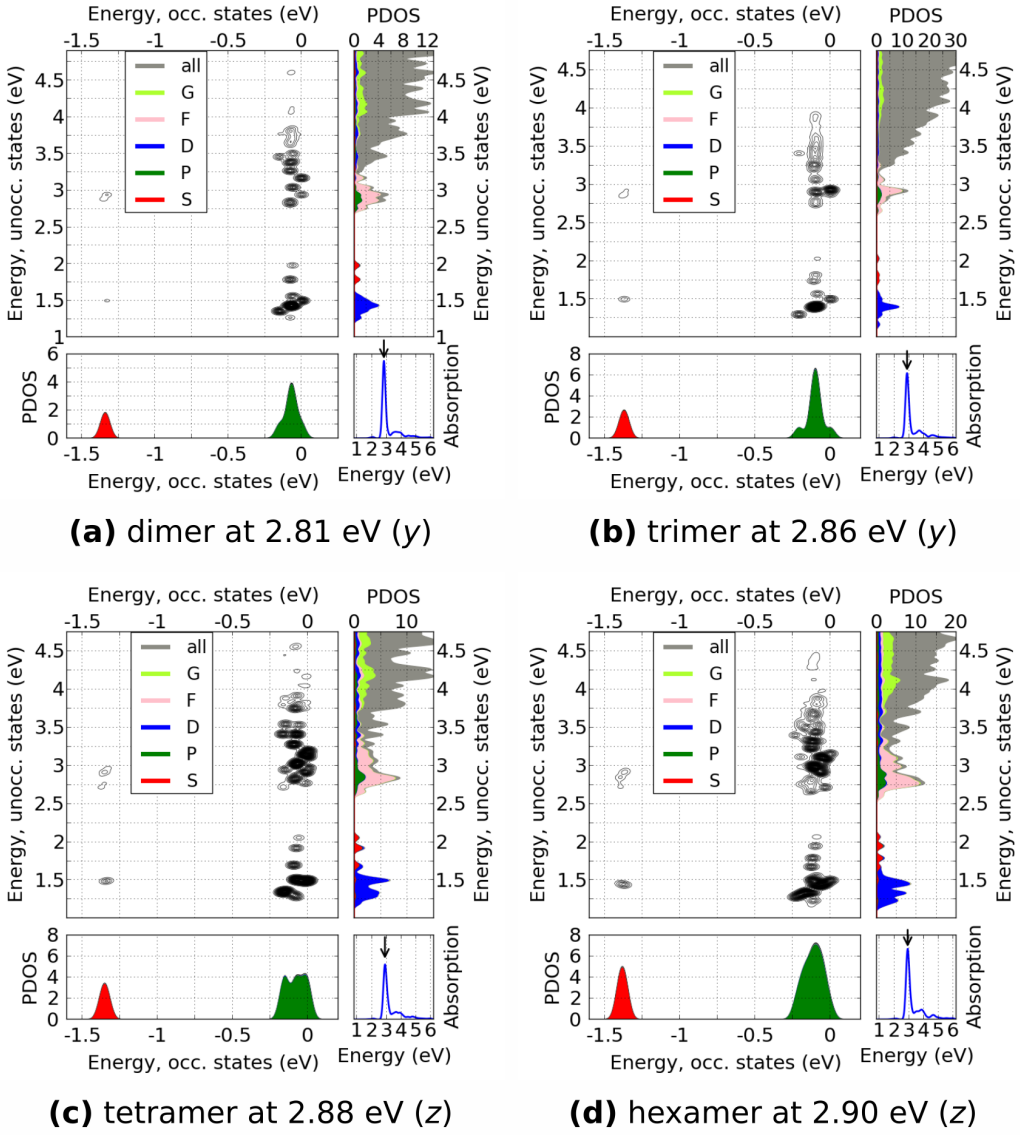

FIGURE 20 TCMs for the perpendicular plasmon peaks for the planar assemblies. The PDOS shows the sum of symmetry analyses performed separately for each cluster. The HOMO energy has been set to zero. Reprinted with permission from Elli Selenius, Sami Malola, Hannu Häkkinen. Analysis of Localized Surface Plasmon Resonance in Spherical Jellium Clusters and Their Assemblies. *The Journal of Physical Chemistry C*, 121 (48), pp. 27036–27052, **2017**. Copyright 2017 American Chemical Society.

For the parallel peaks, the contributions from the 1P→1D transitions are still strong, but also 1P→2S and 1S→1D are prominent. The transitions from 1P to higher energies play less role than for the perpendicular peaks. For these cluster arrangements, the P-type orbitals and D-type orbitals are now different bonding and antibonding states of the orbitals of the 8-electron cluster and oriented either parallel or perpendicular to the cluster plane. Thus, the combinations of

these orbitals involved in the transitions are different for the parallel than for the perpendicular peaks.

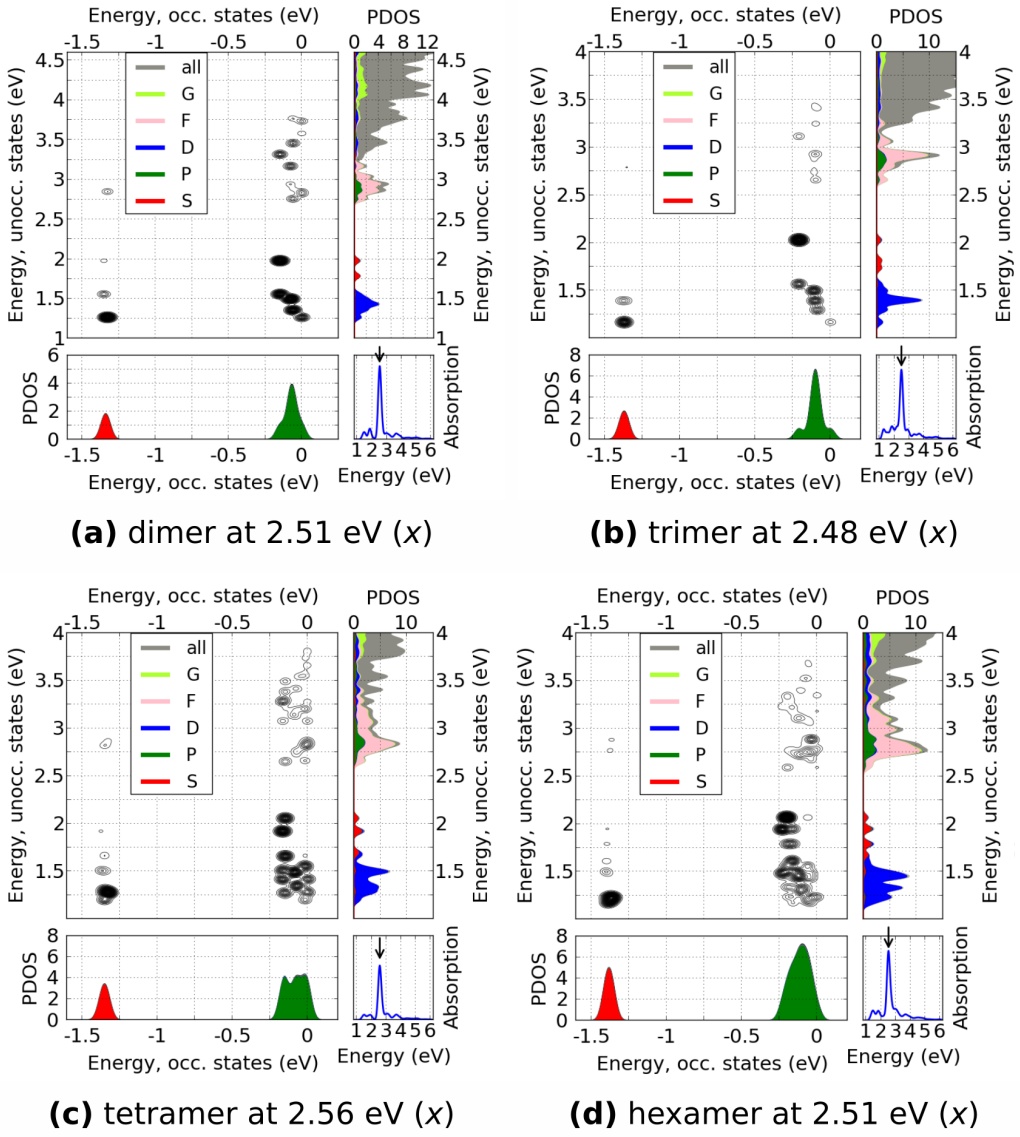

(a) dimer at 2.51 eV (x) **(b)** trimer at 2.48 eV (x)

(c) tetramer at 2.56 eV (x) **(d)** hexamer at 2.51 eV (x)

FIGURE 21 TCMs for the parallel plasmon peaks (light polarized in the x direction) for the planar assemblies. The details are as in figure 20. Reprinted with permission from Elli Selenius, Sami Malola, Hannu Häkkinen. Analysis of Localized Surface Plasmon Resonance in Spherical Jellium Clusters and Their Assemblies. *The Journal of Physical Chemistry C*, 121 (48), pp. 27036–27052, **2017**. Copyright 2017 American Chemical Society.

3.4 Three-dimensional cluster arrangements

Recently, there has been growing interest in three-dimensional nanoparticle arrangements. Plasmonic nanoparticle assemblies have applications for example

in SERS [97, 98, 99, 100] and light-assisted drug release, [101, 102, 103] which is based on the conversion of light to thermal energy by metal NPs. Instead of larger nanoparticles, atomically precise clusters can also be used as building blocks for these arrangements [104, 29]. Both geometric shapes such as tetrahedra [97, 105, 106, 107, 108] and icosahedra [106, 109], and hollow capsid-like assemblies [29, 99] have been fabricated.

To investigate plasmons in geometric and hollow arrangements, we built shell-like jellium cluster assemblies in the shape of a regular tetrahedron with four clusters, icosahedron and cuboctahedron with twelve clusters, and dodecahedron with twenty clusters. The clusters were positioned in the vertices of these shapes, leaving an empty space inside. The cluster arrangements can be seen in figure 22. The building block is the 8-electron cluster, and the for the tetrahedron, icosahedron, and cuboctahedron two systems were constructed; one with a separation of $S = 0.5r$ and one with $S = 0.25r$. For the largest arrangement, the dodecahedron, only the shorter separation was used. We will use the following abbreviations for the systems: *Th1* and *Th2* for the tetrahedra, *Ih1* and *Ih2* for the icosahedra, *Ch1* and *Ch2* for the cuboctahedra, and *Dh* for the dodecahedron. Number *1* refers to the larger and *2* to the smaller separation.

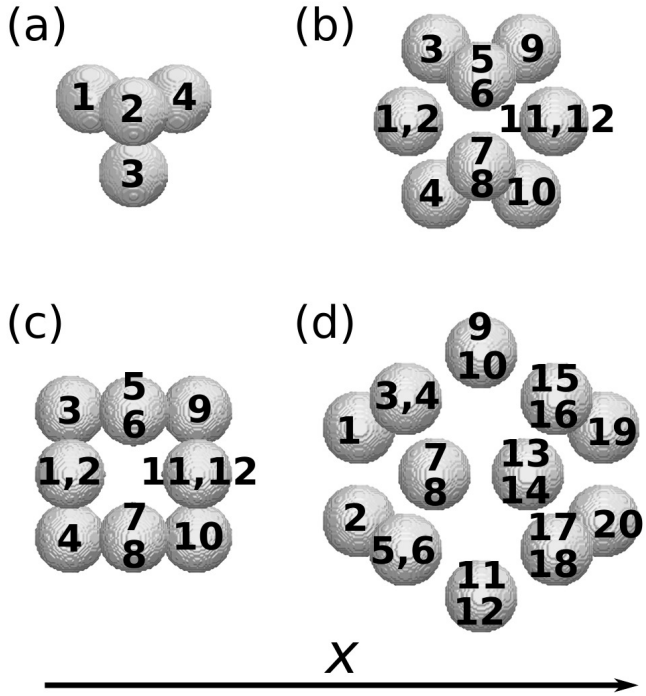

FIGURE 22 The studied cluster arrangements, numbered for further reference. a) tetrahedron, b) icosahedron, c) cuboctahedron, d) dodecahedron. The x axis, which is the direction chosen for the analysis of the absorption peaks, is indicated.

The absorption spectra for the average of light polarized in the x, y, and z directions, and the CTR values for all the studied systems can be seen in figure 23. Since the systems are all highly symmetric, the spectra are almost identical in all the directions. The spectra have been normalized by dividing the absorption

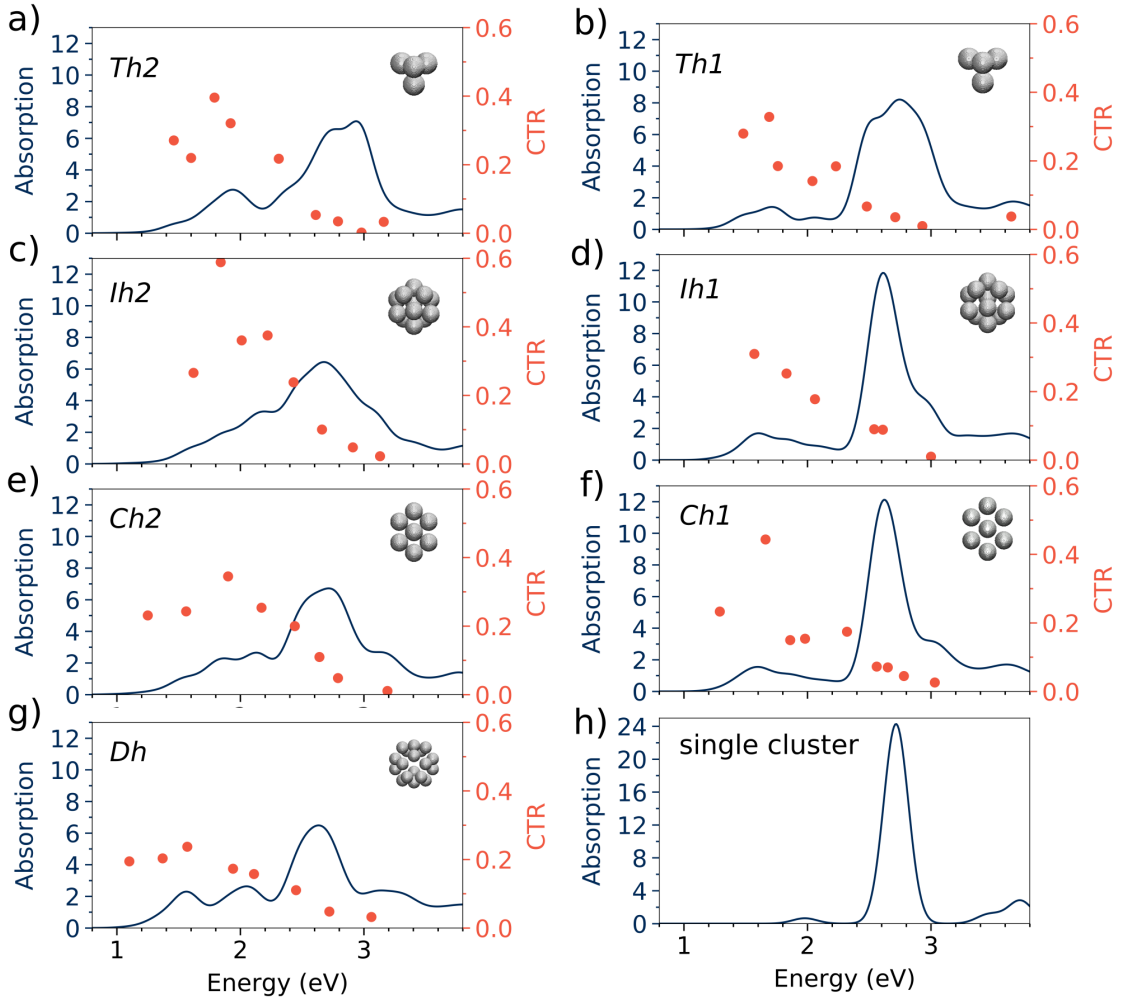

FIGURE 23 The absorption spectra per cluster and CTR values for the studied systems. The spectrum of a single 8-electron cluster is included for reference.

strengths by the number of the clusters in each arrangement.

The TD-DFPT calculations required for the CTR analysis are performed for a laser field polarized in the x direction. The CTR values are calculated using equation 28, and the clusters on the left included in the summation in the numerator are 1 and 2 for the tetrahedron, 1–4 for the icosahedron and for the cuboctahedron, and 1–8 for the dodecahedron. The numbering follows the notation in figure 22.

In comparison to the single cluster, *Ih1* and *Ch1* with the longer separation still preserve the main plasmon peak, which experiences a broadening and a redshift as illustrated in figures 23 d) and f). However, both arrangements already support low-energy excitations with charge transfer character as shown by the CTR values. When the separation is decreased, the main peak is further fragmented and more oscillator strength is transferred to the low-energy excitations with a high charge transfer nature, as seen in figures 23 c) and e). The same trend was also seen for the dimers, as was discussed in chapter 3.2.1. For both separations, the icosahedral and cuboctahedral arrangements have very similar spectra.

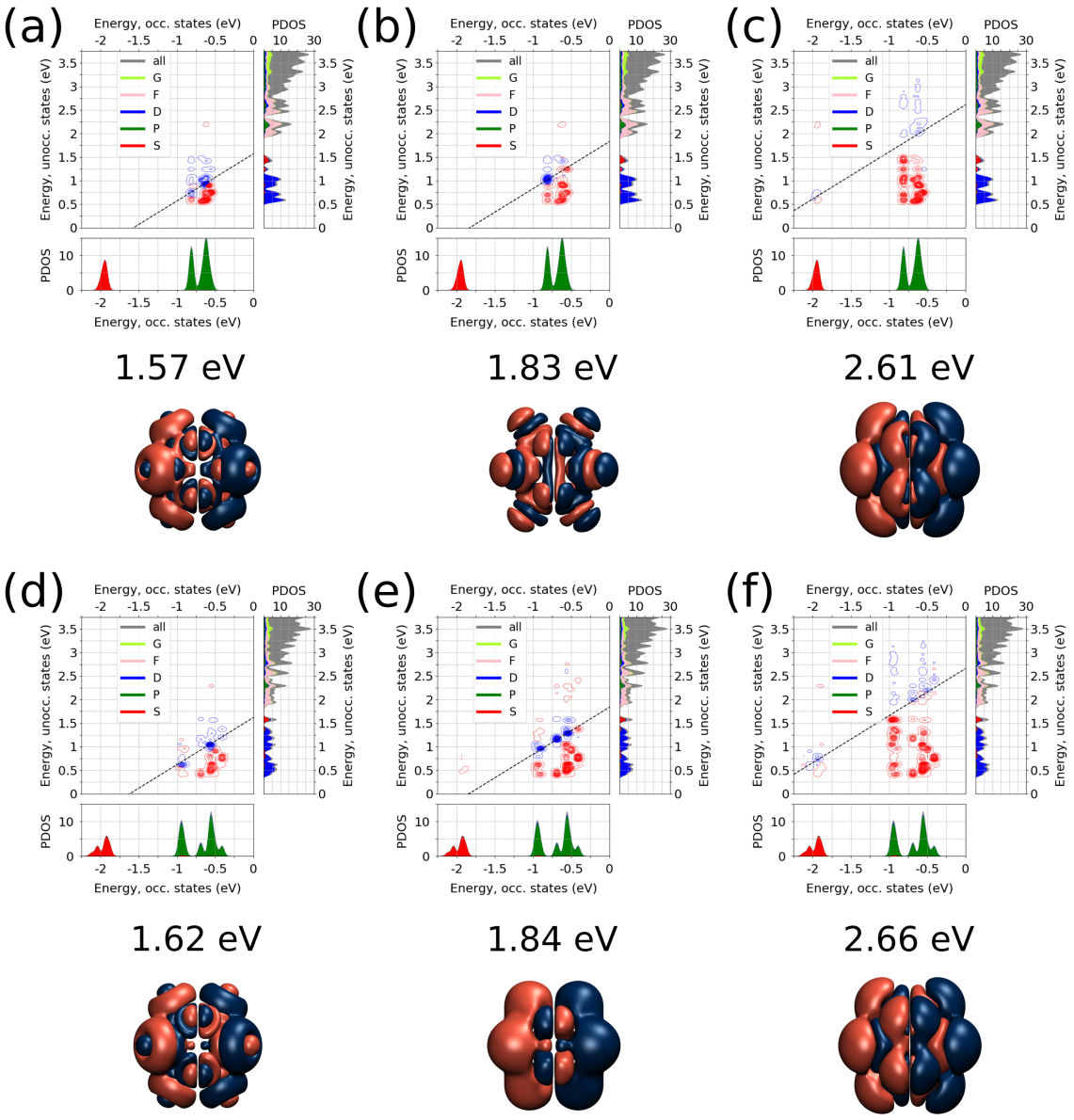

FIGURE 24 The DTCMs and induced densities for selected excitations for *Ih1* (top row) and *Ih2* (bottom row). The PDOS shows the sum of symmetry analyses performed separately for each cluster. The Fermi level has been set to zero.

For the tetrahedron, the average distance between clusters is smaller than for the larger assemblies with the same separation. Thus, the spectra for *Th1* seen in figure 23 b) and *Th2* in 23 a) are quite similar, and the spectrum of *Th1* already has a very broad main plasmon peak and peaks with high CTR values below 2 eV. The spectrum for *Dh* has the same main features as the other spectra with the separation of $S = 0.25r$.

In all the systems, the CTR index reaches its highest values at energies approximately below 2 eV and the lowest values close to the main peak or its shoulder near 3 eV. This indicates that the excitation causing the main peak has the charge density oscillating individually around each cluster. For the systems with the

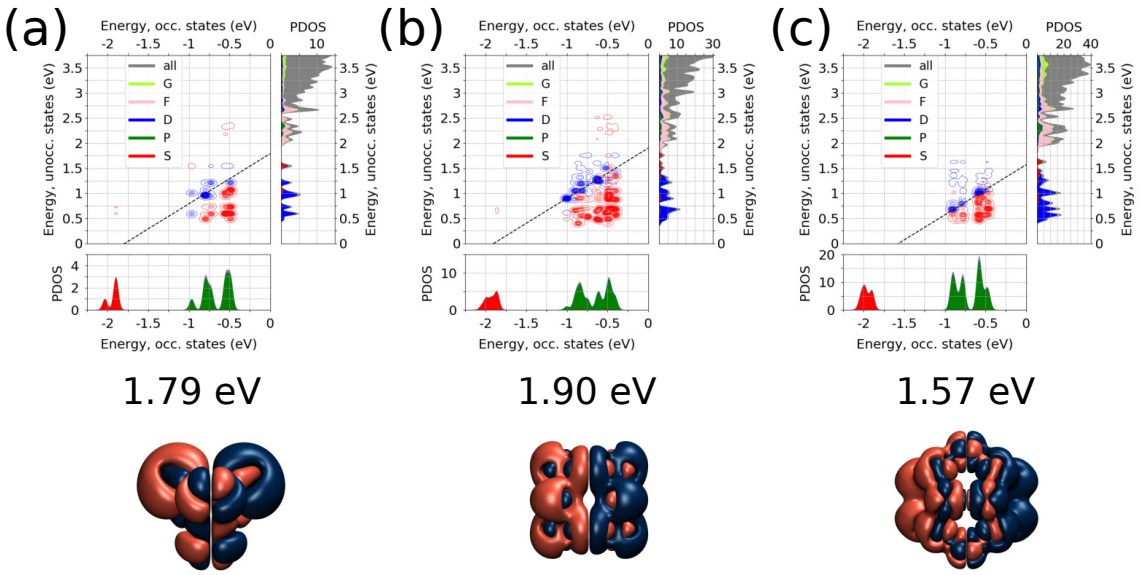

FIGURE 25 DTCMs and induced densities for the absorption peak with the highest CTR value for a) *Th2* b) *Ch2*, and c) *Dh*. The details are as in figure 24.

larger separation, the CTR values diminish faster with the increasing energy than for the systems with the narrower gaps.

The DTCMs and induced densities for selected absorption peaks for *Ih1* and *Ih2* are shown in figure 24. The analysis is performed for light polarized in the x direction. The trends of this geometry are representative also of the other systems. All the peaks analyzed in a), b), d), and e) have a high CTR value, and the peaks in c) and f) correspond to the largest peak with a low CTR value close to the original LSPR energy.

For the larger peaks, the contributions shown in the DTCMs are predominantly positive and involve mostly 1P→1D and 1P→2S transitions. Examination of the induced density confirms the nature of these peaks as bonding combinations of the LSPR peaks of the individual clusters: the electron density oscillations mostly happen separately inside each cluster, and with a similar distribution to the localized surface plasmon of the single cluster.

In contrast, the induced densities for the lower-energy peaks are not symmetric inside one cluster but involve electrons oscillating between clusters, as confirmed by the high CTR values. The contributing transitions are mostly 1P→1D, but unlike for the bonding plasmon peaks there are also strong negative contributions to the transition dipole moment similarly as for the CTP peaks in the dimer systems. In fact, the percentage of the negative contributions of the total dipole strength is largest for the lowest-energy excitations and diminishes up to about 2.5 eV. All these observations indicate that these low-energy features are CTP peaks. It is of notice that all the negative contributions have the transition energy $\Delta\varepsilon_{eh}$ matching to the energy of the whole excitation, whereas there are positive contributions with various transition energies.

Comparing the corresponding peaks between *Ih1* and *Ih2*, we can see that the contributing transitions and the shape of the induced density distribution are similar. Since the orbitals are more split for *Ih2* with the smaller separation than for *Ih1*, there are transitions for a wider range of electron and hole energies ε_e and ε_h for *Ih2*.

Figure 25 shows the DTCMs and induced densities for the absorption peaks with the highest CTR values for systems *Dh2*, *Ch2*, and *Dh*. The DTCMs are similar to the highest-CTR peak for *Ih2* seen in figure 24 with both strong positive and negative contributions, the negative located on the $\Delta\varepsilon_{eh} = E$ line. The cuboctahedron, being the least symmetric of the systems, has the most split orbitals leading to the largest spread of the contributing transitions. The induced densities and CTR values show that also for these peaks the electron density oscillates between the clusters. Thus, these excitations can also be classified as CTPs.

In conclusion, with the chosen cluster size and separations all the studied geometries had quite similar spectra and excitations. However, the exact shapes and positions of the peaks were different, making it possible to distinguish the different geometries. There seems to be a region in the inter-cluster separation where changing the separation even by one Ångström has a drastic effect on the spectra, as seen for the icosahedra and cuboctahedra. For all the studied systems, the excitations below approximately 2 eV have CTP characteristics, whereas the largest peaks around 2.6 - 2.8 eV are bonding combinations of the LSPR peaks.

4 CONCLUSIONS AND OUTLOOK

In this thesis, I have presented my studies of the optical properties of metal clusters and cluster assemblies using the uniform jellium model and the density-funcional theory code GPAW. I started with the birth of the LSPR in separate clusters, moved to plasmon coupling and CTPs in dimers, continued with parallel and perpendicular plasmon modes in planar cluster assemblies, and finished with three-dimensional cluster assemblies with bonding plasmon modes and CTPs.

Studying the separate clusters, all the cluster sizes were found to have one or two large absorption peaks. The TCM analysis showed that these peaks were caused by collective excitations, and radial analysis of the induced density revealed that most of the electron density oscillations were concentrated near the surface of the clusters. These features indicate that the main peak in all the studied clusters is a LSPR peak, which for some cluster sizes is fragmented. Thus, for these jellium clusters, even eight valence electrons is enough to support a LSPR peak.

The detailed knowledge of the plasmons in separate clusters facilitated the study of cluster assemblies. The simplest of these, the dimers, already contain the two main phenomena of arrangements of several clusters: bonding of the localized surface plasmons and CTPs. We developed a new tool, the CTR index, to distinguish the CTP peaks in the optical spectra. The excitations at low energies in the spectra, appearing for linked dimers and small separations, were found to have the largest CTR values, while the strongest absorption peaks close to the LSPR energy had the lowest values.

The effect of the parallel or perpedicular polarization of light with respect to the plane of the clusters was also studied for the dimers and for other planar assemblies with 3–6 clusters. The main peaks were found to be combinations of the individual LSPR peaks with the electron density oscillating in-phase. These peaks were observed to exhibit a blueshift for the perpendicular and a redshift for the parallel direction compared to the single cluster. The redshift depended not

only on the number of clusters in the assembly, but also the geometry through to attractive and repulsive interactions between the plasmons of different clusters.

For the three-dimensional geometric cluster assemblies, the main features in the spectra were CTPs and peaks caused by combinations of the individual localized surface plasmons aligned in the direction of the electric field. We used the same idea of the CTR index as for the dimers, but due to the more complex geometry, developed a new formula to calculate the values. Besides the CTR values, one difference between the surface-plasmon like main peaks and the CTPs was that the DTCMs at the CTP energies had also strong negative contributions to the dipole moment, unlike the DTCMs for the main peaks.

These results have given new insight into the emergence and nature of the localized surface plasmon resonance in small clusters, and the plasmon coupling and CTPs in cluster arrangements. Plasmonic cluster crystals and arrangements used in experiments and applications often have complex electron density responses due to the atomic structure and interplay between the metal core and the ligand layer. The detailed knowledge of the charge density oscillations and e-h transition contributions in the more simple jellium assemblies can help in understanding the nature of optical excitations of these real cluster systems.

Our calculations and results show that the jellium model as it is implemented in GPAW combined with lr-TDDFT provides an efficient way to study the nature of plasmonic excitations in metal clusters and their assemblies. The real-space grid mode of GPAW enables the building and computation of all cluster geometries, no matter how complex, equally easily and with the same computational cost. The jellium model, in turn makes the calculations computationally cheaper than fully atomistic DFT calculations.

The combination of the (D)TCM analysis, visualization of the induced density, and calculation of the CTR index for cluster assemblies provides a cost-effective way to asses the plasmon nature of excitations of the optical spectra. The TD-DFPT calculation needed for TCMs and the induced densities uses the matrix elements already computed in the lr-TDDFT calculation for the optical spectra, and the CTR indices can be computed entirely post-processing using the output of the induced density calculations. The TCM gives information about the collectivity of the excitations, and DTCM also about the additivity of the e-h contributions to the dipole moment. In these schemes, all the transition contributions and their relative strengths can be seen at a glance, without the need to analyze each transition individually. Visualization of the induced density can give an idea about the distribution and strength of the electron density oscillations, and the CTR values indicate which excitations involve charge transfer between clusters.

These methods could be used in further plasmon studies, building on the knowledge already gathered for various systems. For example, the studied assemblies of clusters included in this thesis were relatively small, consisting at most of 20 clusters. One option to increase the size of the three-dimensional arrangements is to add geometric shells. The next step for the icosahedron, for example, would be

two icosahedral shells totaling at 54 clusters. Multiple shells of clusters open up new possibilities for the coupling of the optical excitations. Now all the studied arrangements were hollow, but a cluster could be added to the middle, to further increase the plasmon coupling.

Increasing the number of shells further and further has the logical conclusion of forming a periodic assembly. This would represent a crystal of plasmonic clusters, a metamaterial. The effect of different packings on the plasmonic response could be investigated. Recently there have been successful endeavours to synthesize and crystallize cluster polymers [26, 27, 28]. A model system for these kind of materials could be constructed by building a periodic jellium arrangement with linking in one direction.

For the planar assemblies, two-dimensional periodic systems with different symmetries could also be constructed to mimic arrays of NPs used for example for SERS [110, 111]. In GPAW, the lr-TDDFT approach is currently not implemented for periodic systems, but real-time TDDFT can be used.

We kept the jellium density uniform for all the assemblies. Further variation can be achieved by using different densities, for example to model core-shell clusters consisting of two different metals. Metals such as silver and gold, where d electron screening affects the optical response, can be modeled by adding a region with a polarizable dielectric medium inside the cluster [112, 113]. For mimicking different kinds of ligands or other linkers, the linker density in the connected dimers can also be adjusted.

To model different kinds of linkings between two or several clusters, the jellium model can also be combined with an atomistic calculation. Larger clusters or nanoparticles can be represented by jellium, and an atom or a chain of atoms can be placed between, as has been previously done by Nordlander and coworkers [114, 115]. The linker could also be an atomistic ligand molecule. This has the effect of making the conductive or tunneling properties of the linker more realistic, but maintaining the computational simplicity of the jellium model for the larger parts of the system.

In addition to applying them to new systems, the methods used in this thesis can and should be further extended and improved. The experimental study of metal clusters is still going strong after almost forty years since its birth, with new clusters and cluster materials, synthesis and characterization methods, and applications reported every year. This means that new computational research is also constantly needed, whether it is to confirm and verify experimental results, identify the best materials for a suggested application, or predict novel phenomena that might start a new branch of cluster science. The emerging trends in computational sciences, such as GPU computing and machine learning, might offer a challenge in adapting the old methods, but can also open doors to develop completely new tools. Thus, we computational scientists cannot content ourselves to existing practices, but rather constantly seek to improve them.

REFERENCES

[1] I. Freestone, N. Meeks, M. Sax, and C. Higgitt, The Lycurgus cup - a Roman nanotechnology, *Gold Bull.*, **40**(4), 270–277, (2007)

[2] M. Faraday, The Bakerian Lecture. Experimental relations of gold (and other metals) to light, *Philos. Trans. Royal Soc.*, **147**, 145–181, (1857)

[3] G. Mie, Beiträge zur optik trüber medien, speziell kolloidaler metallösungen, *Ann. Phys.*, **330**(3), 377–445, (1908)

[4] K. L. Kelly, E. Coronado, L. L. Zhao, and G. C. Schatz, The optical properties of metal nanoparticles: The influence of size, shape, and dielectric environment, *J. Phys. Chem. B*, **107**(3), 668–677, (2003)

[5] E. Prodan, C. Radloff, N. J. Halas, and P. Nordlander, A hybridization model for the plasmon response of complex nanostructures, *Science*, **302**(5644), 419–422, (2003)

[6] L. R. Hirsch, R. J. Stafford, J. A. Bankson, S. R. Sershen, B. Rivera, R. Price, J. D. Hazle, N. J. Halas, and J. L. West, Nanoshell-mediated near-infrared thermal therapy of tumors under magnetic resonance guidance, *Proc. Natl. Acad. Sci. U.S.A.*, **100**(23), 13549–13554, (2003)

[7] X. Huang, I. H. El-Sayed, W. Qian, and M. A. El-Sayed, Cancer cell imaging and photothermal therapy in the near-infrared region by using gold nanorods, *J. Am. Chem. Soc.*, **128**(6), 2115–2120, (2006)

[8] C. Clavero, Plasmon-induced hot-electron generation at nanoparticle/metal-oxide interfaces for photovoltaic and photocatalytic devices, *Nat. Photonics*, **8**(2), 95–103, (2014)

[9] C. Sönnichsen, B. M. Reinhard, J. Liphardt, and A. P. Alivisatos, A molecular ruler based on plasmon coupling of single gold and silver nanoparticles, *Nat. Biotechnol.*, **23**(6), 741–745, (2005)

[10] T. Tsukuda and H. Häkkinen, *Protected Metal Clusters: From Fundamentals to Applications*, vol. 9. Elsevier, (2015)

[11] W. A. De Heer, The physics of simple metal clusters: experimental aspects and simple models, *Rev. Mod. Phys.*, **65**(3), 611, (1993)

[12] M. Brack, The physics of simple metal clusters: self-consistent jellium model and semiclassical approaches, *Rev. Mod. Phys.*, **65**(3), 677, (1993)

[13] P. Jena and Q. Sun, Super atomic clusters: design rules and potential for building blocks of materials, *Chem. Rev.*, **118**(11), 5755–5870, (2018)

[14] W. Ekardt, Work function of small metal particles: Self-consistent spherical jellium-background model, *Phys. Rev. B*, **29**(4), 1558, (1984)

[15] D. Beck, Self-consistent calculation of the electronic structure of small jellium spheres, *Solid State Commun.*, **49**(4), 381–385, (1984)

[16] W. D. Knight, K. Clemenger, W. A. de Heer, W. A. Saunders, M. Y. Chou, and M. L. Cohen, Electronic shell structure and abundances of sodium clusters, *Phys. Rev. Lett.*, **52**, 2141–2143, (1984)

[17] M. M. Kappes, P. Radi, M. Schär, and E. Schumacher, Probes for electronic and geometrical shell structure effects in alkali-metal clusters. Photoionization measurements on K_xLi, K_xMg and K_xZn ($x < 25$), *Chem. Phys. Lett.*, **119**(1), 11–16, (1985)

[18] S. Khanna and P. Jena, Atomic clusters: Building blocks for a class of solids, *Phys. Rev. B*, **51**(19), 13705, (1995)

[19] S. Khanna and P. Jena, Assembling crystals from clusters, *Physical Rev. Lett.*, **69**(11), 1664, (1992)

[20] I. Goldby, L. Kuipers, B. Von Issendorff, and R. Palmer, Diffusion and aggregation of size-selected silver clusters on a graphite surface, *Appl. Phys. Lett.*, **69**(19), 2819–2821, (1996)

[21] S. Carroll, P. Weibel, B. Von Issendorff, L. Kuipers, and R. Palmer, The impact of size-selected Ag clusters on graphite: an STM study, *J. Phys. Condens. Matter*, **8**(41), L617, (1996)

[22] N. Vandamme, E. Janssens, F. Vanhoutte, P. Lievens, and C. Van Haesendonck, Scanning probe microscopy investigation of gold clusters deposited on atomically flat substrates, *J. Phys. Condens. Matter*, **15**(42), S2983, (2003)

[23] M. Walter, J. Akola, O. Lopez-Acevedo, P. D. Jadzinsky, G. Calero, C. J. Ackerson, R. L. Whetten, H. Grönbeck, and H. Häkkinen, A unified view of ligand-protected gold clusters as superatom complexes, *Proc. Natl. Acad. Sci. U.S.A.*, **105**(27), 9157–9162, (2008)

[24] R. Jin, C. Zeng, M. Zhou, and Y. Chen, Atomically precise colloidal metal nanoclusters and nanoparticles: fundamentals and opportunities, *Chem. Rev.*, **116**(18), 10346–10413, (2016)

[25] I. Chakraborty and T. Pradeep, Atomically precise clusters of noble metals: emerging link between atoms and nanoparticles, *Chem. Rev.*, **117**(12), 8208–8271, (2017)

[26] M. De Nardi, S. Antonello, D.-e. Jiang, F. Pan, K. Rissanen, M. Ruzzi, A. Venzo, A. Zoleo, and F. Maran, Gold nanowired: a linear $(Au_{25})_n$ polymer from Au_{25} molecular clusters, *ACS Nano*, **8**(8), 8505–8512, (2014)

[27] Z.-R. Wen, Z.-J. Guan, Y. Zhang, Y.-M. Lin, and Q.-M. Wang, $[Au_7Ag_9(dppf)_3(CF_3CO_2)_7BF_4]_n$: a linear nanocluster polymer from molecular Au_7Ag_8 clusters covalently linked by silver atoms, *Chem. Commun.*, **55**(86), 12992–12995, (2019)

[28] P. Yuan, R. Zhang, E. Selenius, P. Ruan, Y. Yao, Y. Zhou, S. Malola, H. Häkkinen, B. K. Teo, Y. Cao, *et al.*, Solvent-mediated assembly of atom-precise gold–silver nanoclusters to semiconducting one-dimensional materials, *Nat. Commun.*, **11**(1), 1–8, (2020)

[29] Nonappa, T. Lahtinen, J. S. Haataja, T.-R. Tero, H. Häkkinen, and O. Ikkala, Template-free supracolloidal self-assembly of atomically precise gold nanoclusters: From 2D colloidal crystals to spherical capsids, *Angew. Chem. Int. Ed.*, **128**(52), 16269–16272, (2016)

[30] J. Zuloaga, E. Prodan, and P. Nordlander, Quantum description of the plasmon resonances of a nanoparticle dimer, *Nano Lett.*, **9**(2), 887–891, (2009)

[31] W. Zhu, R. Esteban, A. G. Borisov, J. J. Baumberg, P. Nordlander, H. J. Lezec, J. Aizpurua, and K. B. Crozier, Quantum mechanical effects in plasmonic structures with subnanometre gaps, *Nat. Commun.*, **7**(1), 1–14, (2016)

[32] G.-T. Bae and C. M. Aikens, Time-dependent density functional theory studies of optical properties of Ag nanoparticles: octahedra, truncated octahedra, and icosahedra, *J. Phys. Chem. C*, **116**(18), 10356–10367, (2012)

[33] J.-H. Li, M. Hayashi, and G.-Y. Guo, Plasmonic excitations in quantum-sized sodium nanoparticles studied by time-dependent density functional calculations, *Phys. Rev. B*, **88**(15), 155437, (2013)

[34] T. P. Rossi, A. Zugarramurdi, M. J. Puska, and R. M. Nieminen, Quantized evolution of the plasmonic response in a stretched nanorod, *Phys. Rev. Lett.*, **115**(23), 236804, (2015)

[35] J. H. Mokkath, Nanoparticle heterodimers: The role of size and interparticle gap distance on the optical response, *Chem. Phys. Lett.*, **699**, 28–31, (2018)

[36] F. Alkan and C. M. Aikens, Understanding plasmon coupling in nanoparticle dimers using molecular orbitals and configuration interaction, *Phys. Chem. Chem. Phys.*, **21**(41), 23065–23075, (2019)

[37] T. P. Rossi, P. Erhart, and M. Kuisma, Hot-carrier generation in plasmonic nanoparticles: The importance of atomic structure, *ACS Nano*, **14**(8), 9963–9971, (2020)

[38] E. B. Guidez and C. M. Aikens, Quantum mechanical origin of the plasmon: from molecular systems to nanoparticles, *Nanoscale*, **6**(20), 11512–11527, (2014)

[39] K. Selby, V. Kresin, J. Masui, M. Vollmer, W. A. de Heer, A. Scheidemann, and W. Knight, Photoabsorption spectra of sodium clusters, *Phys. Rev. B*, **43**(6), 4565, (1991)

[40] S. Malola, L. Lehtovaara, J. Enkovaara, and H. Häkkinen, Birth of the localized surface plasmon resonance in monolayer-protected gold nanoclusters, *ACS Nano*, **7**(11), 10263–10270, (2013)

[41] Y. Negishi, T. Nakazaki, S. Malola, S. Takano, Y. Niihori, W. Kurashige, S. Yamazoe, T. Tsukuda, and H. Häkkinen, A critical size for emergence of nonbulk electronic and geometric structures in dodecanethiolate-protected Au clusters, *J. Am. Chem. Soc.*, **137**(3), 1206–1212, (2015)

[42] P. Nordlander, C. Oubre, E. Prodan, K. Li, and M. Stockman, Plasmon hybridization in nanoparticle dimers, *Nano Lett.*, **4**(5), 899–903, (2004)

[43] R. Zhang, L. Bursi, J. D. Cox, Y. Cui, C. M. Krauter, A. Alabastri, A. Manjavacas, A. Calzolari, S. Corni, E. Molinari, E. A. Carter, F. J. García De Abajo, H. Zhang, and P. Nordlander, How to identify plasmons from the optical response of nanostructures, *ACS Nano*, **11**(7), 7321–7335, (2017)

[44] S. Bernadotte, F. Evers, and C. R. Jacob, Plasmons in molecules, *J. Phys. Chem. C*, **117**(4), 1863–1878, (2013)

[45] G. Piccini, R. W. Havenith, R. Broer, and M. Stener, Gold nanowires: a time-dependent density functional assessment of plasmonic behavior, *J. Phys. Chem. C*, **117**(33), 17196–17204, (2013)

[46] L. Bursi, A. Calzolari, S. Corni, and E. Molinari, Quantifying the plasmonic character of optical excitations in nanostructures, *ACS Photonics*, **3**(4), 520–525, (2016)

[47] D. Casanova, J. M. Matxain, and J. M. Ugalde, Plasmonic resonances in the Al_{13}^- cluster: Quantification and origin of exciton collectivity, *J. Phys. Chem. C*, **120**(23), 12742–12750, (2016)

[48] R. L. Gieseking, A. P. Ashwell, M. A. Ratner, and G. C. Schatz, Analytical approaches to identify plasmon-like excited states in bare and ligand-protected metal nanoclusters, *J. Phys. Chem. C*, **124**, 3260–3269, (2020)

[49] J. J. Mortensen, L. B. Hansen, and K. W. Jacobsen, Real-space grid implementation of the projector augmented wave method, *Phys. Rev. B*, **71**, 035109, (2005)

[50] J. Enkovaara, C. Rostgaard, J. J. Mortensen, J. Chen, M. Dułak, L. Ferrighi, J. Gavnholt, C. Glinsvad, V. Haikola, H. A. Hansen, H. H. Kristoffersen, M. Kuisma, A. H. Larsen, L. Lehtovaara, M. Ljungberg, O. Lopez-Acevedo, P. G. Moses, J. Ojanen, T. Olsen, V. Petzold, N. A. Romero, J. Stausholm-Møller, M. Strange, G. A. Tritsaris, M. Vanin, M. Walter, B. Hammer, H. Häkkinen, G. K. H. Madsen, R. M. Nieminen, J. K. Nørskov, M. Puska, T. T. Rantala, J. Schiøtz, K. S. Thygesen, and K. W. Jacobsen, Electronic structure calculations with GPAW: a real-space implementation of the projector augmented-wave method, *J. Phys. Condens. Matter*, **22**(25), 253202, (2010)

[51] T. P. Rossi, M. Kuisma, M. J. Puska, R. M. Nieminen, and P. Erhart, Kohn–Sham decomposition in real-time time-dependent density-functional theory: an efficient tool for analyzing plasmonic excitations, *J. Chem. Theory Comput.*, **13**(10), 4779–4790, (2017)

[52] P. Hohenberg and W. Kohn, Inhomogeneous electron gas, *Phys. Rev.*, **136**(3B), B864, (1964)

[53] W. Kohn and L. J. Sham, Self-consistent equations including exchange and correlation effects, *Phys. Rev.*, **140**(4A), A1133, (1965)

[54] P. A. Dirac, Note on exchange phenomena in the Thomas atom, *Math. Proc. Camb. Philos. Soc.*, **26**(3), 376–385, (1930)

[55] J. P. Perdew and Y. Wang, Accurate and simple analytic representation of the electron-gas correlation energy, *Phys. Rev. B*, **45**, 13244–13249, (1992)

[56] D. C. Marinica, A. K. Kazansky, P. Nordlander, J. Aizpurua, and A. G. Borisov, Quantum plasmonics: Nonlinear effects in the field enhancement of a plasmonic nanoparticle dimer, *Nano Lett.*, **12**(3), 1333–1339, (2012)

[57] G. Aguirregabiria, D. C. Marinica, R. Esteban, A. K. Kazansky, J. Aizpurua, and A. G. Borisov, Role of electron tunneling in the nonlinear response of plasmonic nanogaps, *Phys. Rev. B*, **97**(11), (2018)

[58] E. Runge and E. K. Gross, Density-functional theory for time-dependent systems, *Phys. Rev. Lett.*, **52**(12), 997, (1984)

[59] M. E. Casida, Time-Dependent Density Functional Response Theory for Molecules, in *Recent Advances in Computational Chemistry*, pp. 155–192, World Scientific, (1995)

[60] M. E. Casida, Time-dependent density functional response theory of molecular systems: theory, computational methods, and functionals, in *Theoretical and Computational Chemistry*, vol. 4, pp. 391–439, Elsevier, (1996)

[61] M. Walter, H. Häkkinen, L. Lehtovaara, M. Puska, J. Enkovaara, C. Rostgaard, and J. J. Mortensen, Time-dependent density-functional theory in the projector augmented-wave method, *J. Chem. Phys.*, **128**(24), 244101, (2008)

[62] N. D. Lang and W. Kohn, Theory of metal surfaces: Charge density and surface energy, *Phys. Rev. B*, **1**(12), 4555–4568, (1970)

[63] D. Lang and W. Kohn, Theory of metal surfaces: Work function, *Phys. Rev. B*, **3**(4), 1215–1223, (1971)

[64] W. Ekardt, Size-dependent photoabsorption and photoemission of small metal particles, *Phys. Rev. B*, **31**(10), 6360, (1985)

[65] W. Ekardt, Collective multipole excitations in small metal particles: Critical angular momentum l^{cr} for the existence of collective surface modes, *Phys. Rev. B*, **32**(4), 1961, (1985)

[66] D. Beck, Self-consistent calculation of the polarizability of small jellium spheres, *Phys. Rev. B*, **30**(12), 6935, (1984)

[67] V. V. Kresin, Collective resonances in silver clusters: Role of d electrons and the polarization-free surface layer, *Phys. Rev. B*, **51**(3), 1844, (1995)

[68] W. Ekardt and Z. Penzar, Self-consistent Sommerfeld droplet as a simple model for an accurate prediction of the electronic properties of small metal particles, *Phys. Rev. B*, **38**(6), 4273, (1988)

[69] G. Lauritsch, P.-G. Reinhard, J. Meyer, and M. Brack, Triaxially deformed sodium clusters in a self-consistent microscopic description, *Phys. Lett. A*, **160**(2), 179–183, (1991)

[70] A. Rubio, L. Balbas, and J. Alonso, Response properties of sodium clusters within a jellium-like model with finite surface thickness, *Z. Phys. D*, **19**(4), 93–96, (1991)

[71] M. Koskinen, P. Lipas, and M. Manninen, Electron-gas clusters: the ultimate jellium model, *Z. Phys. D*, **35**(4), 285–297, (1995)

[72] D. Beck, Self-consistent calculation of the eigenfrequencies for the electronic excitations in small jellium spheres, *Phys. Rev. B*, **35**(14), 7325, (1987)

[73] C. Yannouleas and R. Broglia, Collective and single-particle aspects in the optical response of metal microclusters, *Phys. Rev. A*, **44**(9), 5793, (1991)

[74] J. Pacheco and W. Ekardt, Response of finite many-electron systems beyond the time-dependent local density approximation: Application to small metal clusters, *Ann. Phys.*, **504**(4), 254–269, (1992)

[75] E. Townsend and G. W. Bryant, Plasmonic properties of metallic nanoparticles: The effects of size quantization, *Nano Lett.*, **12**(1), 429–434, (2012)

[76] E. Townsend and G. W. Bryant, Which resonances in small metallic nanoparticles are plasmonic?, *J. Opt.*, **16**(11), 114022, (2014)

[77] J. G. Liu, H. Zhang, S. Link, and P. Nordlander, Relaxation of plasmon-induced hot carriers, *ACS Photonics*, **5**(7), 2584–2595, (2018)

[78] A. Campos, N. Troc, E. Cottancin, M. Pellarin, H. C. Weissker, J. Lermé, M. Kociak, and M. Hillenkamp, Plasmonic quantum size effects in silver nanoparticles are dominated by interfaces and local environments, *Nat. Phys.*, **15**(3), 275–280, (2019)

[79] P. Zhang, J. Feist, A. Rubio, P. García-González, and F. J. García-Vidal, Ab initio nanoplasmonics: The impact of atomic structure, *Phys. Rev. B*, **90**(16), (2014)

[80] M. Barbry, P. Koval, F. Marchesin, R. Esteban, A. G. Borisov, J. Aizpurua, and D. Sánchez-Portal, Atomistic near-field nanoplasmonics: Reaching atomic-scale resolution in nanooptics, *Nano Lett.*, **15**(5), 3410–3419, (2015)

[81] A. Varas, P. García-González, J. Feist, F. J. García-Vidal, and A. Rubio, Quantum plasmonics: from jellium models to ab initio calculations, *Nanophotonics*, **5**(3), 409–426, (2016)

[82] E. Briggs, D. Sullivan, and J. Bernholc, Real-space multigrid-based approach to large-scale electronic structure calculations, *Phys. Rev. B*, **54**(20), 14362, (1996)

[83] P. E. Blöchl, Projector augmented-wave method, *Phys. Rev. B*, **50**(24), 17953–17979, (1994)

[84] M. J. Puska, R. M. Nieminen, and M. Manninen, Electronic polarizability of small metal spheres, *Phys. Rev. B*, **31**(6), 3486, (1985)

[85] X. Andrade, S. Botti, M. A. Marques, and A. Rubio, Time-dependent density functional theory scheme for efficient calculations of dynamic (hyper)polarizabilities, *J. Chem. Phys.*, **126**(18), 184106, (2007)

[86] K. M. Conley, N. Nayyar, T. P. Rossi, M. Kuisma, V. Turkowski, M. J. Puska, and T. S. Rahman, Plasmon excitations in mixed metallic nanoarrays, *ACS Nano*, **13**(5), 5344–5355, (2019)

[87] K. Conley, N. Nayyar, T. P. Rossi, M. Kuisma, V. Turkowski, M. J. Puska, and T. S. Rahman, Plasmon excitations in chemically heterogeneous nanoarrays, *Phys. Rev. B*, **101**(23), 235132, (2020)

[88] T. P. Rossi, T. Shegai, P. Erhart, and T. J. Antosiewicz, Strong plasmon-molecule coupling at the nanoscale revealed by first-principles modeling, *Nat. Commun.*, **10**(1), 1–7, (2019)

[89] C. E. Talley, J. B. Jackson, C. Oubre, N. K. Grady, C. W. Hollars, S. M. Lane, T. R. Huser, P. Nordlander, and N. J. Halas, Surface-enhanced Raman scattering from individual Au nanoparticles and nanoparticle dimer substrates, *Nano Lett.*, **5**(8), 1569–1574, (2005)

[90] L. Zhao, K. L. Kelly, and G. C. Schatz, The extinction spectra of silver nanoparticle arrays: influence of array structure on plasmon resonance wavelength and width, *J. Phys. Chem. B*, **107**(30), 7343–7350, (2003)

[91] J. Grand, M. L. de La Chapelle, J.-L. Bijeon, P.-M. Adam, A. Vial, and P. Royer, Role of localized surface plasmons in surface-enhanced Raman scattering of shape-controlled metallic particles in regular arrays, *Phys. Rev. B*, **72**(3), 033407, (2005)

[92] B. Yan, A. Thubagere, W. R. Premasiri, L. D. Ziegler, L. Dal Negro, and B. M. Reinhard, Engineered SERS substrates with multiscale signal enhancement: nanoparticle cluster arrays, *ACS Nano*, **3**(5), 1190–1202, (2009)

[93] M. Hentschel, M. Saliba, R. Vogelgesang, H. Giessen, A. P. Alivisatos, and N. Liu, Transition from isolated to collective modes in plasmonic oligomers, *Nano Lett.*, **10**(7), 2721–2726, (2010)

[94] N. J. Halas, S. Lal, W.-S. Chang, S. Link, and P. Nordlander, Plasmons in strongly coupled metallic nanostructures, *Chem. Rev.*, **111**(6), 3913–3961, (2011)

[95] T. Chen, M. Pourmand, A. Feizpour, B. Cushman, and B. M. Reinhard, Tailoring plasmon coupling in self-assembled one-dimensional Au nanoparticle chains through simultaneous control of size and gap separation, *J. Phys. Chem. Lett.*, **4**(13), 2147–2152, (2013)

[96] L. S. Slaughter, B. A. Willingham, W.-S. Chang, M. H. Chester, N. Ogden, and S. Link, Toward plasmonic polymers, *Nano Lett.*, **12**(8), 3967–3972, (2012)

[97] N. Pazos-Perez, C. S. Wagner, J. M. Romo-Herrera, L. M. Liz-Marzán, F. J. García de Abajo, A. Wittemann, A. Fery, and R. A. Alvarez-Puebla, Organized plasmonic clusters with high coordination number and extraordinary enhancement in surface-enhanced Raman scattering (SERS), *Angew. Chem. Int. Ed.*, **124**(51), 12860–12865, (2012)

[98] N. Lebedev, I. Griva, W. J. Dressick, J. Phelps, J. E. Johnson, Y. Meshcheriakova, G. P. Lomonossoff, and C. M. Soto, A virus-based nanoplasmonic structure as a surface-enhanced Raman biosensor, *Biosens. Bioelectron.*, **77**, 306–314, (2016)

[99] X. Huang, Y. Liu, J. Barr, J. Song, Z. He, Y. Wang, Z. Nie, Y. Xiong, and X. Chen, Controllable self-assembled plasmonic vesicle-based three-dimensional SERS platform for picomolar detection of hydrophobic contaminants, *Nanoscale*, **10**(27), 13202–13211, (2018)

[100] H. A. Nguyen, I. Jupin, P. Decorse, S. Lau-Truong, S. Ammar, and N. T. Ha-Duong, Assembly of gold nanoparticles using turnip yellow mosaic virus as an in-solution SERS sensor, *RSC Adv.*, **9**(55), 32296–32307, (2019)

[101] A. G. Skirtach, C. Dejugnat, D. Braun, A. S. Susha, A. L. Rogach, W. J. Parak, H. Möhwald, and G. B. Sukhorukov, The role of metal nanoparticles in remote release of encapsulated materials, *Nano Lett.*, **5**(7), 1371–1377, (2005)

[102] T. S. Troutman, S. J. Leung, and M. Romanowski, Light-induced content release from plasmon-resonant liposomes, *Adv. Mater.*, **21**(22), 2334–2338, (2009)

[103] T. L. Doane and C. Burda, The unique role of nanoparticles in nanomedicine: imaging, drug delivery and therapy, *Chem. Soc. Rev.*, **41**(7), 2885–2911, (2012)

[104] V. Marjomäki, T. Lahtinen, M. Martikainen, J. Koivisto, S. Malola, K. Salorinne, M. Pettersson, and H. Häkkinen, Site-specific targeting of enterovirus capsid by functionalized monodisperse gold nanoclusters, *Proc. Natl. Acad. Sci. U.S.A.*, **111**(4), 1277–1281, (2014)

[105] S. J. Barrow, X. Wei, J. S. Baldauf, A. M. Funston, and P. Mulvaney, The surface plasmon modes of self-assembled gold nanocrystals, *Nat. Commun.*, **3**(1), 1–9, (2012)

[106] A. S. Urban, X. Shen, Y. Wang, N. Large, H. Wang, M. W. Knight, P. Nordlander, H. Chen, and N. J. Halas, Three-dimensional plasmonic nanoclusters, *Nano Lett.*, **13**(9), 4399–4403, (2013)

[107] K. J. Park, J.-H. Huh, D.-W. Jung, J.-S. Park, G. H. Choi, G. Lee, P. J. Yoo, H.-G. Park, G.-R. Yi, and S. Lee, Assembly of "3D" plasmonic clusters by "2D" AFM nanomanipulation of highly uniform and smooth gold nanospheres, *Sci. Rep.*, **7**(1), 1–10, (2017)

[108] L. Lermusiaux and A. M. Funston, Plasmonic isomers *via* DNA-based self-assembly of gold nanoparticles, *Nanoscale*, **10**(41), 19557–19567, (2018)

[109] J. Fontana, W. J. Dressick, J. Phelps, J. E. Johnson, R. W. Rendell, T. Sampson, B. R. Ratna, and C. M. Soto, Virus-templated plasmonic nanoclusters with icosahedral symmetry via directed self-assembly, *Small*, **10**(15), 3058–3063, (2014)

[110] H. Wang, C. S. Levin, and N. J. Halas, Nanosphere arrays with controlled sub-10-nm gaps as surface-enhanced Raman spectroscopy substrates, *J. Am. Chem. Soc.*, **127**(43), 14992–14993, (2005)

[111] F. Le, D. W. Brandl, Y. A. Urzhumov, H. Wang, J. Kundu, N. J. Halas, J. Aizpurua, and P. Nordlander, Metallic nanoparticle arrays: a common substrate for both surface-enhanced Raman scattering and surface-enhanced infrared absorption, *ACS Nano*, **2**(4), 707–718, (2008)

[112] A. Liebsch, Surface-plasmon dispersion and size dependence of Mie resonance: silver versus simple metals, *Phys. Rev. B*, **48**(15), 11317, (1993)

[113] L. Serra and A. Rubio, Optical response of Ag clusters, *Z. Phys. D*, **40**(1), 262–264, (1997)

[114] P. Song, P. Nordlander, and S. Gao, Quantum mechanical study of the coupling of plasmon excitations to atomic-scale electron transport, *J. Chem. Phys.*, **134**(7), 074701, (2011)

[115] P. Song, S. Meng, P. Nordlander, and S. Gao, Quantum plasmonics: Symmetry-dependent plasmon-molecule coupling and quantized photoconductances, *Phys. Rev. B*, **86**(12), 121410, (2012)

ORIGINAL PAPERS

PI

ANALYSIS OF LOCALIZED SURFACE PLASMON RESONANCE IN SPHERICAL JELLIUM CLUSTERS AND THEIR ASSEMBLIES

by

Elli Selenius, Sami Malola, Hannu Häkkinen (2017)

The Journal of Physical Chemistry C, **121** (48), 27036–27052

THE JOURNAL OF PHYSICAL CHEMISTRY C

Article

pubs.acs.org/JPCC

Analysis of Localized Surface Plasmon Resonances in Spherical Jellium Clusters and Their Assemblies

Elli Selenius,[†] Sami Malola,[†] and Hannu Häkkinen*[,†,‡]

[†]Department of Physics, Nanoscience Center, and [‡]Department of Chemistry, Nanoscience Center, University of Jyväskylä, FI-40014 Jyväskylä, Finland

ABSTRACT: Because of multiple possible applications of physicochemical properties of plasmonic metal nanoparticles and particle systems, there is high interest to understand the mechanisms that underlie the birth of localized surface plasmon resonance (LSPR). Here we studied the birth of the LSPR in spherical jellium clusters with the density of sodium and with 8, 20, 34, 40, 58, 92, 138, and 186 electrons by using the linear response time-dependent density functional theory (lr-TDDFT). The coupling of the individual plasmon resonances in dimer, trimer, tetramer, and hexamer cluster assemblies consisting of the eight-electron cluster was also studied. The Kohn−Sham electron−hole transitions contributing to the absorption peaks were analyzed using time-dependent density functional perturbation theory (TD-DFPT) and visualized using the transition contribution map (TCM) analysis. The plasmonicity of an absorption peak was analyzed by examining the number of the electron−hole (e−h) transitions contributing to it, the relative strengths of these contributions, and the radial distribution of the induced density. The main absorption peak in all the studied clusters was found to be a LSPR peak, caused by a collective excitation and with most of the induced density concentrated near the surface of the sphere. Fragmentation of the LSPR peak due to close-lying single e−h transition was observed and discussed for 20- and 40-electron clusters. The level of theory and computational and analysis methods applied in this study facilitate detailed analysis of plasmonic properties, both in energy and in real space. These methods enable the study of still significantly larger clusters and cluster assemblies, opening doors to decipher the basic quantum physics behind the collective phenomena arising in plasmonically coupled metal nanoparticle systems.

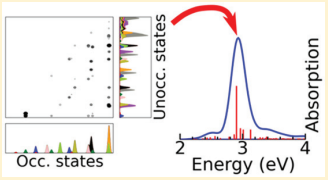

1. INTRODUCTION

The localized surface plasmon resonance of metal clusters has applications in many fields, such as photovoltaics,[1] chemical and biological sensing,[2] and cancer cell imaging and photothermal cancer therapy.[3] Since the optical properties of metal clusters depend on their size, shape, and dielectric environment,[4] the plasmon resonance can be tuned to the energies needed in each application. Clusters and cluster systems used in different applications include nanorods in cancer therapy,[3] nanoshells in surface-enhanced spectroscopies,[5] and nanoparticle dimers as molecular rulers.[6] The starting point to the understanding of these more complex systems is the understanding of localized surface plasmon resonance in simpler systems, such as spherical jellium clusters and their assemblies.

In large metal particles, the plasmon resonance can be explained classically as oscillation of the electron cloud in the external electric field. In nanoparticles smaller than approximately 10 nm, however, a quantum mechanical model is needed to accurately model the plasmonic phenomena.[7,8] In small clusters of only a few electrons, the single-particle effects play a large role, and the indentification of localized surface plasmons is not as straightforward as for larger particles.[9,10] To address this, several methods have been developed to determine whether a certain feature in the absorption spectrum is caused by a collective transition and especially whether it is an LSPR peak.[11−23]

The radial distribution of the induced density has often been used in studying the LSP nature of a transition, as in the jellium studies of Ekardt[11] using RPA and Beck[12] using TDLDA. Li et al.[13] calculated a so-called volume density response proportion (VRP) to classify the absorption peaks of the atomistic sodium clusters depending on the distribution of the induced density. The VRP value is obtained by integrating the absolute value of the linear density response function over the inside of the cluster and dividing this by the same value integrated over the inside and outside of the cluster. It measures the percentage of the electronic response inside the cluster of the total response.

Casanova et al.[14] proposed the transition inverse participation ratio (TIPR), calculated from the transition occupation numbers and measuring the collectivity of an electronic excitation, as a tool to find plasmonic excitations. Another way to separate collective excitations from excitations caused by individual, noncoupled electron−hole (e−h) transitions is to study the effect of the electron−electron interaction. Puska et al.[15] calculated the dynamic polarizability for small Li jellium spheres using RPA with and without interaction between the electrons. Bernadotte et al.[16] developed a method for identifying collective excitations with a dimensionless scaling parameter λ ranging from 0 to 1. The scaling parameter depicts the strength of the electron−electron interactions. When the excitations energies are calculated with increasing λ, the energies of the single-particle excitations do not change significantly, whereas the energies of the collective excitations depend strongly on λ. Piccini et al.[17]

Received: October 13, 2017
Published: November 10, 2017

DOI: 10.1021/acs.jpcc.7b10154
J. Phys. Chem. C 2017, 121, 27036−27052

simplified this approach by calculating only the TDDFT spectrum and so-called KS spectrum, where the excitation energies are calculated from the energy differences between KS states and the oscillation strengths from dipole transition moments between the KS orbitals. The TDDFT calculation corresponds to $\lambda = 1$ and the KS spectrum calculation to $\lambda = 0$.

TDDFT studies have shown that plasmonic excitations are caused by constructive interference between the dipole moments of single-particle excitations.[10] Gieseking et al.[18] utilized this and used the composition of the transition dipole moment to determine the plasmonicity of a transition.

Real-time TDDFT has also been used to study the plasmonic character of excitations. Townsend and Bryant have identified surface plasmons in spherical jellium clusters based on the distribution of the induced electron density oscillations[19] and the oscillation in the occupation of the energy levels near the Fermi level.[20] Ma et al.[21] used the time-dependent transition coefficients and their Fourier transforms to separate plasmonic and single-particle excitations.

Various plasmonicity indexes, attempting to summarize the plasmon nature of an excitation in one number, have been developed. Bursi et al. proposed the plasmonicity index (PI),[22] calculated as the integral of the squared modulus of the induced potential and normalized by the integral of the squared modulus of the transition density for the studied excitation. PI gives larger values to excitations with high induced potential. Recently, Zhang et al. proposed the generalized plasmonicity index (GPI),[23] based on the PI. GPI, unlike PI, is dimensionless and therefore enables direct comparison between nanoparticles of different sizes. GPI uses the Coulomb energy of the induced charges of the studied excitation, normalized by the Coulomb energy of the interaction of the induced charges with the external electromagnetic field. This index effectively measures the strength of the induced potential compared to the external potential, taking large values for excitations with large polarizations. Zhang et al. introduced also another quantity, Δ, which correlates with the shape of the peak in the GPI spectra at the studied energy and which is close to unity for plasmonic excitations.

In this work, we will qualitatively asses the electronic excitations and their LSPR character in small metal clusters based on the collectivity of the excitation and the distribution of the induced density. We will also look at the interactions of the individual plasmons in assemblies made of plasmonic clusters. The analyzed systems are small spherical clusters with 8, 20, 34, 40, 58, 92, 138, and 186 electrons and a dimer, a linear trimer, a square-shaped tetramer, and hexamer in the shape of a regular hexagon consisting of the eight-electron cluster. The self-consistent jellium model for metal clusters[24] was used for the clusters. The clusters have the density of sodium, thus corresponding to sodium clusters with 8−186 atoms. The studied cluster sizes are ones with a spherical shell closing and therefore a large HOMO−LUMO gap. Sodium was chosen because as a group I element it has strongly delocalized electrons in the s orbital and is therefore well suited for the jellium approximation. Sodium has also been widely studied both theoretically using the jellium model,[12,25−28] and experimentally,[29,30] so comparisons with other studies can be made.

The density functional theory (DFT) with the local density approximation (LDA) was used in the ground state calculations and linear response time-dependent DFT (lr-TDDFT) in the calculation of optical spectra. The Kohn−Sham (KS) e−h transitions contributing to the peaks in the spectra were analyzed using time-dependent density functional perturbation theory (TD-DFPT) and visualized using the transition contribution map (TCM) scheme, which has been previously used to study the birth of the localized surface plasmon resonance in ligand-protected gold clusters.[31] The collectivity or "plasmonicity" of the peaks was studied by examining the number of contributing e−h transitions and the relative strengths of these contributions, and the surface nature of the oscillation was analyzed using the distribution of the induced density. The contributions of the individual e−h transitions making up the plasmon peak have been studied previously for jellium clusters[20,27] and for atomistic clusters.[10,14,18] However, the TCM scheme, which allows us to visualize all the participating transitions and their strengths at once, is now used for these sodium clusters and cluster assemblies for the first time. This enables us to study the birth of the plasmon resonance in small metal clusters and the plasmonic coupling in cluster assemblies in a new way. Our scheme is computationally feasible for application to significantly larger clusters and cluster systems as well.

2. THEORY AND METHODS

The uniform jellium model was used in the calculations. In this model, only the valence electrons of the atoms are treated explicitly, and the ion cores are represented by a uniform background charge. The jellium model, while computationally simple, is capable of reproducing the trends in many electron-based phenomena, such as static polarizabilities and optical absorption spectra.[9] Even though nowadays ever larger systems can be computed using atomistic models, the jellium model is still used in the study of plasmonics, for example, in examining the plasmon resonances in nanoparticle dimers[32] or nanoshells.[33] The jellium background of all the clusters was made spherical, since all the clusters studied were so-called magic clusters with closed electronic shells. Here the jellium density of the clusters, n, was calculated from the bulk Wigner−Seitz radius for sodium, $r_{WS} = 2.08$ Å:

$$n = (4/3\pi {r_{WS}}^3)^{-1} \approx 0.0265 \text{ Å}^{-3} \quad (1)$$

The electron density can and will spill out of the sphere of background density, as can be seen in Figure 1, where the radial

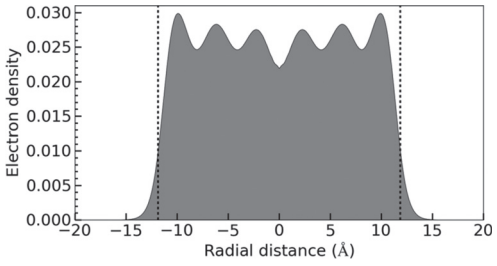

Figure 1. Electron density for the cluster with 186 electrons plotted radially as a function of the distance from the center of the sphere. The dashed lines show the edges of the uniform positive background density.

distribution of the electron density for the 186-electron cluster is shown. The electron density is also not uniform inside the cluster, where the electron shell structure can be seen. The spill-out of electrons is relatively larger for smaller clusters.

The calculations were performed with GPAW,[34,35] a real-space grid-based program which uses the projector augmented wave (PAW)[36] method. GPAW is a program package for ASE

DOI: 10.1021/acs.jpcc.7b10154
J. Phys. Chem. C 2017, 121, 27036−27052

(Atomic Simulation Environment).[37] DFT with LDA was used for the ground-state calculations, with the correlation energy in LDA after Perdew and Wang.[38] In the calculations, the clusters were in vacuum in 0 K. The calculation box was chosen for each cluster size so that approximately 8 Å of vacuum was left between the jellium edge of the cluster and the side of the calculation box. The grid spacing was 0.3 Å for the Na_8 cluster, which has a radius of 4.16 Å, and 0.4 Å for the cluster assemblies and the other clusters, which have radii ranging from 5.65 Å (Na_{20}) to 11.9 Å (Na_{186}). This grid spacing is sufficiently small for these jellium clusters because there are no explicit ion cores, but a smooth background potential. The convergence criteria for the energies was a change of less than 0.5 meV per electron during the last three iterations.

In the calculations of the dipole spectra, lr-TDDFT implemented in GPAW[39] was used, where the excitation energies are solved from the Casida matrix equation in the Kohn−Sham (KS) basis. The energy cutoff was 7 eV for the clusters with 8, 20, 34, 40, 58, and 92 electrons, 6 eV for the cluster with 138 electrons and the assemblies, and 5.5 eV for the cluster with 186 electrons, meaning that all orbitals up to 7, 6, or 5.5 eV from HOMO were included in the lr-TDDFT calculation. All the occupied orbitals were included in the calculation for all the systems, and for the single clusters the number of orbitals in the calculations ranged from 232 for the 8-electron cluster to 952 for the 186-electron cluster. For all the clusters the HOMO level was at −2.7 to −3.3 eV, so all the bound states were included. The absorption spectra were obtained from the calculated dipole oscillator strengths by broadening with a Gaussian. The influence of the cutoff energy on the optical spectra was tested for several systems. The energies of the largest peaks in the broadened absorption spectra changed at most by 0.02 eV when going from 6 to 7 eV or from 5 to 6 eV. The biggest energy change (for the 138-electron cluster) was partly caused by changes in the oscillator strengths of the excitations contributing to these peaks; the energies of the largest excitations changed at most by 0.01 eV. Based on these tests, the cutoff energies used here should be adequately large for these systems to get the right peak energies up to a few hundredths of an electronvolt and allow the accurate study of the largest peaks, which have energies of 3 eV and below.

The contributions from single-particle KS transitions causing a certain peak were analyzed using the TCM method[31] based on TD-DFPT.[40] A cosinoidal laser field at the peak energy was used in solving the first-order KS response wave function from the TD-DFPT. From this wave function the absorption coefficients for the individual transitions can then be extracted. In the TCM scheme a contour plot of the squared absorption coefficients is made, where the x-axis depicts the energy of the occupied KS orbitals and the y-axis the energy of the unoccupied KS orbitals. Thus, the relative strengths of all the individual e−h transitions contributing to the collective transition can be seen at once. The TCM analysis was combined with the Y_{LM} analysis where the KS wave functions are projected onto spherical harmonics, so that the angular types of the initial and final KS orbitals can also be seen. In calculating the transition contributions for a certain energy, a Gaussian broadening of 0.05 eV was used, so that all e−h transitions in a small energy window were included.

3. RESULTS

3.1. Individual Clusters. The optical absorption spectra for the individual clusters can be seen in Figures 2 and 3. On the right are the dipole oscillation strengths, and on the left are the spectra obtained from these by broadening with a Gaussian with a width of 0.1 eV. The excitations that are analyzed further are labeled in the dipole oscillations figures. The energies of the labeled transitions, as well as the percentages of these transitions from the total dipole strength, are listed below the figures. On the broadened spectra, the energies of the largest peaks are indicated.

For each cluster there is a strong absorption peak distinctly larger than the others at approximately 2.5−3.0 eV in the broadened spectrum. These peaks can be identified as the LSPR peak based on the energy and size of the peaks, the collectivity of the excitation, and the radial distribution of the induced density, as shall be discussed in detail in this section. For some cluster sizes the LSPR peak is fragmented into two. The strongest excitations contributing to the LSPR peaks are labeled with numbers and the additional analyzed excitations with "*a*".

Looking at the distribution of the oscillation strength, we can see that the one or two strongest excitations contributing to the LSPR peaks take up a significant amount of the total dipole oscillator strength. The absolute strength of the plasmon peak grows as the cluster gets bigger, as there are more electrons available to participate in the collective excitation. However, when the peak is fragmented, the oscillation strength is divided between the resulting peaks, so the strength of the largest absorption peak does not grow uniformly with cluster size.

The optical spectra obtained here are generally similar to earlier results for spherical Na jellium clusters studied by Beck[12] using time-dependent LDA (TDLDA), Pacheco and Ekardt[25] using self-interaction corrected (SIC) TDLDA, Yannouleas and Broglia[26] and Yannouleas et al.[27] using the random phase approximation (RPA) with LDA, and Guet and Johnson[28] using RPA with the Hartree−Fock approximation. The two-peaked structure in the spectrum of Na_{20} was seen in all these studies. Na_{40} has two larger peaks in the TDLDA studies but a more complex structure with several strong peaks in the RPA studies. Especially the absorption spectra calculated using SIC-TDLDA of Pacheco and Ekardt[25] for Na_8, Na_{20}, and Na_{40} are very similar to the spectra obtained here using lr-TDDFT. However, the SIC results are red-shifted about 0.2 eV compared to the energies calculated here and the TDLDA results without SIC calculated in the same reference.

Beck[12] calculated the plasmon energies for all the cluster sizes studied here. These energies were 2.75 eV for Na_8, 2.69 and 2.99 eV for Na_{20}, 2.88 eV for Na_{34}, 2.61 and 2.72 eV for Na_{40}, 2.86 eV for Na_{58}, 3.18 eV for Na_{92}, 3.05 and 3.10 eV for Na_{138}, and 2.94 and 3.07 eV for Na_{186}. The energies are quite close, albeit a little higher, to the energies of the main peaks found here for cluster sizes 8−58 and 186 and clearly higher for sizes 92 and 138. The splitting in the energies for the clusters Na_{20} and Na_{40} are larger in our calculations. The trends in the evolution of the energy and in the number of plasmonic peaks are nevertheless similar.

The trend in the LSPR energy is illustrated in Figure 4, where the energy of the LSPR peak obtained from the broadened spectra is plotted as a function of $N_e^{-1/3}$ (N_e being the number of electrons). For the 20- and 40-electron clusters, an average of the energies of the two peaks was used. The blue line is a linear fit of the data, with $R^2 = 0.74$. Because the radius of the clusters is linearly proportional to $N_e^{1/3}$, Figure 4 shows the relation of the LSPR energy to the inverse of the radius. The classical Mie LSPR energy for a bulk sodium sphere is

$$E_{SP} = \sqrt{\frac{\hbar^2 n e^2}{3\varepsilon_0 m_e}} \tag{2}$$

where n is the electron density of sodium, e is the elementary charge, ε_0 is the permittivity of free space, and m_e is the mass of an

DOI: 10.1021/acs.jpcc.7b10154
J. Phys. Chem. C 2017, 121, 27036−27052

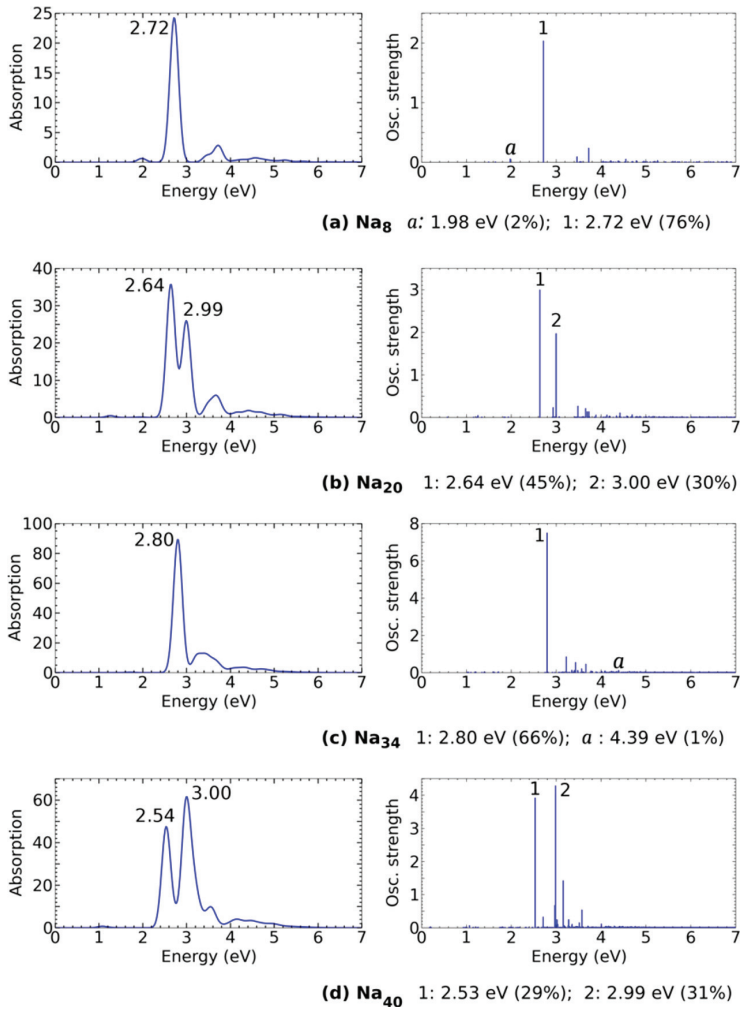

Figure 2. Optical absorption spectra for the spherical jellium clusters with the density of sodium and with 8, 20, 34, and 40 electrons. The dipole oscillator strengths obtained with lr-TDDFT are on the right. The figures on the left have been broadened with a Gaussian with a width of 0.1 eV. Note that the *y*-axis scales are different in the different figures. The energies of the largest peaks (in eV) are indicated next to the peak in the broadened spectra. The excitations that are further analyzed are labeled in the line spectra. The largest excitations contributing to the SPR peak are labeled with numbers. Additional analyzed peaks are labeled with "*a*". The energy of each labeled peak, as well as the oscillation strength of the peak as a percentage of the total oscillation strength in the spectrum, is shown below the line spectra.

electron. Using the density from eq 1, the surface plasmon resonance energy for bulk sodium in the shape of a sphere would then be E_{LSP} = 3.49 eV. We can see that the energy of the LSPR peak gets bigger with increasing cluster size, but the energies for the largest clusters calculated here are still about 0.5 eV from the Mie energy. The bulk limit from the linear fit is 3.04 eV.

The reason for this red-shift of the LSPR energy with decreasing cluster size is the spill-out of electrons, i.e., the spreading of electron density outside the sphere of positive background charge.[9] Since in small clusters the spill-out is relatively larger than in bigger clusters, the electron density is smaller in clusters with fewer electrons. Because the Mie plasmon energy of eq 2 depends on the square root of the electron density, smaller density causes the peak to shift to a lower energy. This red-shift can be seen in atomistic calculations[13] and experiments,[29,41] so it is also a property of the sodium clusters and not just the jellium model.

The transition contribution maps for the labeled excitations of Figures 2 and 3 can be seen in Figures 5−7. The relative strengths of the e−h transitions contributing to the excitation are shown as a contour map. The energies and angular momentum types of the initial (occupied) and final (unoccupied) KS orbitals are shown at the bottom and on the right, respectively. The naming of the orbitals follows the superatomic convention used for spherical clusters (S, P, D, F, ...).[42,43] The broadening of 0.05 eV in the analysis means that for most peaks also some smaller transitions close in energy to the analyzed transition are contributing to the TCM figures. The corresponding radial distributions of the induced densities can be seen in Figures 8−10. Note that the density shown is the sum of all the induced density at each distance.

All the numbered LSPR excitations can be seen to be collective, with many contributing KS e−h transitions. Also, transitions of very different energies contribute to the same absorption peak. For example, in the case of the LSPR peak of the 58-electron cluster, seen in Figure 6c, there is one band of transitions close to the energy of the peak, and another band of transitions at much

DOI: 10.1021/acs.jpcc.7b10154
J. Phys. Chem. C 2017, 121, 27036−27052

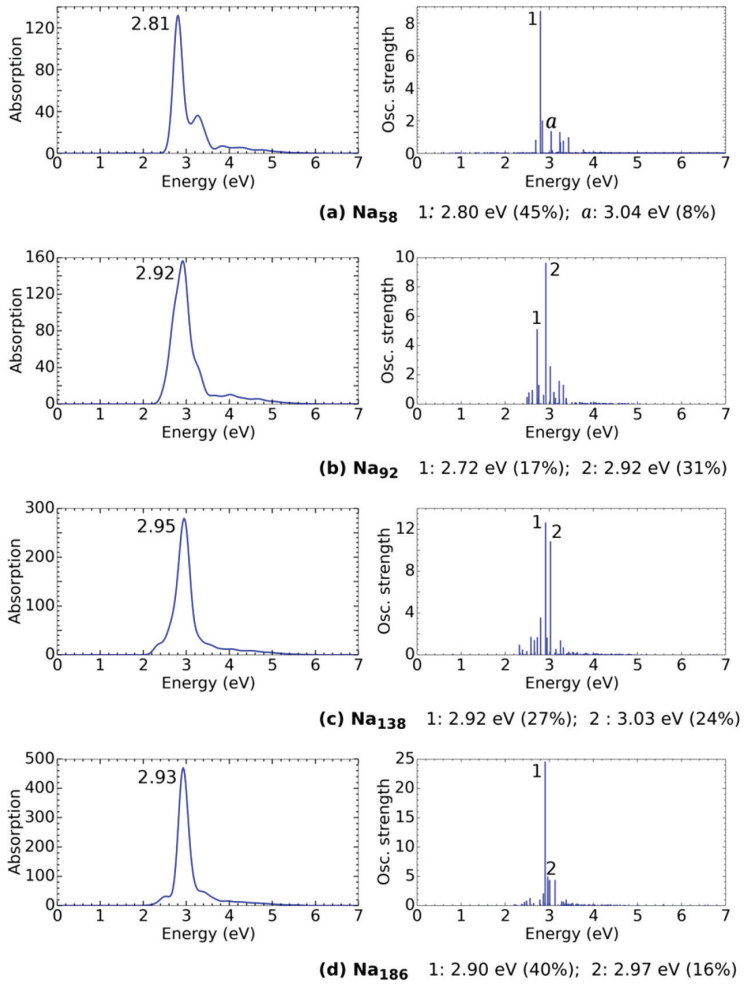

Figure 3. Optical absorption spectra for the spherical jellium clusters with the density of sodium and with 58, 92, 138, and 186 electrons. See caption of Figure 2 for details.

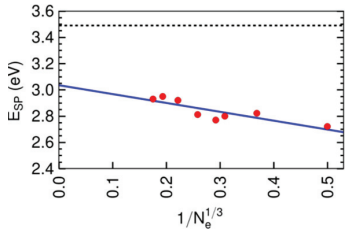

Figure 4. Energy of the SPR peak from the broadened spectrum as a function of $N_e^{-1/3}$ (red dots). Here N_e is the number of electrons in the cluster. For clusters Na_{20} and Na_{40}, an average of the energies of the two largest peaks is used. The blue line is a linear fit of the peak energies. The dashed horizontal line indicates the energy of the bulk surface plasmon peak for a spherical cluster.

lower energy, clearly showing coupling of the individual e−h transitions. For all the LSPR peaks, the transition is not dominated by only one strong contribution, but many e−h transitions contribute with significant strength. As the cluster size grows and more electrons are available to participate in the excitation, the strongest dipole excitations get more collective. All the significant e−h transitions are dipole-allowed; i.e., the angular momentum quantum number l of the orbitals changes by ±1.

Most of the induced density for the numbered LSPR peaks is concentrated on or near the surface of the jellium spheres. However, there are shells of induced density also inside the cluster, so all the charge density oscillation does not happen at the surface. In general, the number of these induced density shells grows as the cluster grows, reflecting the more complex electron shell structures of the larger clusters.

These LSPR peaks can be compared to the small peak of the eight-electron cluster at 1.98 eV, which is caused mainly by one e−h transition, as seen in Figure 5a. The LSPR peak at 2.72 eV for the same cluster has also one contribution that is somewhat stronger than the others, as the TCM displayed in Figure 5b shows. However, the 1P → 1D transition takes up only 55% of the total transition strength for the LSPR peak, as the 1P → 2S transition takes up 95% of the transition strength for the smaller peak. The induced density for the smaller peak, seen in Figure 8a, has a maximum on the surface, but there is also a similar shell of induced density inside the cluster. The electron density oscillations are therefore not concentrated on the surface as for the LSPR peak of the same cluster, seen in Figure 8b. Thus, the

DOI: 10.1021/acs.jpcc.7b10154
J. Phys. Chem. C 2017, 121, 27036−27052

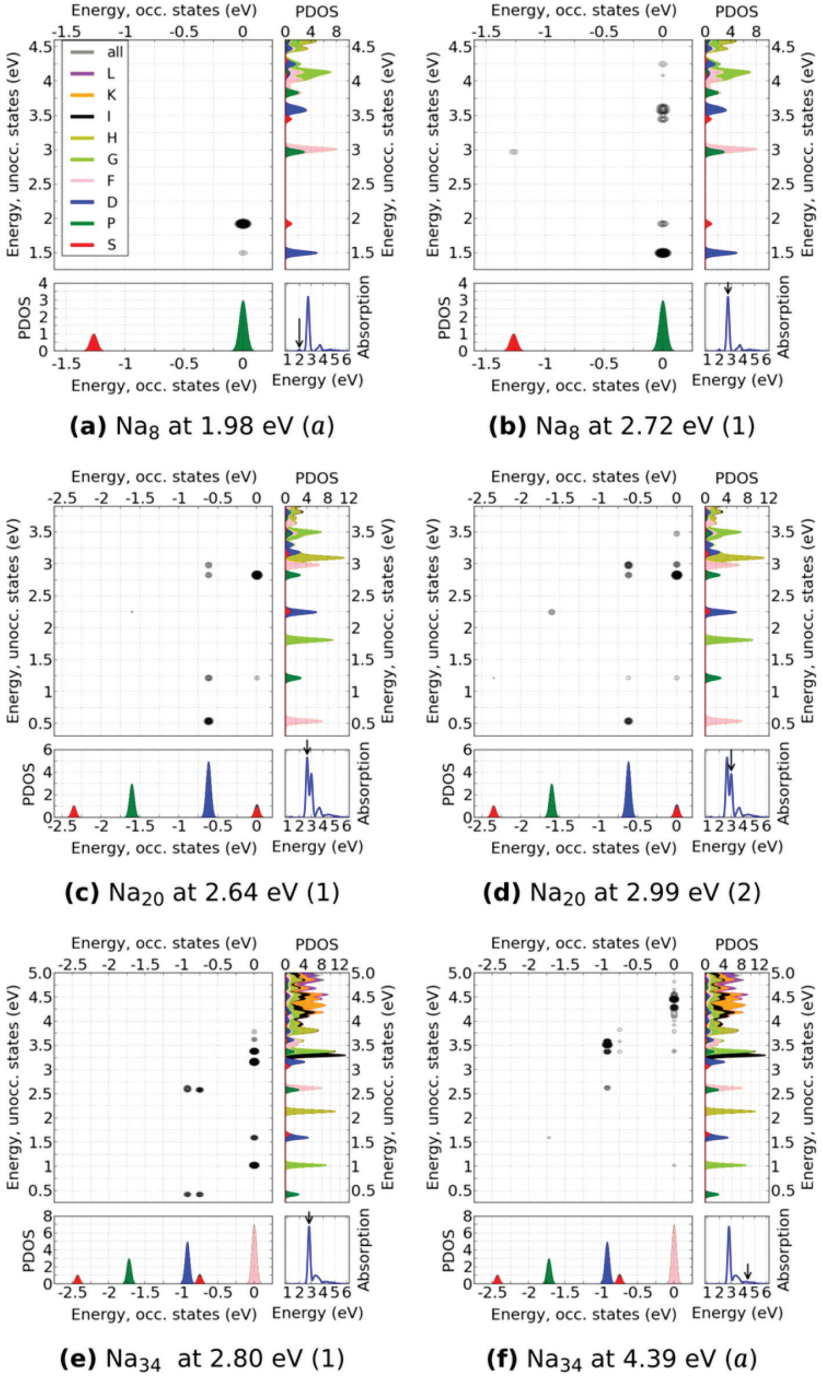

Figure 5. TCMs corresponding to the labeled excitations in the optical absorption spectra for the clusters with 8, 20, and 34 electrons. The numbers in parentheses in the captions refer to the labels given to the transitions in Figures 2 and 3. The projected density of states (PDOS) for the occupied KS orbitals is displayed in the bottom left subplot and for the unoccupied orbitals in the rightmost subplot in each figure. The HOMO level is set to zero in the PDOS plots. A Gaussian broadening of 0.03 eV has been used for the orbitals. The relative strengths of the e−h transitions from the occupied orbitals to the unoccupied orbitals are drawn as a contour plot; the stronger the contribution from a transition, the darker the dot. A two-dimensional Gaussian broadening of 0.025 eV has been used for the transitions. The absorption spectra can be seen in the bottom right subplot in each figure. The arrows show the energy of the analyzed peaks.

LSPR peak distinctly differs in character from this peak caused mainly by one e−h transition.

In the broadened spectra, the LSPR peak is fragmented for the clusters with 20 and 40 electrons. This fragmentation has been observed also in experiments for small sodium clusters.[29] The fragmentation was explained in a RPA-LDA jellium study of Yannouleas and Broglia[26] by strong coupling of the plasmonic transition to one or more single e−h transitions

DOI: 10.1021/acs.jpcc.7b10154
J. Phys. Chem. C 2017, 121, 27036−27052

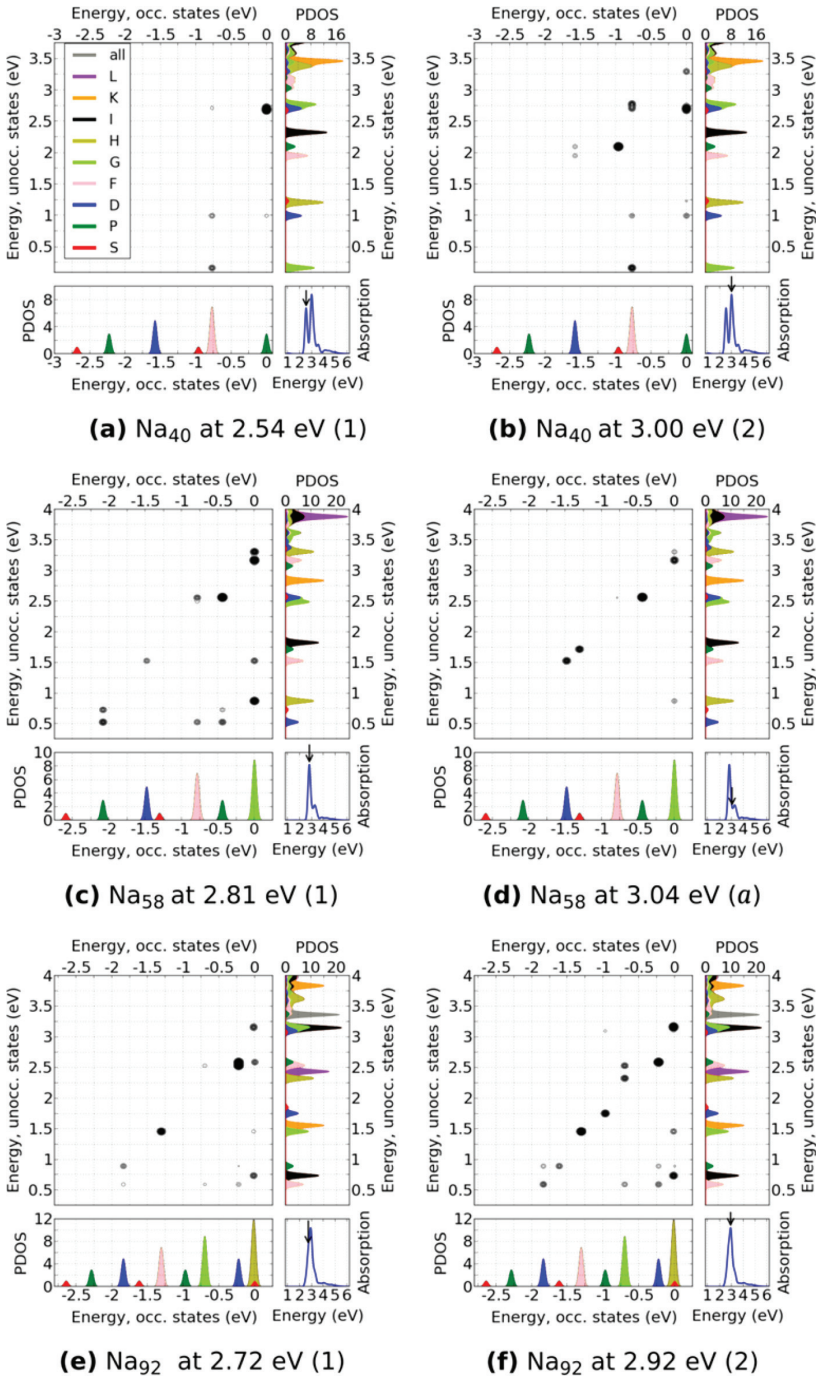

Figure 6. TCMs corresponding to the labeled excitations in the optical absorption spectra for the clusters with 40, 58, and 92 electrons. See the caption of Figure 5 for details.

close in energy. For the cluster with 20 electrons, this is the 2S → 3P transition, and for the cluster with 40 electrons, the transitions are 2P → 3D and 2P → 4S. In this study, the energies for these transitions are 2.83 eV for the 2S → 3P transition for Na_{20} and 2.68−2.72 eV for the transitions 2P → 3D and 2P → 4S for Na_{40}. These transitions thus lie between the two fragments of the LSPR peaks in energy for both clusters. They also contribute strongly to the two plasmon peaks, especially to the lower energy fragments.

The figures displaying the dipole oscillator strengths show that the LSPR peak is caused by several excitation also for the clusters with 58, 92, 138, and 186 electrons. Because there are now more e−h transitions close in energy to the plasmonic excitation, there are also more fragments. However, most of the fragments are

DOI: 10.1021/acs.jpcc.7b10154
J. Phys. Chem. C 2017, 121, 27036−27052

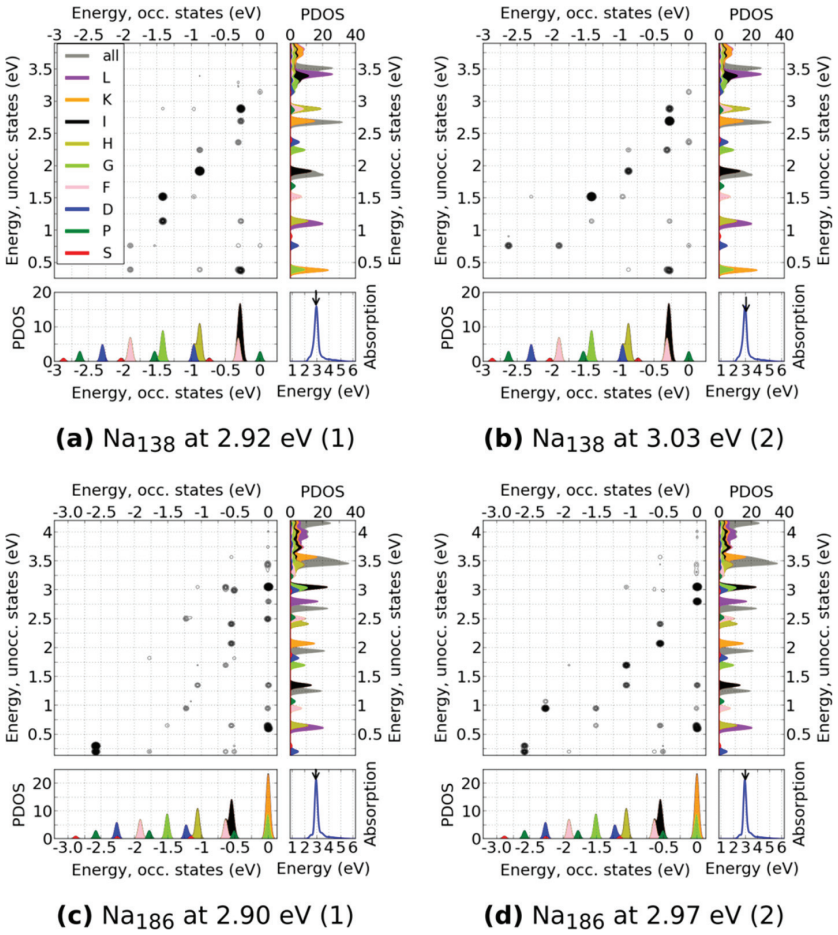

Figure 7. TCMs corresponding to the labeled excitations in the optical absorption spectra for the clusters with 138 and 186 electrons. See the caption of Figure 5 for details.

much smaller than the strongest excitation, and the fragments are closer to each other in energy than for Na_{20} and Na_{40}. This fragmentation is therefore seen in the broadened spectra only as a broadening of the peak. In a RPA-TDDFT jellium study of sodium clusters Yannoleas et al.[27] discovered this trend in the fragmentation as the cluster size grows. They explained it by weaker coupling between the plasmon and the e−h transitions in the larger clusters. In this study, the transitions close in energy to the plasmon peak and contributing strongly to it in the larger clusters are 2D → 3F (2.76 eV), 1F → 2G (2.77 eV) and 2D → 4P (2.82 eV) for Na_{92}; 1G → 3F (approximately 2.95 eV) and 1I → 2K (2.98 eV) for Na_{138}; and 1K → 3I (3.05−3.06 eV) for Na_{186}.

Comparing the TCM figures for the two largest fragments of the same peaks for clusters Na_{20}, Na_{40}, Na_{92}, Na_{138}, and Na_{186} (Figures 5c and 5d; 6a and 6b; 6e and 6f; 7a and 7b; and 7c and 7d), one of the fragments can always be seen to have less e−h transitions, with strong contributions from one or two transitions having an energy close to the peak energy. This less collective excitation is also weaker than the other fragment, except for the 20-electron cluster. The corresponding induced densities can be seen in Figures 8c and 8d; 9a and 9b; 9e and 9f; 10a and 10b; and 10c and 10d. The induced densities for the more collective peaks are concentrated more sharply on the surface of the cluster than the less collective peaks. Thus, one of the fragments is more LSPR like, and the other has more characteristics of an excitation caused by a single e−h transition, supporting the notion of coupling between the plasmon and single e−h transitions.

Some of the larger excitations after the main peak or peaks, forming a shoulder or a bump, were also analyzed for cluster sizes 34, 40, 58, and 92. The electronic contributions and induced density for one of these, for the 58-electron cluster at 3.04 eV, can be seen in Figures 6d and 9d. These excitations are collective with many of the contributing transitions same as in the main peaks, but generally with less individual e−h contributions. For these excitations, the radial distribution of induced density has a maximum near the surface, but the induced density is not as clearly concentrated on the surface as for the main peak. These features indicate that these excitations are smaller fractions of the localized surface plasmon.

The high-energy tails in the absorption spectra between approximately 4 and 5 eV have been interpreted as the highly fragmented and red-shifted compressional volume plasmon in previous jellium studies.[9,11] This feature has also been experimentally measured with the clusters Na_{20} and Na_{92}.[30] At the jellium density used here, the volume plasmon has a bulk energy of $E_V = \sqrt{3}E_{LSP} \approx 6.05$ eV. For the 34-electron cluster, one of the excitations in the area of the possible volume plasmon,

DOI: 10.1021/acs.jpcc.7b10154
J. Phys. Chem. C 2017, 121, 27036−27052

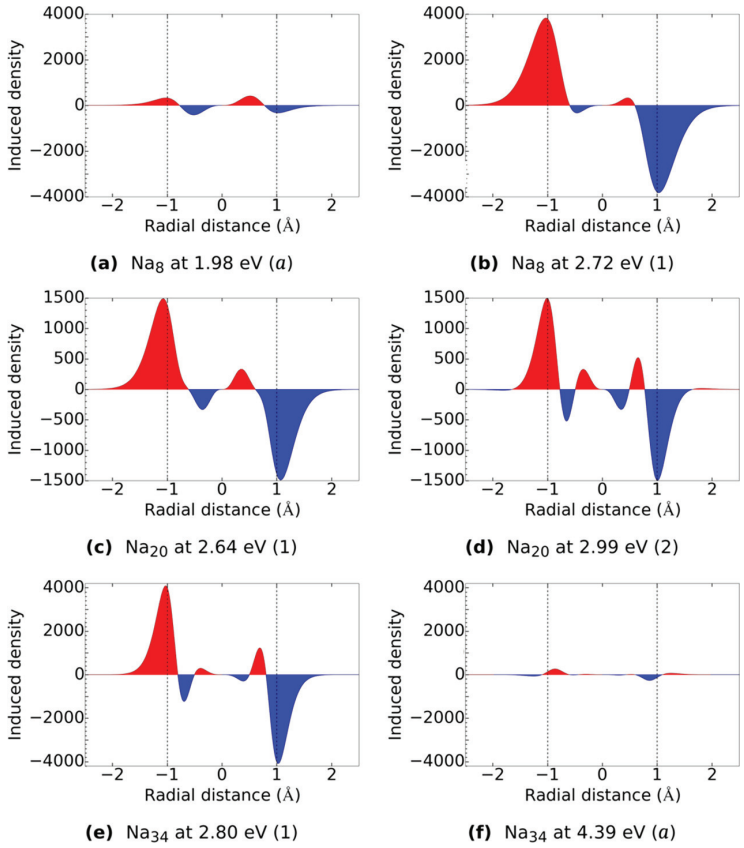

Figure 8. Radial induced densities corresponding to the TCM images in Figure 5 as a function of the distance from the center of the cluster. The radial distance has been normalized by the radius of the positive jellium sphere for each cluster. The dashed lines mark the jellium edges. The density shown is the sum of all induced density at this distance.

at 4.39 eV, was analyzed. This is also a collective excitation, as can be seen from Figure 5f. The initial KS orbitals are mostly the same as for the LSPR peak in Figure 5e, namely 1D, 2S, and 1F (HOMO), but the final orbitals are much higher in energy. As the HOMO energy of the 34-electron cluster is −3.0 eV, most of the transitions are to unbound electron states. The induced density for this high-energy excitation is displayed in Figure 8f. The density is not concentrated in the core: there are electron density oscillations just outside and inside the jellium surface. However, the induced density is not peaked on the surface either, and the radial-induced density profile differs clearly from the one for the LSPR peak, seen in Figure 8e.

As mentioned by Brack,[9] the variations of electron density in small jellium clusters caused by electronic shell structure blur the line between surface plasmons and other kinds of collective excitations, since there are oscillations of induced density also inside the cluster for all excitations. The coupling of the localized surface plasmon to nearby e−h transitions also causes induced density oscillations inside the cluster. Thus, identifying an absorption peak as a localized surface plasmon peak is not as straightforward as for larger clusters of hundreds or thousands of electrons. However, for all the clusters we have studied here, with 8−186 electrons, the largest peaks have the characteristics of a LSPR peak: the peaks take up a large portion of the total oscillation strength, they are caused by one or more collective excitations, and the induced density for the excitations is concentrated on the surface. Also, the energy of the peaks is close to the bulk LSPR energy and shifts closer to it as the cluster size grows. The transition contribution profile and the induced density distribution of the LSPR peaks are also distinctly different from those of volume plasmon like excitations at higher energy and excitations caused mainly by one e−h transition. Thus, it seems reasonable to call the largest absorption peaks LSPR peaks for all these cluster sizes.

3.2. Cluster Assemblies. The studied assemblies with 2, 3, 4, and 6 Na_8 clusters, as well as the single Na_8 cluster, can be seen in Figure 11. The distance between the jellium edges is half of the radius of one cluster, 2.08 Å, in each system. For the dimer and trimer, the clusters are in a row along the *x*-axis. The tetramer is in the shape of a square, and the hexamer in the shape of a regular hexagon, both lying in the *xy*-plane. The red, green, and blue arrows indicate the *x*-, *y*-, and *z*-directions, respectively.

The optical absorption of these assemblies was studied in *x*-, *y*-, and *z*-directions. Here the direction refers to the direction of the polarization of the light, i.e., the direction of the dipole moment of the electric field. For each assembly, a TCM analysis was made of the largest peak in two of these directions: for light polarized parallel and perpendicular to the dimer/trimer axis or the plane of the tetramer/hexamer. In the coordinate system fixed by the arrows in Figure 11, these directions are *x* for parallel polarization and *y* (for the dimer and trimer) and *z* (for the tetramer and hexamer) for perpendicular polarization. The spectra for all the

DOI: 10.1021/acs.jpcc.7b10154
J. Phys. Chem. C 2017, 121, 27036−27052

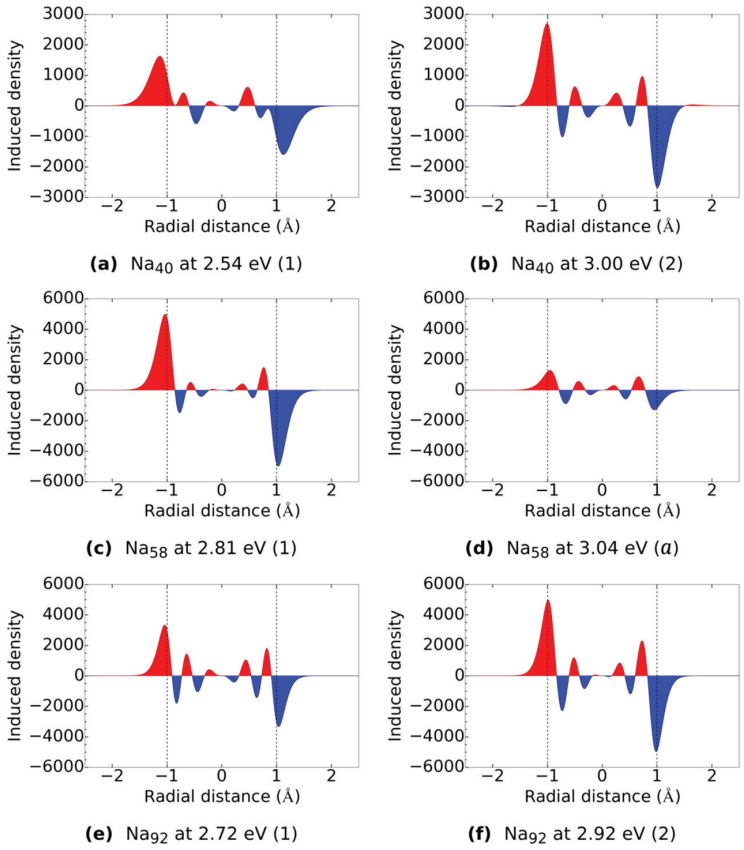

Figure 9. Induced densities corresponding to the TCM images in Figure 6. See the caption of Figure 8 for details.

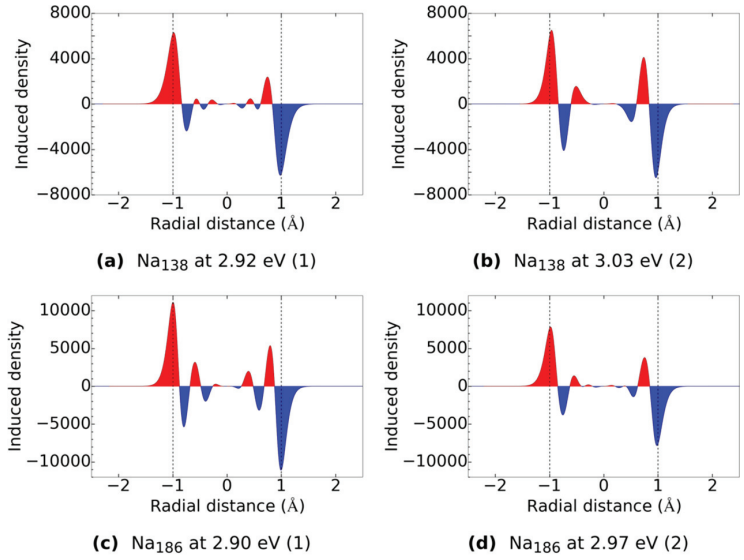

Figure 10. Induced densities for the largest peaks in the optical absorption spectra, corresponding to the TCM images in Figure 7. See the caption of Figure 8 for details.

assemblies are displayed in Figure 12. The labels in the figures indicate the number of clusters in the assembly ("1" meaning the single cluster).

For all the assemblies, the plasmon peak is split. Because of symmetries in the assemblies, the y-direction is identical to z-direction for the dimer and trimer and identical to the x-direction

DOI: 10.1021/acs.jpcc.7b10154
J. Phys. Chem. C 2017, 121, 27036−27052

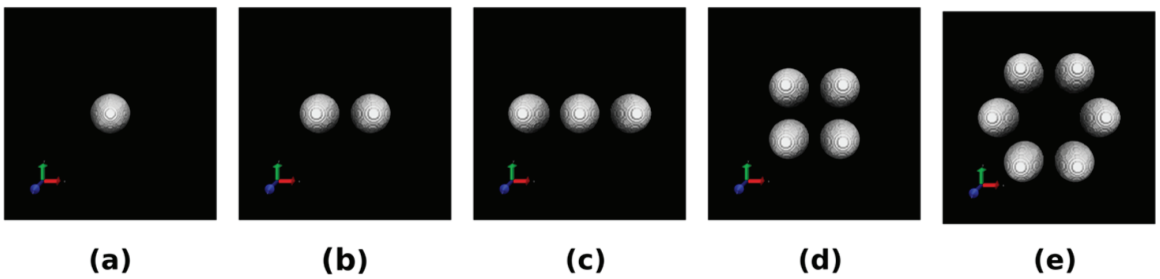

Figure 11. Positive jellium backgrounds of a single Na_8 cluster and the dimer, trimer, tetramer, and hexamer consisting of Na_8 clusters. The separation between the jellium edges is $0.5 \times r = 2.08$ Å for each assembly. All the assemblies lie in the *xy*-plane. The *x*-, *y*-, and *z*-directions are indicated by the red, green, and blue arrows, respectively. The images are made with VMD.[44]

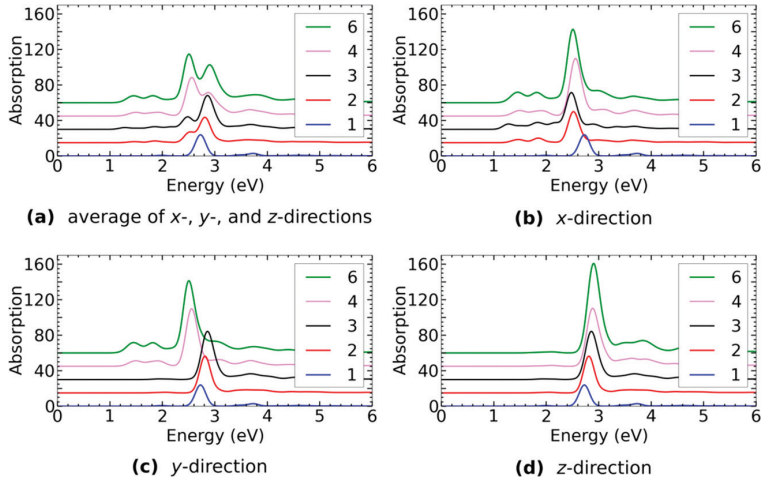

Figure 12. Spectra for the dimer, trimer, tetramer, and hexamer seen in Figure 11. The spectra of a single cluster are also included for comparison. For clarity, the zero level of the absorption has been raised by 60 units for each assembly with respect to the previous assembly.

for the tetramer. For the hexamer, *x*- and *y*-directions are similar but not identical. The energies of the LSPR peaks for parallel and perpendicular polarization are listed in Table 1. For short chains

Table 1. Energies of the LSPR Peaks for Parallel and Perpendicular Polarization for the Assemblies (in Units of eV)

	single	dimer	trimer	tetramer	heptamer
parallel	2.72	2.52	2.48	2.56	2.51
perpendicular	2.72	2.81	2.86	2.88	2.90

of nanoparticles with diameters from tens to hundreds of nanometers, it is known that as the number of particles in the chain grows, the LSPR peak experiences a red-shift for light polarized parallel to the chain axis and a weaker blue-shift for light polarized perpendicular to the chain axis.[45,46] The same trends have been seen in real-time TDDFT studies for chains consisting of silver[47] and sodium[48] atoms. Also here the LSPR peak for perpendicular polarization can be seen to shift to higher energy as the number of clusters gets bigger. For parallel polarization, the peak shifts to smaller energies from the single cluster to the dimer to the trimer as the number of clusters in a row along the axis grows. For both polarizations, the intensity of the peak grows as there are more clusters participating in the plasmon resonance.

The cross sections of the induced densities corresponding to the LSPR peaks for parallel polarization (*x*-direction) can be seen in Figure 13. (For the dimer, the energy of the analysis is the exact energy of the strongest dipole oscillation and thus differs by 0.1 eV from the energy of the LSPR peak in the broadened spectra.) Shown are the isosurfaces of the positive and negative densities at the same absolute density value in the *xy*-plane. The induced density for the single sphere is also shown for comparison. The induced densities show coupling of the plasmons in the clusters: even though the two concentric shells of induced density for the single cluster can still be seen for each cluster, these shells are not identical to each other but distorted by the interaction with the neighboring clusters. The sum of the overall electron density at one moment is therefore negative on one side of the assembly and positive on the other, making individual clusters charged during the oscillation. All the plasmons of the individual clusters are oscillating in phase, i.e., the plasmons are aligned. The attractive interactions between the plasmons of the individual clusters aligned in the *x*-direction lower the energy of this peak when the number of clusters in a row in the *x*-direction grows. Thus, the lowest peak energy is for the trimer, and the dimer and hexamer have almost the same peak energy. However, since the plasmonic interactions are short-range, and clusters affect mostly only their nearest neighbors, this red-shift is much larger from the single sphere to the dimer than from the dimer to the trimer.

For the tetramer, the repulsive interactions between the clusters aligned in the *y*-direction, i.e., perpendicular to the direction of the polarization, make the LSPR energy slightly larger

DOI: 10.1021/acs.jpcc.7b10154
J. Phys. Chem. C 2017, 121, 27036−27052

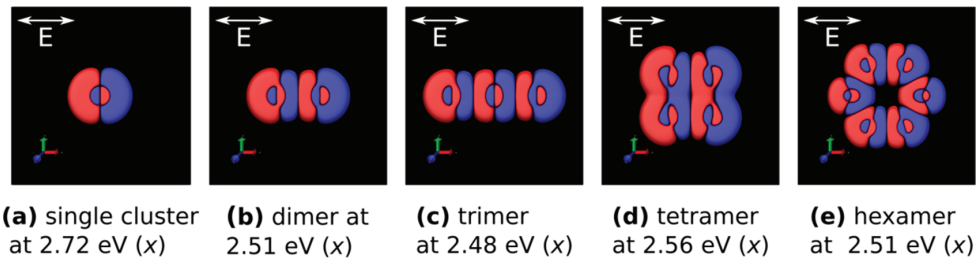

Figure 13. A cross section of the induced densities corresponding to the LSPR peak for parallel polarization (x-direction) for a single Na_8 cluster and the dimer, trimer, tetramer, and hexamer. An isosurface of the positive and negative parts of the induced density at the same absolute value in the xy-plane is shown for each assembly. The isosurface value is the same for all the figures. The length scale for each assembly is the same as the scale for the same assembly in Figure 11. The direction of the polarization is indicated in the figures. The images are made with VMD.

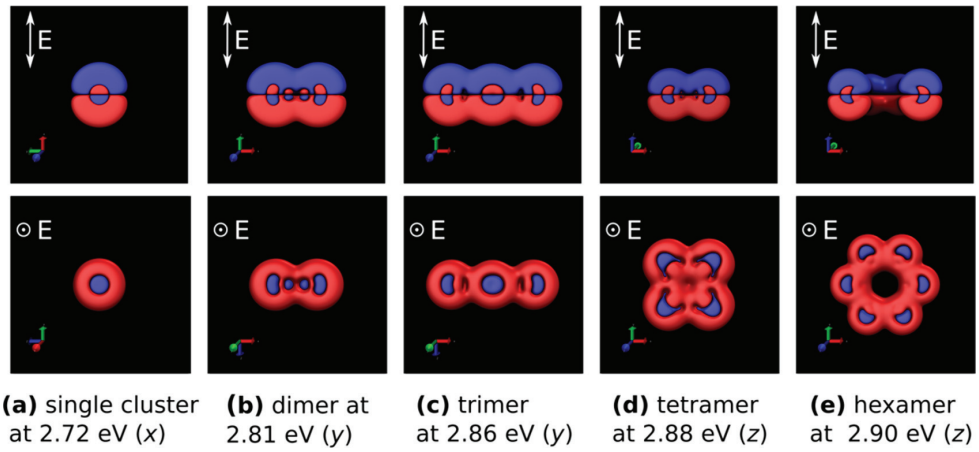

Figure 14. Cross sections of the induced densities corresponding to the LSPR peak for perpendicular polarization (x for the single sphere, y for the dimer and trimer, z for the tetramer and hexamer) in two different directions. In the top row, the images are oriented so that the direction of the polarization is vertical. In the bottom row, the direction of the polarization is perpendicular to the image plane. The cross-section plane goes through the center of the assemblies except for the tetramer in the top row, where it goes through the center of two of the four spheres. See the caption of Figure 13 for further details.

than for the dimer. More generally, it has been found that for short nanoparticle chains the LSPR peak for a double chain, i.e., a chain of dimers, is blue-shifted with respect to the LSPR of a single chain.[49]

The cross sections of the induced densities corresponding to the plasmon peak for perpendicular polarization can be seen in Figure 14. Two cross sections, seen from different directions and cut along different planes, are shown. For the images in the top row, the direction of the polarization is vertical, and the cross section is in a plane perpendicular to the plane of the assembly. In the bottom row, the images are oriented so that the direction of the polarization is perpendicular to the image plane, and the plane of the cross section is the plane of the assembly. The direction of the polarization is shown in the figures. The plane of the cross section is located in the middle of the assemblies in all figures, except in the top row figure for the tetramer, where it is located in the middle of two of the four spheres. As can be seen, the individual plasmons of the single spheres oscillate in phase and hybridize together. When the number of particles in the assembly grows, there is more repulsion between the individual plasmon oscillations, making the LSPR peak shift to higher energy.

The main features of the induced densities can be explained by the plasmon hybridization (PH) model.[50,51] In the parallel direction, the plasmons are bonding, and in the perpendicular direction, antibonding combinations of the individual plasmons. The PH model has been used to investigate the LSPR in dimers,[50] linear trimers,[52] and square-shaped[53] and hexagonal[54] cluster assemblies geometrically similar to those here. The dipolar LSPR causing the largest absorption peak can in all these cases be described mainly as a linear combination of the dipolar plasmons of the individual clusters, even though especially for closer separations, there are also some contributions from higher angular momenta. For the dimer, trimer, and tetramer, the plasmons for parallel and perpendicular polarizations can be constructed simply by making all the plasmons of the individual clusters aligned in the direction of the polarization. For the hexamer, the situation is the same in the perpendicular direction, and in the parallel direction the plasmon of the assembly is a slightly more complicated linear combination constructed from the symmetry-aligned dipolar plasmon modes of the individual clusters. Thus, the largest peak in the parallel direction is caused by the bonding dipolar plasmon for all the assemblies. In the PH model, the valence electrons are modeled as an incompressible fluid on the surface of the positive background charge representing the ion cores. In our jellium model, the valence electrons are not constrained on the surface, which allows us to see the possible charge oscillations inside the clusters and the spill-out of electrons out the clusters.

DOI: 10.1021/acs.jpcc.7b10154
J. Phys. Chem. C 2017, 121, 27036−27052

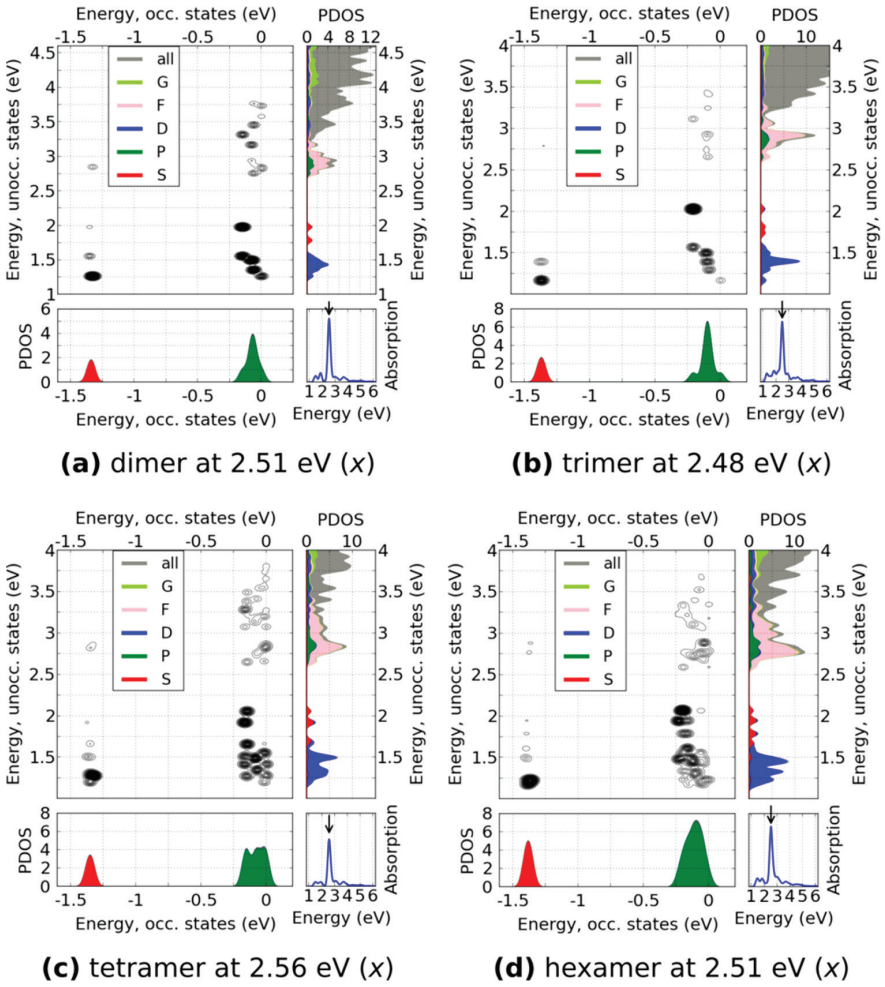

Figure 15. TCMs for the LSPR peaks for the parallel polarization (in the *x*-direction). The PDOSs shown are sum of the PDOSs for each cluster, where states that are inside a sphere with a radius of $1.5 \times r = 6.24$ Å, concentric with the cluster, are included. All the density of states inside the calculation box is shown in gray. The corresponding induced densities can be seen in Figure 13.

The optical spectra of jellium nanoparticle dimers have also been calculated with TDDFT[55] for particles with 1074 electrons and with TDLDA[32] for particles with 302 and 1018 electrons for various interparticle separations. In these studies, the dominating peak in the absorption spectrum is also found to be the bonding dipolar plasmon, except for small separations of almost touching spheres, where the charge transfer plasmon becomes dominant. This seems to be the case also here: even though there is some charge transfer between the clusters, the plasmons can be described as combinations of the plasmons of the individual spheres.

In Figure 15 are displayed the TCMs for the LSPR peaks for parallel polarization (in the *x*-direction). They can be compared to the TCM of a single cluster in Figure 5b. The PDOSs for the cluster systems show that the spherical symmetries of the superatomic orbitals of the clusters have been somewhat split, and all the 1P and 1D states, for example, are no longer degenerate. This lifting of degeneracy enables transitions that are not dipole-allowed and were thus not present in the TCM of a single sphere, such as 1S → 1D and 1P → 2P/1F. The strongest transition for the single sphere, 1P → 1D, is still the dominating transition for the dimer, hexamer, and tetramer and has the second strongest contribution for the trimer. For the trimer, the strongest contribution comes from the 1P → 2S transition, which is also relatively stronger for the other assemblies than for the single sphere. This transition at about 2 eV, along with the strong contribution from the 1S → 1D transition at about 2.5−2.6 eV, getting stronger as the number of clusters grows, shifts the LSPR peak to lower energies compared to the single cluster. Also, contributions from transitions from 1P, the HOMO state, to states over 3 eV in energy above it, have quite a small contribution for the assemblies, whereas for the single cluster the transition 1P → 2D at 3.6 eV accounts for 20% of the total transition strength.

The TCM and cross section of the induced density corresponding to the LSPR peak of the hexamer in the other parallel direction, *y*, at 2.51 eV, can be seen in Figure 16. The TCM is almost identical to the one corresponding to the LSPR peak in the *x*-direction, seen in Figure 15d: all the major transitions are the same, and the slight differences are mainly in the transitions from 1P to 1F/2P and to orbitals higher in energy. In the induced density the different orientation of the spheres can be seen: now there are essentially two dimers perpendicular to the direction of the

DOI: 10.1021/acs.jpcc.7b10154
J. Phys. Chem. C 2017, 121, 27036−27052

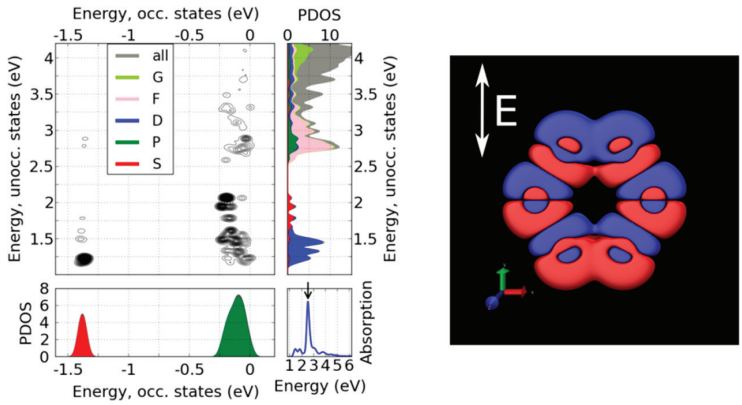

Figure 16. TCM and cross section of the induced density for the hexamer corresponding to the LSPR peak for polarization in the *y*-direction at 2.51 eV. The plane of the cross section is the *xy*-plane at $z = 0$.

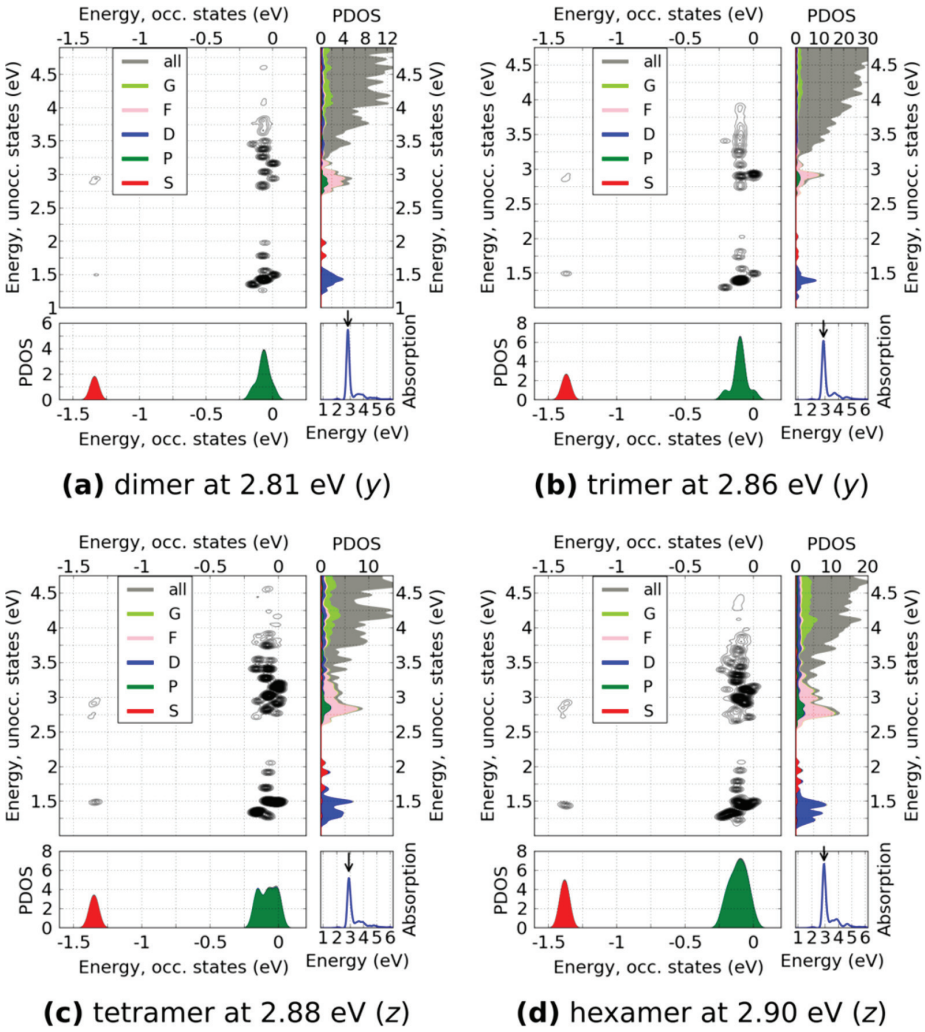

Figure 17. TCMs for the LSPR peaks for perpendicular polarization (in the *y*-direction for the dimer and trimer; in the *z*-direction for the tetramer and hexamer). The corresponding induced densities can be seen in Figure 14. See the caption of Figure 15 for details.

polarization (the two top spheres and the two bottom spheres), which causes repulsion, but also two bent chains of three clusters parallel to the polarization direction with bonding interactions. The energy of the plasmon peak is the same as in the *x*-direction.

DOI: 10.1021/acs.jpcc.7b10154
J. Phys. Chem. C 2017, 121, 27036−27052

The TCMs corresponding to the LSPR peaks for perpendicular polarization can be seen in Figure 17. For the dimer and trimer, the 1P → 1D transitions give the strongest contribution, as for the single sphere, but there are also strong contributions from transitions from 1P to 2P/1F and to states higher in energy. For the tetramer and hexamer, the strongest contribution comes from the 1P → 2P/1F transitions. These transitions at about 3 eV or higher in energy, absent in the case of a single sphere, raise the LSPR energy. The transitions from 1S are not as relevant as in the parallel direction.

The two small peaks in the optical spectra of the assemblies for parallel polarization were also analyzed. The first of these, at around 1.3−1.5 eV, is caused by the 1P → 1D transition. The second, at 1.8−1.9 eV, is caused mainly by the 1P → 2S transitions, with some contribution from 1P → 1D transitions. This peak is present also in the spectrum of the single cluster, but it is not as strong as for the assemblies.

4. DISCUSSION

We analyzed both the collectivity of the excitations and the induced densities associated with them to observe the LSPR nature of the absorption peaks. In the TCM scheme used here, all the e−h transitions in a certain energy window, essentially corresponding to a certain peak in the absorption spectra, can be visualized. Thus, the collectivity of the transition causing the peak can be easily observed from one figure. The transition contribution map also clearly shows how individual transitions of different energies combine to form the plasmon excitation. This is a fast, visual way to observe the coupling between the e−h transitions without the need to perform the spectrum calculation more than once, as in the methods using the scaling parameter for electronic interactions.[16,17] The TD-DFTP calculation needed for the TCM analysis is computationally inexpensive, since it uses the Casida matrix elements already computed in the lr-TDDFT calculation.

The radial distribution of the induced density, also obtained from the TD- DFTP calculation, can then be used to identify the LSPR type transitions from other collective excitations. The study of the radial induced density is best suited for spherical or nearly spherical particles, but even in the case of more complex shapes, the distribution of the electron density oscillations can be observed.

Our method does not give a single quantitative measure of the plasmonicity; there is no "plasmonicity index". However, it provides an immediate qualitative picture of the LSPR nature of an excitation. Some quantitative analysis is also possible: the percentage of each individual e−h contribution from the total oscillation strength can be calculated. Also, although not done here, the percentage of the induced density near the surface of the cluster can be calculated and used as a measure of the surface nature of the oscillations. In the case of concentric shells of induced densities, such as for the individual clusters here, the total induced densities in each shell could be calculated and compared.

As we have shown, our method is also applicable to the study of assemblies consisting of plasmonic clusters. The interactions between the plasmons of the individual clusters can be monitored from both the TCM figures and from the induced densities.

Our results for the single clusters can be compared to other recent studies of the plasmonicity in small metal particles of varying size.[13,20,23,56] Townsend and Bryant[20] studied the electron density oscillations in a 100-electron and a 600-electron jellium cluster with the density of gold using real-time TDDFT. They found that for the strongest peak in both clusters the electron density was oscillating throughout the cluster. These peaks were also close in energy to (although red-shifted from) the classical LSPR value. These responses were named classical surface plasmons, as opposed to "quantum core plasmons" (QCP) also found in the spectra of the 100-electron cluster. The QCP peaks were close to the surface plasmon peak and were somewhat weaker than it. Townsend and Bryant did not assign these peaks as fragments of the surface plasmons because the contributions from different e−h transitions were quite similar in strength, and the electron density oscillations were clearly concentrated in the core.

Zhang et al.[23] used the GPI approach and scaling of the electronic interaction to study the emergence of the plasmon resonance in a jellium sphere with a radius of 40 Å and with 10−300 electrons. The work function and the lattice background polarizability of the clusters were chosen to represent those of gold. TDLDA with RPA was used for the optical calculations. The induced density profiles of the spheres were similar to the ones obtained in this work, with concentric shells of density oscillations. There were two shells in the smallest cluster size, and the number of the shells increased as the number of electrons got larger. The percentage of induced density on the surface also increased with growing size. Based on the shifting of the peak with respect to the scaling parameter and the shape of the GPI spectra, the largest peaks in the clusters with less than 100 electrons were characterized as single-particle excitations, and the plasmon resonance was observed to emerge only in clusters with more than 100 electrons. However, even for the smallest clusters there was a small effect of the scaling to the energy of the absorption peak, and the GPI value showed a slight peak at the absorption maximum.

In a TDDFT study by Li et al.,[13] absorption spectra of atomistic bcc structured sodium clusters with 15, 27, 51, 65, 89, 113, 169, 229, 283, and 331 atoms were calculated, and the induced densities were analyzed for the strongest peaks. A strong principal peak was found for all the studied sizes, but some fragmentation could be seen in all these peaks, either as a clear multipeaked structure or a broad peak. These peaks, interpreted as resulting from coupling between the localized surface plasmon and individual e−h transitions close in energy, were called "Landau fragmented surface plasmons". For the main peak, there were strong electron density oscillations at the edges of the clusters for all sizes. However, the clusters with 27, 51, 65, 89, and 113 atoms had strong density oscillations also inside the cluster, whereas for the other clusters the electronic response inside the cluster was weak. The clusters with stronger electronic response inside the cluster were the ones with strong coupling between the surface plasmon and e−h transitions close in energy.

Aikens et al.[56] studied the absorption spectra of atomistic tetrahedral silver clusters using TDDFT. Clusters with 10, 20, 35, 56, 84, and 120 atoms in multiple different charge states were studied. The clusters with a number of valence electrons corresponding to a filled electron shell, such as Ag_{10}^{+2}, Ag_{20}, Ag_{35}^{-5}, or Ag_{56}^{-2}, displayed sharp absorption peaks with only one strong transition. The main transitions for the closed-shell clusters were found to be collective. The energy of the largest absorption peak scaled linearly with the inverse size of the cluster. These same trends were found also in silver clusters of octahedral, truncated octahedral, and icosahedral shapes with 6−85 atoms in a TDDFT study by Bae and Aikens.[57] The bulk limit obtained from the linear scaling for the tetrahedral clusters was found to predict the peak energy of a large, 32 nm silver

DOI: 10.1021/acs.jpcc.7b10154
J. Phys. Chem. C 2017, 121, 27036−27052

tetrahedron obtained from a DDA calculation. Thus, the absorption peaks of clusters of only a few valence electrons were connected to the classical LSPR of larger clusters.

All these studies show the same trend as ours: small clusters of only tens of valence electrons have collective, plasmon-like excitations. However, it is also clear that single-particle effects play a role in the smallest clusters. Therefore, the exact cluster size where the largest excitation can already be called a localized surface plasmon depends not only on the systems but also on the methods and definitions. In our study, the largest peak in the Na_8 jellium cluster is found to already show all the same characteristics of a localized surface plasmon as the larger clusters and can therefore be classified as a LSPR peak.

5. CONCLUSIONS

We have presented here a systematic analysis of optical absorption of spherical electron−gas (jellium) clusters in the size range of 8−186 electrons. We have shown that a collective optical absorption, describable as the localized surface plasmon resonance, develops already for the smallest system of eight electrons. The TCM method applied here for the first time in a systematic study of jellium clusters gives a convenient "all-in-one-view" analysis of the collectivity of the absorption in the energy space (e−h space), and the real-space visualization of the induced excitation density gives an immediate visual impression of the volume or surface effects. This systematic analysis of the e−h contributions gives new insight into the birth of the localized surface plasmon resonance in small metal clusters. The detailed knowledge of the transitions and the distribution of induced density for the LSPR peaks for single jellium clusters also enables the analysis of plasmonic coupling in assemblies of metallic clusters and nanoparticles. Because of the high degree of parallelization of our simulation and analysis codes, plasmonic properties of large assemblies of clusters in arbitrary topography, having thousands of electrons in total, can be conveniently computed and analyzed. We have demonstrated the applicability of our methods to the study of plasmons in small cluster assemblies. We are now in the process to extend our studies to larger assemblies of electron clusters where the effects of size, shape, assembly dimensionality, and topography on the collective optical properties can be systematically investigated.

AUTHOR INFORMATION

Corresponding Author

*E-mail hannu.j.hakkinen@jyu.fi (H.H.).

ORCID

Hannu Häkkinen: 0000-0002-8558-5436

Notes

The authors declare no competing financial interest.

ACKNOWLEDGMENTS

This work was supported by the Academy of Finland (grant 294217 and H.H.'s Academy Professorship). The computations were done at the CSC−the Finnish IT Center for Science and at the Nanoscience Center of the University of Jyväskylä by utilizing the FGCI−Finnish Grid and Cloud Infrastructure (persistent identifier urn:nbn:fi:research-infras-2016072533).

REFERENCES

(1) Atwater, H. A.; Polman, A. Plasmonics for Improved Photovoltaic Devices. *Nat. Mater.* **2010**, *9*, 205−213.

(2) Mayer, K. M.; Hafner, J. H. Localized Surface Plasmon Resonance Sensors. *Chem. Rev.* **2011**, *111*, 3828−3857.

(3) Huang, X.; El-Sayed, I. H.; Qian, W.; El-Sayed, M. A. Cancer Cell Imaging and Photothermal Therapy in the Near-Infrared Region by Using Gold Nanorods. *J. Am. Chem. Soc.* **2006**, *128*, 2115−2120.

(4) Kelly, K. L.; Coronado, E.; Zhao, L. L.; Schatz, G. C. The Optical Properties of Metal Nanoparticles: The Influence of Size, Shape, and Dielectric Environment. *J. Phys. Chem. B* **2003**, *107*, 668−677.

(5) Le, F.; Brandl, D. W.; Urzhumov, Y. A.; Wang, H.; Kundu, J.; Halas, N. J.; Aizpurua, J.; Nordlander, P. Metallic Nanoparticle Arrays: A Common Substrate for Both Surface-enhanced Raman Scattering and Surface-enhanced Infrared Absorption. *ACS Nano* **2008**, *2*, 707−718.

(6) Sönnichsen, C.; Reinhard, B. M.; Liphardt, J.; Alivisatos, A. P. A Molecular Ruler Based on Plasmon Coupling of Single Gold and Silver Nanoparticles. *Nat. Biotechnol.* **2005**, *23*, 741−745.

(7) Scholl, J. A.; Koh, A. L.; Dionne, J. A. Quantum Plasmon Resonances of Individual Metallic Nanoparticles. *Nature* **2012**, *483*, 421−428.

(8) Manjavacas, A.; García de Abajo, F. J. Tunable Plasmons in Atomically Thin Gold Nanodisks. *Nat. Commun.* **2014**, *5*, 3548.

(9) Brack, M. The Physics of Simple Metal Clusters: Self-Consistent Jellium Model and Semiclassical Approaches. *Rev. Mod. Phys.* **1993**, *65*, 677−732.

(10) Guidez, E. B.; Aikens, C. M. Quantum Mechanical Origin of the Plasmon: From Molecular Systems to Nanoparticles. *Nanoscale* **2014**, *6*, 11512−11527.

(11) Ekardt, W. Size-Dependent Photoabsorption and Photoemission of Small Metal Particles. *Phys. Rev. B: Condens. Matter Mater. Phys.* **1985**, *31*, 6360−6370.

(12) Beck, D. Self-Consistent Calculation of the Eigenfrequencies for the Electronic Excitations in Small Jellium Spheres. *Phys. Rev. B: Condens. Matter Mater. Phys.* **1987**, *35*, 7325−7333.

(13) Li, J.-H.; Hayashi, M.; Guo, G.-Y. Plasmonic Excitations in Quantum-Sized Sodium Nanoparticles Studied by Time-Dependent Density Functional Calculations. *Phys. Rev. B: Condens. Matter Mater. Phys.* **2013**, *88*, 155437.

(14) Casanova, D.; Matxain, J. M.; Ugalde, J. M. Plasmonic Resonances in the Al^{-}_{13} Cluster: Quantification and Origin of Exciton Collectivity. *J. Phys. Chem. C* **2016**, *120*, 12742−12750.

(15) Puska, M. J.; Nieminen, R. M.; Manninen, M. Electronic Polarizability of Small Metal Spheres. *Phys. Rev. B: Condens. Matter Mater. Phys.* **1985**, *31*, 3486−3495.

(16) Bernadotte, S.; Evers, F.; Jacob, C. R. Plasmons in Molecules. *J. Phys. Chem. C* **2013**, *117*, 1863−1878.

(17) Piccini, G.; Havenith, R. W. A.; Broer, R.; Stener, M. old Nanowires: A Time-Dependent Density Functional Assessment of Plasmonic Behavior. *J. Phys. Chem. C* **2013**, *117*, 17196−17204.

(18) Gieseking, R. L.; Ratner, M. A.; Schatz, G. C. Semiempirical Modeling of Ag Nanoclusters: New Parameters for Optical Property Studies Enable Determination of Double Excitation Contributions to Plasmonic Excitation. *J. Phys. Chem. A* **2016**, *120*, 4542−4549.

(19) Townsend, E.; Bryant, G. W. Which Resonances in Small Metallic Nanoparticles Are Plasmonic? *J. Opt.* **2014**, *16*, 114022.

(20) Townsend, E.; Bryant, G. W. Plasmonic Properties of Metallic Nanoparticles: The Effects of Size Quantization. *Nano Lett.* **2012**, *12*, 429−434.

(21) Ma, J.; Wang, Z.; Wang, L.-W. Interplay between Plasmon and Single-Particle Excitations in a Metal Nanocluster. *Nat. Commun.* **2015**, *6*, 10107.

(22) Bursi, L.; Calzolari, A.; Corni, S.; Molinari, E. Quantifying the Plasmonic Character of Optical Excitations in Nanostructures. *ACS Photonics* **2016**, *3*, 520−525.

(23) Zhang, R.; Bursi, L.; Cox, J. D.; Cui, Y.; Krauter, C. M.; Alabastri, A.; Manjavacas, A.; Calzolari, A.; Corni, S.; Molinari, E.; et al. How to Identify Plasmons from the Optical Response of Nanostructures. *ACS Nano* **2017**, *11*, 7321−7335.

(24) Ekardt, W. Work Function of Small Metal Particles: Self-Consistent Spherical Jellium-Background Model. *Phys. Rev. B: Condens. Matter Mater. Phys.* **1984**, *29*, 1558−1564.

DOI: 10.1021/acs.jpcc.7b10154
J. Phys. Chem. C 2017, 121, 27036−27052

(25) Pacheco, J.; Ekardt, W. Response of Finite Many-Electron Systems Beyond the Time-Dependent Local Density Approximation: Application to Small Metal Clusters. *Ann. Phys. (Berlin, Ger.)* **1992**, *504*, 254−269.
(26) Yannouleas, C.; Broglia, R. Collective and Single-Particle Aspects in the Optical Response of Metal Microclusters. *Phys. Rev. A: At., Mol., Opt. Phys.* **1991**, *44*, 5793−5802.
(27) Yannouleas, C.; Vigezzi, E.; Broglia, R. A. Evolution of the Optical Properties of Alkali-Metal Microclusters Towards the Bulk: The Matrix Random-Phase-Approximation Description. *Phys. Rev. B: Condens. Matter Mater. Phys.* **1993**, *47*, 9849−9861.
(28) Guet, C.; Johnson, W. R. Dipole Excitations of Closed-Shell Alkali-Metal Clusters. *Phys. Rev. B: Condens. Matter Mater. Phys.* **1992**, *45*, 11283−11287.
(29) Selby, K.; Kresin, V.; Masui, J.; Vollmer, M.; de Heer, W. A.; Scheidemann, A.; Knight, W. D. Photoabsorption Spectra of Sodium Clusters. *Phys. Rev. B: Condens. Matter Mater. Phys.* **1991**, *43*, 4565−4572.
(30) Xia, C.; Yin, C.; Kresin, V. V. Photoabsorption by Volume Plasmons in Metal Nanoclusters. *Phys. Rev. Lett.* **2009**, *102*, 156802.
(31) Malola, S.; Lehtovaara, L.; Enkovaara, J.; Häkkinen, H. Birth of the Localized Surface Plasmon Resonance in Monolayer-Protected Gold Nanoclusters. *ACS Nano* **2013**, *7*, 10263−10270.
(32) Zuloaga, J.; Prodan, E.; Nordlander, P. Quantum Description of the Plasmon Resonances of a Nanoparticle Dimer. *Nano Lett.* **2009**, *9*, 887−891.
(33) Prodan, E.; Nordlander, P. Structural Tunability of the Plasmon Resonances in Metallic Nanoshells. *Nano Lett.* **2003**, *3*, 543−547.
(34) Mortensen, J. J.; Hansen, L. B.; Jacobsen, K. W. Real-space Grid Implementation of the Projector Augmented Wave Method. *Phys. Rev. B: Condens. Matter Mater. Phys.* **2005**, *71*, 035109.
(35) Enkovaara, J.; Rostgaard, C.; Mortensen, J. J.; Chen, J.; Dułak, M.; Ferrighi, L.; Gavnholt, J.; Glinsvad, C.; Haikola, V.; Hansen, H. A.; et al. Electronic Structure Calculations with GPAW: A Real-Space Implementation of the Projector Augmented-Wave Method. *J. Phys.: Condens. Matter* **2010**, *22*, 253202.
(36) Blöchl, P. E. Projector Augmented-Wave Method. *Phys. Rev. B: Condens. Matter Mater. Phys.* **1994**, *50*, 17953−17979.
(37) Bahn, S. R.; Jacobsen, K. W. An Object-Oriented Scripting Interface to a Legacy Electronic Structure Code. *Comput. Sci. Eng.* **2002**, *4*, 56−66.
(38) Perdew, J. P.; Wang, Y. Accurate and Simple Analytic Representation of the Electron-Gas Correlation Energy. *Phys. Rev. B: Condens. Matter Mater. Phys.* **1992**, *45*, 13244−13249.
(39) Walter, M.; Häkkinen, H.; Lehtovaara, L.; Puska, M.; Enkovaara, J.; Rostgaard, C.; Mortensen, J. J. Time-Dependent Density-Functional Theory in the Projector Augmented-Wave Method. *J. Chem. Phys.* **2008**, *128*, 244101.
(40) Andrade, X.; Botti, S.; Marques, M. A. L.; Rubio, A. Time-Dependent Density Functional Theory Scheme for Efficient Calculations of Dynamic (Hyper)Polarizabilities. *J. Chem. Phys.* **2007**, *126*, 184106.
(41) Parks, J. H.; McDonald, S. A. Evolution of the Collective-Mode Resonance in Small Adsorbed Sodium Clusters. *Phys. Rev. Lett.* **1989**, *62*, 2301−2304.
(42) Khanna, S. N.; Jena, P. Assembling Crystals from Clusters. *Phys. Rev. Lett.* **1992**, *69*, 1664−1668.
(43) Castleman, A. W., Jr.; Khanna, S. N. Clusters, Superatoms, and Building Blocks of New Materials. *J. Phys. Chem. C* **2009**, *113*, 2664−2675.
(44) Humphrey, W.; Dalke, A.; Schulten, K. VMD: Visual Molecular Dynamics. *J. Mol. Graphics* **1996**, *14*, 33−38.
(45) Halas, N. J.; Lal, S.; Chang, W.-S.; Link, S.; Nordlander, P. Plasmons in Strongly Coupled Metallic Nanostructures. *Chem. Rev.* **2011**, *111*, 3913−3961.
(46) Chen, T.; Pourmand, M.; Feizpour, A.; Cushman, B.; Reinhard, B. M. Tailoring Plasmon Coupling in Self-Assembled One-Dimensional Au Nanoparticle Chains through Simultaneous Control of Size and Gap Separation. *J. Phys. Chem. Lett.* **2013**, *4*, 2147−2152.
(47) Ding, F.; Guidez, E. B.; Aikens, C. M.; Li, X. Quantum Coherent Plasmon in Silver Nanowires: A Real-Time TDDFT Study. *J. Chem. Phys.* **2014**, *140*, 244705.
(48) Yan, J.; Gao, S. Plasmon Resonances in Linear Atomic Chains: Free-Electron Behavior and Anisotropic Screening of d Electrons. *Phys. Rev. B: Condens. Matter Mater. Phys.* **2008**, *78*, 235413.
(49) Slaughter, L. S.; Willingham, B. A.; Chang, W.-S.; Chester, M. H.; Ogden, N.; Link, S. Toward Plasmonic Polymers. *Nano Lett.* **2012**, *12*, 3967−3972.
(50) Nordlander, P.; Oubre, C.; Prodan, E.; Li, K.; Stockman, M. I. Plasmon Hybridization in Nanoparticle Dimers. *Nano Lett.* **2004**, *4*, 899−903.
(51) Wang, H.; Brandl, D. W.; Nordlander, P.; Halas, N. J. Plasmonic Nanostructures: Artificial Molecules. *Acc. Chem. Res.* **2007**, *40*, 53−62.
(52) Chuntonov, L.; Haran, G. Trimeric Plasmonic Molecules: The Role of Symmetry. *Nano Lett.* **2011**, *11*, 2440−2445.
(53) Brandl, D. W.; Mirin, N. A.; Nordlander, P. Plasmon Modes of Nanosphere Trimers and Quadrumers. *J. Phys. Chem. B* **2006**, *110*, 12302−12310.
(54) Bao, K.; Mirin, N. A.; Nordlander, P. Fano Resonances in Planar Silver Nanosphere Clusters. *Appl. Phys. A: Mater. Sci. Process.* **2010**, *100*, 333−339.
(55) Marinica, D. C.; Kazansky, A. K.; Nordlander, P.; Aizpurua, J.; Borisov, A. G. Quantum Plasmonics: Nonlinear Effects in the Field Enhancement of a Plasmonic Nanoparticle Dimer. *Nano Lett.* **2012**, *12*, 1333−1339.
(56) Aikens, C. M.; Li, S.; Schatz, G. C. From Discrete Electronic States to Plasmons: TDDFT Optical Absorption Properties of Ag_n (n = 10, 20, 35, 56, 84, 120) Tetrahedral Clusters. *J. Phys. Chem. C* **2008**, *112*, 11272−11279.
(57) Bae, G.-T.; Aikens, C. M. Time-Dependent Density Functional Theory Studies of Optical Properties of Ag Nanoparticles: Octahedra, Truncated Octahedra, and Icosahedra. *J. Phys. Chem. C* **2012**, *116*, 10356−10367.

DOI: 10.1021/acs.jpcc.7b10154
J. Phys. Chem. C 2017, 121, 27036−27052

PII

CHARGE TRANSFER PLASMONS IN DIMERIC ELECTRON CLUSTERS

by

Elli Selenius, Sami Malola, Mikael Kuisma, Hannu Häkkinen (2020)

The Journal of Physical Chemistry C, **124** (23), 12645–12654

THE JOURNAL OF PHYSICAL CHEMISTRY C

pubs.acs.org/JPCC Article

Charge Transfer Plasmons in Dimeric Electron Clusters

Published as part of The Journal of Physical Chemistry virtual special issue "Metal Clusters, Nanoparticles, and the Physical Chemistry of Catalysis".

Elli Selenius, Sami Malola, Mikael Kuisma, and Hannu Häkkinen*

Cite This: *J. Phys. Chem. C* 2020, 124, 12645–12654 Read Online

ACCESS | Metrics & More | Article Recommendations | Supporting Information

ABSTRACT: The tunability of the optical response of dimers of metal clusters and nanoparticles makes them ideal for many applications from sensing and imaging to inducing chemical reactions. We have studied charge transfer plasmons in separate and linked dimers of closed-shell electron clusters of 8 and 138 electrons using time-dependent density functional theory. The simple model clusters enable the systematic study of the charge transfer phenomenon from the electronic perspective. To identify the charge transfer plasmons, we have developed an index, the charge transfer ratio, for quantifying the charge transfer nature of the excitations. In addition, we analyze the induced transition density and the electron transitions contributing to the dipole moment at the charge transfer plasmon energies. Our results show that the optical response of the dimers is very sensitive to changes in the intercluster separation and in the width of the linking channel, with charge transfer plasmon peaks appearing at low energies for dimers with linking or sufficient electron cloud overlap.

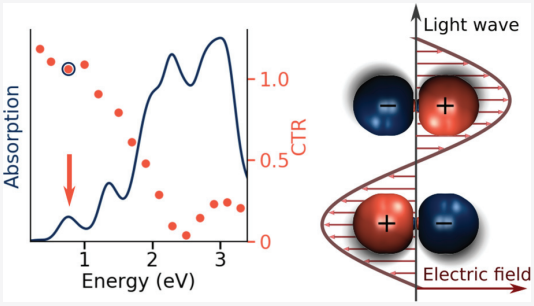

INTRODUCTION

The optical response of metal clusters and nanoparticles is highly dependent on the shape, size, and dielectric environment of the cluster.[1] The response of two adjacent particles depends also on the separation.[2] This tunability makes clusters and cluster assemblies or arrays ideal for many applications, such as surface-enhanced Raman spectroscopy for detecting single molecules,[3] the molecular ruler for measuring distances in the nanoscale,[4] cancer imaging and treatment,[5] and driving chemical reactions.[6]

Plasmons are collective excitations of the conductance electrons, where the electron density of the cluster oscillates in resonance with the external electromagnetic field. In plasmonic metal clusters, the main excitation is the localized surface plasmon resonance (LSPR), where the electron density oscillations happen mostly on the surface of the cluster.[7] There have been several approaches to understand and classify different optical excitations in metal clusters and nanoparticles, especially to recognize the LSPR peaks from the optical spectra. The distribution of the induced density[8,9] and collectivity of the excitation[10,11] have both been used as criteria for plasmonic resonances. Different plasmonicity indices based on the strength of the induced potential have also been developed.[12,13] Recently, Gieseking et al.[14] proposed a method to identify plasmonic resonances based on three criteria—the collectivity of the excitations, the superatomic character of the excitations, and the additivity of the contributions from the single-particle excitations.

In dimers, the plasmons of the two clusters can couple capacitively to form a bonding dipolar plasmon (BDP).[15] The energy of the excitation is lowered, causing the BDP peak to be red-shifted in comparison to the LSPR peak of the single clusters.[2,15] For short separations and chemically linked dimers there can also be charge transfer plasmons (CTPs).[16,17] In these CTPs, the electron density oscillates between the two clusters, making one cluster momentarily positively and the other negatively charged. The CTPs happen at energies lower than BDPs, and thus they add a new energy range for the applications of plasmons. Depending on the chemical coupling between the clusters, the CTPs can be caused by electrons tunneling or flowing between the clusters.[17]

Charge transfer plasmons have been experimentally observed in many dimeric nanostructures, such as nanogaps between two gold coated atomic force microscope tips,[18] gold nanorods connected with a gold nanojunction,[19] and dimers of various nanoparticles, such as gold nanoshells,[16] silver

Received: April 1, 2020
Revised: May 15, 2020
Published: May 18, 2020

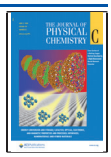

https://dx.doi.org/10.1021/acs.jpcc.0c02889
J. Phys. Chem. C 2020, 124, 12645–12654

spheres,[20] and gold nanoblocks.[21] For atomistically precise thiol-stabilized (SR) gold nanoclusters, Lahtinen et al. observed an absorption peak that they assigned to a tunneling CTP in covalently linked $Au_{\sim 250}(SR)_n$ dimers.[22]

Large nanoparticles and dimers with a separation of several nanometers can be treated with classical methods solving the Maxwell equations, and good agreement with experiments have been found for nanoparticle dimers in such cases.[23] However, for sizes of a few nanometers[24] or for subnanometer separations,[17,25] the quantum effects cannot be ignored. Thus, to model dimer systems with small, atom-precise clusters with more accuracy, time-dependent density functional theory (TDDFT) has been employed in multiple studies.[26−31]

The drawback of TDDFT is that it is computationally heavy. Therefore, in the region where quantum mechanical effects are important, but the size of the system makes atomistic TDDFT calculations unfeasible, some simplifications have to be made. Xiang et al. have employed the time-dependent orbital-free density functional theory (TD-OFDFT) to study dimers and trimers of sodium clusters consisting of 55 or 1415 atoms in order to reduce the computational cost.[32] The quantum-corrected model (QCM)[33,34] includes quantum effects in the optical response of nanoparticles with a small gap by modeling electron tunneling by a fictitious conductive material with the local permittivity reflecting the tunneling probability.

One approach is to combine TDDFT with the simple jellium model to represent the cluster dimers.[17,35−38] There, the nuclei and core electrons are represented as a uniform, positive background charge, and only the valence electrons are modeled explicitly. For elements where the d-electron screening plays a role, such as gold and silver, a dielectric background can be added to model this effect. The simple jellium model with a constant background density is most suitable for alkali metals, such as sodium, for which the s-type valence electrons are strongly delocalized. Different elements of this group can be represented by tuning the background density to correspond to the experimental density.

Since the jellium model allows for electron tunneling and the spilling of the conductance electrons, it enables charge transfer excitations for small gap sizes, and it can thus be used to understand the principles of charge transfer plasmons in dimeric structures. To accurately reproduce experimental results quantitatively, the background charge distribution at the edge of the cluster should be adjusted. In close distances, the atomic structure has been shown to affect the electric field enhancement and the charge transfer current.[24,39,40] Zhang et al.[39] have shown that for spherical jellium clusters of about 300 atoms, the jellium model gives the same trend for the BDP as atomistic models using bcc and icosahedral packing. The CTP peak is also reproduced by the jellium model, but only at about a separation of 10 Å, whereas for the two atomic arrangements a charge transfer mode was seen already at separations of 30−40 Å. The results indicate that the main trends in the spectra are reproduced by the jellium model, and at sufficiently small separations, the jellium model is able to describe the CTP.

Here, we have employed the jellium model with TDDFT for dimers of spherical clusters to study charge transfer plasmons from the electronic perspective. The simplicity of the background charge potential eases the investigation of the electronic phenomena, since the ground state electron density has a very simple structure, and the changes in electron density during excitations are therefore easier to distinguish and analyze as compared to atomic structures. Since we are using the same model for all the systems, we can follow the trends in the shape of the spectra and the peak energies even if the jellium model causes a shift compared to atomic clusters.

We studied homo- and heterodimers of two 8-electron or 138-electron clusters and varied the intercluster separation between the clusters. We also constructed some linked dimers by connecting the clusters with a cylindrical tunnel of the same jellium background density to gain understanding on the effect of conductive linking to the excitations. The conductive jellium linker establishes a coupling of metallic nature between the clusters, allowing electrons to flow between the clusters during a CTP excitation. These linked clusters serve as simple models for clusters that are connected by a conductive linker, such as one or more conductive ligands or a chain of metal atoms. It is possible to modify the background density of the linker to study the effect of the linker conductance. However, here we use the same density as for the clusters to have a linker with the same metallic character. For atomistic clusters, this kind of linking has been studied by Rossi et al.,[29] who studied CTPs in a system with a narrow atomic contact between to metal clusters.

Following the methods of our previous study of the birth of LSPR in jellium clusters,[41] we use the induced density and analysis of the contributions of the single-particle excitations to study the nature of the excitations in the dimer systems. In addition, we have developed an index to quantify the charge transfer nature of the excitations, enabling us to recognize the excitations with charge transfer character from the spectra and follow the development of the CTPs as the separation gets smaller.

THEORY AND METHODS

The GPAW[42,43] program, which performs the calculations using a uniform real-space grid, was used for the density functional theory (DFT) calculations. The local density approximation (LDA) after Perdew and Wang[44] was employed for the exchange-correlation functional. Typically, LDA is considered to yield inappropriate excitation energies due to lack of divergence of exchange-correlation kernel at charge transfer excitations. In the Supporting Information (section S1), we discuss why charge transfer plasmons differ from this picture, and why already LDA yields a balanced description of the intra- and interparticle Coulomb forces. The optical absorption spectra were calculated with linear response time dependent DFT (lr-TDDFT) as implemented in GPAW.[45] Some of the peaks in the spectra were then further analyzed using time-dependent density functional perturbation theory (TD-DFPT),[46] which allows us the solve the contributions of the Kohn−Sham (K−S) electron−hole (e−h) transitions contributing to the excitation and to calculate the induced transition density. The K−S contributions were visualized using the dipole transition contribution map (DTCM) scheme,[47,48] where the relative strengths of the contributions to the transition dipole moment from all the K−S transitions can be seen at the same time. To study the excitations with charge transfer between the two clusters, the DTCM analysis is done for light polarized parallel to the dimer axis for all the systems.

Since the clusters of the dimers are spherical, the symmetries of the superatom-like electron orbitals were identified by doing the Y_{lm} analysis,[49] where the part of the wave function inside a certain projection sphere is projected into spherical harmonics. This analysis was done separately for the two clusters in one

https://dx.doi.org/10.1021/acs.jpcc.0c02889
J. Phys. Chem. C 2020, 124, 12645−12654

dimer, summing the contributions for the projected density of states (PDOS) figures. Thus, these symmetries are the symmetries for one cluster, not the whole dimer system, where the orbitals are bonding and antibonding states of the single-cluster orbitals. Introducing the conductive pathway breaks the local spherical symmetry already at ground state level and thus allows the charge transfer excitations (also discussed in the Supporting Information, section S1).

In the simple jellium model used here, the edges of the positive uniform charge distribution were sharp. The jellium background of a linked dimer can be seen in Figure 1a. The

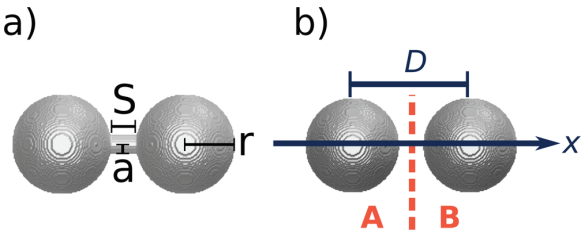

Figure 1. (a) Coupled dimer with radius of the spheres r, separation S, and radius of the linking channel a. Shown is the positive jellium background. (b) Explanation of the symbols used in eq 1. A and B are the left and right sides of the calculation box, D is the distance between the centers of the clusters, and x is the direction of the dimer axis.

radius of the clusters r, the separation between the jellium egdes S, and the radius of the cylindrical linker a are shown. The electron density experiences spill-out from the positive core, and this spill-out is relatively larger for smaller clusters. The electron densities of the studied systems along the dimer axis can be seen in Figure S1.

For the separate spheres, the density used for the positive background was approximately the density of sodium, calculated from the Wigner–Seitz radius r_{ws} = 2.08 Å. For the linked spheres, the volume of the spheres was kept the same, so the volume of the dimer was changed by the volume of the linker. Thus, the jellium density is a little smaller for the linked systems, maximum 5.6% for the 8-electron sphere system with the wider linker.

Because of the smooth jellium background, the grid spacing could be as big as 0.4 Å for the dimers of 8-electron clusters and 0.5 Å for the dimers of 138-electron clusters. The convergence of the energies relative to the grid spacing was tested. The energy of the systems was converged with the accuracy of 0.5 meV per electron. In the optical spectrum calculations, the energy cutoff was 5 eV or larger, meaning that at least all the e–h transitions with a smaller energy difference than this were included. All the spectra are plotted for light polarized along the dimer axis.

To analyze the CT nature of the excitations, we introduce the *charge transfer ratio* (CTR) which is defined in eq 1, and which can be calculated for any energy in the spectrum:

$$\mathrm{CTR} = \left| \frac{D \int_A \rho_{\mathrm{ind}}(\mathbf{r})\, \mathrm{d}\mathbf{r}}{\int_{A+B} x \rho_{\mathrm{ind}}(\mathbf{r})\, \mathrm{d}\mathbf{r}} \right| \quad (1)$$

Here ρ_{ind} is the induced transition density at the studied energy, x the coordinate on the dipole axis and D the distance between the centers of the two clusters. The calculation box is divided into two equal sides, A and B, where the division is in the middle of the gap between the clusters. See Figure 1b for a visual guide to the variables.

The denominator of eq 1 is the dipole moment of the system along the dimer axis, and the numerator is the dipole moment of a system where all the induced charge on side A is concentrated in the center of cluster A, and similarly for side B. The numerator is thus a measure of the charge separation between sides A and B, and as a result also between the two clusters. The numerator acts as normalization. The CTR compares the "CT moment", the expression in the numerator, to the dipole moment: the higher the number is, the bigger the CT nature of the excitation is. If both clusters are neutral, i.e., the electron density oscillates separately inside each cluster, the integral of the induced density on side A, and thus the CTR value, is zero. Depending on the distribution of the charges, the ratio can also be negative or greater than one, but the absolute value is the measure of the charge transfer characteristic. With these numbers we can then plot a charge transfer spectrum showing how the charge transfer characteristics of the excitations evolve as a function of energy. Further discussion on the details of the CTR is given in the Supporting Information text.

RESULTS AND DISCUSSION

The studied dimer systems are named **1**–**12**. The parameters for each system are shown in Table 1. The separations are given in terms of the radii of the systems, $r \approx 4.2$ Å for the 8-electron clusters and $R \approx 10.7$ Å for the 138-electron cluster.

Table 1. Parameters of the Studied Dimer Systems[a]

system	number of electrons	S	a (Å)
1	8 + 8	$2r$	–
2	8 + 8	$0.5r$	–
3	8 + 8	0	–
4	8 + 8	$2r$	1.0
5	8 + 8	$0.5r$	1.0
6	8 + 8	$0.5r$	2.1
7	138 + 138	$0.5R$	–
8	138 + 138	$0.25R$	–
9	138 + 138	$0.1R$	–
10	138 + 138	$0.5R$	1.0
11	138 + 138 + 2	$0.5R$	2.1
12	8 + 138	$0.25R$	–

[a] S is the separation between the jellium edges and a is the radius of the cylindrical linking channel in the case of linked dimers. $r \approx 4.2$ Å and $R \approx 10.7$ Å refer to the radii of the 8-electron and 138-electron clusters, respectively. See Figure 1a for a visual guide to the parameters.

Dimers of 8-Electron Clusters. The absorption spectra and the CTR spectra for the 8-electron cluster dimers can be seen in Figure 2. The spectra are for light polarized in the direction of the dimer axis. The CTR values are calculated at the energies of the electronic excitations seen in the oscillation strength spectra without broadening. The upper row is for separate clusters and the lower for linked.

For dimer **1** with a separation of $S/r = 2$, there is virtually no electron-cloud overlap, as can be seen from Figure S1a. The absorption spectrum is almost identical with that of a single cluster.[41] Here, the CTR is also very close to zero along the whole spectrum, indicating that there is no charge transfer between the clusters at any energies.

https://dx.doi.org/10.1021/acs.jpcc.0c02889
J. Phys. Chem. C 2020, 124, 12645–12654

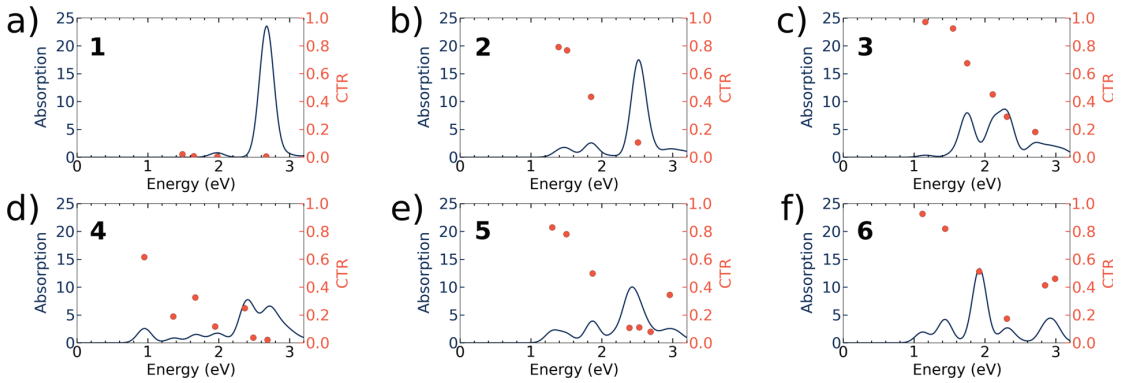

Figure 2. Absorption spectrum and the CTR for the dimers **1**−**6** with two 8-electron clusters.

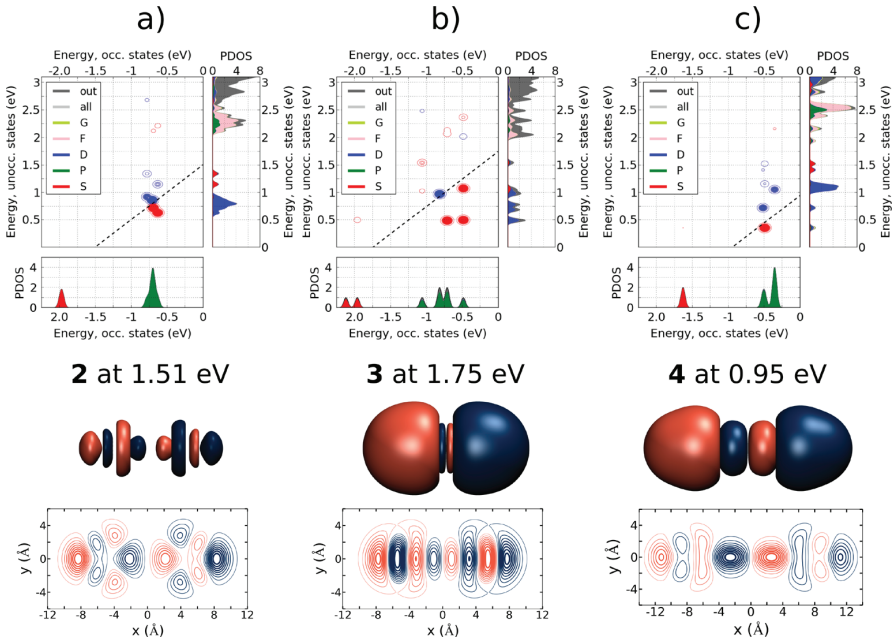

Figure 3. DTCMs and induced densities for the 2 × 8 electron dimers **2**, **3**, and **4** for one CTP peak at energies indicated in the figure. The contour plot shows the relative strength of the contributions of each e−h transition to the induced dipole moment, red indicating a positive and blue a negative contribution. The colors of the projected density of states in the DTCM figures indicate the symmetries of the orbitals, as projected for spherical harmonics. The symmetry analysis is done for both clusters separately. The dashed lines are for $E_{ex} = \epsilon_{unocc} - \epsilon_{occ}$, where E_{ex} is the energy of the excitation, ϵ_{unocc} is the energy of the unoccupied K−S state, and ϵ_{occ} is the energy of the occupied K−S state. The induced densities are visualized as isosurfaces with a certain postive and negative value of the same absolute value in the middle row. The bottom row shows a contour plot of the induced density at $z = 0$, along the dimer plane. The isosurface values are the same for each system.

When the clusters are brought closer together, however, the increasing overlap causes coupling: although the BDP peak is still clearly the strongest peak for dimer **2** with the separation-radius ratio $S/r = 0.5$, some of the strength has already been transferred to lower energies. In the absorption spectrum this is seen as a red shift of the main peak and the appearance of an extra peak at energies less than 2 eV. The lowest-energy excitations have some charge-transfer nature, as proved by the CTR analysis discussed later. For dimer **3** with touching cluster, $S/r = 0$, the shape of the spectrum is already very different from separate cluster, with two larger peaks, and a significant CTR value even near 2 eV.

Going from larger to smaller separation, we can see the transfer of oscillation strength from the BDP peak to lower energies and excitations of CT nature. The spectrum is very sensitive to even small changes of a couple of Ångströms in the separation. This can be explained by changes in the energies and shapes of the electron orbitals, and by the drastic changes in the electron density between the clusters, as seen in Figure S1, parts a and b.

We can also couple the clusters by connecting them with a conducting linker, as for dimers **4**−**6**. From Figure S1, parts d and e, we can see that some of the electron density is now located in the linker. For the systems with the narrower linker (1.0 Å), **4** and **5**, the electron density between the clusters is only moderately bigger than for the separate clusters. For dimer **6** with the stronger linker, however, the electron density

https://dx.doi.org/10.1021/acs.jpcc.0c02889
J. Phys. Chem. C 2020, 124, 12645−12654

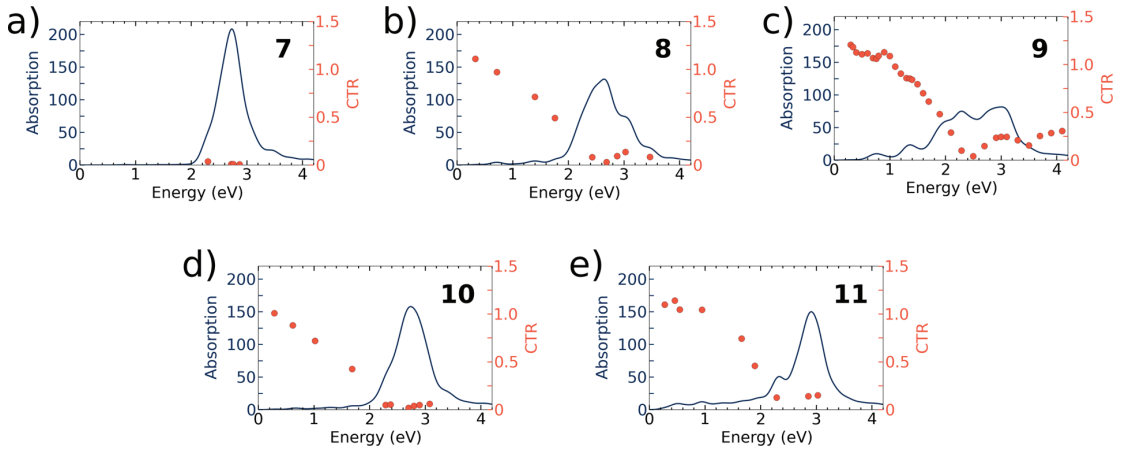

Figure 4. Absorption spectrum and the CTR for the dimers **7**−**11** with two 138-electron clusters.

in the linker is comparable to that of inside the clusters, allowing the electrons to flow freely between the two clusters.

Coupling the clusters with the separation of $S/r = 2$ even with the narrow linker, we can see a drastic change in the spectrum of dimer **4** compared to the separate clusters with the same intercluster distance, dimer **1**. For dimer **4** there is not anymore one main peak, and there are many new peaks at energies lower from the BDP peak. All the peaks below 2 eV have nonzero CTR values.

Bringing the clusters closer together, to $S/r = 0.5$, but if the linker radius is kept constant, the spectrum becomes again more compressed, and less peaks can be seen in the spectrum of dimer **5**. However, the CTR is higher for the smallest peaks for the smaller separation. If we, conversely, keep the distance constant at $S/r = 0.5$ but increase the linker width to 2.1 Å, the change in the positions of the clearest peaks is not very drastic, but the relative strengths of the peaks change, as is evident from the spectrum of dimer **6**.

For the systems **3**−**6** with a strong coupling, the BDP peak is fragmented. Also some of these fragments have some charge transfer nature, but the CTR value goes to a minimum in this energy range, indicating that the electron density oscillations happen mostly separately inside each cluster.

We will now study in more detail one absorption peak with a large CTR value for three of the systems. In Figure 3 are shown the DTCMs and the induced densities for one prominent CTP peak in systems **2**, **3**, and **4** each. In all of the systems, the induced densities of the strongest CTP resonances have a similar shape when looked at an appropriate isosurface value. Here, the isosurface value is the same for each system, which makes the weaker plasmon for system **2** appear to have a different shape.

The main contributions to the dipole moment come from P → D transitions. The coupling between the two clusters has caused some splitting in the orbitals for each system, the most in system **3** with the touching clusters. This hybridization of orbitals due to coupling is an absolute requirement for charge transfer excitations. The first 20 orbitals (1S, 1P, 1D, and 2S symmetries) for dimers **2**−**4** are visualized in Figures S1−S4. For systems **2** and **3**, the lowest-energy 1P orbital is the bonding state of the individual P orbitals, aligned in the dimer axis direction (σ orbital). This is followed by two bonding (π) and after those two antibonding (π^*) states of orbitals aligned in different directions, and finally HOMO is the antibonding state of the individual P orbitals aligned along the dimer axis (σ^*).

For the two separate dimers **2** and **3**, the HOMO−LUMO transition is one of the strongest positive contributions. LUMO in both systems is a bonding state of D orbitals, but for **2** of the D_z^2 orbitals, and for **3** of the other type of D orbitals. For **3**, another positive contribution is from P symmetry π^* to LUMO. For B, the other positive contribution is P symmetry π^* to a bonding state of D orbitals. For **3**, there is a contribution from π^* to LUMO and from HOMO to the antibonding state of 2S orbitals. Both systems have at least one screening contribution from π to antibonding states of 1D.

For the linked dimer, system **4**, the order of the 1P type orbitals is different: from lower to higher energy, the states are σ, σ^*, $2 \times \pi$, and $2 \times \pi^*$, so the orbitals with more electron density in the linker are lower in energy. Of these, the σ and σ^* orbitals are very close to each other in energy, and the π and π^* orbitals are almost degenerate. Here, the positive contribution comes from transition from the P symmetry σ^* orbital to the bonding state of the D_z^2 orbitals aligned along the dimer axis. The main negative contributions are from P type σ to the antibonding state of D_z^2 orbitals aligned along the dimer axis and from the different σ or σ^* orbitals to different D orbital states.

Dimers of 138-Electron Clusters. The absorption spectra and CTR spectra for the 138-electron cluster dimers can be seen in Figure 4. In the upper row are again separate clusters, from larger separation to smaller, and in the bottom row two linked systems with the same separation but different linker width. For these larger clusters, the density of states is bigger than for the 8-electron clusters, and thus the spectrum is more continuous, leading to clearer trends in the response of the spectrum to changes in geometry. Going to smaller separations, more and more absorption strength is transferred to smaller energies, which correspond to excitations with a large CTR. The CTR value has a minimum near the BDP peak. Linking the clusters has a similar effect, except the BDP peak is better preserved. One should notice that since the linker widths are the same here as they were for the smaller clusters, the linkers for these larger systems are relatively narrower compared to the cluster size.

https://dx.doi.org/10.1021/acs.jpcc.0c02889
J. Phys. Chem. C 2020, 124, 12645−12654

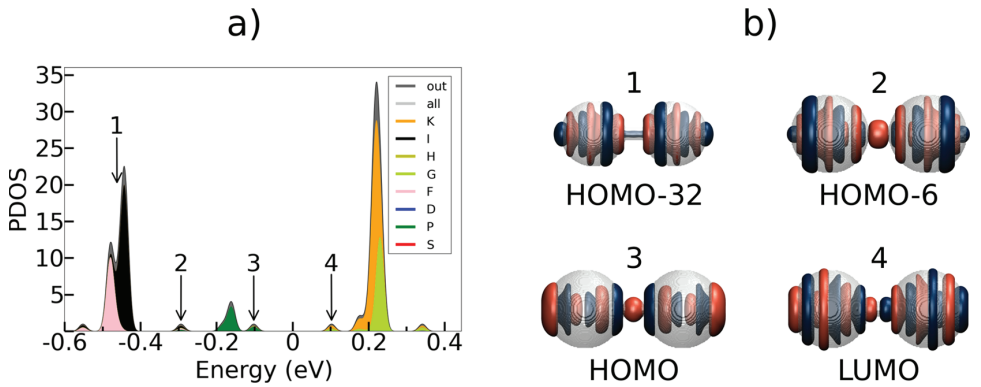

Figure 5. (a) Projected density of states near the HOMO−LUMO gap and (b) selected orbitals for dimer **11**. The arrows and numbers in part a indicate the orbitals that are shown in part b. The jellium surface of the dimer is shown in transparent.

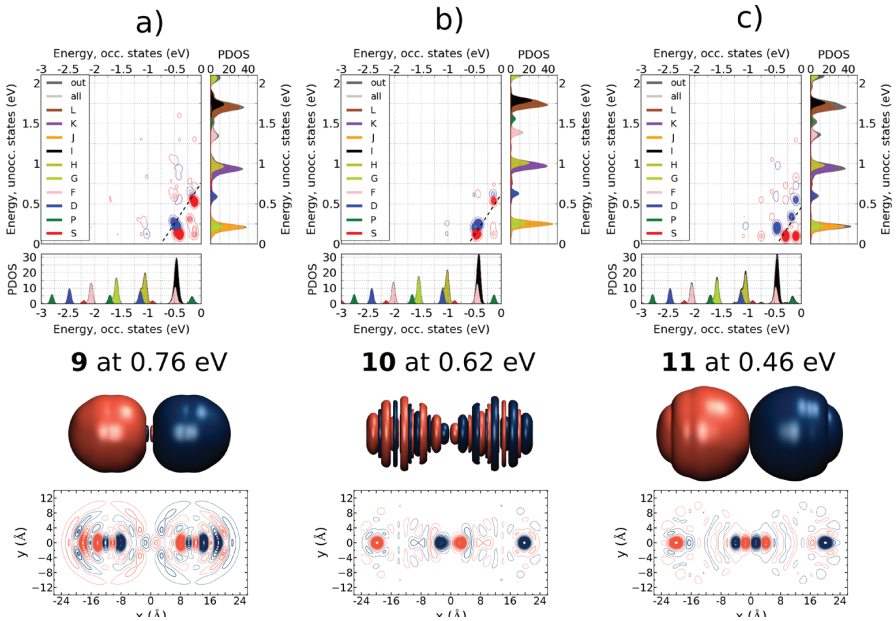

Figure 6. DTCMs and induced densities for the 2 × 138 electron dimer systems **9**, **10**, and **11** for one CTP peak at energies indicated in the figure. See the caption of Figure 3 for details.

The energies of the BDP and CTP peaks agree approximately with those obtained by Rossi et al.[29] using TDDFT for dimeric sodium systems with a total of 261 atoms. They varied the linking between the clusters in the dimer by starting from an uniform nanorod and stretching it to first form a narrow metallic bridge between two thicker ends and then finally breaking the system to two parts. The dimers with a narrow linker were found to have two CTP peaks between 0 and 1 eV and one BDP peak between 2 and 2.5 eV. The completely separate clusters supported a second BDP peak between 1 and 1.5 eV. Here, the highest CTR values are for absorption peaks below 1.5 eV, and the BDP peak, although strongly fragmented for systems **8** and **9**, is found between 2 and 3 eV. Our results are also qualitatively similar to experimental studies of dimeric silver[20] and gold nanoparticles[19,21] and covalently linked gold clusters,[22] with a CTP peak appearing at energies smaller than the BDP peak for small separations or touching or linked clusters.

If 2 × 138 electrons are placed in the potential of the positive jellium background with the wider linker (2.1 Å, the Wigner−Seitz radius used for the jellium background), the dimer is not anymore a closed-shell system, with the HOMO−LUMO gap in the middle of the 3P states. This is caused by an extra electron orbital, HOMO−32, forming between the 2G and 1I orbitals. The orbital has some G and I symmetry inside the two clusters separately, but it is clearly asymmetric inside one cluster, and symmetric only with respect to the whole system. The positive and negative isosurfaces of this orbital can be seen in Figure 5b, where it is orbital number 1. To keep all the studied systems closed-shell, we then added two electrons and calculated the properties of this system. The dimer with the wider linker studied here has thus 2 × 138 + 2 electrons, two electrons more than the rest of the bigger dimers. The order and symmetries of the electronic states stayed the same after the addition of these extra electrons.

https://dx.doi.org/10.1021/acs.jpcc.0c02889
J. Phys. Chem. C 2020, 124, 12645−12654

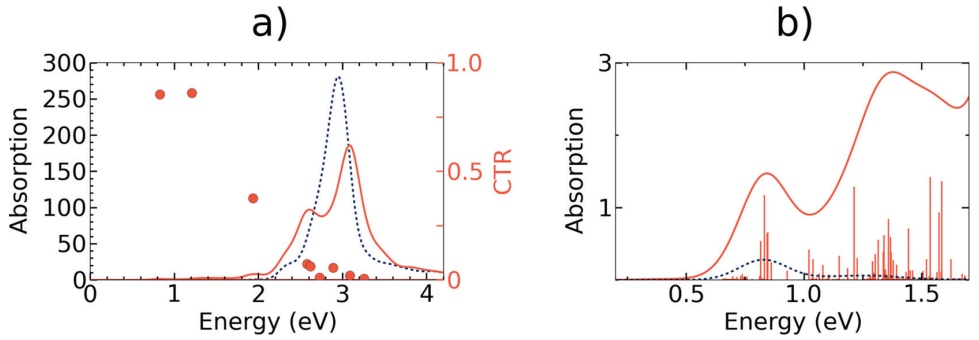

Figure 7. (a) Absorption spectrum of the dimer **12** with 8- and 138-electron clusters (solid orange line) and the summed absorption spectra of the separate clusters with 8 and 138 electrons (dashed blue line). The CTR values are for the dimer. (b) Zoom of the spectra between 0.2 and 1.8 eV, along with the oscillation strengths for the dimer.

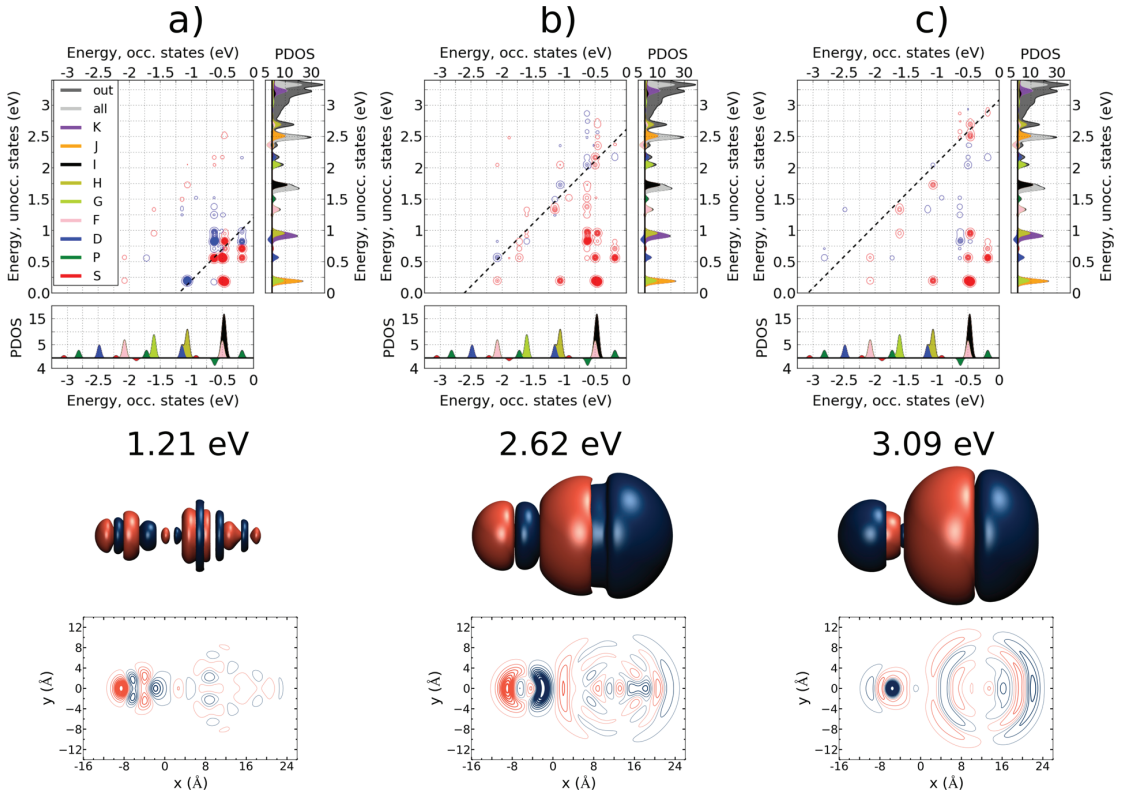

Figure 8. DTCMs and induced densities for three different peaks for the heterodimer at energies indicated in the figure. Here, the PDOS analysis is plotted separately for the smaller cluster (down) and for the larger cluster (up). See further details in the caption of Figure 3.

Closer inspection of the PDOS and the orbitals show that the orbitals aligned in the direction of the dimer axis are markedly separated in energy from the other orbitals, causing splitting in the DOS—the energy of the bonding combination of these orbitals is lowered, and the energy of the antibonding combination raised. The shapes of these orbitals are also distorted from the combination of the orbitals of two noninteracting clusters, making them quite asymmetric inside one cluster, and only symmetric regarding the whole dimer. Three of these orbitals are visualized in Figure 5, where they are labeled as 2−4. In total, there is a considerable amount of electron density in the linker, as can be seen from Figure S1k. As a result, the electrons can freely flow between the two clusters.

The DTCMs and the induced densities for one peak with a high CTR value are shown for systems **9**, **10**, and **11** in Figure 6. In the DTCM, the difference between CTP and BDP excitations is that in the former there are stronger contributions from the screening transitions. The transitions are still mainly those that are allowed for a single spherical cluster, except of the transitions of the HOMO orbitals to the LUMO in system 11. These orbitals are the ones aligned along the dimer axis and having significant electron density in the linker.

https://dx.doi.org/10.1021/acs.jpcc.0c02889
J. Phys. Chem. C 2020, 124, 12645−12654

As the CTR values in Figure 4 show, for all of the energies analyzed in Figure 6, in total one of the clusters is negatively and the other positively charged. However, there are also induced density variations inside the clusters. For the separate clusters, in system **9**, the induced density inside each cluster still somewhat resembles the induced density for the LSPR peak for a single cluster,[41] reflecting the shell structure of the electron density, which can be seen in Figure S1g–i. Here, the highest density changes are near the center of the clusters. For the linked clusters, the picture changes. For system **10**, with the narrower linker, the biggest values for the induced density along the dimer axis are found at both ends of the clusters, forming two temporary dipoles inside each cluster. For the dimer with the wider linker, system **11**, additionally an extra dipole is formed in the linker.

From the DTCMs in Figure 5 we can see that for systems **9** and **10**, the contributions come from transitions from 1I to 1K, 2F to 2G, and 3P to 3D. The main positive contributions for system **11** are from transitions from the HOMO−6 and HOMO orbitals to LUMO, as visualized in Figure 5. The strongest negative contribution comes from transitions from the 1I orbitals to 1J orbitals, although there are some clearly weaker contributions from 3P to 3D and 3P to 1J/2G transitions.

Heterodimer. The heterodimer (dimer **12**) has two clusters of different sizes: the 138-electron cluster with a radius of 10.7 Å and the 8-electron cluster with a radius of 4.2 Å. The separation between the jellium edges was 2.7 Å, which is 1/4 of the radius of the larger cluster. The electron density overlap between the clusters, as shown in Figure S1l, is similar to that of the dimer of the 138-electron clusters with the same separation, seen in Figure S1h. In Figure 7a, the spectrum of the heterodimer is plotted in orange and the sum of the spectra of the two separate clusters in blue. The CTR values are calculated for the dimer. The sides A and B of the calculation box for eq 1 are again chosen so that the division goes halfway between the jellium edges of the cluster. In the ground state, this division gives a total of eight electrons on the side of the smaller cluster, and 138 on the side of the larger cluster when integrating over the electron density. Figure 7b shows a zoom of the region between 0.2 and 1.8 eV, with the oscillation strengths for the heterodimer visible. In Figure 8 are shown the DTCMs and induced densities for the heterodimer at three energies.

The individual 138-electron cluster has its LSPR peak at 2.95 eV, and the 8-electron cluster at 2.72 eV.[41] For the heterodimer, the two largest peaks for light polarized in the dimer axis direction are found at 2.61 and 3.08 eV. The CTR value is close to zero for both of these peaks, indicating little or no charge transfer between the cluster. Also the other analyzed excitations at energies 2.6−3.1 eV have small CTR values.

For the first of the largest peaks, that is analyzed in Figure 8b, the induced density inside the smaller cluster is similar to that of the individual 8-electron cluster at the LSPR energy. From the contour plot, we can see that most of the induced density is concentrated around the smaller cluster. The main transition of the isolated smaller cluster, 1P → 1D, is contributing to the dipole moment also in this system, but many transitions inside the larger cluster are participating in the excitation too.

The shape of the induced density distribution for the largest peak is similar to the induced density of the LSPR peak for the individual 138-electron cluster. Also the main contributions to the dipole moment come from the same e-h transitions as in the single cluster. However, there are also changes in density inside the smaller cluster, and the 1P → 1D transitions have some screening contribution. Here the density oscillations inside the bigger cluster are almost symmetric, as can be seen from the contour plot of the induced density, but very asymmetric inside the smaller cluster.

The latter peak around 3 eV is clearly smaller in the heterodimer than the LSPR peak for the individual 138-electron cluster, and the peak at 2.62 eV is larger than the LSPR peak for the 8-electron cluster. A clear coupling is thus present between the clusters, and the larger cluster "borrows" some oscillation strength to the smaller one. Since the shape, the energy of the largest peak, and the maximum absorption strength of the spectrum is changing drastically from the single 138-electron cluster to the heterodimer, the larger cluster can also be thought of as a sensor, as the presence of the smaller cluster can be detected from the optical response of the system. The amplification of the main peak for the smaller cluster also helps in this detection.

The CTR values are larger for the excitations below 2 eV in energy. One of these excitations, at 1.21 eV, is analyzed in Figure 8a. At this energy, there are no excitations in the absorption spectra of the individual clusters, as can be seen from Figure 7b. For this excitation, the biggest changes in the electron density are around the smaller cluster. The induced density distribution is also quite asymmetric inside both of the clusters. The difference in the DTCM compared to the higher energy peaks is the presence of many screening transitions (blue color), one of which is the 1P → 1D transition of the smaller cluster.

■ CONCLUSIONS

We have studied the coupling of plasmons and the emergence of the charge transfer plasmon in dimers of metal clusters from the electronic perspective using the simple jellium model. Here all the systems had cylindrical symmetry, but the real-space grid based GPAW code enables the study of clusters and cluster assemblies of any kind of geometries. The high scalability of the code made possible the lr-TDDFT calculations of the systems with the larger dimers of 276 or 278 electrons, where the number of electron−hole pairs included in the calculation was approximately 90 000.

The charge transfer ratio index, calculated postprocessing from the induced densities, makes it possible to identify the excitations with the most charge transfer nature. The CTR spectra show that the excitations visible at small energies in the absorption spectra of dimers with electron cloud overlap or linking all have charge transfer nature. These transitions are not present in the spectrum of dimers with a large separation,

For the smaller clusters, the effect of the linker on the optical spectra is quite drastic. Here, the radius of the narrower linker is about 1/4, and the wider linker 1/2 of the radius of the spheres, which changes the electron density profile and the energies of the orbitals significantly from that of separate clusters with the same separation. For the larger clusters, the ratio of the radius of the linker and the radius of the sphere is about 0.20 for the wider linker. For these dimers, the shape of the spectra changes less with linking, but especially for the wider linker, a significant amount of the oscillation strength is transferred to low-energy charge transfer nature excitations. The wider linker, the radius of which corresponds to the

https://dx.doi.org/10.1021/acs.jpcc.0c02889
J. Phys. Chem. C 2020, 124, 12645−12654

Wigner−Seitz radius used for the jellium density, also enables the emergence of a new occupied K−S orbital.

One heterodimer system with an 8-electron and 138-electron cluster was also studied. The larger cluster is observed to borrow oscillation strength to the smaller, so that the LSPR peak of the larger cluster is diminished while the LSPR peak for the smaller cluster gains strength. Some excitations with charge transfer nature are also present at lower energies.

Experimental systems such as cluster dimers linked with ligands, colloidal cluster assemblies and arrays of clusters on a substrate all require knowledge of the effect of the coupling of the electronic excitations to the optical properties. The jellium linker used here can act as a simplified model for one or several conducting linker molecules, or metal atom chain between clusters, showing the trend for the absorption spectrum when conductive linker is introduced. When modeling the complex ligand-protected clusters, the results of these simple jellium clusters can help to sort the different kind of excitations and to understand the underlying principles of the electronic behavior.

■ ASSOCIATED CONTENT

Supporting Information

The Supporting Information is available free of charge at https://pubs.acs.org/doi/10.1021/acs.jpcc.0c02889.

Electron densities along the dimer axis for all the dimers, the 20 first electron orbitals for dimers **2**−**4**, a discussion about the choice of the LDA functional, and derivation of the CTR equation (PDF)

■ AUTHOR INFORMATION

Corresponding Author

Hannu Häkkinen − *Department of Physics, Nanoscience Center and Department of Chemistry, Nanoscience Center, University of Jyväskylä, FI-40014 Jyväskylä, Finland;* orcid.org/0000-0002-8558-5436; Email: hannu.j.hakkinen@jyu.fi

Authors

Elli Selenius − *Department of Physics, Nanoscience Center, University of Jyväskylä, FI-40014 Jyväskylä, Finland;* orcid.org/0000-0003-4286-0861

Sami Malola − *Department of Physics, Nanoscience Center, University of Jyväskylä, FI-40014 Jyväskylä, Finland*

Mikael Kuisma − *Department of Chemistry, Nanoscience Center, University of Jyväskylä, FI-40014 Jyväskylä, Finland*

Complete contact information is available at: https://pubs.acs.org/10.1021/acs.jpcc.0c02889

Notes

The authors declare no competing financial interest.

■ ACKNOWLEDGMENTS

This work was supported by the Academy of Finland (Grants 294217 and 319208, H.H.'s Academy Professorship, and M.K.'s Academy Postdoctoral Grant 295602) and the Emil Aaltonen Foundation (E.S.'s PhD scholarship). The computations were done at the CSC - the Finnish IT Center for Science (Project COUPLES) and in the FGCI - Finnish Grid and Cloud Infrastructure (persistent identifier urn:nbn:fi:research-infras-2016072533).

■ REFERENCES

(1) Kelly, K. L.; Coronado, E.; Zhao, L. L.; Schatz, G. C. The Optical Properties of Metal Nanoparticles: The Influence of Size, Shape, and Dielectric Environment. *J. Phys. Chem. B* **2003**, *107*, 668−677.

(2) Su, K.-H.; Wei, Q.-H.; Zhang, X.; Mock, J.; Smith, D. R.; Schultz, S. Interparticle Coupling Effects on Plasmon Resonances of Nanogold Particles. *Nano Lett.* **2003**, *3*, 1087−1090.

(3) Nie, S.; Emory, S. R. Probing Single Molecules and Single Nanoparticles by Surface-Enhanced Raman Scattering. *Science* **1997**, *275*, 1102−1106.

(4) Sönnichsen, C.; Reinhard, B. M.; Liphardt, J.; Alivisatos, A. P. A Molecular Ruler Based on Plasmon Coupling of Single Gold and Silver Nanoparticles. *Nat. Biotechnol.* **2005**, *23*, 741−745.

(5) Hirsch, L. R.; Stafford, R. J.; Bankson, J. A.; Sershen, S. R.; Rivera, B.; Price, R.; Hazle, J. D.; Halas, N. J.; West, J. L. Nanoshell-Mediated Near-Infrared Thermal Therapy of Tumors Under Magnetic Resonance Guidance. *Proc. Natl. Acad. Sci. U. S. A.* **2003**, *100*, 13549−13554.

(6) Linic, S.; Aslam, U.; Boerigter, C.; Morabito, M. Photochemical Transformations on Plasmonic Metal Nanoparticles. *Nat. Mater.* **2015**, *14*, 567−576.

(7) Guidez, E. B.; Aikens, C. M. Quantum Mechanical Origin of the Plasmon: from Molecular Systems to Nanoparticles. *Nanoscale* **2014**, *6*, 11512−11527.

(8) Li, J.-H.; Hayashi, M.; Guo, G.-Y. Plasmonic Excitations in Quantum-Sized Sodium Nanoparticles Studied by Time-Dependent Density Functional Calculations. *Phys. Rev. B: Condens. Matter Mater. Phys.* **2013**, *88*, 155437.

(9) Townsend, E.; Bryant, G. W. Which Resonances in Small Metallic Nanoparticles Are Plasmonic? *J. Opt.* **2014**, *16*, 114022.

(10) Bernadotte, S.; Evers, F.; Jacob, C. R. Plasmons in Molecules. *J. Phys. Chem. C* **2013**, *117*, 1863−1878.

(11) Casanova, D.; Matxain, J. M.; Ugalde, J. M. Plasmonic Resonances in the Al_{13}−Cluster: Quantification and Origin of Exciton Collectivity. *J. Phys. Chem. C* **2016**, *120*, 12742−12750.

(12) Bursi, L.; Calzolari, A.; Corni, S.; Molinari, E. Quantifying the Plasmonic Character of Optical Excitations in Nanostructures. *ACS Photonics* **2016**, *3*, 520−525.

(13) Zhang, R.; Bursi, L.; Cox, J. D.; Cui, Y.; Krauter, C. M.; Alabastri, A.; Manjavacas, A.; Calzolari, A.; Corni, S.; Molinari, E.; et al. How to Identify Plasmons from the Optical Response of Nanostructures. *ACS Nano* **2017**, *11*, 7321−7335.

(14) Gieseking, R. L.; Ashwell, A. P.; Ratner, M. A.; Schatz, G. C. Analytical Approaches to Identify Plasmon-Like Excited States in Bare and Ligand-Protected Metal Nanoclusters. *J. Phys. Chem. C* **2020**, *124*, 3260.

(15) Nordlander, P.; Oubre, C.; Prodan, E.; Li, K.; Stockman, M. Plasmon Hybridization in Nanoparticle Dimers. *Nano Lett.* **2004**, *4*, 899−903.

(16) Lassiter, J. B.; Aizpurua, J.; Hernandez, L. I.; Brandl, D. W.; Romero, I.; Lal, S.; Hafner, J. H.; Nordlander, P.; Halas, N. J. Close Encounters Between Two Nanoshells. *Nano Lett.* **2008**, *8*, 1212−1218.

(17) Zuloaga, J.; Prodan, E.; Nordlander, P. Quantum Description of the Plasmon Resonances of a Nanoparticle Dimer. *Nano Lett.* **2009**, *9*, 887−891.

(18) Savage, K. J.; Hawkeye, M. M.; Esteban, R.; Borisov, A. G.; Aizpurua, J.; Baumberg, J. J. Revealing the Quantum Regime in Tunnelling Plasmonics. *Nature* **2012**, *491*, 574−577.

(19) Fontana, J.; Charipar, N.; Flom, S. R.; Naciri, J.; Piqué, A.; Ratna, B. R. Rise of the Charge Transfer Plasmon: Programmable Concatenation of Conductively Linked Gold Nanorod Dimers. *ACS Photonics* **2016**, *3*, 904−911.

(20) Scholl, J. A.; García-Etxarri, A.; Koh, A. L.; Dionne, J. A. Observation of Quantum Tunneling Between Two Plasmonic Nanoparticles. *Nano Lett.* **2013**, *13*, 564−569.

(21) Su, M.-N.; Sun, Q.; Ueno, K.; Chang, W.-S.; Misawa, H.; Link, S. Optical Characterization of Gold Nanoblock Dimers: from

Capacitive Coupling to Charge Transfer Plasmons and Rod Modes. *J. Phys. Chem. C* **2018**, *122*, 18005−18011.
(22) Lahtinen, T.; Hulkko, E.; Sokołowska, K.; Tero, T.-R.; Saarnio, V.; Lindgren, J.; Pettersson, M.; Häkkinen, H.; Lehtovaara, L. Covalently Linked Multimers of Gold Nanoclusters $Au_{102}(p\text{-MBA})_{44}$ and $Au_{250}(p\text{-MBA})_n$. *Nanoscale* **2016**, *8*, 18665−18674.
(23) Jain, P. K.; Huang, W.; El-Sayed, M. A. On the Universal Scaling Behavior of the Distance Decay of Plasmon Coupling in Metal Nanoparticle Pairs: a Plasmon Ruler Equation. *Nano Lett.* **2007**, *7*, 2080−2088.
(24) Varas, A.; García-González, P.; Feist, J.; García-Vidal, F.; Rubio, A. Quantum Plasmonics: from Jellium Models to Ab Initio Calculations. *Nanophotonics* **2016**, *5*, 409−426.
(25) Zhu, W.; Esteban, R.; Borisov, A. G.; Baumberg, J. J.; Nordlander, P.; Lezec, H. J.; Aizpurua, J.; Crozier, K. B. Quantum Mechanical Effects in Plasmonic Structures with Subnanometre Gaps. *Nat. Commun.* **2016**, *7*, 1−14.
(26) Zhao, L. L.; Jensen, L.; Schatz, G. C. Surface-Enhanced Raman Scattering of Pyrazine at the Junction between Two Ag_{20} Nanoclusters. *Nano Lett.* **2006**, *6*, 1229−1234.
(27) Zhao, K.; Troparevsky, M. C.; Xiao, D.; Eguiluz, A. G.; Zhang, Z. Electronic Coupling and Optimal Gap Size Between Two Metal Nanoparticles. *Phys. Rev. Lett.* **2009**, *102*, 186804.
(28) Bae, G.-T.; Aikens, C. M. TDDFT and CIS Studies of Optical Properties of Dimers of Silver Tetrahedra. *J. Phys. Chem. A* **2012**, *116*, 8260−8269.
(29) Rossi, T. P.; Zugarramurdi, A.; Puska, M. J.; Nieminen, R. M. Quantized Evolution of the Plasmonic Response in a Stretched Nanorod. *Phys. Rev. Lett.* **2015**, *115*, 236804.
(30) Mokkath, J. H. Nanoparticle Heterodimers: The Role of Size and Interparticle Gap Distance on the Optical Response. *Chem. Phys. Lett.* **2018**, *699*, 28−31.
(31) Alkan, F.; Aikens, C. M. Understanding Plasmon Coupling in Nanoparticle Dimers Using Molecular Orbitals and Configuration Interaction. *Phys. Chem. Chem. Phys.* **2019**, *21*, 23065−23075.
(32) Xiang, H.; Zhang, M.; Zhang, X.; Lu, G. Understanding Quantum Plasmonics from Time-Dependent Orbital-Free Density Functional Theory. *J. Phys. Chem. C* **2016**, *120*, 14330−14336.
(33) Esteban, R.; Borisov, A. G.; Nordlander, P.; Aizpurua, J. Bridging Quantum and Classical Plasmonics with a Quantum-Corrected Model. *Nat. Commun.* **2013**, *3*, 1−9.
(34) Esteban, R.; Zugarramurdi, A.; Zhang, P.; Nordlander, P.; García-Vidal, F. J.; Borisov, A. G.; Aizpurua, J. A Classical Treatment of Optical Tunneling in Plasmonic Gaps: Extending the Quantum Corrected Model to Practical Situations. *Faraday Discuss.* **2015**, *178*, 151−183.
(35) Song, P.; Nordlander, P.; Gao, S. Quantum Mechanical Study of the Coupling of Plasmon Excitations to Atomic-Scale Electron Transport. *J. Chem. Phys.* **2011**, *134*, 074701.
(36) Song, P.; Meng, S.; Nordlander, P.; Gao, S. Quantum Plasmonics: Symmetry-Dependent Plasmon-Molecule Coupling and Quantized Photoconductances. *Phys. Rev. B: Condens. Matter Mater. Phys.* **2012**, *86*, 121410.
(37) Marinica, D. C.; Kazansky, A. K.; Nordlander, P.; Aizpurua, J.; Borisov, A. G. Quantum Plasmonics: Nonlinear Effects in the Field Enhancement of a Plasmonic Nanoparticle Dimer. *Nano Lett.* **2012**, *12*, 1333−1339.
(38) Aguirregabiria, G.; Marinica, D. C.; Esteban, R.; Kazansky, A. K.; Aizpurua, J.; Borisov, A. G. Role of Electron Tunneling in the Nonlinear Response of Plasmonic Nanogaps. *Phys. Rev. B: Condens. Matter Mater. Phys.* **2018**, *97*, 115430.
(39) Zhang, P.; Feist, J.; Rubio, A.; García-González, P.; García-Vidal, F. Ab Initio Nanoplasmonics: The Impact of Atomic Structure. *Phys. Rev. B: Condens. Matter Mater. Phys.* **2014**, *90*, 161407.
(40) Barbry, M.; Koval, P.; Marchesin, F.; Esteban, R.; Borisov, A. G.; Aizpurua, J.; Sánchez-Portal, D. Atomistic Near-Field Nanoplasmonics: Reaching Atomic-Scale Resolution in Nanooptics. *Nano Lett.* **2015**, *15*, 3410−3419.
(41) Selenius, E.; Malola, S.; Häkkinen, H. Analysis of Localized Surface Plasmon Resonances in Spherical Jellium Clusters and Their Assemblies. *J. Phys. Chem. C* **2017**, *121*, 27036−27052.
(42) Mortensen, J. J.; Hansen, L. B.; Jacobsen, K. W. Real-Space Grid Implementation of the Projector Augmented Wave Method. *Phys. Rev. B: Condens. Matter Mater. Phys.* **2005**, *71*, 035109.
(43) Enkovaara, J.; Rostgaard, C.; Mortensen, J. J.; Chen, J.; Dułak, M.; Ferrighi, L.; Gavnholt, J.; Glinsvad, C.; Haikola, V.; Hansen, H. A.; et al. Electronic Structure Calculations with GPAW: a Real-Space Implementation of the Projector Augmented-Wave Method. *J. Phys.: Condens. Matter* **2010**, *22*, 253202.
(44) Perdew, J. P.; Wang, Y. Accurate and Simple Analytic Representation of the Electron-Gas Correlation Energy. *Phys. Rev. B: Condens. Matter Mater. Phys.* **1992**, *45*, 13244−13249.
(45) Walter, M.; Häkkinen, H.; Lehtovaara, L.; Puska, M.; Enkovaara, J.; Rostgaard, C.; Mortensen, J. J. Time-Dependent Density-Functional Theory in the Projector Augmented-Wave Method. *J. Chem. Phys.* **2008**, *128*, 244101.
(46) Andrade, X.; Botti, S.; Marques, M. A.; Rubio, A. Time-Dependent Density Functional Theory Scheme for Efficient Calculations of Dynamic (Hyper) Polarizabilities. *J. Chem. Phys.* **2007**, *126*, 184106.
(47) Malola, S.; Lehtovaara, L.; Enkovaara, J.; Häkkinen, H. Birth of the Localized Surface Plasmon Resonance in Monolayer-Protected Gold Nanoclusters. *ACS Nano* **2013**, *7*, 10263−10270.
(48) Rossi, T. P.; Kuisma, M.; Puska, M. J.; Nieminen, R. M.; Erhart, P. Kohn−Sham Decomposition in Real-Time Time-Dependent Density-Functional Theory: an Efficient Tool for Analyzing Plasmonic Excitations. *J. Chem. Theory Comput.* **2017**, *13*, 4779−4790.
(49) Walter, M.; Akola, J.; Lopez-Acevedo, O.; Jadzinsky, P. D.; Calero, G.; Ackerson, C. J.; Whetten, R. L.; Grönbeck, H.; Häkkinen, H. A Unified View of Ligand-protected Gold Clusters as Superatom Complexes. *Proc. Natl. Acad. Sci. U. S. A.* **2008**, *105*, 9157−9162.

https://dx.doi.org/10.1021/acs.jpcc.0c02889
J. Phys. Chem. C 2020, 124, 12645−12654

Supporting information for "Charge Transfer Plasmons in Dimeric Electron Clusters"

Elli Selenius,[†] Sami Malola,[†] Mikael Kuisma,[‡] and Hannu Häkkinen[*,†,‡]

†*Department of Physics, Nanoscience Center, University of Jyväskylä, FI-40014 Jyväskylä, Finland*

‡*Department of Chemistry, Nanoscience Center, University of Jyväskylä, FI-40014 Jyväskylä, Finland*

E-mail: hannu.j.hakkinen@jyu.fi

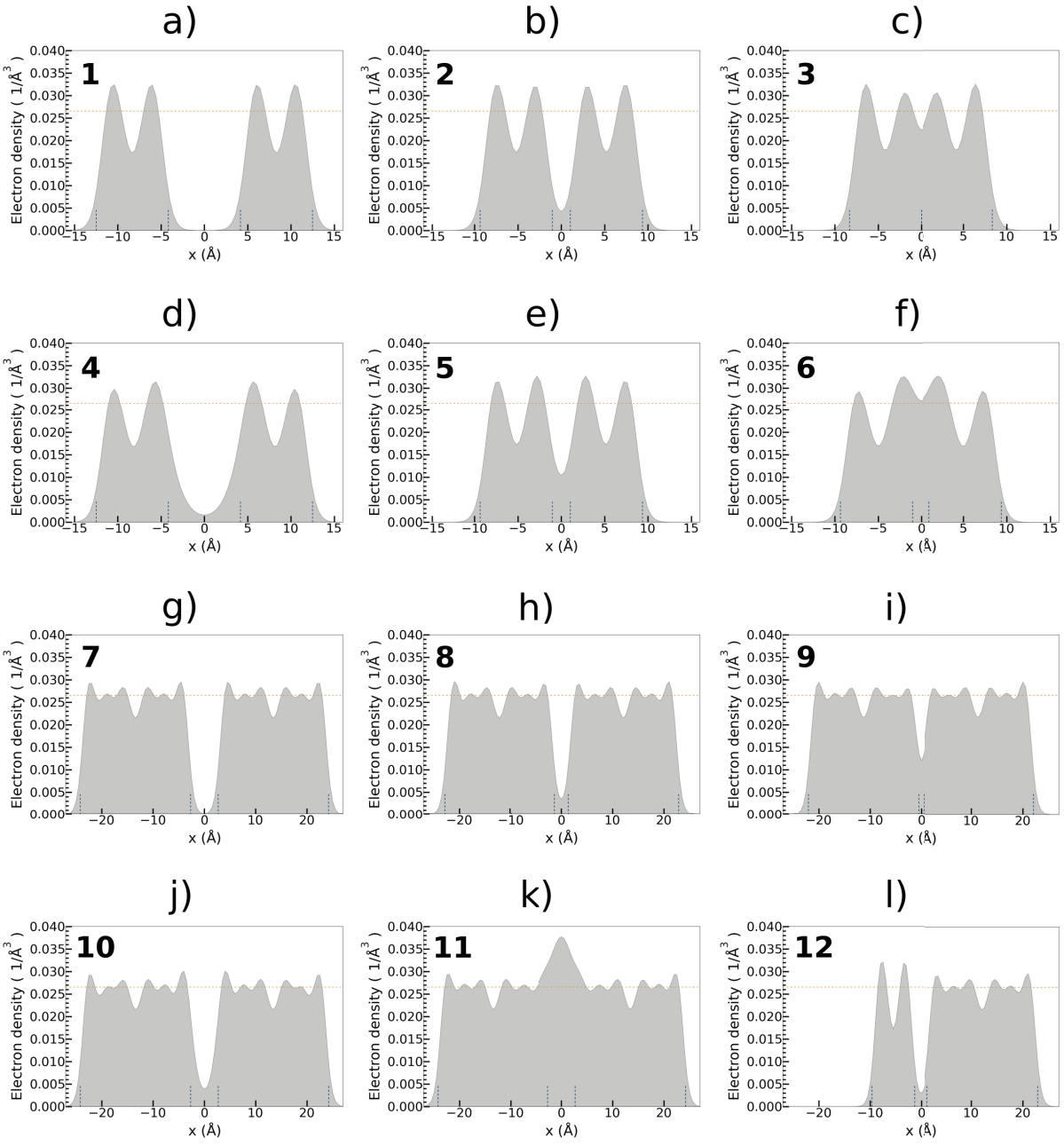

Figure S1: The electron density along the dimer axis (x axis) for dimers **1**–**12**. The horizontal dashed line shows the value of the positive jellium background density, and the short vertical lines show the edges of the jellium spheres. Note that the x axis scale is different in figures a)–f) than in figures g)–l).

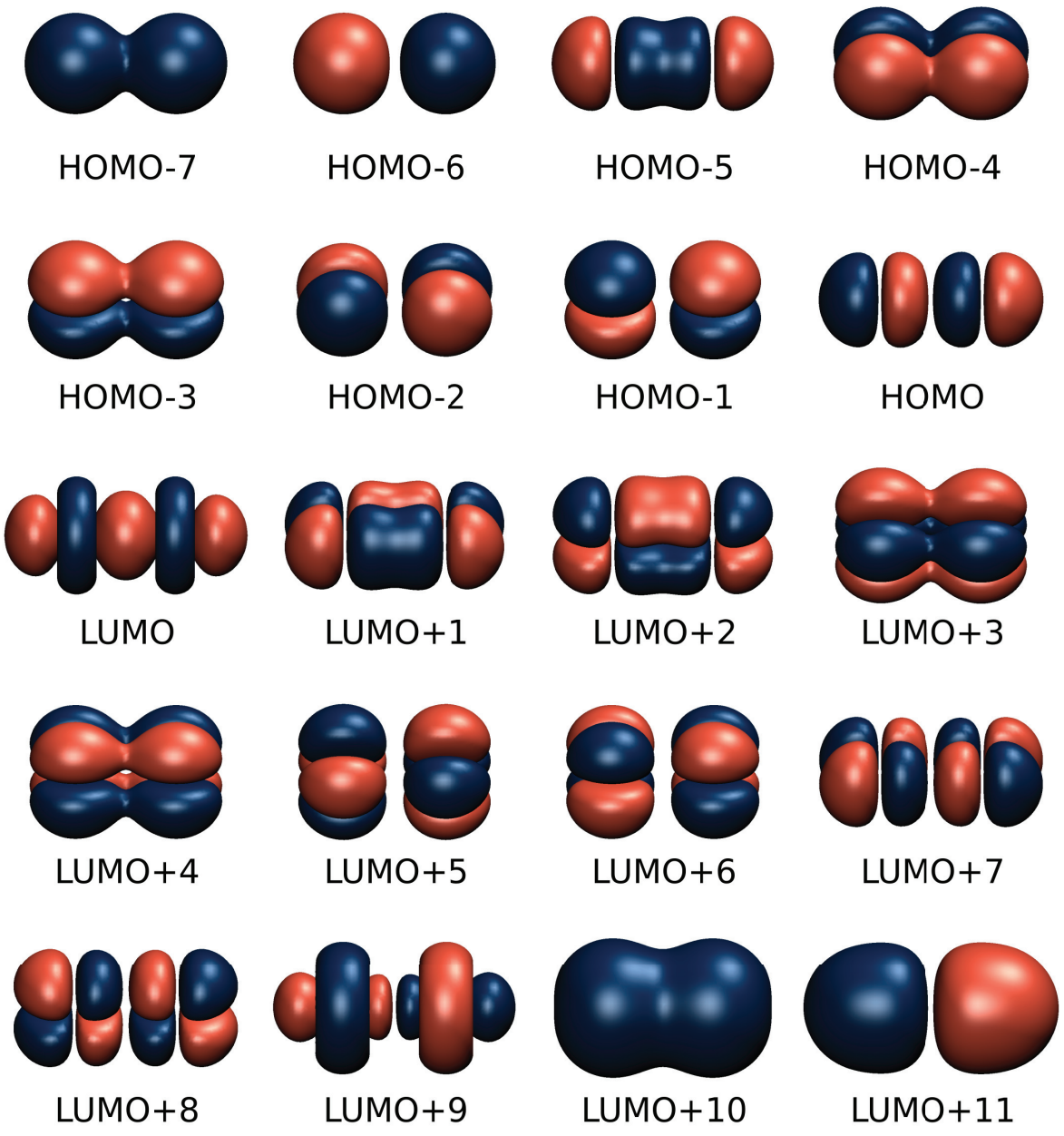

Figure S2: The 20 first Kohn-Sham electron oribitals for dimer **2**.

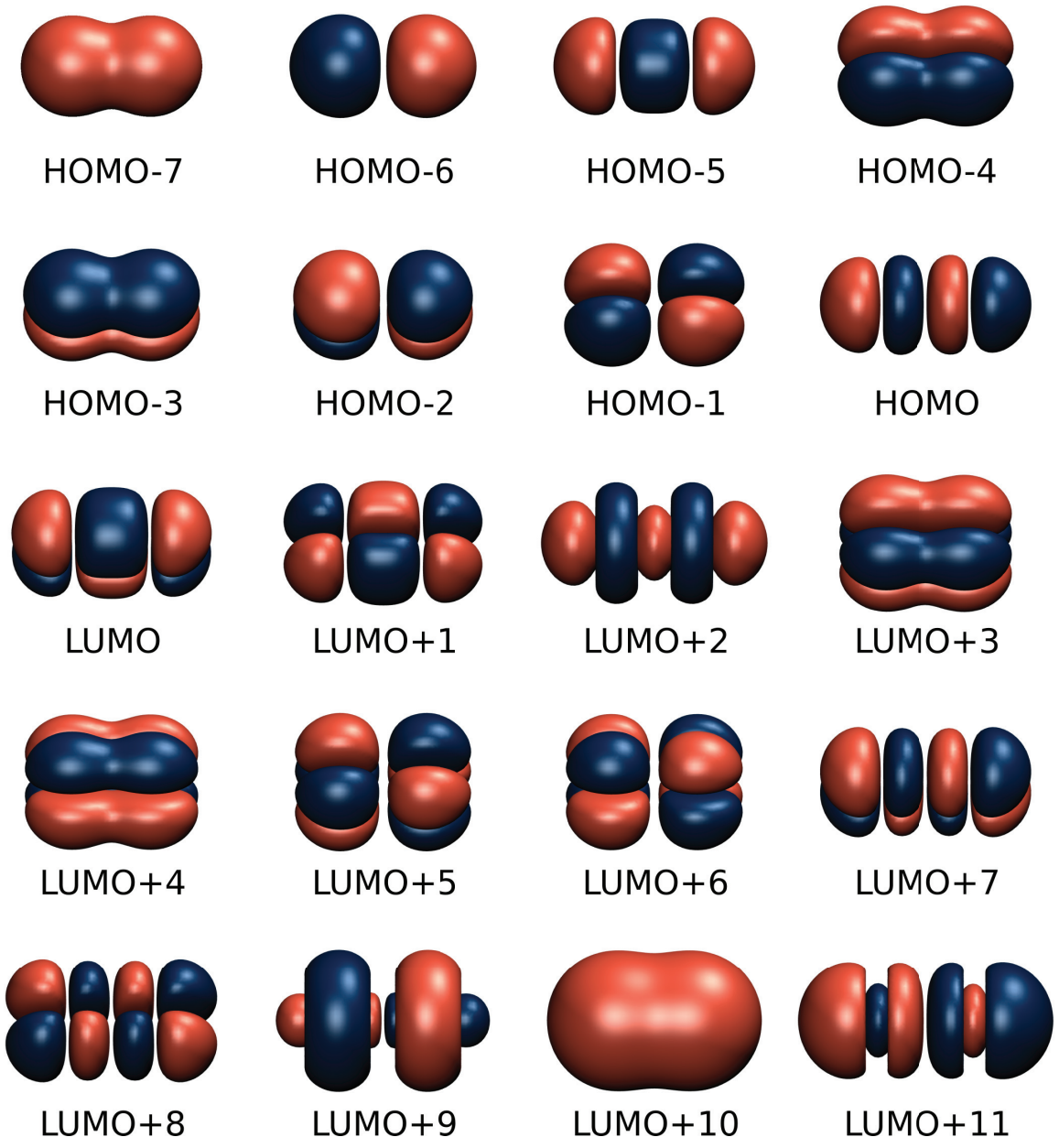

Figure S3: The 20 first Kohn-Sham electron oribitals for dimer **3**.

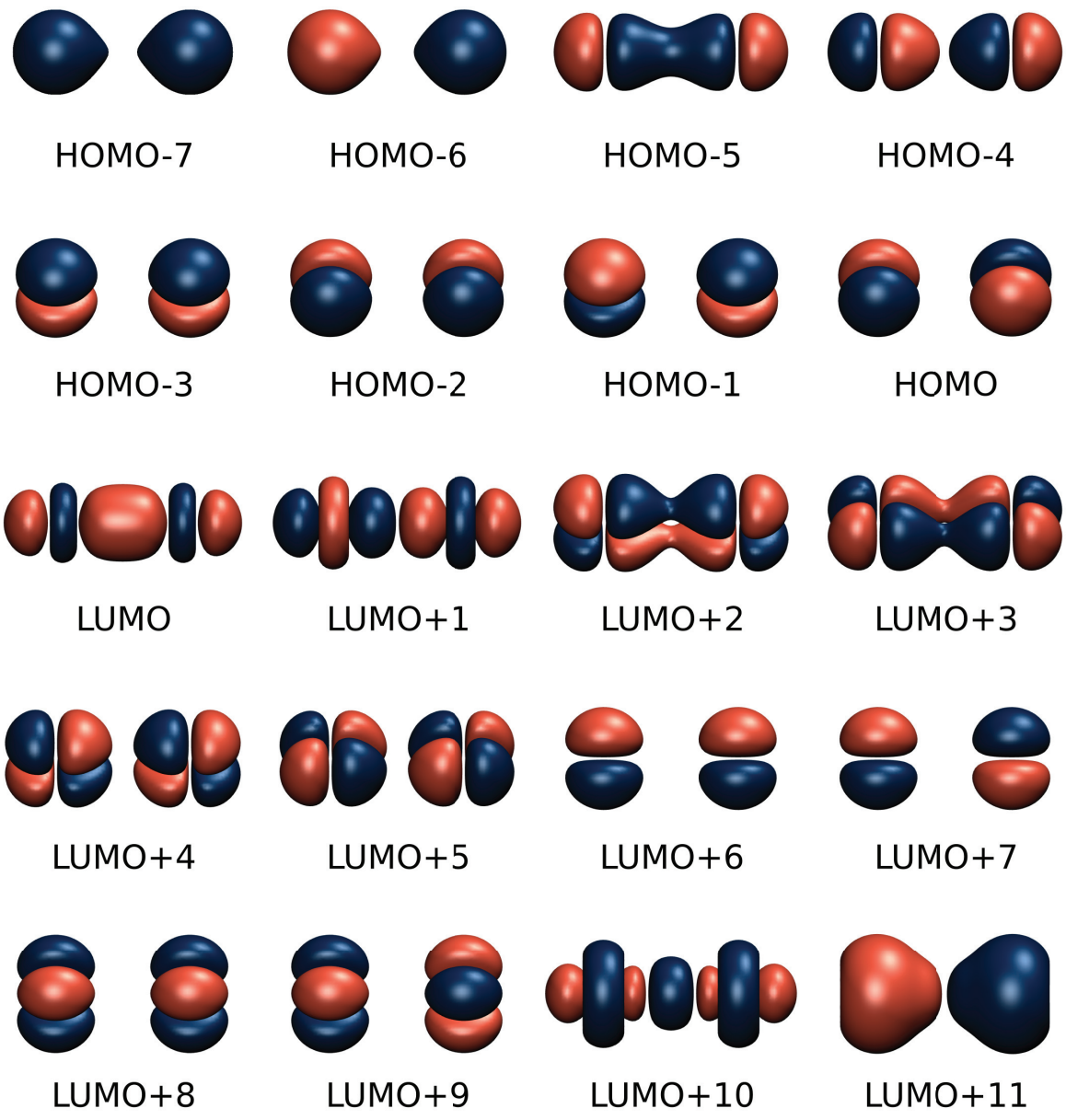

Figure S4: The 20 first Kohn-Sham electron oribitals for dimer **4**.

1. Discussion about the use of the LDA functional to study charge transfer plasmons

It is beneficial to compare plasmonic charge transfer transitions to regular charge transfer transitions of e.g. a complex. In the latter case, we would find a HOMO-orbital at cluster A (ψ_i^A) and LUMO-orbital at cluster B (ψ_a^B) with low spatial overlap. Due to insignificant common support of the wavefunctions, the induced density $\psi_i^A(r)\psi_a^B(r)$ will be negligible, and thus also the Coulomb matrix element of the induced density with itself at the Casida matrix will be negligible. In such cases the exchange-correlation kernel from LDA is unable to restore the transition, but either a hybrid functional is required, or exchange-correlation kernel which diverges.

Consider two uncoupled spherical symmetric nanoparticles (A and B) with one occupied superatomic S-orbital and one unoccupied superatomic P_z-type orbital. In uncoupled case, we are free to choose the subspace at degenerate eigenvalues. We could imagine, that the occupied subspace hybridizes into bonding and antibonding s-type orbitals, and similarly the unoccupied subspace creates bonding and antibonding states from P_z superatomic orbitals. However, any excitation from this system always conserves the charge at each subsystem.

Now we introduce coupling, i.e. some small hopping matrix elements. It is clear that these matrix elements break the spherical symmetry. The coupling to other nanocluster is at other side, and thus the hopping operator in this basis is best represented in rank-1 form with linear combination of polarized orbitals, for example as $\hat{h}^1 = (|sA\rangle + \beta|pA\rangle)t(\langle sB| - \beta\langle pB|) + h.c.$. Indeed, the coupling of these orbitals are seen as sp-hybridization i.e. the local orbitals polarize due to the coupling (effectively mixing their uncoupled elecron-hole spaces). This makes the charge transfer excitations formidable, as both the occupied and unoccupied subspaces at individual particle contain both, s and p-type excitations, which can in superposition overall create a total charge transfer excitation since $|\psi_s^A(r)|^2$ and $|\psi_p^A(r)|^2$ have a finite integral. The majority of the energy of this excitation comes from electrostatics i.e. the Coulomb matrix elements (Hartree-potential), including both the self repulsion of

charge at each cluster, and their mutual attraction. The exchange-correlation kernel matrix elements play a negligible role in this coupling.

2. Derivation of the Charge Transfer Ratio equation

The photoabsorption spectrum is closely related to dynamical polarizability

$$\alpha_{zz}(\omega) = \int \mathrm{d}\mathbf{r} \int \mathrm{d}\mathbf{r}' z z' \chi(r, r', \omega) \tag{1}$$

We may also represent this as

$$\alpha_{zz}(\omega) = \int \mathrm{d}\mathbf{r} z n_{z,\mathrm{ind}}(r, \omega), \tag{2}$$

where the induced density due to z-polarized dipolar coupling is given as[1]

$$n_{z,\mathrm{ind}}(r, \omega) = \int \mathrm{d}r' \chi(r, r', \omega) z'. \tag{3}$$

We may also evaluate another quantity from the induced density, namely the transferred charge. To this end, we need to separate the system into two regions, A and B and integrate

$$Q = \int_A \mathrm{d}r n_{\mathrm{ind}}(r) = -\int_B \mathrm{d}r n_{\mathrm{ind}}(r), \tag{4}$$

where the latter follows due to conservation of charge $\int \mathrm{d}r n_{\mathrm{ind}}(r) = 0$.

Metals have freely moving electrons, and the excess charge always moves to the surface. This is true dynamical case of plasmonic excitations also, see for example.[2] In order to proceed, we need to make one assumption. That is, that the charge centerof each volume will be at the geometric center of the nanocluster due to electrostatic repulsion of charges in metallic nanoclusters. If we utilize the geometric centers of clusters A and B (which need not to be of equal sizes) we can calculate the dipole moment of the charge transfer as $D \int_A \mathrm{d}r n_{\mathrm{ind}}(r)$, where D is the distance between the charge centers.

Due to conservation of charge, the origin of dipole operator does not matter, and we choose it to be at be at the surface separating the volumes A and B. We redefine the dipole operator

$$z = \mu_D(z) + \mu_C(z) = \underbrace{z - D\frac{\Theta(z) - \Theta(-z)}{2}}_{\mu_D(z)} + \underbrace{D\frac{\Theta(z) - \Theta(-z)}{2}}_{\mu_C(z)}. \tag{5}$$

Due to linearity of response, we can imagine Eq. 1 written as

$$\alpha_{zz}(\omega) = \int \mathrm{d}\mathbf{r} \int \mathrm{d}\mathbf{r}'(\mu_D(z) + \mu_C(z))(\mu_D(z') + \mu_C(z'))\chi(r, r', \omega) \tag{6}$$

which ultimately yields the dipole squared dependence of oscillator strength. There are total of four terms, but to keep things simple, we decompose this into two parts, keeping the dipole induced density together

$$\alpha_{zz}(\omega) = \underbrace{\int \mathrm{d}\mathbf{r}\mu_D(z)n_{\mathrm{ind}}(r, \omega)}_{X} + \underbrace{\int \mathrm{d}\mathbf{r}\mu_C(z)n_{\mathrm{ind}}(r, \omega)}_{Y} \tag{7}$$

To characterize the ratio, we compare the amount of dipole moment of charge transfer excitations, (Y) to the total dipole moment (X+Y) and finally arrive at the expression presented at article

$$\mathrm{CTR} = \left|\frac{Y}{X + Y}\right| \tag{8}$$

In Fig. S5 we present the simplest case, where the dipole moment field z has been divided with equal sizes clusters into two parts. In Fig. S6 we consider the case, where the space division is not exactly in between the geometric centres of the clusters. The situation seems unsymmetric, and the dipole field μ_D apprarently seems to contain also some charge integrating terms. However, we are free to add a constant term into any potential, due to gauge symmetry induced conservation of charge, and in Fig. S7 we have added a such constant to μ_D restoring the situation back to normal.

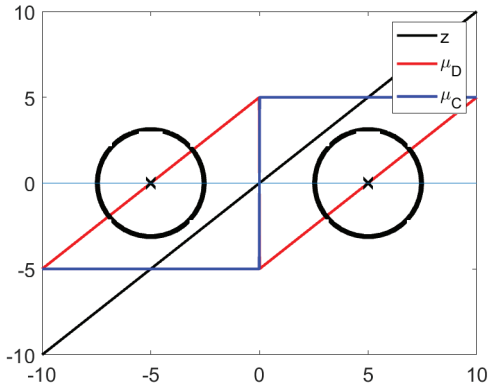

Figure S5

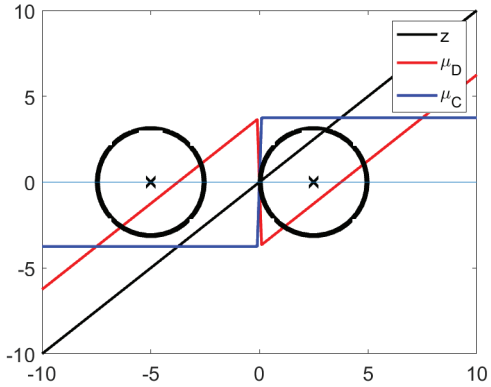

Figure S6

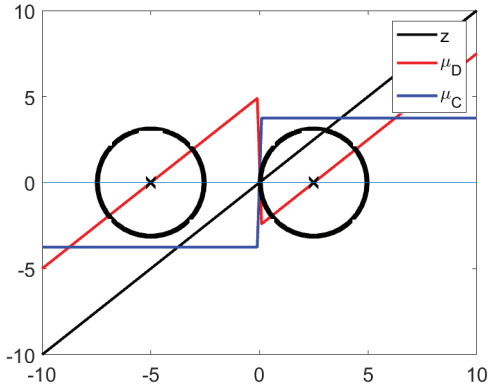

Figure S7

References

(1) Strubbe, D. A.; Lehtovaara, L.; Rubio, A.; Marques, M. A. L.; G. Louie, S. G. Response Functions in TDDFT: Concepts and Implementation. `https://digital.csic.es/bitstream/10261/95749/1/D._A._Strubbe__2011_749.pdf`

(2) Kuisma, M.; Sakko, A.; Rossi, T. P.; Larsen, A. H.; Enkovaara, J.; Lehtovaara, L.; Rantala, T. T. Localized Surface Plasmon Resonance in Silver Nanoparticles: Atomistic First-Principles Time-Dependent Density-Functional Theory Calculations. *Phys. Rev. B* **2015**, *91*, 115431

PIII

ANALYSIS OF THE PLASMONIC EXCITATIONS IN ASSEMBLIES OF THREE-DIMENSIONAL ELECTRON CLUSTERS

by

Elli Selenius, Sami Malola, Hannu Häkkinen (2020)

Physical Review B, accepted

Analysis of the Plasmonic Excitations in Assemblies of Three-Dimensional Electron Clusters

Elli Selenius and Sami Malola
Department of Physics, Nanoscience Center, University of Jyväskylä, FI-40014 Jyväskylä, Finland

Hannu Häkkinen*
Departments of Physics and Chemistry, Nanoscience Center, University of Jyväskylä, FI-40014 Jyväskylä, Finland
(Dated: November 9, 2020)

In the quest to built novel metamaterials with unique optical properties, three-dimensional assemblies of metal clusters and nanoparticles are gathering a lot of attention. Organized geometries, such as tetrahedra and icosahedra, can be built for example by using DNA strands or virus capsids as templates. Here, we use the jellium model and time-dependent density functional theory to study the plasmonic resonances in different arrangements of 8-electron clusters from the electronic perspective. A charge transfer ratio index based on the induced transition densities is used to quantify the charge transfer nature of the excitations at different energies. We vary the size, shape, and inter-cluster separation, building systems of 4-cluster tetrahedra, 12-cluster icosahedra and cuboctahedra, and 20-cluster dodecahedra. All the studied systems are found to have charge transfer plasmon type excitations at low energies. Analysis of the electron-hole transitions contributing to the transition dipole moment is further used to characterize these excitations, showing that they have significant screening contributions unlike the higher-energy excitations. The understanding gained for the optical response of these simple model systems can help in interpreting the properties of real, complex cluster systems.

I. INTRODUCTION

Since the coupling of the plasmonic excitations in adjacent metal clusters or nanoparticles (NPs) changes the optical response [1], assemblies of such clusters or NPs is a way to create materials with novel optical properties. The creation, characterization, and application of these metamaterials, such as three-dimensional (3D) assemblies or aggregates of plasmonic NPs, has received a lot of attention in recent years [2, 3].

Single metal clusters or nanoparticles can support localized surface plasmon resonances (LSPR), which are collective oscillations of the conduction electrons on the surface of the clusters. In dimers or other cluster assemblies, these plasmon peaks can couple to form a bonding combination of the individual plasmons [1]. Clusters or NPs that have a sufficiently small separation can also support charge transfer plasmons (CTP), which involve the electron density oscillating between the individual clusters [4].

Three dimensional arrangements of plasmonic NPs can be assembled for example by using DNA templates [5, 6], manipulation with atomic force microscope [7], tethering or coating the clusters with block copolymers [8–10], or using viruses or virus-like particles as templates [11–13]. The geometries achieved include among others spherical vesicles [10], tetrahedra [5–9], icosahedra [9, 11], and other arrangements with 5-fold symmetries [12, 13].

Spherical gold NPs in tetrahedral arrangements were studied theoretically by Urzhumov et al. [14] using the plasmon hybridization (PH) model [1] and finite element frequency domain calculations. They proposed the concept of *metafluids*, which are fluids containing these plasmonic metaclusters. Using the PH model and Drude theory, they found the plasmon resonance energies dependent on the separation of the clusters.

One application for these plasmonic assemblies or 'plasmonic molecules' is surface enhanced Raman scattering (SERS). Via the creation of hotspots between the plasmonic NPs, these assemblies were found to enhance the signal compared to single NPs [8, 10, 12, 13]. Pazos-Perez et al. fabricated several 2D and 3D geometries of block copolymer-protected Au NPs using evaporation of emulsion droplets [8]. The NPs in the arrangements had a diameter of approximately 50 nm and inter-particle separations of around 2 nm. A big jump in the SERS enhancement was observed going from planar geometries to the tetrahedron. In the case of the plasmonic vesicles, Huang at al. manufactured structures of several hundreds of nanometers using different block copolymers as ligands and and gold NPs with diameters of 20, 50, and 80 nm [10]. The assembly of the NPs was also achieved by subsequent emulsification and evaporation, and the separations between clusters varied from 0.5 nm for the largest clusters to 11.6 nm for some of the vesicles of the smallest clusters. They measured the largest enhancements for the largest used Au NPs, proposing that this might be due to the smallest inter-cluster separations in these structures.

Arrangements of plasmonic nanoclusters can also be used in light-assisted drug delivery [15]. The release of cargo can be achieved for example by embedding metal NPs in the outer layers of microcapsules [16] or coating

* hannu.j.hakkinen@jyu.fi

loaded liposomes with metal NPs [17]. In these techniques, the plasmon resonance of the metal NPs is used to convert light into thermal energy, damaging the capsule or liposome and allowing the material inside to exit.

In addition to larger nanoparticles, assemblies can also be built of atomically precise clusters. Nonappa et al. have fabricated spherical, hollow capsids with a diameter of around 200 nm consisting of Au_{102}-pMBA$_{44}$ (pMBA = p-mercaptobenzoic acid) clusters [18]. The self-assembly of the clusters in a water-methanol mixture seems to be guided by the balance of protonated and deprotonated carboxylic acids in the ligands. Marjomäki et al. used Au_{102}-pMBA$_{44}$ clusters to coat enteroviruses with tens of clusters [19]. The clusters were functionalized with maleimide linkers to attach to specific sites in the virus capsid. In the study the clusters were used as labels for transmission electron microscopy, but the authors suggested also using the geometry- and separation-dependent optical properties of the clusters for spectroscopy of the viruses and manipulation of the virus capsid by electromagnetic radiation. The clusters used in these two studies were not plasmonic, but similar techniques could be used to built plasmonic cluster assemblies.

To understand the plasmonic coupling and the optical properties in different cluster assemblies from the electronic perspective, we use the jellium model and density functional theory (DFT) to study geometric arrangements of 8-electron clusters with a tetrahedral, icosahedral, cuboctahedral, and dodecahedral shape. We have previously studied the LSPR in single clusters and bonding dipolar plasmons (BDP) in planar assemblies [20] and CTPs in dimers [21] using the same methods. The simple jellium model enables us to concentrate on the electronic response and to handle large systems with lower computational cost than with fully atomistic models. In addition, we have seen that assemblies of even the small 8-electron jellium clusters can support collective excitations such as CTPs and bonding combinations of the LSPRs.

Since there is a spherical shell-closing for 8 electrons in the jellium model, we use a positive background in the shape of a sphere for the clusters. This spherical symmetry of the individual clusters also simplifies the analysis of the different cluster assemblies, making it easier to observe the effect of the geometry of the arrangement. For real clusters, the atomic structure obviously prevents the shape of the 8-electron sodium cluster from being exactly spherical. In atomistic *ab initio* calculations, Na_8 is found to prefer a shape with the T_d point group, higher in symmetry than the neighbouring cluster sizes [22, 23].

Zhang et al. have showed that for dimers of sodium clusters with about 300 atoms, the atomic structure affects the exact energies of the main absorption peaks and the maximum separation at which the CTP peak is manifested [24]. However, the main trends for the absorption spectra were reproduced also by the jellium model. The shape of Na_8 differs more from a sphere than the shape of these larger clusters, but we can still expect that the jellium assemblies can qualitatively reproduce results of the corresponding atomic systems.

Classical simulations have been previously performed for three-dimensional cluster arrangements with clusters the size of tens of nanometers [5, 7–10, 12, 14]. Unlike the LSPR-based plasmons, the tunneling CTPs present at small separations cannot be modeled using classical approaches [4]. Since our methods and systems allow us to reach the CTP region, we will focus more on these less studied excitations.

The analyzed cluster assemblies have been chosen to be shell-like or capsid-like to mimic the experimental set-ups with capsids of clusters or clusters or NPs arranged on a virus. In the experiments thus far, either the capsid or the NPs have mostly been far bigger than the systems studied here. However, our jellium systems serve as smaller-scale models to study the optical phenomena of cluster systems with subnanometer gaps in detail, using the methods and tools that we have already developed for these jellium clusters. In the future, our analysis can help to interpret the more complex optical responses of real, atomistic cluster systems.

II. THEORY AND METHODS

The studied systems consist of spherical 8-electron clusters, arranged in a hollow capsid-like formation. Tetrahedral, icosahedral, cuboctahedral, and dodecahedral symmetry were used, with 4, 12, 12, and 20 clusters, respectively. The clusters were placed on the vertices of these shapes. The density of sodium was used for the jellium background, resulting in a radius of $r = 4.1\,\text{Å}$ for one cluster. The largest system, dodecahedron, had an inter-cluster separation of $S = 1.0\,\text{Å} = 0.25r$. For the other geometries, two different separations were used: $S = 1.0\,\text{Å}$ and $S = 2.1\,\text{Å} = 0.5r$. The jellium systems can be seen in figure 1.

The DFT calculations were performed with the real-space grid GPAW program [25, 26], which allowed us to easily construct the systems. Because of the uniform background, the LDA functional [27] was chosen for the exchange-correlation. In the case of charge transfer between clusters, LDA can reproduce also charge transfer plasmons (see the supporting information of [21]). The optical spectrum was calculated using the linear response time-dependent DFT (lr-TDDFT) as implemented in GPAW [28].

In GPAW, the jellium background is constructed by assigning the positive background charge to certain gridpoints. For the spherical jellium clusters, these are the gridpoints with coordinates $\mathbf{r}$ for which

$$|\mathbf{r} - \mathbf{R_0}|^2 < N^{1/3} r_s, \tag{1}$$

where $\mathbf{R_0}$ is the center of the cluster, N is the number of electrons of the cluster, and r_s is the Wigner-Seitz radius of sodium. We used the value $r_s = 2.08\,\text{Å}$. Since

the charge is divided uniformly, inside the jellium spheres the background density is approximately

$$\rho_J = \left(\frac{4}{3}\pi r_s^3\right)^{-1} \approx 0.0265\,\text{Å}^{-3}. \quad (2)$$

This positive density is then added to the electron density when calculating the Hartree potential, which contains the Coulombic repulsion and attraction of the charges. The self-consistently calculated electron density is not uniform, but experiences oscillations and spill-out from the positive background.

To illustrate the extent of this spill-out of electrons and the electron density overlap for adjacent clusters, the electron density along x axis for a single cluster and dimer are shown in gray in figure 2. The uniform positive background density ρ_J is indicated with a dashed line. The dimer has a separation of $S = 0.25r$. The electron density for a dimer of a separation of $S = 0.5r$ can be seen in the supporting information of reference [21], where the effect of the electron density overlap on the CTPs is discussed for dimers. Figure 2 (a) shows that the electron density tail extends about 2 Å outside of the jellium surface. For clusters with a separation of $S = 0.25r = 1.0$ Å, there is significant electron density between the clusters, as can be seen from figure 2 (b). For the separation of $S = 0.5r = 2.1$ Å, the electron density overlap is smaller but non-negligible.

The calculations were performed at 0 K in vacuum, and a minimum of approximately 8 Å of empty space was left between the jellium edges and the edge of the calculation box. Because of the uniform jellium background, a relatively large grid-spacing of $h = 0.4$ Å was employed. Testing the convergence with respect to the grid-spacing,

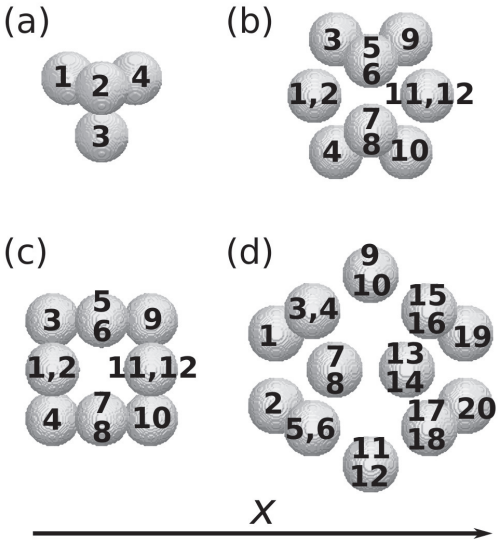

FIG. 1. The jellium backgrounds for the studied geometries: (a) tetrahedron, (b) icosahedron, (c) cuboctahedron, and (d) dodecahedron. The clusters are numbered for further reference. The direction of the optical analysis (x) is indicated.

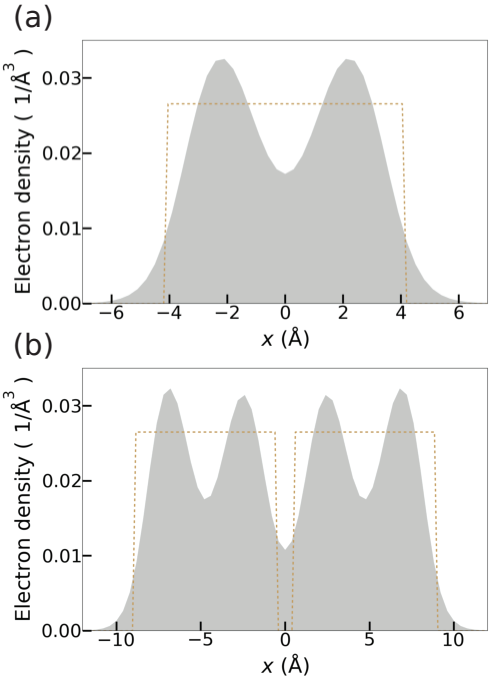

FIG. 2. The electron density (in gray) along the x axis for (a) a single 8-electron cluster and (b) a dimer of two 8-electron clusters with a separation of $S = 0.25r$. The x axis is the dimer axis. The positive jellium background density is indicated with a dashed line.

the spectrum of one of the tetrahedral systems was found to be the same for $h = 0.3$ Å and $h = 0.4$ Å. For the optical spectrum calculation, the used energy cut-off was 7 eV for the tetrahedra, 6 eV for the icosahedra and cuboctahedra, and 5 eV for the dodecahedron.

Selected peaks of the spectra were also further analyzed using the time-dependent density functional perturbation theory (TD-DFPT) [29], where the system is excited with a cosinoidal laser pulse. This allows us to separate the contributions from different Kohn-Sham electron-hole transitions to the transition dipole moment and also to calculate the induced density. Here we use a laser pulse polarized in the x direction, as indicated in figure 1. We visualized these contributions employing the dipole transition contribution map (DTCM) scheme [30, 31]. This was combined with the Y_{lm} analysis [32], where the Kohn-Sham orbitals of the clusters are projected into spherical harmonics to show the superatomic symmetries. This analysis was done for each spherical 8-electron cluster separately, and the contributions were summed for the total system.

To have a quantitative measure of the charge transfer character of an excitation, we have employed an index, the Charge Transfer Ratio (CTR). In our previous study of dimeric systems [21], we employed a similar index which was calculated using the dipole moment of the charge transfer and the induced dipole moment of the system. Now, due to the more complicated symmetries of

the systems, we employ a new way to calculate a similar index. We want to compare the ratio of the total induced charge momentarily transferred between clusters at the studied excitation energy to the total induced charge oscillating in the whole system.

Due to symmetry, the clusters that have a center at the $x = 0$ plane have a total of zero induced charge, and the clusters at the left (right) have all either a positive or negative charge. Thus, we can have a measure of the total charge transfer between clusters by summing the induced charge for all the clusters on the left. To normalize, we divide by the total positive induced charge in the whole system, or half of the integral of the absolute value of the induced density. Let us use the index i for the clusters in one system, and divide the calculation box to the left and right sides. Now we can write the CTR index as

$$\mathrm{CTR} = \frac{|\sum_{i \text{ in left}} \int_{\text{cluster } i} \rho_{ind}(\mathbf{r})\, d\mathbf{r}|}{\int_{\text{all}} |\rho_{ind}(\mathbf{r})|/2\, d\mathbf{r}}, \qquad (3)$$

where $\rho_{ind}(\mathbf{r})$ is the induced density and the summation goes over all the clusters on the left side of the system. For example for the icosahedron visualized in figure 1 (b), these clusters are numbered 1–4. The integral in the numerator is performed over the volume assigned for each cluster. The division of the space between the clusters is done by using a Wigner-Seitz type definition, assigning each grid point to the cluster that it is closest to. In the integration in the denominator, we integrate over the whole calculation cell.

If the CTR index is zero, the charge oscillations are only happening inside the clusters, and no net charge is transferred between different clusters. The maximum value of the index is one, which would mean that all the induced density oscillations happen between clusters. The absolute value in the numerator makes sure that the index is always positive, since the magnitude is the measurement of the amount of charge transfer between clusters.

III. RESULTS

A. Binding energies and HOMO-LUMO gaps

The binding energies E_b per cluster and the HOMO-LUMO (H-L) gaps for the different shapes and separations are listed in table I, as are the abbreviations given to each system. The values for two systems of dimers consisting of the same 8-electron clusters are also included for comparison. The binding energy for the cluster arrangement is calculated as $E_b = M \cdot E_{single} - E_{sys}$, where M is the number of clusters in the arrangement, E_{single} the energy of the single cluster, and E_{sys} the ground-state energy of the cluster system.

We can see that all the system have relatively large H-L gaps close to 1 eV, as a consequence of the magic nature of the spherical 8-electron cluster. A single, isolated cluster has a H-L gap of 1.50 eV. The H-L gaps and binding energies per cluster are quite similar for the different geometries. The arrangements with 12 clusters have stronger binding energies per cluster than the systems with other sizes, with the icosahedra having the biggest energies for both separations. This trend in the binding energies follows the number of nearest-neighbor interactions per cluster in the different geometries, the tetrahedra and dodecahedra having three, the cuboctahedra four, and the icosahedra five nearest-neighbors for each cluster.

TABLE I. The binding energy per cluster and HOMO-LUMO gap for all the studied systems in units of eV. The abbreviations used in the text are also shown. The values for two dimer systems consisting of spherical 8-electron clusters are included for comparison.

abbr.	shape	S/r	E_b/cluster	H-L gap
Th1	tetrahedron	0.5	0.073	1.17
Th2	tetrahedron	0.25	0.19	0.98
Ih1	icosahedron	0.5	0.12	1.11
Ih2	icosahedron	0.25	0.32	0.82
Ch1	cuboctahedron	0.5	0.098	1.12
Ch2	cuboctahedron	0.25	0.26	0.80
Dh	dodecahedron	0.25	0.20	0.92
-	dimer	0.5	0.023	1.27
-	dimer	0.25	0.066	1.13

Decreasing the separation between the clusters from $S/r = 0.5$ to $S/r = 0.25$ has the same trend for each three-dimensional shape: the binding energy per cluster increases by 0.12–0.20 eV, and the H-L gap decreases by 0.19–0.32 eV. The changes in the H-L gap can be explained by the further hybridization and subsequent splitting of the electron orbitals of the individual clusters when the clusters are brought closer together.

B. Absorption spectra and CTR values

The absorption spectra and the CTR values for all the systems are shown in figure 3. The absorption strengths have been normalized by dividing by the number of clusters for each system. The spectrum of a single 8-electron cluster is shown for comparison. The clusters on the left side of the cluster arrangement, included in the CTR calculations using equation 3, are 1 for the tetrahedra, 1-4 for the icosahedra, 1-4 for the cuboctahedra, and 1-8 for the dodecahedron, using the numbering from figure 1.

The spectra shown are the average for light polarized in x-, y- and z-directions. The cluster arrangements are highly symmetric, and the spectra were checked to be almost identical for all the directions. The same has been observed for the scattering spectra of tetrahedral and icosahedral superclusters of larger nanoparticles both experimentally and computationally [9].

For the larger separation, the *Ih1* in panel (f) and *Ch1* in panel (g) both have one relatively sharp main peak at the energies 2.61 eV and 2.62 eV, respectively. This peak

is, however, broader than and slightly red-shifted from the LSPR peak of the single 8-electron cluster, at 2.72 eV, as seen in panel (h). The red-shift and broadening of the plasmon peak in the absorption spectra has been also observed in experiments of plasmonic NP arrangements [10–13]. The spectrum of *Th1*, however, supports a broad peak at 2.75 eV with a shoulder at approximately 2.5 eV. This is because, on average, the clusters in the tetrahedral arrangement are closer to each other than in the other geometries, which have a larger empty space in the middle. For all the cluster arrangements, the spectrum has a low-energy tail that is absent for the single sphere.

We can observe that going from the larger separation to the smaller, the main peak broadens and absorption strength is transferred to smaller energies, as has been seen also for the dimer systems [21]. This is clearer for the icosahedral and cuboctahedral symmetries, that support quite a narrow peak for $S/r = 0.5$, than for the tetrahedra. In these systems, we can see that the optical spectra change drastically with respect to changes in the inter-cluster separation. For $S/r = 0.25$, the highest peak appears at slightly higher energies than for $S/r = 0.5$ for all the geometries.

Comparing the two different geometries with the same number of clusters, icosahedron and cuboctahedron, we can see that the spectra are very similar for the larger separation. For $S/r = 0.25$, the spectra, while still similar, differ somewhat in the details. One explanation is the splitting of the orbitals, which is similar for *Ch1* and *Ih1*, but larger for *Ch2* than for *Ih2*, as seen in figures 4 and 5. The larger splitting can be explained by the lower symmetry of the cuboctahedral shape.

Following the CTR analysis, we can see that all the systems have high CTR values at low energies, approximately up to 2 eV. The CTR index reaches its minimum at about 3 eV, approximately the energy of the higher-energy shoulder of the main peak. This indicates that the low-energy excitations have a high charge transfer character, and the largest peak and its shoulder are a result of charge oscillations inside each cluster separately.

The increase in the CTR values going from the larger separation to the smaller are not very high, with *Ch1* even having one higher CTR values than *Ch2*. However, for the tetrahedra and the icosahedra, the highest CTR value for $S/r = 0.25$ is larger than for $S/r = 0.5$, and appears at higher energies. For all the studied systems with two different separations, the CTR values diminish faster when going to bigger energies for the larger separation, which can be seen for example from the data points near 2 eV in figure 3.

C. Analysis of the absorption peaks

In figure 4 we show the DTCMs and induced transition densities for three selected excitations for both of the icosahedral clusters. The main trends with respect to the energy of the excitations are representative also of the three other geometries. The analysis was made for light polarized in x direction. The contour plot shows the relative strengths of the positive (red) and negative (blue) contributions to the dipole moment. The dashed line marks e-h transitions from initial K-S state i to final state f, with energies ϵ_i and ϵ_f, respectively, for which the energy of the excitation is $E = \epsilon_f - \epsilon_i$.

The low-energy excitations shown in figures 4 (a), (b), (d), and (e) have a high CTR value, the highest for *Ih1* being the one at 1.57 eV and for *Ih2* the one at 1.84 eV. The isosurfaces of the induced densities show that the induced charge distributions inside one cluster are different on the left and on the right side of the arrangement, clusters on the left being more positively charged. From the DTCMs we can see that the contributions to these excitations below 2 eV are mainly from transitions from the 1P orbitals to the 1D orbitals.

The higher-energy excitations, at 2.61 eV and 2.66 eV, correspond to the largest peak and have a low CTR value. From the induced density figures we can see that these excitations correspond to the electronic charge oscillating inside each cluster separately in-phase. These features indicate that these peaks are bonding combinations of the LSPR peaks. In addition to the 1P→1D transitions, there are also some appreciable contributions from 1P→2S.

The other clear difference between the high- and low-CTR excitations is the ratio of positive and negative contributions to the dipole moment. The percentage of the total strength from the negative contributions of the total strength from all the contributions is largest for the lowest-energy excitations and decreases with increasing energy at least until about 2.5 eV. This percentage for *Ih1* is 34 %, 31 %, and 6 %, for the peaks shown in figures 4 (a), 4 (b), and 4 (c), respectively. Similarly, for *Ih2*, the percentages are 35 % for the peak in 4 (d), 30 % for 4 (e), and 8 % for 4 (f). Thus, the low-energy excitations exhibiting a large CTR have relatively more contributions from screening transitions than the excitations close to the original LSPR peak. These transitions contributing negatively lie mostly on the $E = \epsilon_f - \epsilon_i$ line, meaning that the energy of the transitions is approximately the energy of the whole excitation. In contrast, the strongest positive excitations lie mostly below this line.

The DTCMs and induced densities for the peak with the highest CTR value for the rest of the systems with $S/r = 0.25r$, *Th2*, *Ch2*, and *Dh2*, can be seen in figure 5. The features are similar to those for the peaks with highest CTR values for the icosahedral systems. The cuboctahedron, which has the most splitting in the 1P orbitals of all the geometries, has consequently the biggest spread of energy differences $\epsilon_f - \epsilon_i$ in the contributing e-h transitions. The largest splitting can be explained by the cuboctahedron having lower symmetry than the icosahedron and the dodecahedron, and having more clusters than the tetrahedron.

We can see strong negative contributions approximately on the $E = \epsilon_f - \epsilon_i$ line also for all the excitations

in figure 5. The percentages of the negative e-h contributions are 29 % for the excitation in figure 5 (a), 26 % for (b), and 30 % for (c). The induced densities again show that the temporary induced charge distributions are not symmetric with respect to all the single clusters, only with respect to the whole arrangement. These features are similar to those for the CTP excitations for dimers of the 8-electron clusters with separations of $S/r = 0.5r$ and $S/r = 0$ [21], which also appear in the same energy range between approximately 1.5 and 2 eV. Using the same terminology, the excitations seen in figures 4 (a), (b), (d), and (e), and 5 can also be classified as CTPs.

IV. SUMMARY AND CONCLUSIONS

We have studied the plasmonic excitations in geometric assemblies of 8-electron jellium clusters using lr-TDDFT. We have also calculated the CTR index, a measure of the charge transfer nature of the excitations, at different excitation energies for each cluster. With the studied separations of approximately one or two Ångströms, even a one Ångström change can have a big effect on the spectra. However, we found excitations with CTP character at low energies for both separations.

For all the studied geometries, we see the same trends in the optical response. The two arrangements with the same number of clusters but different geometries, icosahedron and cuboctahedron, have very similar spectra especially for the longer separation. In addition, all the clusters support one larger bonding plasmon peak (in some cases with a shoulder), and one or several CTP peaks at lower energies.

The different nature of the excitations can be also seen in the DTCM analysis: for the peaks with significant charge transfer nature, the e-h transitions contributing to the transition dipole moment are mainly from 1P to 1D, and they involve transitions with strong negative contributions. The plasmon peaks at higher energies, on the other hand, are formed mainly from positively contributing transitions, and include also $1P \rightarrow 2S$ contributions.

The combination of the GPAW code and the simple jellium model lends itself readily to the study of different cluster arrangements. The geometries studied here are regular polyhedra. Since GPAW is a real-space grid based code, any arrangement of clusters is easy to assemble and compute. The same methods and analysis tools can be extended to more complicated or larger geometries, and clusters of different shapes. Conductive linking between the clusters can also be modeled by channels of suitable jellium background density.

Compared to real 8-electron sodium clusters, the uniform spherical jellium background is an oversimplification. For example, since atomic Na_8 clusters are polygons in shape, the relative orientations of the neighboring clusters can also affect the charge transfer and plasmon coupling in an assembly. The effect of the shape could be studied by changing the jellium background from spherical to the experimental geometry, which would be an interesting follow-up work. Here, we concentrated on the general trends varying the separation and arrangement, the results representing rather an assembly of different cluster orientations than a single atomic system.

In the experimental studies and applications, the clusters usually consist of gold or silver atoms, not sodium. In these noble metals, the d electron screening weakens the surface plasmon resonance and thus reduces the interaction between the plasmons of neighboring clusters [33]. Additionally, gold and silver have smaller Wigner-Seitz radii than sodium, resulting in larger background density. This corresponds to smaller electron spill-out lengths for these noble metals [34, 35]. Since the CTPs require electron density overlap, this indicates that the onset of the CTPs would happen at smaller separation in gold or silver arrangements. Because of these differences, noble metal assemblies are expected to show a weaker coupling in the absorption spectra than the jellium arrangements with the density of sodium studied here.

Exact comparison to existing experiments is also hindered by the generally much larger size of the NPs and inter-particle separations in the experimental plasmonic assemblies, such as those mentioned in the introduction, compared to the jellium arrangements studied here. Specifically, none of the articles [5–13] report CTPs, which require very small inter-cluster separations. So far, CTPs have not been observed for cluster systems with similar arrangements and cluster sizes as studied here. Atomically precise monolayer-protected metal clusters [36] are promising candidates for building blocks of assemblies that would enable the experimental study of the plasmon coupling and charge transfer oscillations in this size range.

The jellium studies can pave way to more realistic atomistic calculations for modeling these systems. For example, even though the induced densities and DTCMs are more complex for assemblies of monolayer-protected gold clusters, the trends can be expected to be the same as here. By comparing the results of jellium calculations and atomistic calculations, the effect of the atomic structure can be separated. In addition, the results for jellium assemblies can help to identify the different features in the optical spectra for the atomistic systems.

ACKNOWLEDGMENTS

The authors thank Mikael Kuisma for useful discussions. This work was supported by the Academy of Finland (grants 294217 and 319208, H.H.'s Academy Professorship), the Emil Aaltonen Foundation and the Finnish Cultural Foundation (E.S.'s PhD scholarships). The computations were done at the CSC - the Finnish IT Center for Science (Grand Challenge project COUPLES).

[1] E. Prodan, C. Radloff, N. J. Halas, and P. Nordlander, A hybridization model for the plasmon response of complex nanostructures, Science **302**, 419 (2003).

[2] L. Polavarapu, J. Pérez-Juste, Q.-H. Xu, and L. M. Liz-Marzán, Optical sensing of biological, chemical and ionic species through aggregation of plasmonic nanoparticles, J. Mater. Chem. C **2**, 7460 (2014).

[3] G. Haran and L. Chuntonov, Artificial plasmonic molecules and their interaction with real molecules, Chem. Rev. **118**, 5539 (2018).

[4] J. Zuloaga, E. Prodan, and P. Nordlander, Quantum description of the plasmon resonances of a nanoparticle dimer, Nano Lett. **9**, 887 (2009).

[5] S. J. Barrow, X. Wei, J. S. Baldauf, A. M. Funston, and P. Mulvaney, The surface plasmon modes of self-assembled gold nanocrystals, Nat. Commun. **3**, 1 (2012).

[6] L. Lermusiaux and A. M. Funston, Plasmonic isomers *via* DNA-based self-assembly of gold nanoparticles, Nanoscale **10**, 19557 (2018).

[7] K. J. Park, J.-H. Huh, D.-W. Jung, J.-S. Park, G. H. Choi, G. Lee, P. J. Yoo, H.-G. Park, G.-R. Yi, and S. Lee, Assembly of 3D plasmonic clusters by 2D AFM nanomanipulation of highly uniform and smooth gold nanospheres, Sci. Rep. **7**, 1 (2017).

[8] N. Pazos-Perez, C. S. Wagner, J. M. Romo-Herrera, L. M. Liz-Marzán, F. J. García de Abajo, A. Wittemann, A. Fery, and R. A. Alvarez-Puebla, Organized plasmonic clusters with high coordination number and extraordinary enhancement in surface-enhanced Raman scattering (SERS), Angew. Chem. Int. Ed. **124**, 12860 (2012).

[9] A. S. Urban, X. Shen, Y. Wang, N. Large, H. Wang, M. W. Knight, P. Nordlander, H. Chen, and N. J. Halas, Three-dimensional plasmonic nanoclusters, Nano Letters **13**, 4399 (2013).

[10] X. Huang, Y. Liu, J. Barr, J. Song, Z. He, Y. Wang, Z. Nie, Y. Xiong, and X. Chen, Controllable self-assembled plasmonic vesicle-based three-dimensional SERS platform for picomolar detection of hydrophobic contaminants, Nanoscale **10**, 13202 (2018).

[11] J. Fontana, W. J. Dressick, J. Phelps, J. E. Johnson, R. W. Rendell, T. Sampson, B. R. Ratna, and C. M. Soto, Virus-templated plasmonic nanoclusters with icosahedral symmetry via directed self-assembly, Small **10**, 3058 (2014).

[12] N. Lebedev, I. Griva, W. J. Dressick, J. Phelps, J. E. Johnson, Y. Meshcheriakova, G. P. Lomonossoff, and C. M. Soto, A virus-based nanoplasmonic structure as a surface-enhanced Raman biosensor, Biosens. Bioelectron. **77**, 306 (2016).

[13] H. A. Nguyen, I. Jupin, P. Decorse, S. Lau-Truong, S. Ammar, and N. T. Ha-Duong, Assembly of gold nanoparticles using turnip yellow mosaic virus as an in-solution SERS sensor, RSC Adv. **9**, 32296 (2019).

[14] Y. A. Urzhumov, G. Shvets, J. Fan, F. Capasso, D. Brandl, and P. Nordlander, Plasmonic nanoclusters: a path towards negative-index metafluids, Opt. Express **15**, 14129 (2007).

[15] T. L. Doane and C. Burda, The unique role of nanoparticles in nanomedicine: imaging, drug delivery and therapy, Chem. Soc. Rev. **41**, 2885 (2012).

[16] A. G. Skirtach, C. Dejugnat, D. Braun, A. S. Susha, A. L. Rogach, W. J. Parak, H. Möhwald, and G. B. Sukhorukov, The role of metal nanoparticles in remote release of encapsulated materials, Nano Lett. **5**, 1371 (2005).

[17] T. S. Troutman, S. J. Leung, and M. Romanowski, Light-induced content release from plasmon-resonant liposomes, Adv. Mater. **21**, 2334 (2009).

[18] Nonappa, T. Lahtinen, J. S. Haataja, T.-R. Tero, H. Häkkinen, and O. Ikkala, Template-free supracolloidal self-assembly of atomically precise gold nanoclusters: From 2D colloidal crystals to spherical capsids, Angew. Chem. Int. Ed. **128**, 16269 (2016).

[19] V. Marjomäki, T. Lahtinen, M. Martikainen, J. Koivisto, S. Malola, K. Salorinne, M. Pettersson, and H. Häkkinen, Site-specific targeting of enterovirus capsid by functionalized monodisperse gold nanoclusters, Proc. Natl. Acad. Sci. U.S.A. **111**, 1277 (2014).

[20] E. Selenius, S. Malola, and H. Häkkinen, Analysis of localized surface plasmon resonances in spherical jellium clusters and their assemblies, J. Phys. Chem. C **121**, 27036 (2017).

[21] E. Selenius, S. Malola, M. Kuisma, and H. Häkkinen, Charge transfer plasmons in dimeric electron clusters, J. Phys. Chem. C **124**, 12645 (2020).

[22] V. Bonačić-Koutecký, P. Fantucci, and J. Koutecký, Systematic ab initio configuration-interaction study of alkali-metal clusters. II. Relation between electronic structure and geometry of small sodium clusters, Phys. Rev. B **37**, 4369 (1988).

[23] I. A. Solovyov, A. V. Solovyov, and W. Greiner, Structure and properties of small sodium clusters, Phys. Rev. A **65**, 053203 (2002).

[24] P. Zhang, J. Feist, A. Rubio, P. García-González, and F. J. García-Vidal, Ab initio nanoplasmonics: The impact of atomic structure, Phys. Rev. B **90**, 161407 (2014).

[25] J. J. Mortensen, L. B. Hansen, and K. W. Jacobsen, Real-space grid implementation of the projector augmented wave method, Phys. Rev. B **71**, 035109 (2005).

[26] J. Enkovaara, C. Rostgaard, J. J. Mortensen, J. Chen, M. Dułak, L. Ferrighi, J. Gavnholt, C. Glinsvad, V. Haikola, H. A. Hansen, H. H. Kristoffersen, M. Kuisma, A. H. Larsen, L. Lehtovaara, M. Ljungberg, O. Lopez-Acevedo, P. G. Moses, J. Ojanen, T. Olsen, V. Petzold, N. A. Romero, J. Stausholm-Møller, M. Strange, G. A. Tritsaris, M. Vanin, M. Walter, B. Hammer, H. Häkkinen, G. K. H. Madsen, R. M. Nieminen, J. K. Nørskov, M. Puska, T. T. Rantala, J. Schiøtz, K. S. Thygesen, and K. W. Jacobsen, Electronic structure calculations with GPAW: a real-space implementation of the projector augmented-wave method, J. Phys. Condens. Matter **22**, 253202 (2010).

[27] J. P. Perdew and Y. Wang, Accurate and simple analytic representation of the electron-gas correlation energy, Phys. Rev. B **45**, 13244 (1992).

[28] M. Walter, H. Häkkinen, L. Lehtovaara, M. Puska, J. Enkovaara, C. Rostgaard, and J. J. Mortensen, Time-dependent density-functional theory in the projector augmented-wave method, J. Chem. Phys. **128**, 244101 (2008).

[29] X. Andrade, S. Botti, M. A. Marques, and A. Rubio, Time-dependent density functional theory scheme for efficient calculations of dynamic (hyper)polarizabilities, J.

Chem. Phys. **126**, 184106 (2007).
[30] S. Malola, L. Lehtovaara, J. Enkovaara, and H. Häkkinen, Birth of the localized surface plasmon resonance in monolayer-protected gold nanoclusters, ACS Nano **7**, 10263 (2013).
[31] T. P. Rossi, M. Kuisma, M. J. Puska, R. M. Nieminen, and P. Erhart, Kohn–Sham decomposition in real-time time-dependent density-functional theory: an efficient tool for analyzing plasmonic excitations, J. Chem. Theory Comput. **13**, 4779 (2017).
[32] M. Walter, J. Akola, O. Lopez-Acevedo, P. D. Jadzinsky, G. Calero, C. J. Ackerson, R. L. Whetten, H. Grönbeck, and H. Häkkinen, A unified view of ligand-protected gold clusters as superatom complexes, Proc. Natl. Acad. Sci. U.S.A. **105**, 9157 (2008).
[33] D. W. Brandl, C. Oubre, and P. Nordlander, Plasmon hybridization in nanoshell dimers, J. Chem. Phys. **123**, 024701 (2005).
[34] N. Lang and W. Kohn, Theory of metal surfaces: charge density and surface energy, Phys. Rev. B **1**, 4555 (1970).
[35] N. Lang and W. Kohn, Theory of metal surfaces: work function, Phys. Rev. B **3**, 1215 (1971).
[36] T. Tsukuda and H. Häkkinen, *Protected Metal Clusters: From Fundamentals to Applications*, Vol. 9 (Elsevier, 2015).

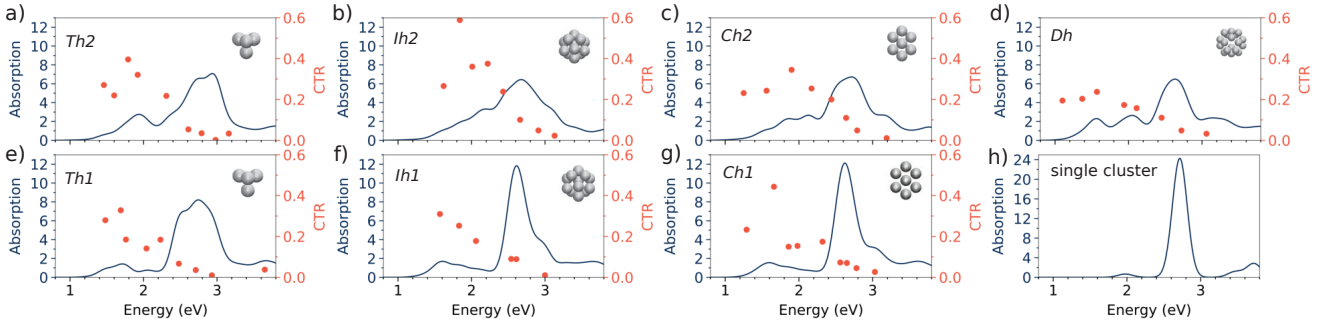

FIG. 3. The absorption spectra and CTR values for all the studied systems. The absorption strength has been divided by the number of clusters for each system. The spectrum of a single cluster, shown with a different y axis scale, is included for comparison.

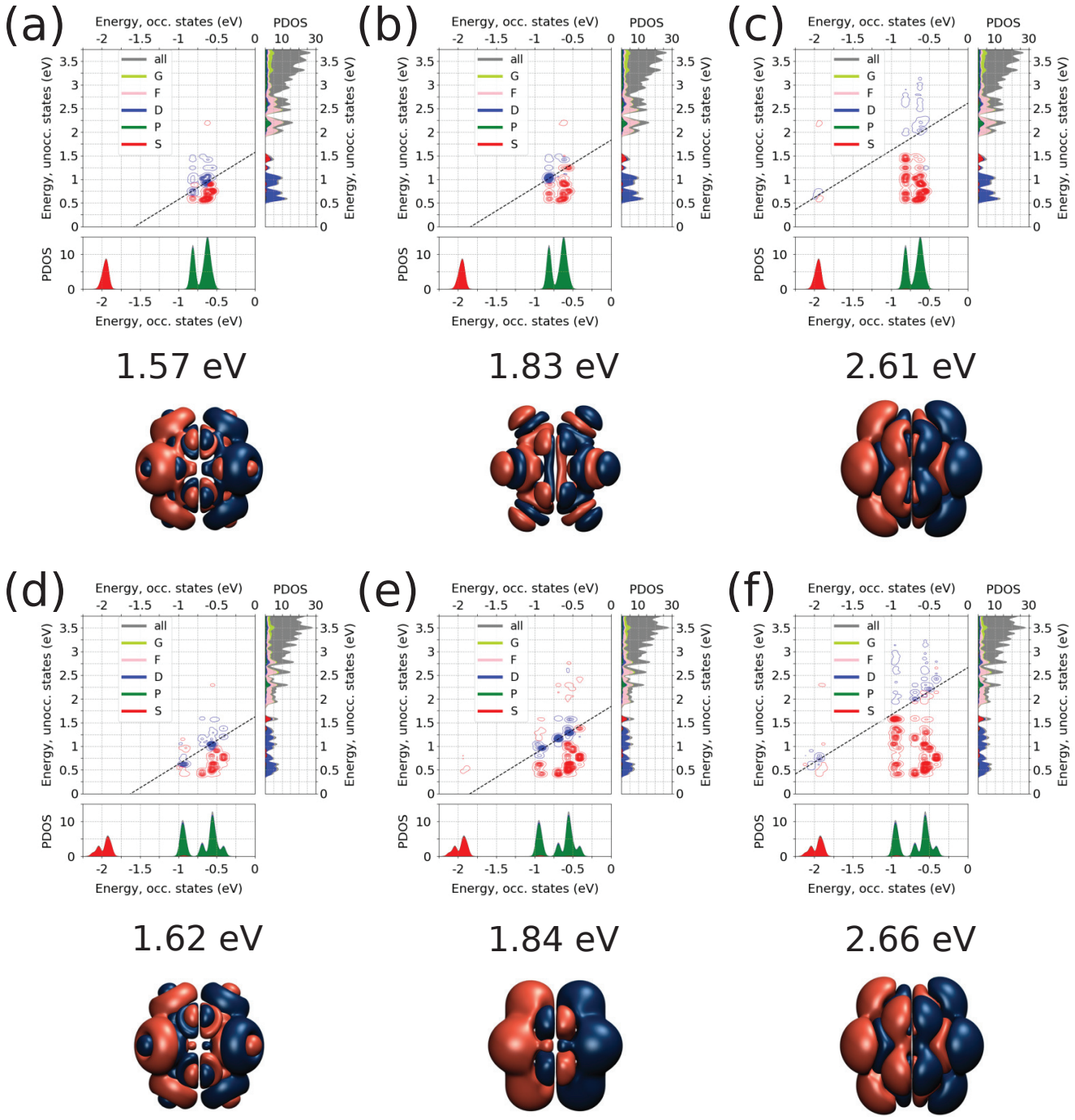

FIG. 4. The DTCM figures and isosurfaces of induced densities for selected peaks for the icosahedral geometries. (a)–(c): separation $S = 0.5r$ (*Ih1*), (d)–(f): separation $S = 0.25r$ (*Ih2*). The red and blue colours of the contour plot show positive and negative contributions to the transitions dipole moment, respectively. The colors of the PDOS indicate the superatomic symmetries of the orbitals around each individual cluster in the arrangement, and the PDOS shown is the sum of these projections. The gray color indicates higher symmetries and electron density outside of the projection spheres.

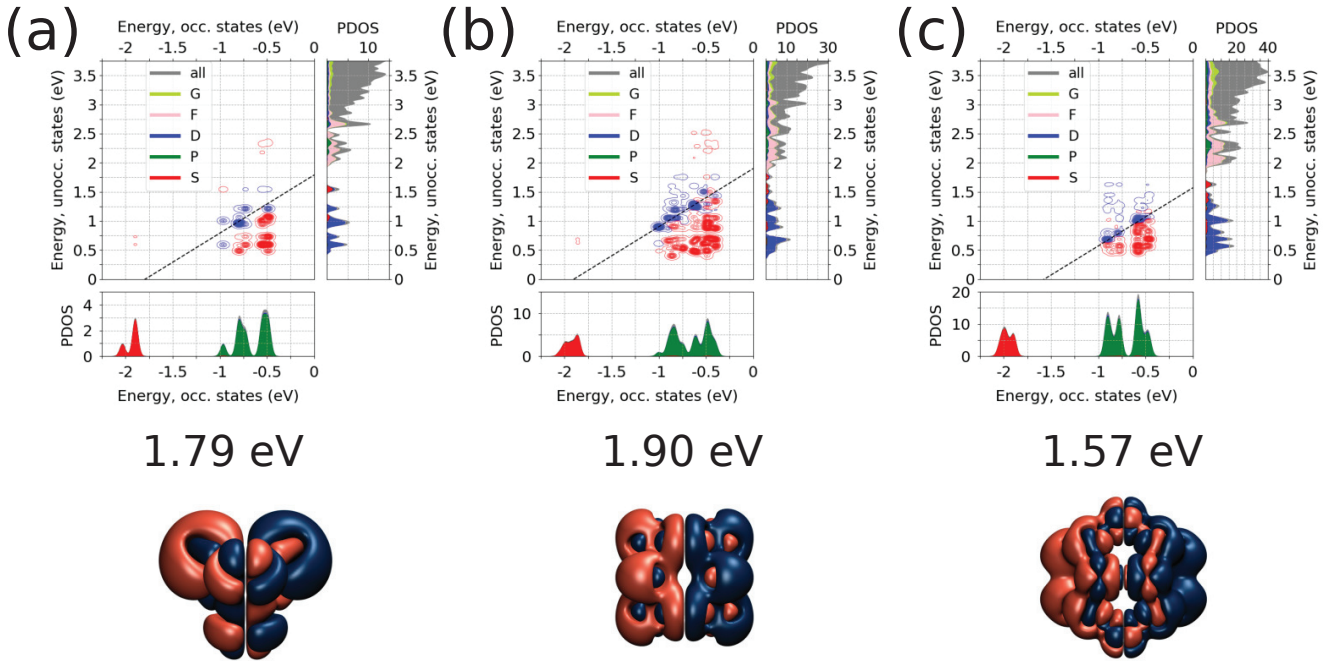

FIG. 5. The DTCM figures and isosurfaces of induced densities for the peak with the highest CTR value for (a) *Th2*, (b) *Ch2*, and (c) *Dh*, which all have a separation of $S = 0.25r$.